University of Maribor Press

ISSN 1854-0171

ACTA GEOTECHNICA SLOVENICA

2018/1

VOL. 15

ISSN: 1854-0171

ACTA GEOTECHNICA SLOVENICA

Ustanovitelji | Founders

Univerza v Mariboru, Fakulteta za gradbeništvo, prometno inženirstvo in arhitekturo
University of Maribor, Faculty of Civil Engineering, Transportation Engineering and Architecture

Univerza v Ljubljani, Fakulteta za gradbeništvo in geodezijo
University of Ljubljana, Faculty of Civil and Geodetic Engineering

Univerza v Ljubljani, Naravoslovnotehniška fakulteta
University of Ljubljana, Faculty of Natural Sciences and Engineering

Slovensko geotehniško društvo
Slovenian Geotechnical Society

Društvo za podzemne in geotehniške konstrukcije
Society for Underground and Geotechnical Constructions

Izdajatelj | Publisher

Univerza v Mariboru, Fakulteta za gradbeništvo, prometno inženirstvo in arhitekturo
Faculty of Civil Engineering, Transportation Engineering and Architecture

Naklada | Circulation

200 izvodov - issues

Cena | Price

25 EUR/letnik - 25 EUR/vol.; (50 EUR for institutions/za institucije)

Tisk | Print

Tiskarna Saje

Revija redno izhaja dvakrat letno. Članki v reviji so recenzirani s strani priznanih mednarodnih strokovnjakov. Baze podatkov v katerih je revija indeksirana: SCIE - Science Citation Index Expanded, JCR – Journal Citation Reports / Science Edition, ICONDA - The international Construction database, GeoRef. Izid publikacije je finančno podprla Javna agencija za raziskovalno dejavnost Republike Slovenije iz naslova razpisa za sofinanciranje domačih periodičnih publikacij.

Založnik | Published by

Univerzitetna založba Univerze v Mariboru
Slomškov trg 15, 2000 Maribor, Slovenija
e-pošta: zalozba@um.si, http://press.um.si/, http://journals.um.si/

University of Maribor Press
Slomškov trg 15, 2000 Maribor, Slovenia
e-mail: zalozba@um.si, http://press.um.si/, http://journals.um.si/

Naslov uredništva | Address

ACTA GEOTECHNICA SLOVENICA
Univerza v Mariboru, Fakulteta za gradbeništvo, prometno inženirstvo in arhitekturo
Smetanova ulica 17, 2000 Maribor, Slovenija
Telefon / Telephone: +386 (0)2 22 94 300
Faks / Fax: +386 (0)2 25 24 179
E-pošta / E-mail: ags@uni-mb.si

Spletni naslov | web Address

http://zalozba.um.si/index.php/ags/index

The journal is published twice a year. Papers are peer reviewed by renowned international experts. Indexation data bases of the journal: SCIE - Science Citation Index Expanded, JCR – Journal Citation Reports / Science Edition, ICONDA- The international Construction database, GeoRef. The publication was financially supported by Slovenian Research Agency according to the Tender for co-financing of domestic periodicals.

DOLOČITEV STRIŽNEGA MODULA GLINENO PEŠČENIH MEŠANIC S PREIZKUSOM Z BENDERJEVIM ELEMENTOM

Ali Firat Cabalar *(vodilni avtor)*
University of Gaziantep,
Civil Engineering Department
27310 Gaziantep, Turčija
E-pošta: cabalar@gantep.edu.tr

M. M. Khalaf
University of Gaziantep,
Civil Engineering Department
27310 Gaziantep, Turčija

Z. Karabash
University of Gaziantep,
Civil Engineering Department
27310 Gaziantep, Turčija

Ključne besede

pesek, glina, benderjev element, enoosna tlačna trdnost

Izvleček

Na glineno peščenih mešanicah so bili izvedeni preizkusi z benderjevim elementom (BE). Z njimi se je raziskalo spreminjanje strižnega modula majhnih deformacij (G_{max}) v odvisnosti od vsebnosti peska in fizikalnih karakteristik zrn peskov (velikosti, oblike) v preiskovanih mešanicah. Tri različne granulacije peskov (0.6-0.3 mm, 1.0-0.6 mm in 2.0-1.0 mm) s posebnimi oblikami (okrogle, oglate) so bile dodane malo stisljivi glini v deležih 0 % (čista glina), 10 %, 20 %, 30 %, 40 % in 50 %. Za korelacijsko analizo so bili na enakih vzorcih izvedeni tudi enoosni preizkusi tlačne trdnosti (UC). Preizkusi so pokazali, da so izmerjene vrednosti za G_{max} in enoosno tlačno trdnost (q_u) preizkušancev z oglatimi zrni peska nižje kot za okrogla zrna peska, in sicer za vse velikosti in razmerja mešanja. Z naraščanjem vsebnosti peska v mešanicah, narašča vrednost G_{max}, medtem, ko vrednost q_u upada. Rezultati nadalje kažejo, da tako vrednosti G_{max}, kot tudi vrednosti q_u upadajo z zmanjšanjem velikosti zrn peska.

SHEAR MODULUS OF CLAY-SAND MIXTURES USING BENDER ELEMENT TEST

Ali Firat Cabalar *(corresponding author)*
University of Gaziantep,
Civil Engineering Department
27310 Gaziantep, Turkey
E-mail: cabalar@gantep.edu.tr

M. M. Khalaf
University of Gaziantep,
Civil Engineering Department
27310 Gaziantep, Turkey

Z. Karabash
University of Gaziantep,
Civil Engineering Department
27310 Gaziantep, Turkey

Keywords

sand, clay, bender element, unconfined compressive strength

DOI https://doi.org/10.18690/actageotechslov.15.1.3-15.2018

Abstract

Bender-element (BE) tests were conducted on clay-sand mixtures to investigate the variation of small strain-shear modulus (G_{max}) with the sand content and the physical characteristics (size, shape) of the sand grains in the mixtures. Three different gradations (0.6–0.3 mm, 1.0–0.6 mm and 2.0–1.0 mm) of sands having distinct shapes (rounded, angular) were added to a low-plasticity clay with mixture ratios of 0% (clean clay), 10%, 20%, 30%, 40%, and 50%. For the purposes of performing a correlation analysis, unconfined compression (UC) tests were also carried out on the same specimens. The tests indicated that both the G_{max} and unconfined compressive strength (q_u) values of the specimens with angular sand grains were measured to be lower than those with rounded sand grains, for all sizes and percentages. As the percentage of sand in the mixture increases, the G_{max} values increase, while the q_u values decrease. The results further suggested that the G_{max} values decrease as the q_u values decreases as the size of the sand grains reduces.

1 INTRODUCTION

Most of the experimental studies for determining the engineering characteristics of soils focused on the behavior of clean soil samples. However, site investigations showed that most of the soil types contain both cohesive and cohesionless grains with various chemical and physical properties [1]. The governing role of either cohesive or cohesionless grain matrices on the overall behavior of the sample can be expected to change based on the properties of both materials. The interaction between cohesionless and cohesive grain matrices can affect the overall behavior of such mixed soils subjected to various dynamic loadings as well as monotonic loadings. Actually, it is of great importance to identify the dynamic behavior of such soils in order to make an accurate stability analysis of any systems subjected to cyclic loads, for example, those resulting from earthquakes, machine foundation, sea waves, wind, and traffic loads [2,3]. Many problems in such loadings are dominated by wave propagation effects where only low levels of strain are induced in the soil. The shear modulus and the damping ratio are the most significant soil properties influencing such small strain behavior. Small strains, typically shear strains of less than 0.001%, do not cause an important nonlinear stress-strain response in the soil. Hence, an equivalent linear model can be assumed. The most significant stiffness parameter at this level is the small strain shear modulus, G_{max}, which is a parameter required for advanced soil modeling as well as solving soil dynamic problems. A common way of determining

the small strain shear modulus is to measure the shear wave velocity and then compute G_{max} as follows [4,5]:

$$G_{max} = \rho v_s^2 \text{ with } v_s = L/t \qquad (1)$$

where ρ is the density of the soil, v_s is the shear wave velocity, L is the wave path length between the tips of source and receiver elements, and t is the shear wave travel time. In order to determine the small strain shear modulus of soils, one of the commonly used laboratory tests is the Bender Element (BE), which consists of two thin plates of piezoelectric material bonded together, with two conductive outer layers and a metal shim at the center [6]. In spite of the difficulties in determining the shear wave's arrival time [7], a soil sample can be tested subsequently for other soil characteristics, because the BE tests do not disturb the soil samples, thus facilitating a comparison with other results [8-11]. As characterizing the behaviour of specimens under dynamic loading becomes much more complex and expensive than that of specimens subjected to monotonic loading, only a few researchers have been carried out on correlating a dynamic test with a static test so far [12-13]. Therefore, there is a real need for an in-depth investigation of a comparison between dynamic tests and static tests. Actually, both studies by Consoli et al. [12] and Flores et al. [13] suggest that the unconfined compressive strength (q_u) values and G_{max} defined by the BE can be closely correlated for artificially cemented soils. The unconfined compression (UC) test is by far the most popular technique for soil shear testing as it is one of the cheapest and fastest techniques for measuring shear strength. The technique is employed primarily for cohesive soils recovered from thin-walled sampling tubes [14].

It has long been understood that the physical properties (e.g., size, shape) of sand grains have a significant influence on the engineering properties of a soil matrix [15-23]. Terzaghi [15] postulated that the compressibility of a cohesionless material is governed by the grain size, uniformity, volume of voids and mica content. The observations, made by Gilboy [16], that any system of analysis or classification of soil that neglects the presence and effect of the shape will be incomplete and erroneous. Holubec and D'Appolinia [24] showed that the results of dynamic penetration tests in sands depend on the grain shape. Cornforth [25] and Holtz and Kovacs [26] demonstrated how the grain shape impacts on the internal fiction angle (φ). Cedergen [27] pointed out that the grain shape affects the permeability. Holubec and D'Appolinia [24], Wadell [28], Krumbein [29], Powers [30], Youd [31], and Cho et al. [32] have introduced detailed explanations relating to grain shape. Two independent properties are typically employed to describe the shape of a soil grain: (i) Roundness is a measure of the extent to which the edges and corners of a grainhave been rounded; (ii) Sphericity (form) describes the overall shape of a grain (it is a measure of the extent to which a grain approaches a sphere in shape). Wadell [28] proposed a simplified sphericity (S) parameter, ($D_{max\text{-}insc}/D_{min\text{-}circ}$), where $D_{max\text{-}insc}$ is the diameter of a maximum inscribed circle and $D_{min\text{-}circ}$ is the diameter of a minimum sphere circumscribing a gravel grain. Wadell [28] defined roundness (R) as $D_{i\text{-}ave}/D_{max\text{-}insc}$,

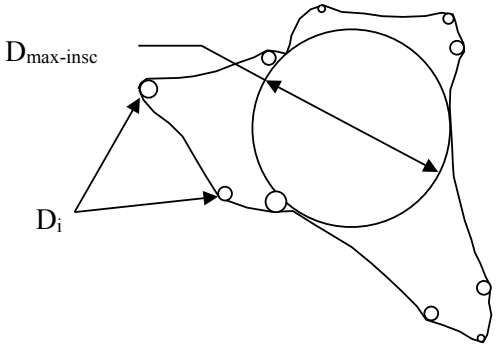

Figure 1. Graphical representation of roundness, R (redrawn from Muszynski and Vitton, 2012).

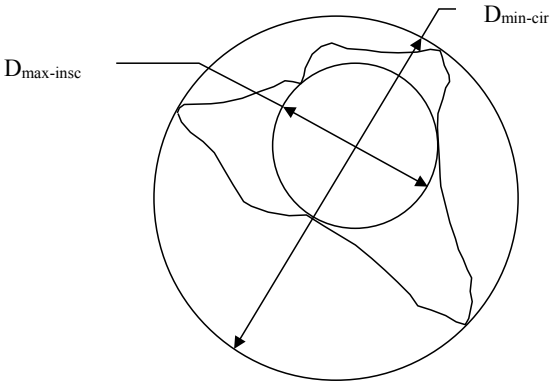

Figure 2. Graphical representation of sphericity, S (redrawn from Muszynski and Vitton, 2012).

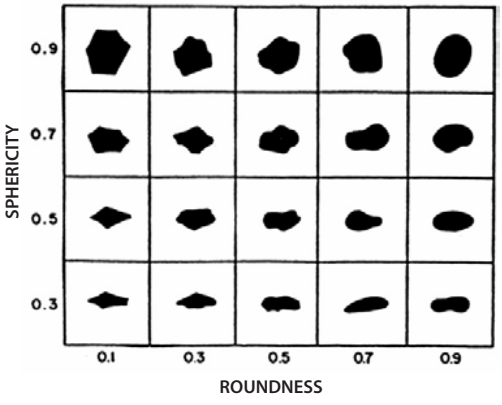

Figure 3. Comparison chart (Santamarina and Cho, 2004).

(2)

where $D_{i\text{-}ave}$ is the average diameter of the inscribed circle for each corner of the grain. Figures 1-3 define R, S and a chart for comparing them to determine grain shape, respectively [29, 30].

The soils are usually obtained from different sites having a wide range of cohesive and cohesionless grains. The main focus of this investigation is defining the small strain shear modulus (G_{max}) of clay-sand mixtures whose properties are intermediate between those of clays and sands. G_{max} is a significant factor representing the small strain response of soils under seismic load, and an important parameter in the design of foundations where only a small deformation takes place. In the present study, small strain shear modulus measurements (G_{max}) of various compacted clay-sand mixtures were performed at optimum water content (w_{opt}) conditions. The tests were carried out using a testing apparatus that allows Bender Element (BE) and Unconfined Compression (UC) tests to be conducted on an identical specimen, and in this way a more reliable comparison will be obtained. Tests on the mixtures of clay and sands with different contents and physical properties were performed in an attempt to explain the differences in the behaviors of the shear waves between the test specimens. The objective of this study was partly scientific curiosity, but also to judge the usefulness of UC tests in predicting the G_{max} of clay-sand mixtures. Accordingly, this study will focus on two important aspects of measuring the G_{max} of clay-sand mixtures: (i) identifying the specific influence of quantity, size, and shape of sand grains in the mixtures,where factors such as density were maintained constant for each specimen, (ii) assessing the testing results deduced from the BE and UC tests on the same specimens.

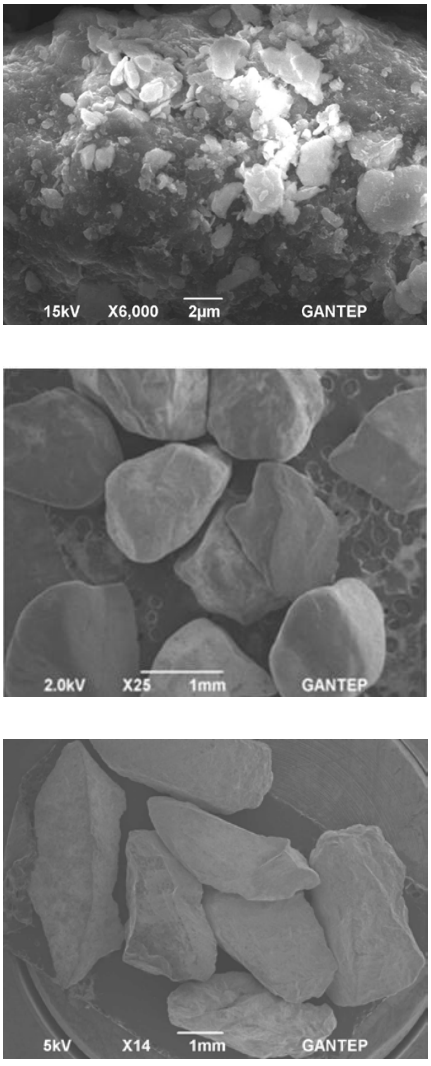

Figure 4. SEM pictures of the (top) clay, (middle) rounded sand, (bottom) angular sand used during the experimental study.

2 EXPERIMENTAL STUDY

2.1 Materials

The materials used in the tests to produce the mixtures were clay, Crushed Stone Sand, Narli Sand, and de-aired water.

The clay used in the experimental studies was quarried from the Gaziantep University Campus. Its plastic limit and liquid limit values are 23, and 48, respectively [33]. The specific gravity (G_s) of the clay grains was found to be 2.61. Based on the Unified Soil Classification System (USCS), the clay was classified as 'low plasticity clay' (CL). Figure 4 shows the scanning electron micrograph (SEM) pictures of the clay used during the experimental investigations. Narli Sand (NS), representing a type of rounded sand, was quarried in and around Narli, Kahramanmaras in southern-central Turkey; it is widely consumed in earthworks in certain regions of Turkey. As can be seen clearly from Figure 4, Narli Sand grains have a rounded, whereas the Crushed Stone Sand grains have angular, shape of grains. The specific gravity of the grains was found to be 2.65 for Narli Sand, and 2.68 for Crushed Stone Sand. Three different gradations of the sands falling between 0.6 mm and 0.3 mm, 1.0 mm and 0.6 mm, and 2.0 mm and 1.0 mm were artificially selected to provide uniform specimens for visual classification purposes (Figure 5), and then were added to the CL type clay at mixture ratios of 0%, 10%, 20%, 30%, 40%, and 50%. The roundness (R) estimates for the angular sand (CSS) and rounded sand (NS) were obtained as 0.16 and 0.43, while the sphericity (S) estimates were found to be 0.55 and 0.67, respectively. Further observations of the grain size and shape analysis

Table 1. Some properties of the sands used during the experimental study.

No	Gradation (mm)	D_{10} (mm)	D_{30} (mm)	D_{50} (mm)	D_{60} (mm)	c_u	c_c	USCS	R		S	
									NS	CSS	NS	CSS
1	0.6-0.3	0.33	0.39	0.45	0.48	1.45	0.96	SP				
2	1.0-0.6	0.64	0.72	0.80	0.84	1.31	0.96	SP	0.43	0.16	0.67	0.55
3	2.0-1.0	1.10	1.30	1.50	1.60	1.45	0.96	SP				

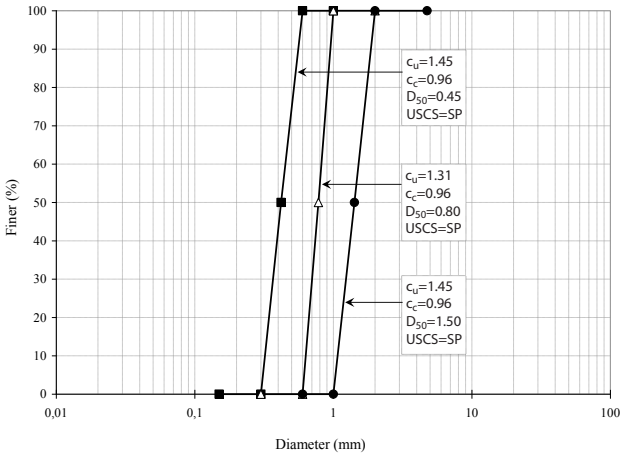

Figure 5. Particle size distributions for the sands used during the experimental study.

including roundness (R) and sphericity (S) estimations based on the study by Muszynski and Vitton [34] are presented in Table 1.

The specimens were tested by using de-aired tap water as the pore fluid.

2.2 Testing apparatus and specimen preparation

Bender-element (BE) tests were conducted on the different clay-sand mixtures to measure the shear wave velocity at various states in order to estimate the small strain shear modulus (G_{max}). The tests were carried out just before applying a uniaxial load to the compacted specimens taken out from a two-part split mould with a 70-mm diameter and a 147-mm height. The shear wave velocity measurements were performed with a pair of bender elements, one of which was installed on the pedestal, and the other one was placed in the top cap. The bender element on the pedestal was used as transmitter, while the other in top cap was used as a receiver to measure the shear wave propagated through a specimen. The software package for data acquisition as well as the BE testing equipment used during the experimental works is a product of GDS Instruments Limited. The v_s estimates were achieved by employing a sinusoidal wave input with a magnitude of 10 V, and periods of 0.01 mV. The received wave was acquired using a sampling frequency of 15kHz, and a sampling interval of 5 ms, which were selected to provide a received signal with an optimal resolution. From the study by Viggiani and Atkinson [35], the shear wave velocity transmitted through the specimens was estimated using the 'tip-to-tip' distance between the bender elements, and then the wave travel time was measured. In order to obtain the arrival time value, the first major peak-to-peak method was employed. The arrival time in this method was defined as the time measured between the peak of the transmitted signal and the first major peak of the received signal.

The unconfined compression (UC) test, which is used for measuring undrained shear strength of cohesive soils because of the simplicity of the test technique, was employed on various clay-sand specimens compacted in a mould with a 70-mm in diameter and a 147-mm height [14]. The performance of the specimens was investigated with the clean clay, and clay with sand at the

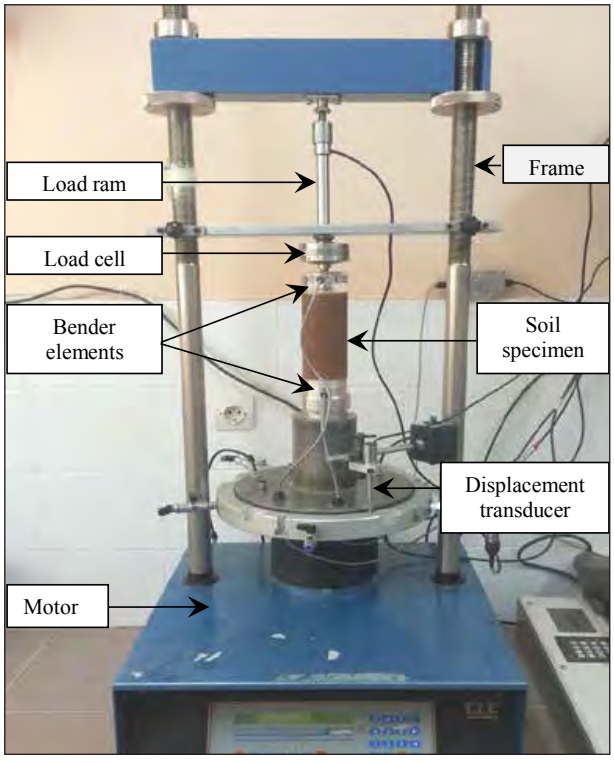

Figure 6. The equipment combining BE and UC tests.

mixture ratios of 10%, 20%, 30%, 40%, and 50% using the dry weight of the specimens. The amount of each constituent in a mixture was determined by employing a compaction test in order to prepare the specimens at the maximum dry unit weight (γ_{drymax}) and the optimum moisture content (w_{opt}) values. In this experimental work, the required amount of sand, clay, and water were weighed, and then mixed until a uniform mixture was reached. The specimens were kept within plastic bags for a period of 24 hours to avoid the loss of moisture, and to obtain a homogeneous paste. The mixture to be tested was then statically compacted into a two-part cylindrical mould (70mm × 147mm) in three layers. Then, the specimens were taken out of the mould, trimmed out, and placed on to the UC testing equipment in order to estimate the shear wave velocity first, and then the q_u value for each specimen. The rate of strain employed in the UC tests was 0.7 mm/min. Figure 6 presents the equipment used for the experimental determination of both the G_{max} and q_u values.

3 RESULTS AND DISCUSSION

Table 3 gives a summary of the UC testing results reported here. From the tests with both clay and clay-sand mixtures compacted at w_{opt} and γ_{drymax}, the unconfined compressive strength (q_u) values were observed to be significantly affected by the addition of sands. The q_u values decreased as the amount of sand content increased in all size, shape, and content of the sand grains. Similar results were also reported by Stavridakis [36] for an investigation of problematic soils. It is interpreted that the difference in testing results can be attributed to the soil suction as well as quantity and physical characteristics of the sand grains (shape, size) leading to various void ratios. The soil suction could be effective in the shear strength and the deformation characteristics of soils for the highly saturated condition at the unconfined compression test [37-39]. However, it seems to be beyond the scope of this study to provide a detailed discussion on the soil suction, since the amount of water was selected as wopt for each specimen that creates a very similar range of saturation degree as well as soil suction in all the specimens tested (Table 2).The shape of the sand grains in the mixtures is of great importance to the undrained shear strength behavior of the mixtures tested in the UC tests. As can be seen from Figure 7, the q_u obtained for the clay with CSS grains between 0.6mm and 0.3mm have the minimal values, while the the q_u obtained for the clay with NS grains between 2.0mm and 1.0mm have the maximal values. Actually, the mixtures with angular shaped grains (CSS) at all three gradations exhibited much lower q_u values for all the contents of sands. For instance, the q_u values of the specimens with 30% rounded sand content (NS)

Table 2. Compaction testing results and values of saturation degree for different mixtures.

Gradation (mm)	Sand content (%)	NS			CSS		
		γ_{drymax} (kN/m^3)	w_{opt} (%)	S_r (%)	γ_{drymax} (kN/m^3)	w_{opt} (%)	S_r (%)
(0.6-0.3)	0	17.12	18.4	86.1	17.12	18.4	86.1
	10	17.41	16.8	82.6	17.24	16.3	77.8
	20	17.83	15.8	83.6	17.65	15.3	78.2
	30	18.25	14.6	83.2	18.02	14.2	77.3
	40	18.59	13.5	81.9	18.41	13.1	76.3
	50	18.93	12.7	82.2	18.74	12.3	76.0
(1.0-0.6)	10	17.58	16.2	81.9	17.44	15.7	77.4
	20	18.04	15.2	83.3	17.86	14.8	78.3
	30	18.57	14.3	86.1	18.39	13.9	80.5
	40	18.88	13.4	85.6	18.69	13.0	79.5
	50	19.12	12.6	84.5	18.93	12.3	78.6
(2.0-1.0)	10	17.76	15.5	80.7	17.58	15.1	76.2
	20	18.23	14.6	82.6	18.08	14.2	77.9
	30	18.76	13.8	85.9	18.57	13.4	80.1
	40	19.07	12.9	85.3	18.90	12.5	79.3
	50	19.31	12.2	84.7	19.16	11.8	78.6

Table 3. q_u values (kPa) for the mixtures tested.

Sand content (%)	NS						CSS					
	0.6-0.3 mm	*e*	1.0-0.6 mm	*e*	2.0-1.0 mm	*e*	0.6-0.3 mm	*e*	1.0-0.6 mm	*e*	2.0-1.0 mm	*e*
0	355	0.577	355	0.577	355	0.577	355	0.577	355	0.577	355	0.577
10	278	0.548	295	0.533	314	0.518	266	0.565	280	0.547	296	0.535
20	250	0.508	267	0.491	288	0.476	231	0.528	253	0.506	263	0.491
30	221	0.471	246	0.446	254	0.431	206	0.495	222	0.465	237	0.451
40	190	0.442	209	0.419	223	0.405	174	0.462	197	0.440	209	0.424
50	163	0.413	174	0.399	187	0.385	151	0.435	163	0.421	176	0.404

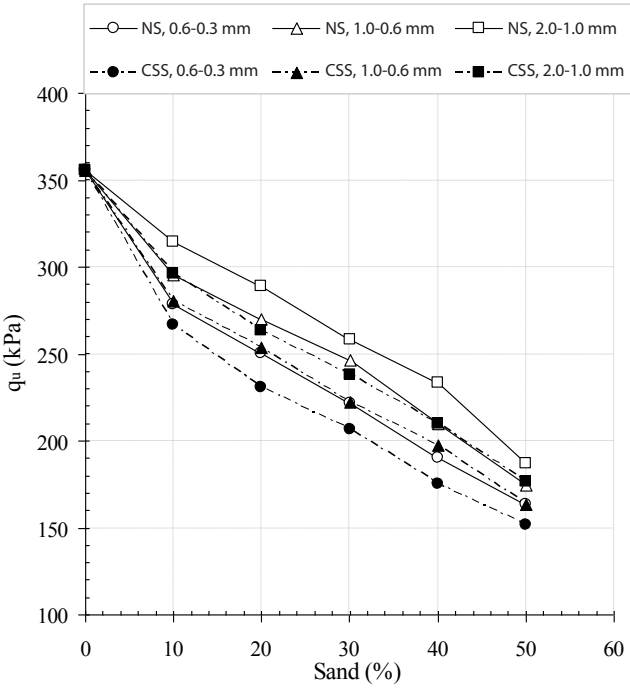

Figure 7. The effect of sand content (%) on the change of q_u (kPa).

were found to be 221 kPa, 246kPa, and 254 kPa, while those with same amount of angular sand content (CSS) were 206 kPa, 222 kPa, and 237 kPa for the cohesionless materials of 0.6–0.3mm, 1.0–0.6mm, and 2.0–1.0mm, respectively. In the light of the papers by Cabalar et al. [22], Cho et al. [32], Rothenburg and Bathurst [40], Thornton [41], Cabalar [42], it is probably because of the open fabric structure in the specimens with angular sand grains (CSS). Hence, based on the grain fabric taking place in the specimens, the contact points (coordination number) among soil grains decrease, the overall behaviour of the mixture is controlled by the void ratio, *e* (Table 3). The sands used during the experimental study have the same classification (SP) although they have different gradation curves. The grain size distribution of the cohesionless materials used in the tests plays a significant role in determining the UC testing results. It was realized that the smaller the size of sand grains the specimens have, the less the q_u (Figure 7).For example, the specimens with 30% angular sand grains have 206 kPa, 222 kPa, and 237 kPa for the sizes of 0.6–0.3mm, 1.0–0.6mm, and 2.0–1.0mm, respectively. The authors' interpretation is that the soil grains have much less contact points in the specimens prepared with smaller size sand grains than those with larger sand grains, hence the overall strength behavior of the specimens is mainly governed by the void ratio (*e*).

It has long been understood that the void ratio (*e*) of a soil matrix is the ratio of voids to the volume of solid grains. The resulting void ratios by the clean angular sand grains are larger than those for clean rounded grains [32,43]. However, the testing results described here have not been conducted on the clean sands, rather the results have been obtained on the sand-clay mixtures, which are thought of as a composite matrix of finer and coarser soil grains. Therefore, in the light of the numerous investigations [44,47], analyzing the test results on sand-clay mixtures becomes more versatile if the effects of sand and clay grains are studied separately. This separation appears to be important in describing the use of the intergranular void ratio (e_s) as an alternative parameter to define the undrained shear-strength behaviour of sand-clay mixtures rather than using traditional void ratio (*e*) values [23,48,49,50]. Actually, the intergranular void ratio concept was first proposed by Mitchell [51], and followed by Kenny [52], Lupini et al. [53], and Thevanayagam [54] by assuming that the sand grains can be thought of as the skeleton of soil matrix, and the clay grains occupy the voids between the sand grains, which are defined as the intergranular void ratio (e_s). The researchers indicated that, based on the amount of clay grains present, the sand grains are in contact with each other and the overall behaviour of the mixture is controlled by the sand grains. On the other hand, when the contact points between the sand grains decrease, the

behaviour of the mixture is controlled by the clay grains. From the investigation by Monkul and Ozden[45], the establishment of direct contacts of the sand grains can be initiated when the intergranular void ratio of the mixture becomes equal to the maximum void ratio of the sand grains, i.e., e_s=e_{max}. The clay content in the case of e_s=e_{max} is referred to as 'transition fines content'. The fact is that the value of e_s is always higher than the value of e employed in both tests performed in the present study due to the characteristics of the undrained shear strength tests, although the interactions between e_s and e were found to be changed with certain test equipment, including an oedometer, triaxial compression, cyclic triaxial, and resonant column [21,45,55,58]. Hence, the grains of both angular (CSS) and rounded (NS) sands used in the present study are considered as floating in the clay matrix. Then, it was seen that the clay with angular sand grains (CSS) resulted in lower q_u values in UC tests, since the random packing of angular grains resulting void ratios are larger than those of rounded grains (NS). Thus, it was concluded that the less angularity in sand grains the more q_u values obtained in the sand-clay mixtures.Cabalar and Hasan [23] had further stated that (i) mixtures of clay and sand grains with a lower roundness exhibit higher transition fines content (FC_t) values and that a (ii) smaller size of sands with clay gives a higher compressibility.

As Hardin [57] stated the void ratio is also influential on the shear modulus (G_{max}). Jamiolkowski et al. [58] supported Hardin [57] considering the statement of void ratio dependence on G_{max} estimates. As several other researchers have also indicated (Vucetic and Dobry, [59]; Shibuya and Tanaka, [60]; Santagata et al., [61]), the effect of increasing G_{max} with decreasing void ratio (e). An analysis of the results of the bender-element tests on clay only and clay with various types of sands indicated that the G_{max} tended to increase at severallevelsby adding different amount of sands (Table 4).Therefore, the G_{max} estimates in each condition should be investigated individually. For example, the G_{max} value of clay only increased sharply from 23 MPa to 40 MPa by adding 10% rounded sand at a 2.0–1.0mm grain size interval. However, the increment observed for the clay with angular sand at both same amount and grain sizeinterval was found to be slightly lower, i.e., 39 MPa.It was realized that the difference in G_{max} values of the specimens with same size sand grains is generally less than 5%, which means that the difference observed should not be primarily because of the difference in the grain shape of the sands used in the mixtures. Because they have similar values for coefficient of uniformity (c_u), and the coefficient of curvature (c_c), besides the mean particle size (D_{50}) has an ignorable influence on the elastic modulus [62,63]. Two possible reasons could be the difference in the individual grain contact stiffness due to difference (i) in the mineralogy or the surface roughness, and (ii) the size of the grains. Santamarina and Cascante [64] determined the wave velocity in mildly rusted and rusted steel sphere sand indicated that the surface roughness can decrease the stiffness. However, the sand grains of both angular (CSS) and rounded (NS) sands in the present study are thought to be covered with clay grains, then they do not contact with each other directly. Therefore, it is postulated that the mineralogy or the surface roughness of the sand grains seems to be beyond the scope of this study.To evaluate the influence of the size of sand grains on the G_{max} values, the results obtained for the same shape of both sand grains with different amounts of clay were compared. For example, the G_{max} values for the specimen prepared with 40% angular sand between 0.6 mm and 0.3 mm, 1.0 mm and 0.6 mm, and2.0 mm and 1.0 mm are 37 MPa, 40 MPa, and 42 MPa, respectively. Actually, the G_{max} values for the clay with smaller grains were found to be always lower than those with larger sand grains. It was seen that the difference in G_{max} values of the 0.6–0.3mm and 1.0–0.6mm specimens with the same shape sand grains is generally more than 5%, and those of the 0.6–0.3mm and 2.0–1.0mm is more than 10%, which means that the grain size of the sands used in the mixtures has the primary importance. Similar to the observations made

Table 4. G_{max} values (MPa) for the mixtures tested.

Sand content (%)	NS						CSS					
	0.6-0.3 mm	e	1.0-0.6 mm	e	2.0-1.0 mm	e	0.6-0.3 mm	e	1.0-0.6 mm	e	2.0-1.0 mm	e
0	23	0.577	23	0.577	23	0.577	23	0.577	23	0.577	23	0.577
10	36	0.548	38	0.533	40	0.518	34	0.565	37	0.547	39	0.535
20	37	0.508	39	0.491	41	0.476	35	0.528	38	0.506	40	0.491
30	38	0.471	40	0.446	42	0.431	36	0.495	39	0.465	41	0.451
40	39	0.442	41	0.419	43	0.405	37	0.462	40	0.440	42	0.424
50	40	0.413	42	0.399	44	0.385	38	0.435	41	0.421	43	0.404

by Hardin and Kalinski [65], that the G_{max} increases with an increase in the mean effective grain size, D_{50} (Figure 8). In addition, the amount of cohesionless material in the mixtures has an obvious influence on the overall behaviour as well as the G_{max} of such mixtures [44,45,47,66,67] (Figure 9). The evaluated G_{max} values for the mixtures have been almost doubled when the clay is mixed with 50%sand addition for any size and shape. The G_{max} of mixtures shows significant changes for a sand content of 10%, which suggests that the threshold value of the sand content at which the trend changing the e_{max} of the mixtures with clay content should be at less than 10%. The void ratio values, strongly effective on the shear modulus, were found to be changed from 0.577 to 0.385 by adding 50% rounded sand between 2.0–1.0 mm size. Such a decrease in the void ratio has resulted in an increase in G_{max} from 23 MPa to 44 MPa. Figure 10 reveals that the G_{max} decreased with an increase of the void ratio for all sizes and both shapes of grains in clay-sand mixtures. The reason for the decrease in G_{max} is mainly attributed to the increase in the void ratio, which changes based on the size and shape characteristics of the soil grains[5,68,69].The packing features of the soil control the void ratio andthe fabric, which represents the grains' orientation, and the contact patterns of the grains [69,70,71]. The shear waves propagate through a soil matrix with a maximum influence from the contact network. The variation of the void ratio can change the travel length for the wave. The larger the void ratio is, the more travel length is created. Actually, more travel time would be spent in the contact network of the loose

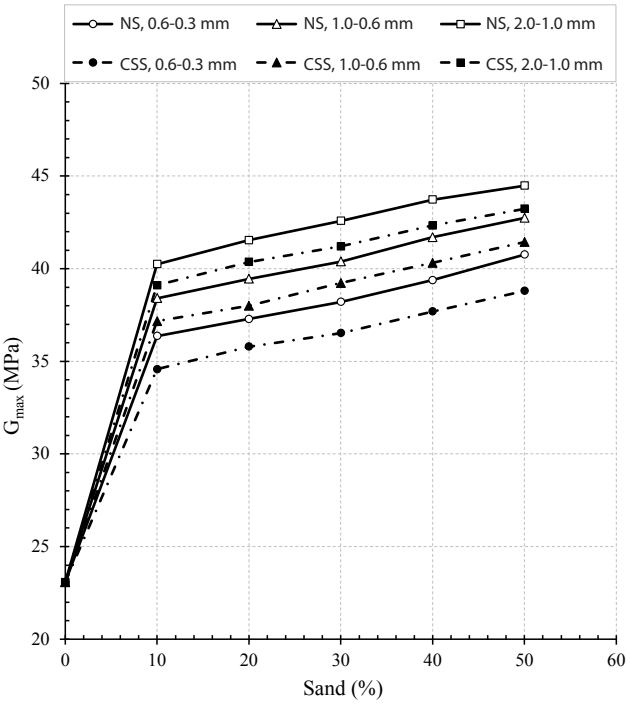

Figure 9. The relationship between G_{max} (MPa) and sand content (%).

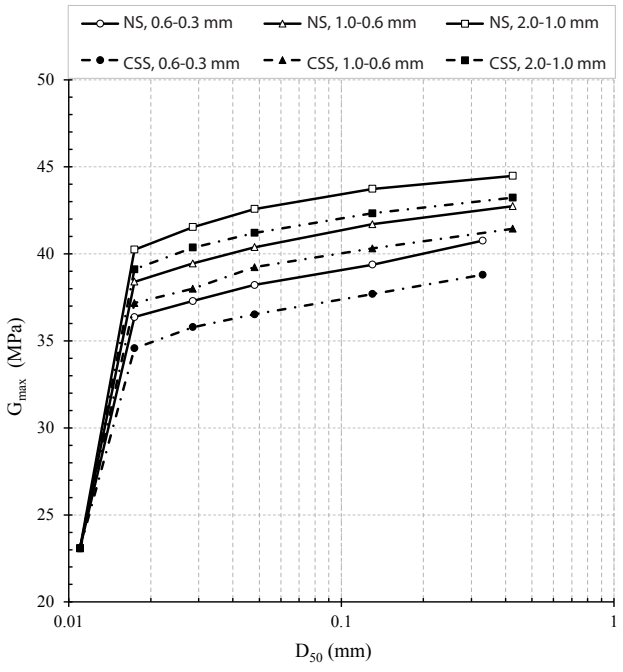

Figure 8. The relationship between G_{max} (MPa) and D_{50} (mm) for various sands in mixtures.

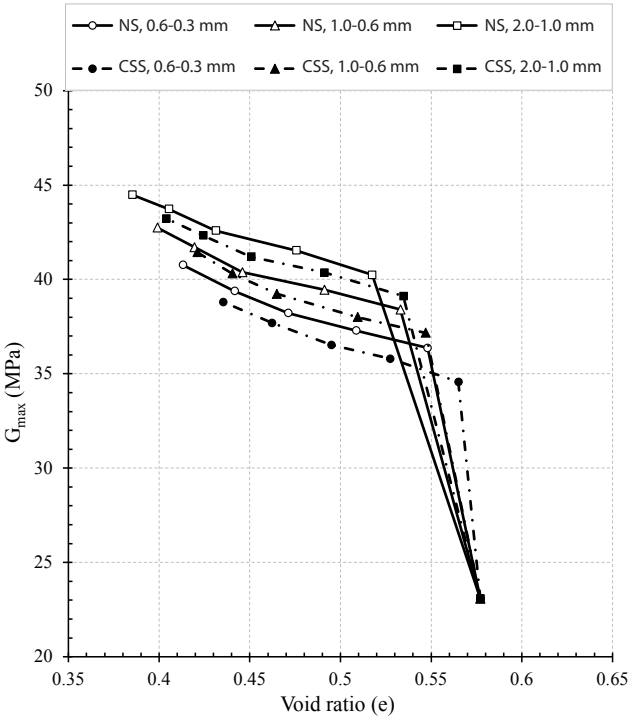

Figure 10. The relationship between G_{max} (MPa) and sand content (%).

sample. Conversely, a dense specimen would create a more stable connection, and thus avoids the micro-rotation of the grains. For example, well graded soils with a wide range of grain sizes tend to have smaller average void ratios, and exhibit larger values of the shear wave velocity (v_s). Hence, the present study has pointed out that G_{max} is dependent on the void ratio controlled by the grain contents and the characteristics, including size, shape, gradation, and roughness.

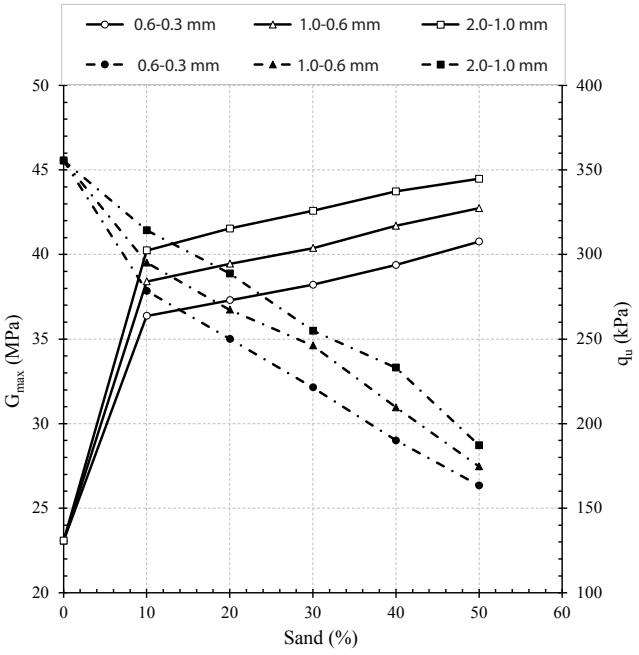

Figure 11. Comparison of G_{max} (kPa) and q_u (kPa) of the NS-clay mixtures.

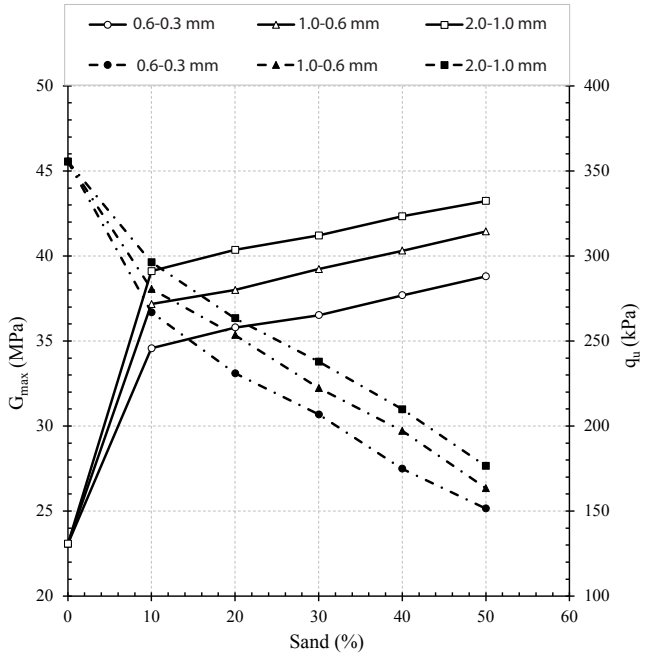

Figure 12. Comparison of G_{max} (kPa) and q_u (kPa) of the CSS-clay mixtures.

The differences between the G_{max} and q_u values are influenced by different conditions under which the dynamic (BE)and static (UC) tests are carried out. The values of q_u in the UC tests are of several hundred of kPa, while the G_{max} during the BE tests does not exceed the value of 50 MPa (Figures 11-12). The loading during UC tests can produce the micro-cracks, which results in the growth of deformation and consequently in the failure of the specimen. However, the BE tests do not change the structure of the material, which is the biggest advantage of their use. The time of applying stress is also different, it lasts several minutes forthe UC tests, while it lasts only several microseconds for the BE tests. The fact is that the purpose of the methods for determining the q_u and G_{max} differs based on the demands in practice. If the requirement for determining the quis formulated by a long-term loading point of view, such as the problem of stability for building works, mining works etc., the q_u values can be obtained from the UC tests. Conversely, if the loading is short term, such as the blasting works, earthquakes, etc., the determination of G_{max} is required. The measurements of G_{max} can be made relatively sophisticated, which is why an alternative method for its determination could be beneficial.Based on the above discussion, the following derived empirical formulas for estimating the G_{max} from the UC tests is suggested for the mixtures of clay-angular sand (R^2=0.83),and clay-rounded sand (R^2=0.76), respectively.

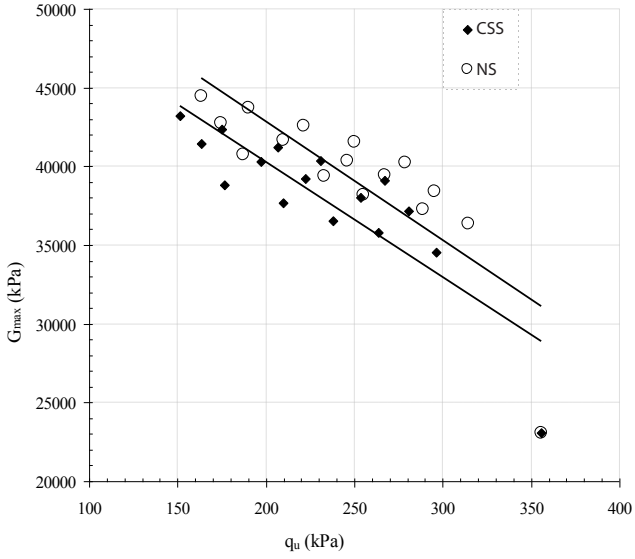

Figure 13. The G_{max} - q_u correlation with sand content (%).

$$G_{max} = -91q_u + 58689 \quad (2)$$

$$G_{max} = -99q_u + 63277 \quad (3)$$

where G_{max} and q_u values are to be found in kPa.

When the values of q_u decreased with an increase of the sand percentages in the clay-sand mixtures, the values of G_{max} increased for all sizes and both types of sand. From Figure13 it can also be observed that the values of G_{max} increased with an increase of the sand percentages for all sizes and both types of sand for the clay-sand mixtures.

4 CONCLUSIONS

Dynamic deformation characteristics including the small strain shear modulus (G_{max}) are the key parameters for the seismic design and a performance evaluation of structures. In the present study, bender-element (BE) tests were performed on various clay-sand mixtures in order to evaluate the effects of quantity (0%, 10%, 20%, 30%, 40%, and 50% by weight), gradation (0.6–0.3 mm, 1.0–0.6 mm, and 2.0–1.0 mm) and shape (rounded, angular) of sand grains on the small strain shear modulus (G_{max}) ofthe mixtures.The unconfined compression (UC) tests were also conducted on the same specimens in order to make a correlation between the two testing results, which enables a platform for the comparison between static load test results and dynamic test results. Based on the outputs obtained, the following conclusions can be drawn.

i) The G_{max} of the clay-sand mixtures nearly doubled from about 23 MPa for clean clay to more than 40 MPa for clay with 50% sand, while the q_u values of the clean clay were found to be about halfway down (from 355 kPa to about 170 kPa) when it was mixed with 50% sand for all sizes and shapes.

ii) For the same amount and shape of the sand grains mixed with clay, the G_{max} values of the mixtures decreased for about 5–12%, while the q_u values of the same specimens increased at about 5–15% by an increase in the mean effective grain size (D_{50}) of the sands.

iii) Both the G_{max} and q_u values in the specimens prepared with angular sand grains were found to be less than those with rounded grains in the range of about 5–7%, and 2–3%, respectively.

iv) There was a correlation expressed in the form of an analytical function between the G_{max} and q_u.

This suggests that both the G_{max} and q_u of the specimens in the way prepared here primarily depend on the void ratio and the size, while they were slightly affected by the grain shape in the mixtures.

REFERENCES

[1] Monkul, M.M. 2005. Influence of intergranular void ratio on one dimensional compression. M.Sc. Thesis, Dokuz Eylul University, Izmir, Turkey.

[2] Lehane, B.M., Jardine, R.J., Bond, A.J., Frank, R. 1993. Mechanisms of shaft friction in sand frominstrumented pile tests. J. Geotech. Eng.119(1), 19-35. doi:10.1061/(ASCE)0733-9410 (1993) 119:1(19)

[3] Fakharian, K., Evgin, E. 1997. Cyclic simple-shear behavior of sand-steel interfaces under constant normal stiffness condition.J. Geotech. Geoenviron. Eng. 123(12), 1096-1105.doi:10.1061/(ASCE)1090-0241(1997)123:12(1096)

[4] Kramer, S.L. 1996. Geotechnical Earthquake Engineering. Prentice-Hall Inc, Upper Saddle River, NJ.

[5] Clayton, C.R.I. 2011. Stiffness at small strain: research and practice. Géotechnique 61(1), 5-37. doi:10.1680/geot.2011.61.1.5

[6] Lee, J.S., Santamarina, C. 2005. Bender elements: Performance and signal interpretation. Journal of Geotechnical and Geoenvironmental Engineering 131(9). doi:10.1061/(ASCE)1090 -0241(2005)131:9(1063)

[7] Ibrahim, A., Orense, R., Pender, M. 2011. Determination of very small strain shear modulus of Auckland residual soils using bender elements. Proc of the 9th Pacific Conference on Earthquake Engineering Building and Earthquake-Resilient Society, New Zealand.

[8] Youn, J.U., Choo, Y.W., Kim, D.S. 2008. Measurement of small strain shear modulus g_{max} of dry and saturated sands by bender element, resonant column, and torsional shear tests. Canadian Geotechnical Journal 45(10), 1426-1438. doi:10.1139/T08-069

[9] Dyvik, R., Madshus, C. 1985. Lab measurements of Gmax using bender elements. Advances in the art of testing soils under cyclic conditions. Proceedings of the ASCE conference, Detroit, MI, 24 October 1985. NewYork: American Society of Civil Engineerings (ASCE); p.186–96. doi:519-526.10.1680/geot.1994.44.3.519

[10] Souto, A., Hartikainen, J., Özüdogru, K. 1994. Measurement of dynamic parameters of road pavement materials by the bender element and resonant column tests. Géotechnique 44(3), 519-526.

doi:519-526.10.1680/geot.1994.44.3.519
[11] Gu, X.Q. 2012. Dynamic properties of granular materials at the macro and micro scales. PhD thesis, Hong Kong: The University of Hong Kong.
[12] Consoli, N.C., Viana da Fonseca, A., Cruz, R.C., Heineck, K.S. 2009. Fundamental parameters for the stiffness and strength control of artificially cemented sand. Journal of Geotechnical and Geoenvironmental Engineering 135(9), 1347-1353. doi: 10.1061/ (ASCE)GT.1943-5606.0000008
[13] Flores, R.D., Di Emidio, G., Van Impe, W.F. 2010. Small-strain shear modulus and strength increase of cement-treated clay. Geotechnical Testing Journal 33(1), 1-10. doi:10. 1520/GTJ102354
[14] ASTM D2166 / D2166M-16, Standard Test Method for Unconfined Compressive Strength of Cohesive Soil, ASTM International, West Conshohocken, PA, 2016. doi:10.1520 /D2166_D2166M-16
[15] Terzaghi, K. 1925. Erdbaumechanik auf bodenphysikalischergrundlage. Deuticke, Leipzig/ Vienna.
[16] Gilboy, G. 1928. The compressibility of sand–mica mixtures. Proceedings of the ASCE, 2, 555-568.
[17] Lees, G. 1964. A new method for determining the angularity of particles. Sedimentology 3, 2-21. doi:10.1111/j.1365-3091.1964.tb00271.x
[18] Olson, R. E., Mesri, G. 1970. Mechanisms controlling compressibility of clays. Journal of Soil Mechanics & Foundations Div. 96(SM6), 1863-1878.
[19] Abbireddy, C.O.R., Clayton, C.R.I., Huvenne, V.A. 2009. A method of estimating the form of fine particulates. Geotechnique 59 (6), 503- 511. doi: 10.1680/geot.2008.P.009
[20] Clayton, C.R.I., Abbireddy, C.O.R., Schiebel, R.2009.A method of estimating the form of coarse particulates. Geotechnique 59(6), 493-501. doi:10.1680/geot.2007.00195
[21] Cabalar, A.F. 2010. Applications of the oedometer, triaxial and resonant column tests to the study of micaceous sands. Engineering Geology 112, 21-28. doi:10.1016/j.enggeo. 2010.01.004
[22] Cabalar, A.F., Dulundu, K., Tuncay, K. 2013. Strength of various sands in triaxial and cyclic direct shear tests. Engineering Geology 156, 92-102.doi:10.1016/j.enggeo. 2013. 01. 011
[23] Cabalar, A.F., Hasan, R.A. 2013. Compressional behaviour of various size/shape sand- clay mixtures with different pore fluids. Engineering Geology 164, 36- 49. doi:10.1016/ j.enggeo.2013.06.011
[24] Holubec, I., D'Appolonia, E. 1973. Effect of particle shape on the engineering properties of granular soils. Evaluation of relative density and its role in geotechnical projects involving cohesionless soils. ASTM, STP523, West Conshohocken, PA, 304-318.
[25] Cornforth, D.H. 1973. Prediction of drained strength of sands from relative density measurements. Evaluation of relative density and its role in geotechnical projects involving cohesionless soils. Special technical publication 523, ASTM, West Conshohoken, PA, 281- 303. doi: 10.1520/ STP37878S
[26] Holtz, R.D., Kovacks, W.D. 1981. An introduction to geotechnical engineering. Prentice-Hall, Englewood Cliffs, NJ, 517.
[27] Cedergen, H.R. 1989. Seepage, drainage, and flownets, 3rd ed., Wiley, New York, 26. doi:10.2113/gseegeosci.II.1.134
[28] Wadell, H. 1932. Volume, shape, and roundness of rock particles. J. Geol. 40 (5), 443-451. doi:10.1086/623964
[29] Krumbein, W.C. 1941. Measurement and geological significance of shape and roundness of sedimentary particles. J. Sediment. Petrol. 11 (2), 64-72. doi:10.1306/D42690F3-2B26-11D7-8648000102C1865D
[30] Powers, M.C. 1953. A new roundness scale for sedimentary particles. J. Sediment. Petrol. 23(2), 117-119. doi:10.1306/D4269567-2B26-11D7-8648000102C1865D
[31] Youd, T.L. 1973. Factors controlling maximum and minimum densities of sands. Evaluation of relative density and its role in geotechnical projects involving cohesionless soils. ASTM STP523, West Conshohocken, PA, 98- 112. doi:10.1520/10.1520/ STP37866S
[32] Cho, G.C., Dodds, J.S., Santamarina, J.C. 2006. Particle shape effects on packing density, stiffness and strength: Natural and crushed sands. J. Geotech. Geoenviron. Eng. 132 (5), 591- 602. doi:10.1061/(ASCE)1090-0241(2006)132:5(591)
[33] ASTM D4318 / D4318–10, Standard Test Methods for Liquid Limit, Plastic Limit, and Plasticity Index of Soils, ASTM International, Philadelphia, PA, 2010. doi:10.1520/10. 1520/STP37866S
[34] Muszynski, M.R., VittonS.J. 2012. Particle shape estimates of uniform sands: visual and automated methods comparison. J. Mater. Civ. Eng. 24(2), 194-206. doi:10.1061 /(ASCE)MT.1943-5533.0000351
[35] Viggiani, G., Atkinson, J.H. 1995. Stiffness of fine-grained soil at very small strains. Géotechnique 45(2), 249-265. doi:10.1680/geot.1995.45.2.249
[36] Stavridakis, E.I. 2005. Presentation and assessment of clay influence on engineering parameters of cement-treated clayey mixtures. Electronic Journal

of Geotechnical Engineering, paper no: 508.
[37] Shogaki, T. 1995. Effective stress behavior of clays in unconfined compression tests. Soils and Foundations 35 (1), 169- 171.
[38] Fredlund, D.G., Xing, A., Fredlund, M.D., Barbour, S.L. 1996. The relationship of unsaturated soil shear strength to the soil-water characteristic curve. Canadian Geotechnical Journal 33, 440-448. doi.org/10.1139/t96-065
[39] Chae, J., Kim, B., Park, S., Kato, K. 2010. Effect of suction on unconfined compressive strength in partly saturated soils. KSCE Journal of Civil Engineering 14(3), 281-290. doi: 10.1007/s12205-010-0281-7
[40] Rothenburg, L., Bathurst, R.J. 1989. Analytical study of induced anisotropy in idealized granular material. Géotechnique 49, 601-614. doi:10.1680/geot.1989.39.4.601
[41] Thornton, C. 2000. Numerical Simulations of Deviatoric Shear Deformation of Granular Media. Geotechnique 50, 43-53. doi: 10.1680/geot.2000.50.1.43
[42] Cabalar, A.F. 2015. Stress fluctuations in granular material response during cyclic direct shear tests. Granular Matter 17 (4), 439- 446. doi:10.1007/s10035-015-0568-y
[43] Santamarina, J.C., Cho, G.C. 2004. Soil behaviour: the role of particle shape. Proc. Skempton Conference, March, London. doi: 10.1680/aigev1.32644.0035
[44] Ni, Q., Tan, T.S., Dasari, G.R., Hight, D.W. 2004. Contribution of fines to the compressive strength of mixed soils. Geotechnique 54 (9), 561-569. doi:10.1680/geot.2004. 54.9.561
[45] Monkul, M.M., Ozden, G. 2007. Compressional behavior of clayey sand and transition fines content. Engineering Geology 89, 195-205. doi:10.1016/j.enggeo.2006.10.001
[46] Rahman, M.M., Lo, S.R. 2008. The prediction of equivalent granular steady state line of loose sand with fines. Geomech. Geoeng. 3(3), 179-190. doi:10.1080/17486020802206867
[47] Cabalar, A.F., Mustafa, W.S. 2015. Fall cone tests on clay-sand mixtures. Engineering Geology 192, 154-165. doi:10.1016/j.enggeo.2015.04.009
[48] Yamamuro, J.A., Bopp, P.A., Lade, P.V. 1996. One dimensional compression of sands at high pressures. Journal of Geotechnical Engineering 122 (2), 147-154. doi:10.1061/(ASCE) 0733-9410(1996)122:2(147)
[49] Thevanayagam, S., Mohan, S. 2000. Intergranular state variables and stress–strain behaviour of silty sands. Geotechnique 50 (1), 1-23. doi:10.1680/geot.2000.50.1.1
[50] Yamamuro, J.A., Wood, F.M. 2004. Effect of depositional method on the undrained behaviour and microstructure of sand with silt. Soil Dynamics and Earthquake Engineering 24, 751-760. doi:10.1016/j.soildyn.2004.06.004
[51] Mitchell, J.K. 1976. Fundamental of soil behaviour. John Wiley & Sons, Inc.
[52] Kenny, T.C. 1977. Residual strength of mineral mixture. Proc. 9th International Conference of Soil Mechanics and Foundation Engineering, 155-160.
[53] Lupini, J.F., Skinner, A.E., Vaughan, P.R. 1981. The drained residual strength of cohesive soils. Geotechnique 31(2), 181-213. doi:10.1680/geot.1981.31.2.181
[54] Thevanayagam, S. 1998. Effect of fines and confining stress on undrained shear strength of silty sands. Journal of Geotechnical and Geoenvironmental Engineering 124(6), 479-491.
[55] Troncoso, J.H., Verdugo, R. 1985. Silt content and dynamic behaviour of tailing sands. Proc. 11th International Conference on Soil Mechanics and Foundation Engineering 3, 1311-1314.
[56] Tan, T.S., Goh, T.C., Karunaratne, G.P., Lee, S.L. 1994. Shear strength of very soft clay-sand mixtures. Geotechnical Testing Journal 17 (1), 27-34.
[57] Hardin, B.O. 1978. The nature of stress-strain behaviour for soils. Proceedings of the ASCE specialty conference on earthquake engineering and soil dynamics, 3-90. doi:10.1520/GTJ10069J
[58] Jamiolkowski, M., Leroueil, S., Lo Presti, D.C.F. 1991. Theme lecture: Design parameters from theory to practice. Proceedings of the international conference on geotechnical engineering for coastal development, Geo-Coast 1991, Yokohama, Japan, 877-917.
[59] Vucetic, M., Dobry, R.1991. Effect of soil plasticity on cyclic response. Journal of Geotechnical Engineering 117(1), 89-107. doi:10.1061/(ASCE)0733-9410(1991)117:1(89)
[60] Shibuya, S., Tanaka, H. 1996. Estimate of elastic shear modulus in holocene soil deposits. Soils and foundations 36(4), 45-55. doi:10.3208/sandf.36.4_45
[61] Santagata, M., Germaine, J.T., Ladd, C.C. 2005. Factors affecting the initial stiffness of cohesive soils. Journal of Geotechnical and Geoenvironmental Engineering 131(4), 430-441. doi:10.1061/(ASCE)1090-0241(2005)131:4(430)
[62] Wichtmann, T.,Triantafyllidis,T.2010. On the influence of the grain size distribution curve on P-wave velocity, constrained elastic modulus M_{max} and Poisson's ratio of quartz sands. Soil Dynamics and Earthquake Engineering 30(8), 757-766.

doi:10.1016/j.soildyn. 2010.03.006
[63] Yang, J., Gu, X. Q.2013. Shear stiffness of granular material at small-strain: does it depend on grain size? Géotechnique 63(2), 165–179. doi:10.1680/geot.11.P.083
[64] Santamarina, J.C., Cascante, G.1998.Effect of surface roughness on the wave propagation parameters. Géotechnique 48(1), 129-136. doi:10.1680/geot.1998.48.1.129
[65] Hardin, B.O., Kalinski, M.E. 2005. Estimating the shear modulus of gravelly soils. ASCE Journal of Geotechnical and Geoenvironmental Engineering 131 (7), 867-875. doi:10. 1061/(ASCE)1090-0241(2005)131
[66] Yamada, S., Hyodo, M., Orense, R., Dinesh, S.V. 2008. Initial shear modulus of remoulded sand-clay mixtures. Journal of Geotechnical and Geoenvironmental Engineering 134 (7), 960-971. doi:10.1061/(ASCE)1090-0241(2008)134:7(960)
[67] Cabalar, A.F., Mustafa, W.S. 2017. Behavior of sand-clay mixtures for road pavement subgrade. International Journal of Pavement Engineering, 18, 714-726. doi:10.1080/ 10298436.2015. 1121782. doi:10.1080/10298436.2015. 1121782
[68] Jia, X., Williams, R.A. 2001. A packing algorithm for particles of arbitrary shapes. Powder Technology 120(3), 175-186. doi:10.1016/S0032-5910(01)00268-6
[69] Cubrinovski, M., Ishihara, K. 2002. Maximum and minimum void ratio characteristics of sands. Soils and foundations 42(6), 65-78. doi:10.3208/sandf.42.6_65
[70] Lo Presti, D.C.F., Jamiolkowski, M., Pallara, O., Cavallaro, A., Pedroni, S. 1997. Shear Modulus and Damping of Soils. Géotechnique 47(3), 603-617. doi:10.1680/geot. 1997.47.3.603
[71] Santamarina, J.C., in collaboration with Klein, K. and Fam, M., 2001. Soils and Waves, J. Wiley and Sons, Chichester, UK, 488 pages.

METODA MERJENJA GEOSTATIČNIH NAPETOSTI, KI TEMELJI NA VGRAJENEM VRTALNEM IN OPTIČNO MIKROSKOPSKEM SLIKOVNEM SISTEMU

Jinchao Wang
Chinese Academy of Sciences,
Institute of Rock and Soil Mechanics,
Key Laboratory of Geomechanics and Geotechnical Engineering
Wuhan, Kitajska

University of Chinese Academy of Sciences
Beijing ,China

Chuanying Wang
Chinese Academy of Sciences,
Institute of Rock and Soil Mechanics,
Key Laboratory of Geomechanics and Geotechnical Engineering
Wuhan, Kitajska

Zengqiang Han *(vodilni avtor)*
Chinese Academy of Sciences,
Institute of Rock and Soil Mechanics,
Key Laboratory of Geomechanics and Geotechnical Engineering
Wuhan, Kitajska
E-pošta: zqhan@whrsm.ac.cn

Yiteng Wang
Chinese Academy of Sciences,
Institute of Rock and Soil Mechanics,
Key Laboratory of Geomechanics and Geotechnical Engineering
Wuhan, Kitajska

University of Chinese Academy of Sciences
Beijing, Kitajska

Xinjian Tang
Chinese Academy of Sciences,
Institute of Rock and Soil Mechanics,
Key Laboratory of Geomechanics and Geotechnical Engineering
Wuhan, Kitajska

Ključne besede

geostatična napetost; sonda; optična mikroskopija; merjenje med vrtanjem; iskalni krog

Izvleček

Konvencionalne metode merjenja geostatičnih napetosti so omejene zaradi pomanjkljivosti, vključno z izmerljivo globino, kompleksnostjo in dolgim trajanjem izvedbe. Da bi rešili te probleme in dosegli merjenje geostatičnih napetosti v globokih vodnjakih v pogojih kompleksnih visokih tlakov in visokih temperatur, je predlagana nova merilna metoda za geostatične napetosti na osnovi integriranega sistema vrtanja in optičnega mikroskopa. Njena inovativna integrirana konstrukcija odpravlja probleme, povezane s kompleksnimi postopki in globinskimi omejitvami, ter se izogiba lezenju kamnin zaradi dolgotrajnosti postopka, kar bistveno izboljša natančnost in obseg meritev. Deluje s pomočjo mikroskopskega slikanja in neposrednimi sondami, da zajame spremembe zunanje površine prereza vrtine pred in po zmanjšanju napetosti. Rezultirajoče slike se analizirajo z iskalnimi krogi, da se pridobijo položaji vrhov sond, ki so lahko vstavljeni v elipse, ki opisujejo obrise, in izračunajo stanje napetosti. Veljavnost in natančnost metode sta bili preverjeni z laboratorijskimi preizkusi in aplikacijami na terenu v vrtini ZK1. Rezultati kažejo, da: (1) se integrirani sistem lahko uporablja za merjenje mikrometerskih deformacij; (2) pristop iskalnega kroga lahko natančno pridobi položaje vrhov sond; (3) metoda merjenja napetosti, ki temelji na tem sistemu, je točna in izvedljiva.

A GEOSTRESS MEASUREMENT METHOD BASED ON AN INTEGRATED DRILLING AND OPTICAL MICROSCOPIC IMAGING SYSTEM

Jinchao Wang
Chinese Academy of Sciences,
Institute of Rock and Soil Mechanics,
Key Laboratory of Geomechanics and Geotechnical Engineering
Wuhan, China

University of Chinese Academy of Sciences
Beijing ,China

Chuanying Wang
Chinese Academy of Sciences,
Institute of Rock and Soil Mechanics,
Key Laboratory of Geomechanics and Geotechnical Engineering
Wuhan, China

Zengqiang Han *(corresponding author)*
Chinese Academy of Sciences,
Institute of Rock and Soil Mechanics,
Key Laboratory of Geomechanics and Geotechnical Engineering
Wuhan, China
E-mail: zqhan@whrsm.ac.cn

Yiteng Wang
Chinese Academy of Sciences,
Institute of Rock and Soil Mechanics,
Key Laboratory of Geomechanics and Geotechnical Engineering
Wuhan, China

University of Chinese Academy of Sciences
Beijing, China

Xinjian Tang
Chinese Academy of Sciences,
Institute of Rock and Soil Mechanics,
Key Laboratory of Geomechanics and Geotechnical Engineering
Wuhan, China

Keywords

geostress; probe; optical microscopy; measurement while drilling; search circle

DOI https://doi.org/10.18690/actageotechslov.15.1.17-27.2018

Abstract

Conventional geostress measurement methods are limited by deficiencies including the measurable depth, the complexity, and the long duration of operation. To address these problems and achieve the measurement of geostress in deep wells under conditions of complex high pressures and high temperatures, we propose a new measurement method for geostress based on an integrated drilling and optical microscopy system. Its innovative integrated structure eliminates the problems associated with complex procedures and depth limits, and avoids rock creep caused by long delays, significantly improving the accuracy and range of the measurements. It works by using microscopic imaging and direct contact probes to capture the changes of a borehole's cross-sectional outlines before and after stress relief. The resulting images are analyzed with search circles to obtain the positions of probe apices, which can be fitted into ellipses that describe the outlines, and calculate the state of the stress. The validity and accuracy of the method was verified by in-door tests and field applications in the ZK1 borehole. The results show that: (1) the integrated system can be used to measure micrometer-grade deformations; (2) the search-circle approach can accurately obtain the positions of probe apices; and (3) the stress measurement method based on the system is accurate and feasible.

1 INTRODUCTION

Geostress, while a universal phenomenon, has been difficult to assess and measure. As we continue our exploration into the deeper crusts, their stresses will play an increasingly greater role in the design and decision-making of our deep engineering projects. Work on the theory and practice of stress measurements has led to the creation of new techniques and instruments. The most typical such device was the USBM gauge, developed by the U.S. Bureau of Mines in the 1950s, and the stress-relief method it represents has remained the most commonly used approach [1,2,3].

The stress-relief method is based on the theory of elasticity. It assumes a homogeneous and continuous rock mass, and the same stress-strain function when both loading and unloading stress. It also considers the rock elements being removed as having negligible weight (gravity stress) compared to their load. The measurements are usually made with the following steps:

1) A large borehole is drilled to a predetermined depth close to the measurement position;
2) A smaller hole concentric with the borehole is drilled into the bottom, and three-axis strain gauges (for

measuring wall strains) or deformation transducers (for diameter deformations) are installed into the hole;
3) The larger borehole is then extended down, separating the now pipe-like core from the base rock to relieve the stress.

This conventional method involves a series of complicated tasks: drilling the large well, leveling the bottom, shaping the pilot hole, drilling the measurement hole, installing transducers, and drilling the relief well. In this process, the drilling rod must be lifted several times from the well, have the drill replaced, and lower back to the bottom. The usefulness of the method in deeper wells is further impeded by the lengths of the transducer cables. For these reasons the utilization of the stress-relief method has often been restricted to the testing of shallow wells [4,5].

Another problem stems from the time delays in measurements. The duration from the installation of the transducers to the end of the stress relief lasts a few days at least, and the test process lasts several tens of minutes by itself. The delays are long enough for rock creep to significantly alter the body's mechanical parameters, deviating from the assumed elastic relationships [6,7]. The resulting stress data are seldom very accurate for this reason [8].

To address these common issues, this paper introduces an integrated drilling and optical microscopic measurement system. It incorporates an outer drill and an inner drill, respectively, for relief and measurement holes. A control module connects and disconnects the drills as needed, replacing the complicated traditional approach. An optical module is used to directly acquire deformation data from the walls. This system can be utilized in deep wells, mitigates the delay-induced errors by real-time measurements, and effectively solves the major technical issues encountered in stress relief. A stress-measurement method based on the system is also introduced.

2 INTEGRATED DRILLING AND OPTICAL MICROSCOPIC MEASUREMENT SYSTEM

The system can be divided into the drilling and acquisition sub-systems, the former for drilling the measurement and relief holes, and the latter for acquiring and recording the borehole's diameter deformations.

2.1 Theory

The integrated system is still based on the principles of stress relief. It measures the deformations of the rock body before and after the stress relief, and extrapolates the initial stress from them in the following steps:

1) The integrated system drills the measurement hole, and lowers the optical module to the measurement position (see Fig. 1(a));
2) After the optical module arrives at the position, the control module separates the inner and outer drills, the inner drill stays at rest, while the outer drill resumes drilling (see Fig. 1(b));
3) The outer drill overtakes the measurement hole, separating the pipe-like core from the rock mass (see Fig. 1(c)), which relieves the stress around the optical module;
4) The optical module detects the minuscule diameter changes, which is used to compute the deformation of the cross-section and its horizontal stress;
5) Measurements are made in three intersecting boreholes to determine the three-dimensional state of stress [9,10,11,12].

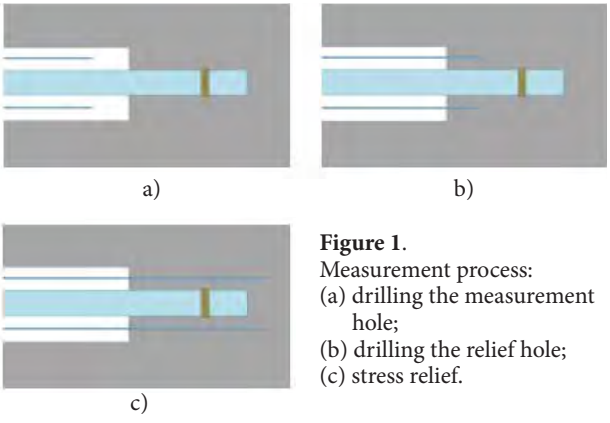

Figure 1.
Measurement process:
(a) drilling the measurement hole;
(b) drilling the relief hole;
(c) stress relief.

2.2 Structure of the drilling system

The drilling system consists of the outer drill, the control module, and the inner drill, shown in Fig. 2. The inner drill is used to create the measurement hole, and lower the optical microscopic component to the measurement position. After the preset bottom of the measurement hole is reached, the control module will decouple the two drills, and the inner drill will be stationary relative to the surrounding rock body, allowing the acquisition system inside to perform its measurements, while the outer drill continues drilling downwards to create the relief well. As the relief well takes shape, stress can be completely relieved from the core, which is detected by the optical module. At the end of the entire operation, all the system components can be retrieved together.

(a) Outer drill (relief) (b) Control module (decoupling) (c) Inner drill (measurement)

Figure 2. Structure of the drilling system.

2.3 Structure of the acquisition system

The acquisition system consists of a number of probes, a camera, and an electronic compass, shown in Fig. 3. As the surrounding rock core becomes separated from the larger rock mass, it is relieved of the rock mass' stresses, causing the measurement hole to deform. Each probe is in direct contact with the walls of the hole via a prod protruding from the drill, allowing the deformation to be recorded in real time.

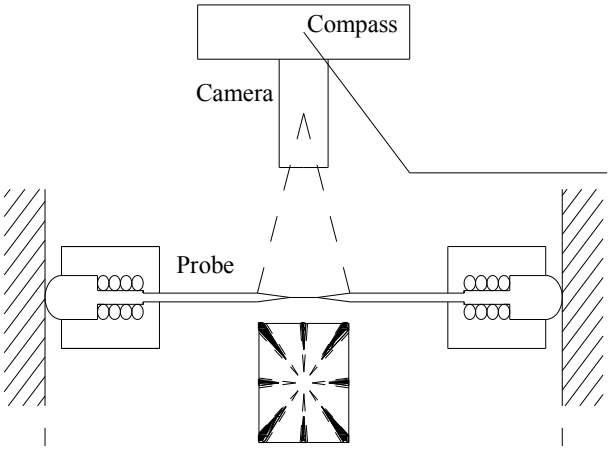

Figure 3. Structure of the acquisition system.

The changing positions of the probes are captured by the camera, consisting of a fixed-focus lens and a microscopic CCD component (see Fig. 4). Since the target area is small, a lens with a small FOV is chosen. Since the CCD image has a greater width than its height, the shorter side is used to determine its physical resolution, which is the physical length of the side divided by its number of pixels, e.g., 576px for a standard capturing component with a resolution of 768*576. The device used in this study captures a 500px-tall image from a 3.5mm-tall area, meaning the image has a physical resolution of 0.007mm.

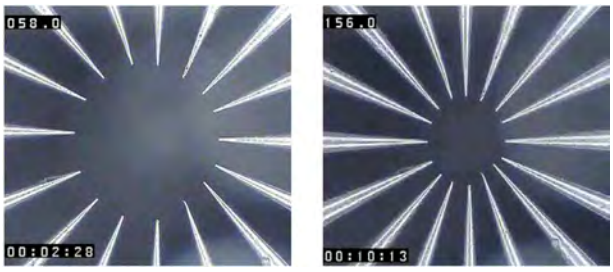

Figure 4. Image data from the probes.

The directional data of the deformation are an important parameters that cannot be accurately recorded by the images. Hence, an electronic compass is used, with its north set to be the same direction as one of the probes. The direction of each probe can then be derived.

2.4 Advantages of the system

The proposed system has the following standout features. Firstly, its deployment is vastly simpler than the conventional method. This is accomplished by using a control module to coordinate the movements of the outer and inner drills, integrating the functions of downward drilling, borehole shaping, and measurement in one device. Additionally, the measurement module can start working as soon as the measurement hole is formed, and continue its recording throughout the relief operation, generating more valid data. By eliminating the long delay that comes from replacing drills, the influence of rock creep can be minimized, and the resulting errors can be avoided. This means that the system is more efficient, and less vulnerable to external disturbances than conventional devices.

Secondly, the system uses probes in direct contact with the walls, captures their deformation with microscopic imaging, calculates the borehole's deformation after relief from the images, and determines the stress from the deformation. The microscopic imaging allows accuracy at the micrometer level; the probes are made with

materials resistant to abrasion, ensuring the system can be operational under unusually harsh conditions. These features give the system high accuracy and adaptability, and present a solution to the limited reach and accuracy in conventional stress-relief methods.

3 ACQUISITION OF DEFORMATION DATA

From the image data, it is possible to directly identify the positions of the probes' sharp apices by computer. However, for our required accuracy, this is a process prone to errors. In this study, the images are pre-processed, allowing the probe edges to be detected. The precise coordinates of the apices are then determined as the intersections of these edge lines.

3.1 Pre-processing

The inside of a borehole is not a homogeneous environment. The image data can be affected by the noises from external signals and a minor turbidity in the liquid between the camera and the probes, as seen in Fig. 5(a). Since the adaptive median filter (AMF) algorithm can preserve the edges in an image, it is chosen for the de-noise operation. AMF functions by adjusting the filter window based on noise density, using different methods to process noise and signal pixels, maintaining the gray-scale values of the signals, while applying a median filter to the noises.

Let the grayscale of the pixel (x,y) be f_{xy}, the current work window be A_{xy}, and the preset largest window permitted be A, in which the minimum, median and maximum gray scales are respectively f_{min}, f_{med} and f_{max}. When $f_{min}<f_{med}<f_{max}$, f_{med} is not a noise, and whether f_{xy} is a noise can also be determined by $f_{min}<f_{xy}<f_{max}$. When neither fmed nor f_{xy} is a pulse noise, f_{xy} is preferred as the result (see Fig. 5(b)).

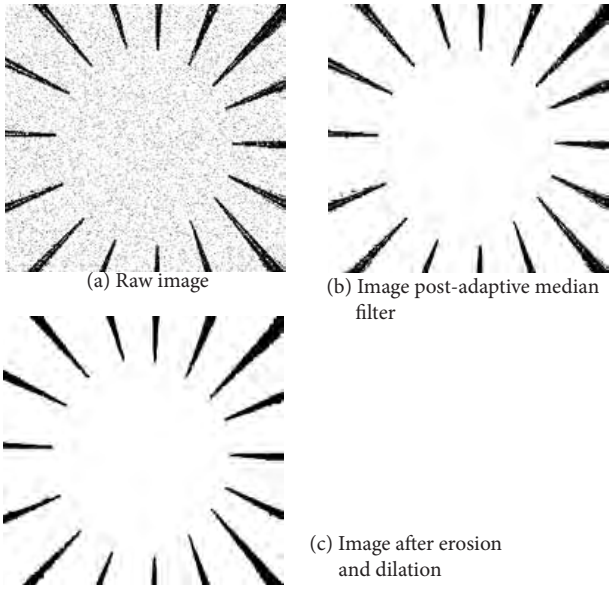

(a) Raw image

(b) Image post-adaptive median filter

(c) Image after erosion and dilation

Figure 5. Pre-processing of image data.

Since some hollow spots and rough edges are present in the image post-AMF, the erosion and dilation processes [13] are used to eliminate them. The rough edges are cleaned up by erosion, and the hollow spots are filled with dilation. The final result is shown in Fig. 5(c).

3.2 Acquiring probe edges

Even with the pre-processing, the silhouettes of the probes are still not smooth or straight as they should be. In this section, the probe edges are acquired by first drawing circles to find points on the edges, then fitting the points to straight lines.

Based on the image center, multiple circles can be drawn, each intersecting with all the probes. We define such a search circle as c_j, with j denoting the j-th circle starting from the inside. The probe in the top-center is denoted probe 1, and the rest are numbered clockwise. Along a circle, the entry and exit points of a probe can be identified by the color values of the pixels. An entry point is denoted dn_{1j} (i.e., the entry point for the overlapping section between the n-th probe and the$j$-th circle), and an exit point is dn_{2j}. All the probes can then be identified as seen in Fig. 6(a). Since all the probes are standard cones with straight edges, a line can be fitted from each edge, denoted ln_i, with i representing either the entry into or the exit from the circles.

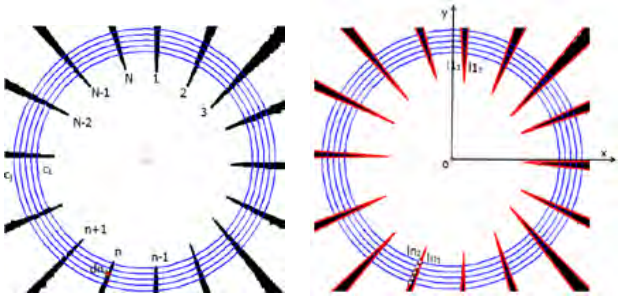

(a) Intersections of probes and search circles

(b) Establishing Cartesian coordinates

Figure 6. Search circles.

Let the image center be the origin O, the width be the x-axis, and the height be the y-axis, a Cartesian coordinates system can be created as Fig. 6(b). The point dn_{ij} has coordinates (xn_{ij}, yn_{ij}), which have the following relationships:

$$\begin{cases} \overline{xn}_i = \sum_{j=1}^{J} xn_{ij} / J \\ \overline{yn}_i = \sum_{j=1}^{J} yn_{ij} / J \end{cases} \quad (1)$$

$$\begin{cases} kn_i = \dfrac{\sum_{j=1}^{J} (\left| xn_{ij} - \overline{xn}_i \right|)(\left| yn_{ij} - \overline{yn}_i \right|)}{\sum_{j=1}^{J} (\left| xn_{ij} - \overline{xn}_i \right|)^2} \\ bn_i = \overline{yn}_i - k\overline{xn}_i \end{cases} \quad (2)$$

$$yn_i = kn_i xn_i + bn_i \quad (3)$$

where J is the total number of search circles. Equation (3) is the equation of the line ln_i.

3.3 Determining the positions of the apices

With the edges obtained, the apex of each probe can be pinpointed through their intersection, as seen in Fig. 7(a); the coordinates of these intersections are taken to be their accurate positions (see Fig. 7(b)). The apex of the n-th probe is denoted Dn (xn,yn).

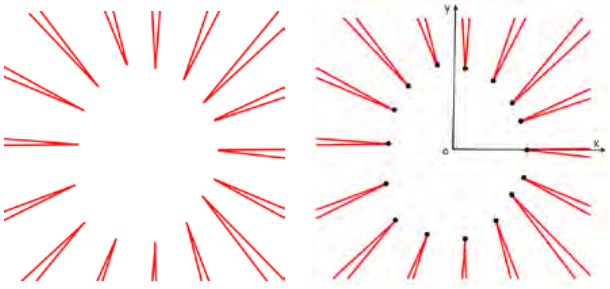

(a) Intersections of probe edges (b) Locations of probe apices

Figure 7. Locations of probe apices.

The coordinates xn and yn can be solved from the equations of the edges, as the following:

$$\begin{cases} xn = \dfrac{bn_2 - bn_1}{kn_1 - kn_2} \\ yn = \dfrac{kn_2 bn_1 - kn_1 bn_2}{kn_2 - kn_1} \end{cases} \quad (4)$$

4 DETERMINING THE STRESS

Using the integrated system, the stress along a borehole's cross-section can be determined. By measuring three intersecting boreholes, the three-dimensional stress at their intersection can then be calculated.

4.1 Conversion between the borehole and the ground coordinates

Determining three-dimensional stress requires knowing the angles between the boreholes and the ground. We begin by establishing a ground coordinate system $oxyz$, with the x-axis pointing east, the y-axis pointing north, the z-axis pointing up, and the origin o as the center of the borehole cross-section at the measurement position. A borehole coordinate system $ox'y'z'$ is also established, with x' in the xy plane, z' pointing in the same direction as the axis of the borehole, and y' determined by the right-hand rule [14,15], shown in Fig. 8.

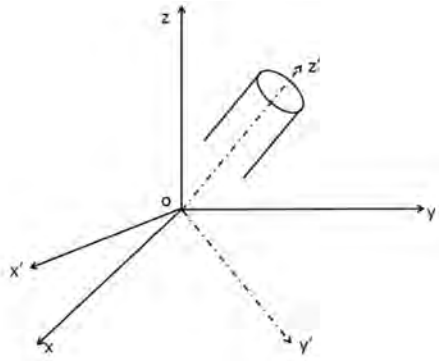

Figure 8. Ground and borehole coordinate systems.

Suppose both $oxyz$ and $ox'y'z'$ are two Cartesian coordinate systems in an infinite space, the six 3-dimensional stress components σ_x', σ_y', σ_z', τ_{xy}', τ_{yz}', τ_{zx}' in $ox'y'z'$ can be converted into their counterparts σ_x, σ_y, σ_z, τ_x, τ_y, τ_z in $oxyz$ with the following equations:

$$\begin{cases} \sigma_x' = \sigma_x l_1^2 + \sigma_y m_1^2 + \sigma_z n_1^2 + 2\tau_{xy} l_1 m_1 + 2\tau_{yz} m_1 n_1 + 2\tau_{zx} n_1 l_1 \\ \sigma_y' = \sigma_x l_2^2 + \sigma_y m_2^2 + \sigma_z n_2^2 + 2\tau_{xy} l_2 m_2 + 2\tau_{yz} m_2 n_2 + 2\tau_{zx} n_2 l_2 \\ \sigma_z' = \sigma_x l_3^2 + \sigma_y m_3^2 + \sigma_z n_3^2 + 2\tau_{xy} l_3 m_3 + 2\tau_{yz} m_3 n_3 + 2\tau_{zx} n_3 l_3 \\ \tau_{xy}' = \sigma_x l_1 l_2 + \sigma_y m_1 m_2 + \sigma_z n_1 n_2 + \tau_{xy}(l_1 m_2 + l_2 m_1) + \\ \quad + \tau_{yz}(m_1 n_2 + m_2 n_1) + \tau_{zx}(n_1 l_2 + n_2 l_1) \\ \tau_{yz}' = \sigma_x l_2 l_3 + \sigma_y m_2 m_3 + \sigma_z n_2 n_3 + \tau_{xy}(l_2 m_3 + l_3 m_2) + \\ \quad + \tau_{yz}(m_2 n_3 + m_3 n_2) + \tau_{zx}(n_2 l_3 + n_3 l_2) \\ \tau_{zx}' = \sigma_x l_3 l_1 + \sigma_y m_3 m_1 + \sigma_z n_3 n_1 + \tau_{xy}(l_3 m_1 + l_1 m_3) + \\ \quad + \tau_{yz}(m_3 n_1 + m_1 n_3) + \tau_{zx}(n_3 l_1 + n_1 l_3) \end{cases} \quad (5)$$

where l_1, l_2 and l_3 are, respectively, the cosines from x', y' and z' to x; m_1, m_2 and m_3 are similar cosines from x', y' and z' to y; and n_1, n_2 and n_3 are cosines from x', y' and z' to z.

4.2 Relationship between the deformations and the 3-dimensional stress components

When determining stresses we can base the global coordinate system on the earth, and establish a local system for each borehole. As long as we know the angles between the local systems and the global system, all the results from the local systems can be converted to the global system using Equation (5). Now we know the diameter of the borehole cross-section is deformed under stress, as shown in Fig. 9.

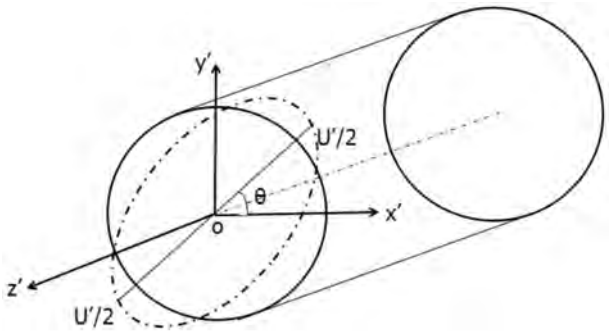

Figure 9. Deformation in the borehole coordinate system.

Assuming the borehole exists in a 3-dimensional, infinite frame, the following relationship can be found between the deformation U' and the 3-dimensional stress components:

$$U' = \sigma_x'(\frac{d}{E}[(1+2\cos 2\theta)(1-\nu^2)+d\nu^2])+ \\ \sigma_y'(\frac{d}{E}[(1-2\cos 2\theta)(1-\nu^2)+d\nu^2])+\sigma_z'(-\frac{d\nu}{E})+\tau_{xy}'(\frac{d}{E}4(1-\nu)\sin 2\theta) \quad (6)$$

where d is the borehole diameter; θ is the angle between the direction of the deformed diameter and x'; rotating counterclockwise (CCW) from x' to the direction of the said diameter is positive; E and ν are, respectively, the elastic modulus and Poisson's ratio of the rock at the measurement position; and σ_x', σ_y', σ_z', τ_{xy}' can be converted to the global coordinate system via Equation (5).

4.3 Equation of deformed cross-section

After the stress is completed relieved, the borehole cross-section becomes elliptic in shape [16]. Under ideal conditions, the probe apices should also fall onto points on an ellipse, but since the borehole walls are not perfectly smooth, deviations and errors can still be present. Here, we approximate the ellipse with the least-squares method.

Now the apices have coordinates (xn,yn) with n=1,2,…, N, N being the total number of probes. The target function can be constructed:

$$F(A,B,C,D,E)=\sum_{n=1}^{N}(xn^2+Axn\cdot yn+Byn^2+Cxn+Dyn+E)^2 \quad (7)$$

We need to find the parameters (A,B,C,D,E) that allow the apices (xn,yn) to fall onto an ellipse as much as possible. This problem can be represented as obtaining the minimum value of $F(A,B,C,D,E)$. Based on the least-squares theory, this implies the following relationships:

$$\frac{\partial F}{\partial A}=\frac{\partial F}{\partial B}=\frac{\partial F}{\partial C}=\frac{\partial F}{\partial D}=\frac{\partial F}{\partial E}=0 \quad (8)$$

The following can be derived from Equation (8):

$$\begin{bmatrix} \sum xn^2\cdot yn^2 & \sum xn\cdot yn^3 & \sum xn^2\cdot yn & \sum xn\cdot yn^2 & \sum xn\cdot yn \\ \sum xn\cdot yn^3 & \sum yn^4 & \sum xn\cdot yn^2 & \sum yn^3 & \sum yn^2 \\ \sum xn^2\cdot yn & \sum xn\cdot yn^2 & \sum xn^2 & \sum xn\cdot yn & \sum xn \\ \sum xn\cdot yn^2 & \sum yn^3 & \sum xn\cdot yn & \sum yn & \sum yn \\ \sum xn\cdot yn & \sum yn^2 & \sum xn & \sum yn & N \end{bmatrix} \cdot \\ \cdot \begin{bmatrix} A \\ B \\ C \\ D \\ E \end{bmatrix} = -\begin{bmatrix} \sum_{i=1}^{N} xn^3\cdot yn \\ \sum_{i=1}^{N} xn^2\cdot yn^2 \\ \sum_{i=1}^{N} xn^3 \\ \sum_{i=1}^{N} xn^2\cdot yn \\ \sum_{i=1}^{N} xn^2 \end{bmatrix} \quad (9)$$

Solving the five-order linear system results in A, B, C, D and E, which are the parameters of an elliptical equation. For the ellipse, the center (x_0,y_0), major axis a, minor axis b, and angle θ between the major axis and x can then be determined as the following:

$$\begin{cases} (x_0,y_0)=(\frac{2BC-AD}{A^2-4B},\frac{2D-AD}{A^2-4B}) \\ a=\sqrt{\frac{2(ACD-BC^2-D^2+4BE-A^2E)}{(A^2-4B)(B-\sqrt{A^2+(1-B)^2}+1)}} \\ b=\sqrt{\frac{2(ACD-BC^2-D^2+4BE-A^2E)}{(A^2-4B)(B+\sqrt{A^2+(1-B)^2}+1)}} \\ \theta=\tan^{-1}\sqrt{\frac{a^2-b^2B}{a^2B-b^2}} \end{cases} \quad (10)$$

4.4 Obtaining the stress data

The system can measure the stress in a cross-section perpendicular to the borehole axis. But only three equations can be obtained from one borehole, which is not enough to solve for the six components in a 3-dimensional system. To obtain the 3-dimensional stress data, the measurements must be made in three intersecting boreholes. The following uses one borehole as an example to show the process.

As in Fig. 10(a), the outline of the cross-section has changed from the circle before the stress relief to an ellipse. The deformation can be represented and compared using the outline's elliptical equation. From the origin *o*, three rays are drawn: the first along the positive *x*-axis, the second rotated CCW 60 degrees, and the third rotated CCW 120 degrees. The three rays, respectively, intersect with the pre-relief circle at N_1, N_2 and N_3, and with the post-relief ellipse at M_1, M_2 and M_3, with the coordinates $N_i(x_{ni},y_{ni})$ and $M_i(x_{mi},y_{mi})$, i=1,2,3. Therefore, the distance between each pair of points $|M_iN_i|$ is:

$$\left|M_iN_i\right| = \sqrt{(x_{mi}-x_{ni})^2+(y_{mi}-y_{ni})^2} \qquad (i=1,2,3) \qquad (11)$$

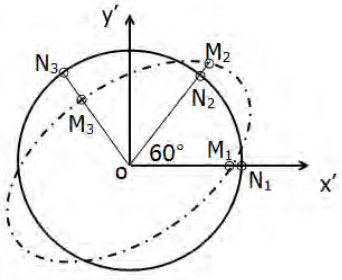

(a) Intersections of rays and the outline pre- and post-deformation

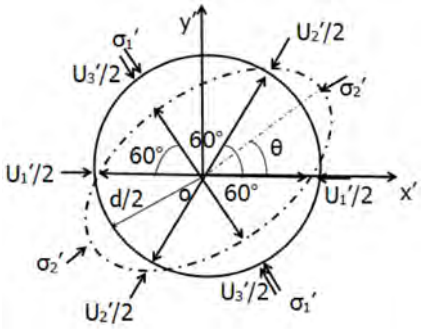

(b) Directions of deformation and stress

Figure 10. Deformation and state of stress in a cross-section perpendicular to the borehole.

Along the directions of the three rays, three diameter deformations U_1', U_2' and U_3' are defined as $2|M_1N_1|$, $2|M_2N_2|$ and $2|M_3N_3|$, rotated 60 degrees from each other, as shown in Fig. 10(b). Let β be the angle between the first deformation U_1' and the maximum principal stress σ_1', and a CCW rotation from U_1' to σ_1' as positive, the state of stress, i.e., the amounts and directions of the stresses σ_1' and σ_2' can be computed from the three deformations:

$$\begin{cases} \sigma_1' = \dfrac{E}{6d(1-\mathrm{n}^2)}[(U_1'+U_2'+U_3')+\dfrac{\sqrt{2}}{2}]\times \\ \qquad \times\sqrt{(U_1'-U_2')^2+(U_2'-U_3')^2+(U_3'-U_1')^2} \\ \sigma_2' = \dfrac{E}{6d(1-\mathrm{n}^2)}[(U_1'+U_2'+U_3')-\dfrac{\sqrt{2}}{2}]\times \\ \qquad \times\sqrt{(U_1'-U_2')^2+(U_2'-U_3')^2+(U_3'-U_1')^2} \\ \beta = \theta+\dfrac{\pi}{2} \end{cases} \qquad (12)$$

where v is the rock's Poisson's ratio and E is its elastic modulus.

If we attach an axial strain gauge to the core obtained from the borehole, and apply a confining pressure to it, the ratio of its axial and radial strain is its Poisson's ratio. The elastic modulus can be obtained by using a borehole deformation gauge to measure its confining pressure-deformation curve, using the following equation:

$$E = \frac{4P_0rR^2}{U(R^2-r^2)} \qquad (13)$$

where P_0 is the confining pressure; U is the average fine deformation caused by the confining pressure; R and r are, respectively, the outer and inner radii of the core.

If the axis of the borehole is along the same direction as a principal stress, the amount of which is already known, e.g., the gravity stress in a perfectly vertical well, measuring one borehole will be enough to determine the 3-dimensional state of stress at the measurement point.

5 CASE STUDY

We used the system to measure the stresses in the bottom outlets of a certain hydropower station. For the borehole ZK1 with diameter 168 mm, the system performed the measurement operation along a depth of 150 m, using a 91-mm outer drill, and a 40-mm inner drill. The cross-sectional stress data were obtained at 15 points, each separated by a depth interval of 10 m. As an example, data from the first three points are analyzed below.

5.1 Solving for stress

First, the system conducted data acquisition from depths 10, 20 and 30 m, generating images of probes before and after the stress relief. The images were processed by computer and stored as image data with directional information. The data then went under pre-processing, edge detection, and determination of probe apices.

With the positions of the probe apices known, they were fitted using least squares into circles and ellipses representing the statuses of the borehole before and after the stress relief. The circles or ellipses were described by equations, as shown in Fig. 11, Cartesian systems were established, and rays were drawn to calculate the three deformations U_1', U_2' and U_3' in each instance.

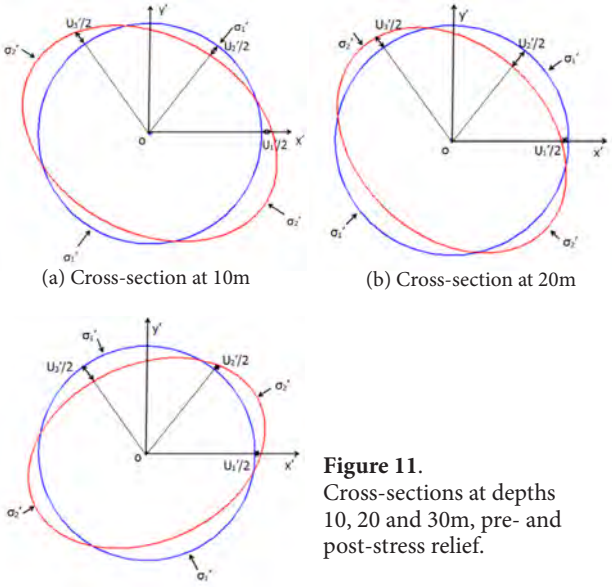

(a) Cross-section at 10m (b) Cross-section at 20m

Figure 11. Cross-sections at depths 10, 20 and 30m, pre- and post-stress relief.

Since the calculation requires knowing the rocks' Poisson ratios and elastic moduli, a RMT-150C rock testing machine was used to measure these parameters, with results shown in Table 1.

Table 1. Poisson's ratios and elastic moduli for cores at depths 10, 20 and 30 m.

Core location	10 m	20 m	30 m
Elastic modulus E/GPa	25.1	37.5	34.0
Poisson's ratio ν	0.27	0.27	0.27

The deformations U_1', U_2' and U_3' can then be used to determine the stresses in each cross-section using Equation (12), while the elliptical equation in each instance can be used to determine the angle θ between the major axis and the x-axis, thus obtaining the directions of two principal stresses for each measurement point. The results are shown in Table 2.

5.2 Analyses of the result

We conducted tests to validate the feasibility and reliability of the integrated system and the method. First, a three-axis compressor was used to perform a series of compression tests. For each core, confining pressures were applied that have the same amount and direction as the cross-sectional principal stresses above. Standard instruments were then used to measure the diameters of each hole before and after applying the pressures. The instrument is an inside micrometer with a precision of 0.001mm. The deformations caused by applying the known stresses were compared with the integrated system's results (see Fig. 12).

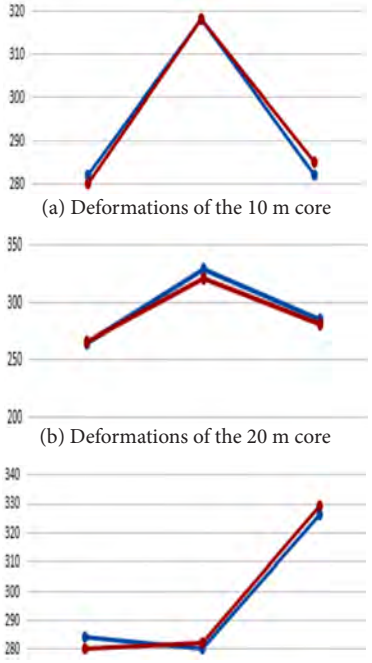

(a) Deformations of the 10 m core
(b) Deformations of the 20 m core
(c) Deformations of the 30 m core
(Blue: borehole measurements; Red: compression test results)

Figure 12. Comparison of deformations in borehole measurements and compression tests.

Table 2. Deformations and principal stresses along the cross-sections.

Location	Deformation			Principal stresses along the cross-section			
	$U_1'/\mu m$	$U_2'/\mu m$	$U_3'/\mu m$	σ_1' amount	σ_1' direction	σ_2' amount	σ_2' direction
10 m	282	318	282	9.1MPa	N29.88°E	1.0MPa	S60.12°E
20 m	264	328	284	14.3MPa	N55.34°E	1.5MPa	S44.66°E
30 m	287	280	326	10.7MPa	N39.67°W	1.3MPa	S50.33°W

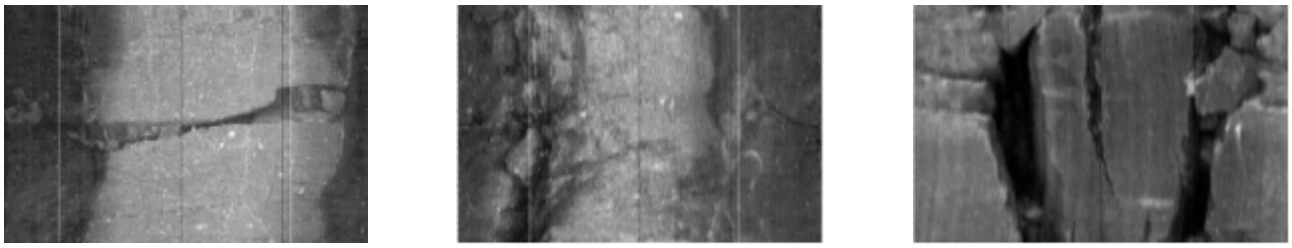

(a) 20m depth (b) 49m depth (c) 58m depth

Figure 13. Partial borehole images.

The greatest variance between the two is 1.06% at U_3' in Fig. 12(a), 2.44% at U_2' in Fig. 12(b), and 2.44% at U_1' in Fig. 12(c). It can be seen that the general tendencies of the deformations are similar between the two groups of results, with errors below 2.5%. Therefore, the system's measurements can be deemed valid.

The inner surfaces of a borehole might crack or peel off when the stress reaches a certain level. Such occurrences can also be used to determine the direction of the stress [17,18,19]. In our validation of the system, we used it to observe this borehole, and found the existence of cracks at 20 m (see Fig. 13(a)), and peeled off surfaces at 49 m and 58 m (see Figs. 13(b) and (c)). Their directions were consistent with calculations of the system, which were, respectively, along the west-east and north-south axes.

For the measurements of ZK1, the borehole was along the vertical direction. If we consider the geostress to be a principal stress, one measurement is enough to determine a point's 3-dimensional state of stress. Hence, the measurements over the full lengths of the borehole can be used to describe the vertical distribution of the stresses, which is depicted as rose diagrams in Table 3. The circumferential direction represents the directions of the stresses, and rotates clockwise from true north. The radial direction represents the amount of stress, with weaker stresses closer to the center, and stronger ones farther away from the center.

It can be seen in Table 3 that ZK1's maximum principal stress largely falls in the 10 MPa range, existing along the west-east direction, while the minimum principal

Table 3. Summary of stress distribution in ZK1.

Principal Stress σ_1 Rose Diagram	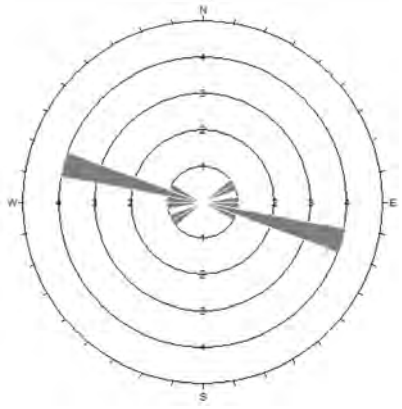	Principal Stress σ_2 Rose Diagram	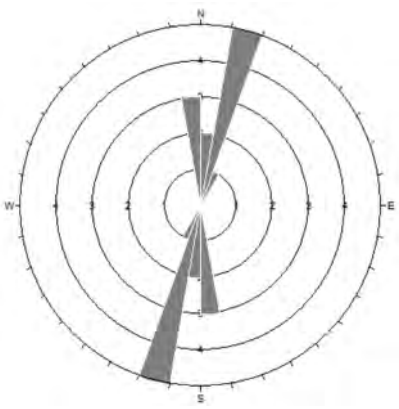
Principal stress-depth correlations Blue: σ_1; Red: σ_2 (Ver.: MPa; Hor.: 10m)	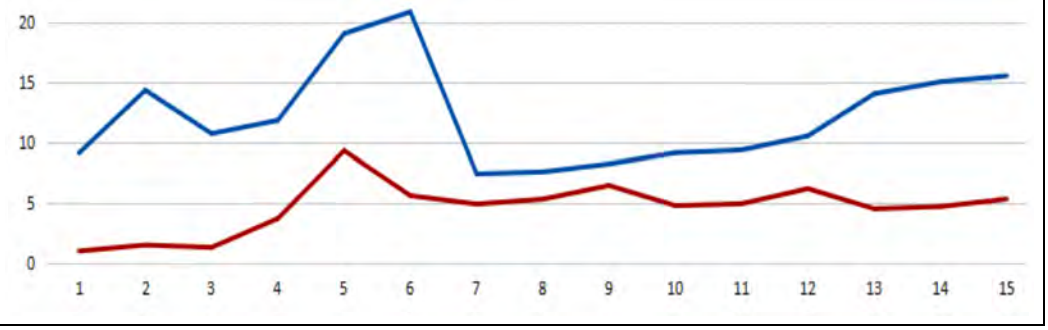		

stress is around 1.3 MPa along the north-south direction. There is no linear correlation between the stress and depth; the stresses are affected by multiple factors, and vary greatly between the depths. The distribution of stress is at least partially stochastic. It can only be described using a unified equation when the distribution is normal or log-normal [20]. For this survey, linear interpolation is used to describe the stress within each 10 m segment between measurement points, and reduce the complexity of stochasticity. The stress at each depth value is assumed to be a linear function of the two measurement points before and after it.

The results show that the stress varies considerably with depth. We chose the maximum values as an intuitive way to describe the borehole's stress characteristics. The maximum values of the principal stresses σ_1 and σ_2 are used as the reference values of the stress in this borehole, while the reference directions are obtained by observing the rose diagram.

The measurements of ZK1 indicate the system can effectively acquire the borehole deformations along the well, avoiding changes caused by rock creep during the long periods of waiting, which leads to more accurate results. The system also enables more efficient measurements of greater depths. The method of stress determination based on the system is a good approach to describe the movements of the probes, which can be used to calculate the deformations and principal stresses. The resulting cross-sectional stresses from the depths can be used to provide an intuitive depiction of the borehole's stress variations using rose and contoured diagrams.

6 CONCLUSION

This paper proposes a measurement method for geostress based on an integrated drilling and optical microscopy system. It employs microscopic imaging and direct contact probes to capture the changes of a borehole's cross-sections before and after the stress relief. The resulting images are analyzed with search circles to obtain the positions of the probe apices, which can be fitted into ellipses that describe the cross-sectional outlines, and calculate the states of stress. The validity and accuracy of the method was verified by tests and field application in the ZK1 borehole. The results show that: (1) the integrated system avoids inaccuracies caused by time delays; (2) the integrated system can be used to measure micrometer-grade deformations; (3) the search circle approach can accurately obtain the positions of probe apices; (4) the stress-measurement method based on the system is accurate and feasible; (5) the method can be used for stress measurements in deep positions and complex environments.

REFERENCES

[1] Liu, Y. F. 2000. Rock Body Geostress and Construction Engineering [in Chinese], Hubei Science & Technology, Wuhan.

[2] Ge, X.R., Hou, M.X. 2012. Principle of in-situ 3D rock stress measurement with borehole wall stress relief method and its preliminary applications to determination of in-situ rock stress orientation and magnitude in Jinping hydropower station. Sci China Tech Sci. 55, 939-949. DOI: 10.1007/s11431-011-4680-x

[3] Worotnicki, G., Walton, R. 1976. Triaxial "hollow inclusion" gauges for determination of rock stresses in-situ. Investigation of Stress in Rock - Advances in Stress Measuremnent, Proc, Int, Symp, Sydney,1-8 (supplement).

[4] Nur, A., Slmmons, G. 1969. Stress-induced velocity anisotropy in rock: an experimental study. J. of Geophys. Res. 74(27), 667~6674. DOI: 10.1029/JB074i027p06667

[5] AI Kai, Han Xiao-yu, Li Yong-song 2006. Regression Analysis of In-situ Stress for Wudongde Hydropower Station, Jinsha River [in Chinese]. Chinese Journal of Underground Space and Engneering 2, (26), 930-933. DOI: 10.3969/j.issn.1673-0836.2006.06.011

[6] Xu, Z.L. 2006. Elastic Mechanics [in Chinese], China Higher Education, Beijing.

[7] Luo, C.H., Wang, W. 2003. Refined theory of generalized plane-stress problems in elasticity. Acta Mechanica Solida Sinica 24(02), 192-196. DOI: 10.3969/j.issn.0254-7805.2003.02.009

[8] Yoshikawa, S., Mogi, K. 1981. A new method for estimation of the crustal stress from cored rock samples: laboratory study in the case of uniaxial compression. Tectonophysics 74, 323-339. DOI: 10.1016/0040-1951(81)90196-7

[9] Cai, M.F., Qiao, L., Li, H.B. 1995. Theory and Techniques of Geostress Measurement [in Chinese]. China Science, Beijing.

[10] Amadei, B., Stephansson, O. 1997. Rock stress and its measurement, Chapman and Hall, London.

[11] Duncan Fama, M.E., Pender, M.J. 1980. Analysis of the hollow inclusion technique for measuring in-situ rock stress. Int. J. Rock Mech. Min. Sci. And Geomech. Abstr. 17, 137-146. DOI: 10.1016/0148-9062(80)91360-1

[12] Wang, L.J., Pan, L.Z. 1991. Geostress Measurement and Its Application in Engineering [in Chinese]. China Geology, Beijing.

[13] Zhang, Z., Xu, C. 2014. Digital Image Processing and Machine Vision, China Posts & Telecom, Beijing.

[14] Brudy, M., Zoback, M.D., Fuchs, K. et al. 1997. Estimation of the complete stress tensor to 8 km depth in the KTB scientific drill holes: implications for crustal strength. Journal of Geophysical Research 102(B8), 18453-18475. DOI: 10.1029/96JB02942

[15] Sun, W.C., Min, H., Wang, C.Y. 2008. Three-dimensional geostress measurement and geomechanical analysis. Chinese Journal of Rock Mechanics and Engineering 27(z2), 3778-3784. DOI: 10.3321/j.issn:1000-6915.2008.z2.070

[16] Wang, C.Y., Han, Z.Q., Wang, J.C., Wang, Y.T. 2016. Study of borehole geometric shape features under plane stress state, Chinese Journal of Rock Mechanics and Engineering 35(z1), 2836-2846. DOI: 10.13722/j.cnki.jrme.2015.1045

[17] Quan Jiang, Xia-ting Feng, Jing Chen, Ke Huang, Ya-li Jiang 2013. Estimating in-situ rock stress from spalling veins: A case study. Engineering Geology 152(1), 38–47. DOI: 10.1016/j.enggeo.2012.10.010

[18] Jiang, Q., Feng, X.T., Xiang, T.B., Su, G.S. 2010. Rockburst characteristics and numerical simulation based on a new energy index: a case study of a tunnel at 2500 m depth. Bulletin of Engineering Geology and the Environment 69, 381-388. DOI: 10.1007/s10064-010-0275-1

[19] Quan Jiang, Xia-ting Feng, Yilin Fan, Qixiang Fan, Guofeng Liu, Shufeng Pei 2017. In situ experimental investigation of basalt spalling. Tunnelling and Underground Space Technology 68, 82-94. DOI: 10.1016/j.tust.2017.05.020

[20] Jiang Q., Zhong S., Cui J., Feng X.T., Song, L. 2016. Statistical Characterization of the Mechanical Parameters of Intact Rock Under Triaxial Compression_ An Experimental Proof of the Jinping Marble. Rock Mechanics & Rock Engineering 49 (12), 4631-4646. DOI: 10.1007/s00603-016-1054-5

VREDNOTENJE ZMANJŠANJA VELIKOSTI ZOŽITVE ZRNATIH FILTROV ZARADI INTERNE EROZIJE OSNOVNIH KOHEZIVNIH ZEMLJIN

Samira Azirou
Université de Bejaia,
Faculté de Technologie,
Laboratoire de Génie de la Construction et Architecture
06000 Bejaia, Alžirija
E-pošta: azirousamira@gmail.com

Normandie Univ
UNIHAVRE, CNRS, LOMC, 76600 Le Havre, Francija

Ahmed Benamar
Normandie Univ
UNIHAVRE, CNRS, LOMC, 76600 Le Havre, Francija

Abdelkader Tahakourt
Université de Bejaia,
Faculté de Technologie,
Laboratoire de Génie de la Construction et Architecture
06000 Bejaia, Alžirija

Ključne besede

resonančna kolona; resonančna frekvenca; strižni modul; relativna gostota; efektivni konsolidacijski tlak; dinamični strižni modul

Izvleček

Ta študija obravnava analizo filtrirnih zožitev in njeno uporabo glede zmanjšanja por in zožitev med filtriranjem tal. Eksperimentalna preiskava vključuje kombinirane preizkuse erozije-filtriranja v luknji z več zemljinami in filtri. Osnovno zemljino predstavlja peščena glina, medtem, ko so zrnati filtri izbrani glede na običajna filtracijska merila. Kombinacija eksperimentalnih podatkov o spreminjanju poroznosti in analitičnih rezultatov analize porazdelitve zožitve (CSD) je bila uporabljena za vrednotenje zmanjšanja velikosti zožitev zaradi filtracijskih procesov. Globina filtracije je bila ocenjena tudi glede na zadržano maso zemljine in zmanjšanje poroznosti, ki izhaja iz izmerjene hidravlične prepustnosti. Za ocenitev zmanjšanja zožitev je bil uporabljen analitični model CSD, ki je upošteval eksperimentalne rezultate. Glede na dobljene rezultate je predlagana neenakomerna zožitev glede na efektivno globino filtracije, ki potrjuje dinamično delovanje filtra.

EVALUATION OF THE CONSTRICTION SIZE REDUCTION OF GRANULAR FILTERS DUE TO UPSTREAM COHESIVE BASE-SOIL EROSION

Samira Azirou
Université de Bejaia,
Faculté de Technologie,
Laboratoire de Génie de la Construction et Architecture
06000 Bejaia, Algeria
E-mail: azirousamira@gmail.com

Normandie Univ
UNIHAVRE, CNRS, LOMC, 76600 Le Havre, France

Ahmed Benamar
Normandie Univ
UNIHAVRE, CNRS, LOMC, 76600 Le Havre, France

Abdelkader Tahakourt
Université de Bejaia,
Faculté de Technologie,
Laboratoire de Génie de la Construction et Architecture
06000 Bejaia, Algeria

Keywords
granular filter, internal erosion, constriction, porosity, filtration index

DOI https://doi.org/10.18690/actageotechslov.15.1.29-41.2018

Abstract

This study is devoted to filter-constrictions analysis and its application with respect to void and constrictions reduction during soil filtration. The experimental investigation involves combined Hole Erosion-Filtration tests using several soils and filters. The base soils are lean clays and the granular filters are selected according to the usual filtration criteria. The combination of the experimental data for porosity variation and the analytical results from the Constriction Size Distribution (CSD) analysis was used to evaluate the constrictions size reduction subsequent to the filtration process. The filtration depth was also estimated according to the retained soil mass and the porosity reduction deduced from the measured hydraulic conductivity. An analytical model of the CSD was applied to the experimental results in order to assess the constrictions reduction. As regards the obtained results, a non-uniform constriction reduction was suggested according to the effective filtration depth, advocating a dynamic filter action.

1 INTRODUCTION

Filters in hydraulic works are designed and constructed to achieve specific goals such as preventing the internal soil erosion and controlling the drainage. The filters managed in zoned dams are designed according to criteria based on the grain size distribution of both filter and erodible soil. Many laboratory researches devoted to filter criteria have been developed for cohesionless soils, and resulted in relationships related to grain size [1, 2, 3, 4, 5, 6, 7, 8]. Since filter pores and their connectivity define their ability to retain transported particles by seepage, very important basic concepts defined the voids (constrictions) in the filter and the material density as the key parameters governing filtration and preventing the erosion of base soil. The filter criteria are often designed using the particle size distribution (PSD) [1, 3, 9, 10], whereas the filtration process mainly involves the constriction size distribution (CSD).

A spherical particle model can provide an estimation of the apparent pore size of a granular filter, and it is controlled by the grain size distribution and material density. A new approach based on the constrictions distribution was introduced by Silveira (1964) [11] in a geometrical model of the pore space existing between a filter's grains. Silveira et al. (1975) [12] suggested a cubic pack (four particles) for assessing the constriction size. Ziems (1968) [13] brought criteria from the Silveira (1964) [11] method and transformed the volumetric or mass distribution to a number distribution of particles. In this way, he reached a distribution involving smaller

pores $d_{p,min}$ with a limit of $0.155D_{min}$, and larger pores $d_{p,max}$ limited by $0.155D_{max}$, where D_{min} and D_{max} are the smallest and largest particle sizes of the filter, respectively. Wittmann (1979) [14] proposed the concept of soil filtration, taking more care of the real geometrical and structural properties of the porous media, and an average pore area was determined theoretically and verified in initial experiments by measuring the whole distribution of the pore areas. A granular soil is modeled as a three-dimensional collection of particles that forms pores of different size and shape. These models assume pores involving a regular three--dimensional structure, such as a cubic or tetrahedral arrangement [11, 12, 15].

Previous approaches [11, 12, 14, 15] could not provide a constrictions distribution at intermediate densities between the densest and the loosest states. A critical review of the two models based on three or four particles, reported by Silveira (1964, 1975) [11, 12], was proposed by Wang and Yousif (2014)[16], who indicated that a number of likely particle groups is missed, leading to the fact that the number of unique groups calculated in these models is less than the actual number. They then proposed correction factors that are not intrinsic, but depend on both the density and the particle size distribution. Indraratna et al. (1997, 2007), Locke et al. (2001), Reboul et al. (2008), Vincens et al. (2014) [17, 18, 19, 20, 21] grouped all the parameters and suggested a complete model of the voids distribution for any relative density, usually based on a filter's particle size distribution (PSD) by area. Taylor et al. (2015) [22] proposed a new method to measure and visualize void constrictions in sands using micro-CT data, with a view to assessing the granular filter's performance.

In this study the CSD model of Locke et al. (2001) [18] was used to address the constrictions size reduction of filters tested downstream of cohesive base soils. An analysis of the constriction size reduction was presented, based on a filter porosity variation under successive hydraulic loads.

2 EXPERIMENTAL METHODOLOGY

2.1 Materials

In order to investigate the filter's efficiency with respect to base soil erosion from a simulated crack (hole), two cohesive base soils and two granular filters were selected. Table 1 summarizes the main characteristics and classification of different tested materials according to ASTM D2487 (2011) [23]. The two selected base soils are classified as Lean Clay (*CL*), whereas filters F_1 and F_2 are classified as Poorly Graded sand according to the Standard Soil Classification System [23]. Table 2 summarizes the additional geotechnical parameters of the used base soils, measured according to ASTM standards. The shear resistance was measured using a vane shear test and the plasticity index (Atterberg Limits) provides a slightly plastic clay for both CL_1 and CL_2.

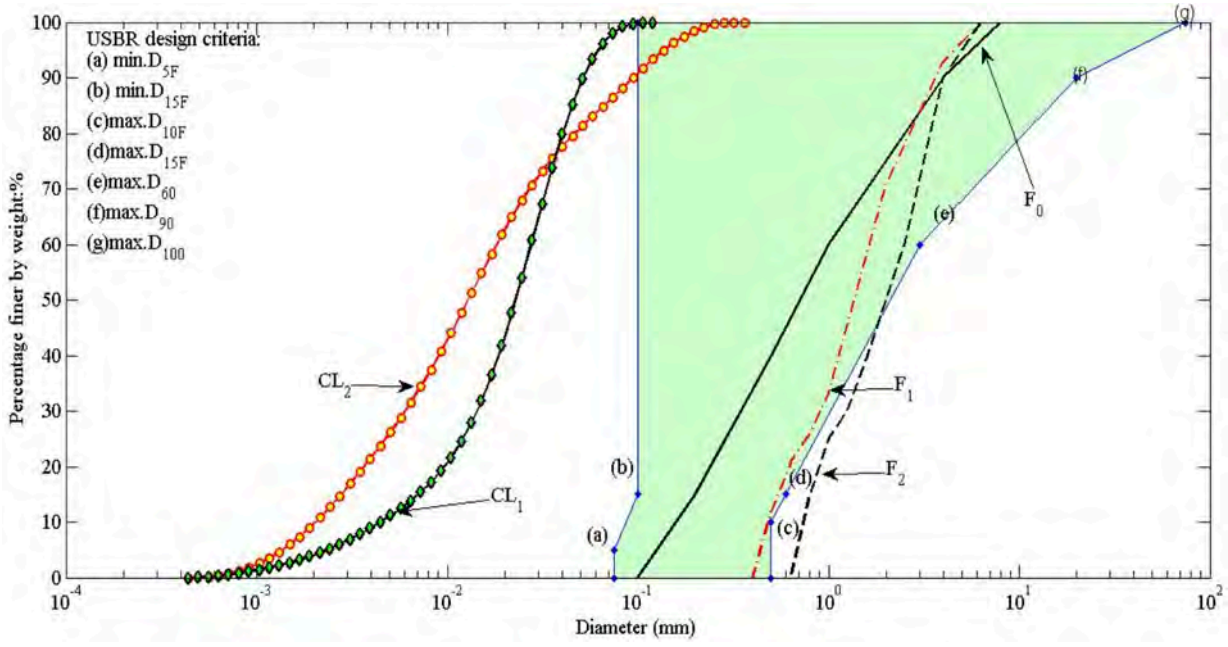

Figure 1. Particle size distribution of used materials (filters and base soils) [24].

Table 1. Classification of different tested materials (ASTM D2487 [23]).

Soil Type	Coefficient						Soil classification (ASTM D2487, [23])
	F_c[a] (%)	G_c[b] (%)	Dry density	Specific gravity	Uniformity (C_u[c])	Curvature (C_c[d])	
F_1	0	10	1.65	2.65	5	1.25	SP: Poorly graded sand
F_2	0	10	1.65	2.65	3.15	0.78	SP: Poorly graded sand
CL_1	85	0	1.60	2.60	7.97	1.83	CL: lean clay
CL_2	85	0	1.60	2.60	8.77	0.96	CL: lean clay

F_c[a]: fines content (mass fraction in percentage of particles finer than 75μm).
G_c[b]: gravel content (mass fraction in percentage of particles coarser than 4.75mm).
C_u[c]: uniformity coefficient ($C_u = D_{60} / D_{10}$)
C_c[d]: curvature coefficient ($C_c = (D_{30})^2 / (D_{10} \times D_{60})$)

Table 2. Geotechnical parameters of used soils (ASTM D2487, 2011)[23].

Lean Clay type	Atterberg limits			Shear resistance (kPa)	D_{15}/d_{85}		
	WL (%)	W_p (%)	Plasticity Index (%)		F_0	F_1	F_2
CL_1 (Namur)	33	21	12 (slightly Plastic)	7	4.4	11	13.8
CL_2 (Normandy)	34	21	13 (slightly Plastic)	8	2.7	6.7	10.8

Fig. 1 shows the PSD curves of different materials used in the laboratory Erosion-Filtration tests, and the grading range limit of the USBR design criteria [24] for dam filters. The grain size of the base soil CL_1 ranges from 0.40 μm to 120 μm, while the CL_2 grains provide a larger size (from 0.40 μm to 361 μm). The base soils CL_1 and CL_2 were collected from Namur (Belgium) and Normandy region (France), respectively. Two granular filters made of silica sand, collected from Seine River (France) were selected by sieving according to USBR (1994) filter criteria [24]. The finer filter F_1 presents a grading range between 0.40 mm and 6.30 mm, whereas the coarser filter F_2 provides a grain size ranging from 0.63 to 6.30 mm. As illustrated in Fig. 1, filter F_2 was designed to not meet the usual filter criteria. It is important to emphasize that a first designed filter F_0 was tested, and owing to its internal instability it was rapidly suffering suffusion and so not included in this study.

In order to investigate the filtration process involving constrictions size, the CSD model described in Appendix A was implemented using a material relative density close to D_r=0.65, involving the loosest and the densest states of the filters. Fig. 2 displays PSD and CSD

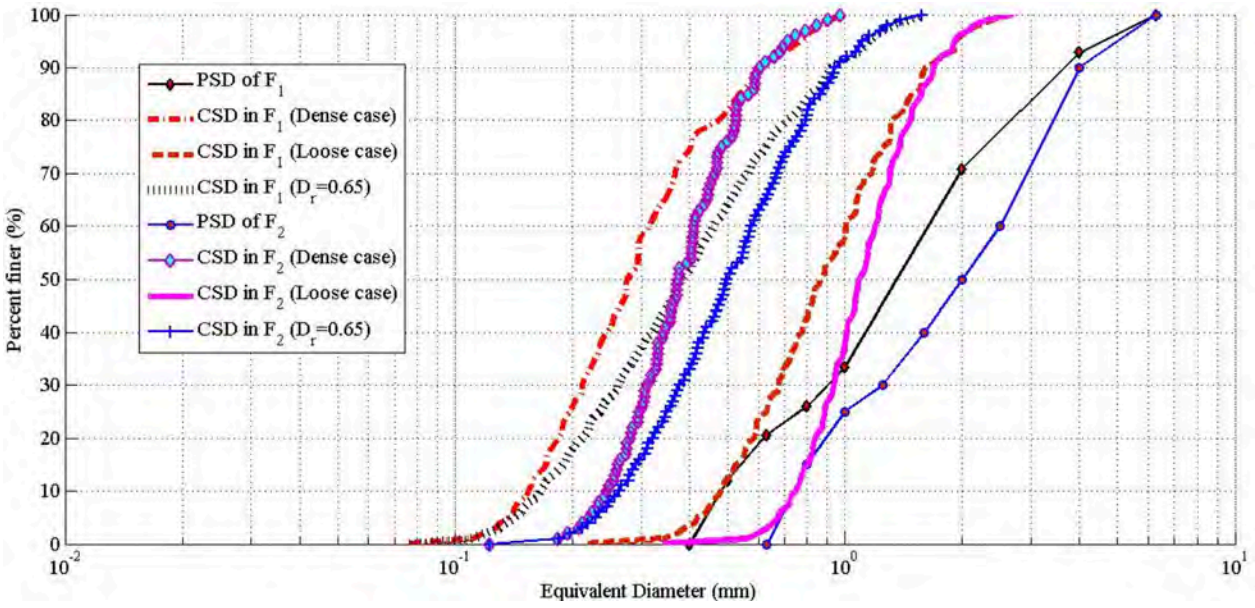

Figure 2. CSD of filters F_1 and F_2 (densest, loosest and for D_r = 0.65 cases).

plots for the filters F_1 and F_2 in the loosest and densest cases calculated from the analytical model using Eq.11 (Appendix A) with different available series of grain diameters. The CSD obtained for a relative density of 0.65 for both filters, as expected from the Locke et al. (2001) [18] model, highlights that the CSD of filter F_2 provides larger constrictions than that of filter F_1.

2.2 Test setup

For studying filtration, the processes of particles erosion from the base soil and their subsequent filtration by a downstream filter are investigated. Filtration studies usually involve direct experimentation through laboratory tests. Sherard and Dunnigan (1989) [10] designed the NEF (No Erosion Filter) test to simulate the filtration of cohesive soils (arising from base soil crack erosion) in a granular filter. The used experimental apparatus, shown in Figure 3, involves a permeameter (cylindrical cell made of Plexiglas) that is 140 mm in diameter and 280 mm high, connected to a tap-water (temperature of 18°C and pH of 6.8) supply, which provides a selected pressure. The inlet cell is equipped with a pressure gauge and the outlet is directed to a turbidity meter and a flow meter providing continuous records of the measured values. The cell is mainly composed of four compartments: The filter layer (150 mm) compacted on a glass-beads (8-mm diameter) layer, the base soil (25-mm thin) compacted (water content close to 12 %) to a target density (Table 1) above a steel plate, and at the top of the cell a gravel layer is placed for flow spreading. A 10-mm diameter pinhole was drilled through the base soil and the steel plate in order to introduce a concentrated flow through the hole and simulate how to match the erosion results. Glass beads forming the bottom layer involve a sufficiently high filtration to avoid the retention of particles released from the tested filter above.

A vertical upstream flow was induced with a very low pressure through the soil-filter system and once saturation is reached, the downstream flow generates the water pressure, gradually increased by steps corresponding to selected pressure test values (25, 50 and 75 kPa). The particle concentration of the outlet suspension is derived using a previous correlation between the concentration and the turbidity (NTU: Nephelometric Turbidity Unit). The processes of particle erosion from the base soil and the filtration are first decoupled by performing the hole erosion test alone.

2.2.1 Hole Erosion Test

In order to investigate the internal erosion of the base soil a series of hole erosion experiments without a filter are conducted. They are devoted to evaluate the solid flux eroded from the base soil under fixed hydraulic conditions and thereby the susceptibility of the base soil to erosion. The results will also be used later as the limit conditions at the filter inlet to quantify the soil mass entering at each pressure step. For each applied pressure, the turbidity of the outflow and the flow rate are recorded continuously, and so the erosion rate and the eroded mass are derived.

2.2.2 Combined Erosion-Filtration Test

Experiments combining the base soil erosion with a downstream filter are carried out in order to investigate the extent to which the internal erosion is minimized from the soil protected by a filter. The filtration tests involve the different base soils combined with each filter. Fig. 3 shows the cell used in the filtration test with a water supply and data-acquisition systems. The measurements performed during the test include the flow rate and the particle concentration of the effluent. The performance of the filter is observed during a processing time of up to one hour. The results presented in this study involve two base soils and two filters.

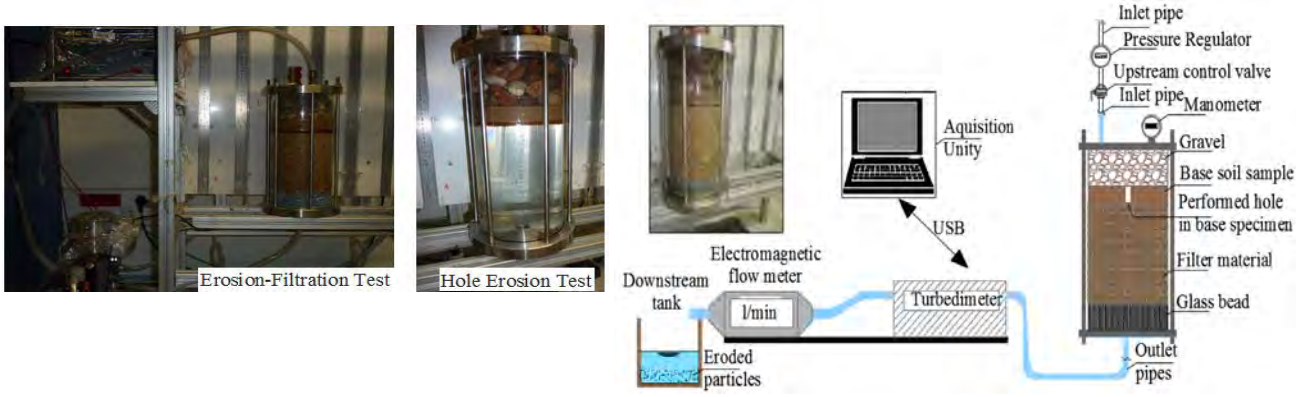

Figure 3. Experimental set-up of the Hole-Erosion and Erosion-Filtration tests and device pictures.

3 CONSTRICTION SIZE REDUCTION APPROACH

A continuous approach of the filtration process can be integrated as an internal variable in the cumulated distribution of constriction sizes. Appendix A details the approach developed for constriction size reduction during filtration. Starting from this point, the deposited particles of base soil within the filter pores modify the constrictions distribution by reducing the space of accessible constrictions (constrictions that are many times larger than filtered particle size).

3.1 Effective filtration volume: Iteration model

Filtration processes can be classified in accordance with the location of the retained particles that can either be deposited on the outer surface of the filter medium (surface filtration) or inside the whole filter medium (depth filtration). Filtration is affected by CSD, which continuously evolves with the porosity reduction, leading to more and more retention of the base soil during the filtration process. Understanding the factors that control the transport of soil particles detached by the water flow is essential for predicting the contingency of the internal and surface erosion of embankments. The effective volume (V_{ef}) was defined as the actual volume in which the filtration occurs. To evaluate the effective volume (V_{ef}) of filtration it is assumed that the filter medium is homogeneous. For each pressure step P_i (where i represents the pressure value: 25, 50 or 75kPa), the retained dry mass m_i in the filter was derived as the difference between the eroded mass from the base soil (the hole-erosion test) and the eroded mass from the soil-filter system. Then the void occupied by the deposited particles (m_i/γ_d) within the filter was subtracted from the total void volume of the filter (V_{vi}) to obtain the released void volume. The actual porosity (n_i) is calculated as the ratio of this released void volume to the total volume (V_T). The actual porosity n_i was compared to the porosity (n_{ki}) deduced from the measured hydraulic conductivity through the Kozeny-Carman formula [25, 26]. Because the decrease of the hydraulic conductivity is due to the deposited particles within the constrictions, this parameter can be linked to the CSD evolution. Whereas the retained mass is a global amount, non-uniformly distributed (Benamar, 2013) [27], the hydraulic conductivity decrease is strongly impacted by the particle accumulation and so advocates the concept of a local depth where the porosity decreases. The ratio of the two porosity values (n_{ki}/n_i) is defined as the filtration index for each pressure step. The iterative process for such an assessment is described in the flowchart of Fig.4.

The effective filtration volume is distributed through the filter according to the CSD and can fill, in the first approximation, a partial height of the sample containing the effective constrictions and defined by the filtration index λ (Eq. 1). The effective height (volume) can be described by the filtration depth as:

$$H_f = \lambda \times H \qquad (1)$$

where H_f is the filtration depth, H is the filter height.

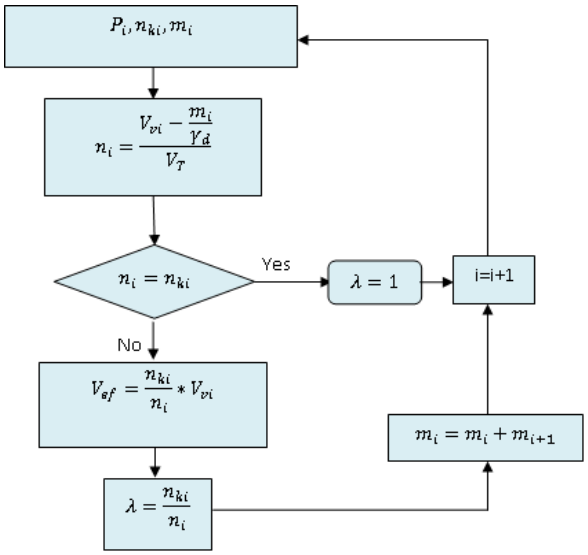

P_i : pressure step (i= pressure value (25, 50 or 75kPa);
m_i : retained mass within a filter
γ_d : dry unit weight of the deposited particles
V_{vi} : total void volume of the filter (V_{vi}= n_0*V_T)
n_i : actual porosity
V_T : total volume
n_k : porosity from the Kozeny-Carman relation
λ : filtration index

Figure 4. Flowchart of the evaluation of the filtration index.

3.2 Evaluation of the constrictions size reduction

In granular soil, many authors provide a correlation between the grain sizes of the filter material and the hydraulic conductivity [8, 24], whereas other models relate the hydraulic conductivity to the porosity like the Kozeny-Carman relation (Eq. 2). The work presented here attempts an alternative to previous approaches by linking the constrictions size variation to the filter porosity reduction. Since the porosity reduction is deduced from the hydraulic conductivity decrease, which is mainly due to the constrictions size reduction, it is permissible to allocate the void decrease to the constrictions size reduction. In order to study the dimensions variation of the constrictions, some assumptions are allowed, such as:

- the particle deposition in the constriction void was uniformly distributed along the constriction wall (Fig. 5);
- the particles are assimilated to spheres;
- if a large particle is blocked in any constriction, its diameter will be reduced and then smaller particles arriving at this same constriction will be blocked again;
- the constriction size decrease is related to the porosity reduction in the filter, estimated by the relative value n_k/n_0;
- in order to calculate the constriction reduction, the retained particles are deposited within the constrictions. To take into consideration the error from such an assumption, the size reduction of the constriction is addressed in terms of the constriction volume as defined by Eq. 3;
- the filtration is uniform, according to the filter depth.

The average diameter of the constrictions change can be estimated using Eq.4, moving from the initial constriction size D_{c0} to the final constriction size D_{cf}, using the values of the initial porosity n_0 of the clear filter and the final porosity n_k (deduced from the Kozeny-Carman relation [25, 26], Eq. 2). The formula's applicability is generally limited to particles that meet the following relation: 0.01 cm < D_{10} (particle size for which 10% of the filter is finer) < 0.3 cm [25]. The filters used in this study provide a D_{10} value in the range of 0.1 to 3 mm (Fig. 1), thus allowing the use of the Kozeny-Carman equation [25, 26], defined as follows:

$$k = k_0 \frac{n_k^3 (1-n_0)^2}{n_0^3 (1-n_k)^2} \qquad (2)$$

where k_0 is the initial hydraulic conductivity (global value) of the filter measured in an additional test with the filter alone; k is the hydraulic conductivity (global value) mesured during the erosion-filtration test from the flow measurement; n_0 is the initial porosity of the clean filter; and n_k is the porosity from Eq. 2.

The final volume of the constriction V_{cf} is related to the initial constriction volume V_{C0} by the porosity ratio, as follows (Eq. 3):

$$V_{Cf} = \frac{\pi D_{Cf}^3}{6} = \left(\frac{n_k}{n_0}\right) \times V_{C0} \qquad (3)$$

So the diameter of the reduced constriction (D_{Cf}) can be deduced from the initial constriction (D_{c0}), as follows:

$$D_{Cf} = \sqrt[3]{\frac{n_k}{n_0}} \times D_{C0} \qquad (4)$$

The equivalent hydraulic conductivity measured over the specimen length can be a significant global parameter of the filtration magnitude, but if a great local reduction occurs, the use of the filtration depth will make the model more realistic.

During filtration the constriction size reduction also depends on the depth filtration. Eq. 3 provides a uniform distribution of the void constrictions over the whole filter volume, but if using the filtration index λ (Eq. 1) of accessible constrictions, which was assumed by describing the effective volume of filtration, the results must be improved.

In order to start from the same principle as that of constriction (combining the densest and loosest cases through the relative density, D_r [18]) and to investigate the quantitative void reduction following the filter depth, the constriction size reduction caused by the retained base soil is carried out using Eq. 5, where the reduced diameter (d_r) is computed as a value located between the initial constriction (D_{c0}) and the extreme case (D_{cf}). The two cases being related to the filtration index λ, as defined by Eq. 5.

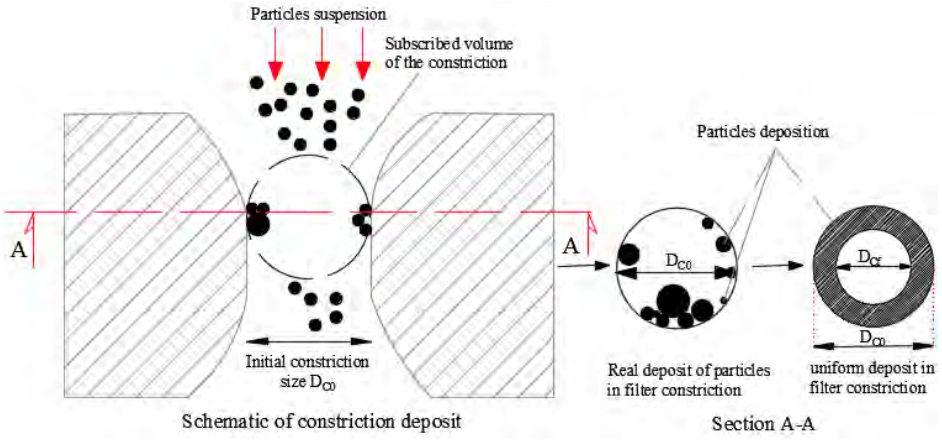

Figure 5. Schematic drawing of the constriction (diameter) size reduction.

$$d_r = D_{cf} + \lambda\left(D_{c0} - D_{cf}\right) \qquad (5)$$

As a result, for a greater value of λ the constriction size d_r is reduced by a smaller amount because the depth of the filtration is greater, allowing the particles to deposit on a larger depth (deep filtration). A smaller value of λ produces a larger size reduction (lower value of d_r), meaning that all the particles remain in a reduced filter layer (surface filtration).

4 RESULTS AND DISCUSSION

4.1 Hydraulic conductivity and porosity reduction

The filtration process induces soil-particle retention within the medium, leading to porosity and hydraulic conductivity reduction. During the test, the hydraulic conductivity (using flow-rate measurements) of the filter was recorded periodically at the outlet and this parameter variation indicates the consistency of the particle retention within the filter. In order to assess the porosity reduction during the test, including several loading steps, the Kozeny-Carman equation [25] was used to derive the filter porosity (n_k). The results of the porosity and the hydraulic conductivity evolution versus the applied pressure for different combinations of soil-filter are illustrated in Figs 6 and 7 below. They described the hydraulic conductivity and porosity decrease over the testing time as a nonlinear trend, showing a severe decrease during the first pressure step before reaching an asymptotic value after successive pressure steps.

The hydraulic conductivity in the filter initially decreased drastically as the erosion of the soil operates and detached particles flow into the filter under pressure load, where most of them deposit. It is obvious that the soil CL_2 causes the highest hydraulic conductivity reduction in filter F_1, while filter F_2 presents the lowest hydraulic conductivity reduction, whatever the tested soil. The drastic hydraulic conductivity decrease, similar to clogging, can be caused by the surface-deposition process of large particles of the soil CL_2 on the upper side of the filter F_1. As regards to the hydraulic conductivity requirement in the filter design, filter F1 combined with base soil CL_2 evolves towards a clogged filter, which rapidly drives to uplift pressures. Filter F_2 shows a similar trend with both base soils (CL_1 and CL_2).

As regards to the porosity reduction (Fig. 6), Filter F_1 shows the highest reduction, reaching a porosity value close to 0.22, when operating with soil CL_2, while filter F_2 reaches a porosity close to 0.36 with the same base soil (CL_2) (Fig. 7). If comparing the filtration ability of filter F_1 towards the tested soils, after successive hydraulic loads, the porosity is lowered to 0.33 and 0.22 when filtering CL_1 and CL_2 soils, respectively. So, the porosity reduction of filter F1 caused by the soil erosion is much more important with CL_2 than with CL_1 owing to the large particles encountered in the soil CL_2. This drastic reduction of the filter porosity can be attributed to the kind of filtration process that can be a surface filtration when the soil particles are enough large, while a deep filtration (filtration occurs more deeply in the filter and the eroded particles are moved in the filter at a distance farther than the top of the filter) is expected when the particles are smaller than they are in soil CL_2. The lowest porosity value (0.36) was obtained for filter F_2, whatever the tested soil (Fig. 7), owing to the larger voids available in that porous medium. The highest porosity reduction is operated in filter F_1 with soil CL_2 and approaches a relative value of 0.22, providing the lowest hydraulic conductivity close to 2.27×10^{-5}m/s (Fig. 6).

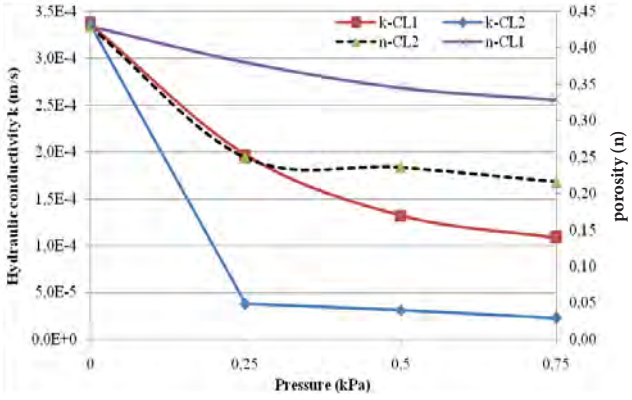

Figure 6. Hydraulic conductivity and porosity evolution in filter F_1.

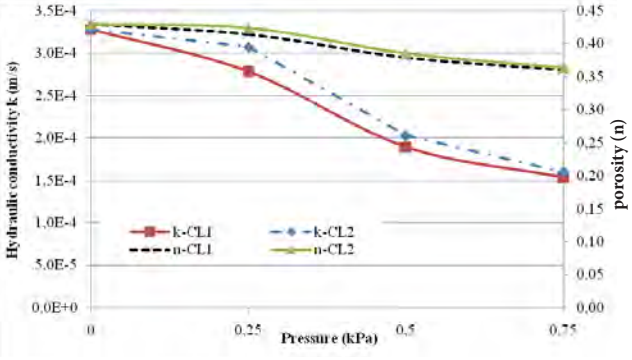

Figure 7. Hydraulic conductivity and porosity evolution in filter F_2.

4.2 Filtration depth and constrictions size reduction

The concept of filtration depth was reported in several studies [11, 17, 28] showing an asymptotic distribution of the retained mass along a porous medium. The effective void volume contributing to the particle retention can be expressed as a filtration depth (Eq. 1). Fig.8 illustrates the evolution of the filtration depth in filter F_1 at various steps of the applied pressure and the resulting filter porosity (displayed within the chart histogram bars). The chart's bars describe the filtration depth for each base soil (CL_1 and CL_2) in the filter F_1 and the value inside represents the porosity along this depth. The comparison between the filtration of soils CL_1 and CL_2 indicates that the filtration depth is more important with CL_1 (13.1 cm at a pressure of 25kPa, representing 87.5% of the filter height) than with CL_2 (9 cm, representing 60% of the filter height) over all the tested pressures. Because of the fine particles contained in soil CL_1, they deposit deeply, while large particles involved in the soil CL_2 provide self-filtration (surface filtration), leading to a reduced filtration depth. We can note that large values of the final porosity are recorded in the cases of deep filtration.

Because soil CL_2 creates a strong porosity reduction and likely clogging occurrence within filter F_1, the comparison of the behavior of both tested filters against the flowing particles of soil CL_2 was assessed. Fig.9 illustrates a comparison of the filtration depth and reduced porosity in both filters after successive load

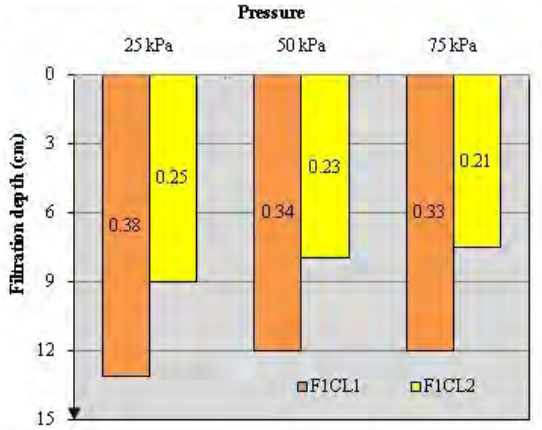

Figure 8. Evolution of the porosity and filtration depth with hydraulic pressure in filter F_1 with soils CL_1 and CL_2.

pressure steps. As regards to the filtration process, filter F_2 is more efficient, reaching a filtration depth of 99 % and holding the filter in a range of sustainable porosity and easy water flow, whereas filter F_1 concentrates the particle retention within a thin layer, drastically reducing the local pore volume, leading to severe hydraulic conductivity reduction and likely clogging. The operating difference between the two filters is related to the large constriction size of the filter F_2, which provides an easy transport of the largest particles of soil CL_2 and so a deeper penetration within the filter. Unlike the smaller constriction size of filter F_1 this leads to the easy retention of the soil particles, involving self-filtration, which in turn leads to a thin (9 cm) depth filtration.

For the first load step (P=25 kPa) the relative depth filtration obtained in filter F_1 operating with soil CL_2 is close to 9/15 (the eroded particles can be transported to a depth of 9 cm among 15 cm, see Fig. 9), representing 60 % of the accessible constrictions that undergo a size reduction. At the second pressure step (P=50 kPa) only 53 % of the filter depth is so submitted to a second successive size reduction. When applying a pressure of 75 kPa, only 50 % of the depth is of concern and the constriction size is reduced again by particle retention.

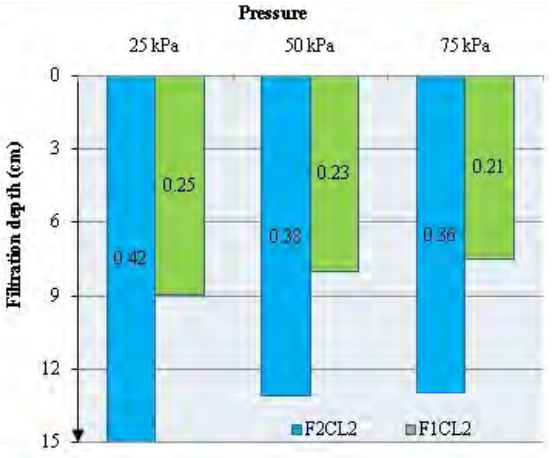

Figure 9. Comparison of the variation of porosity and filtration depth with hydraulic pressure in filters F_1 and F_2 operating with soil CL_2.

In order to investigate the constriction size reduction after filtration, the test of filter F_1 operating with soil CL_2 (critical case) was conducted. Fig. 10 shows the initial CSD curve of the filter F_1 and the modified one after filtering soil CL_2, obtained by Eq. 5. The gap observed between the initial and final CSD curves is quite important, indicating a significant constriction size reduction. This gap is less important for large constrictions. The result is in agreement with the strong porosity reduction obtained in filter F_1 when operating with soil CL_2 (Fig. 6). The retention of coarser particles with a maximum size of 360 μm within the filter advocates the blocking of an important number of further flowing particles by the self-filtering process. The main CSD gap was produced at the first pressure step (25 kPa), whereas further applied loads provide low variations of CSD.

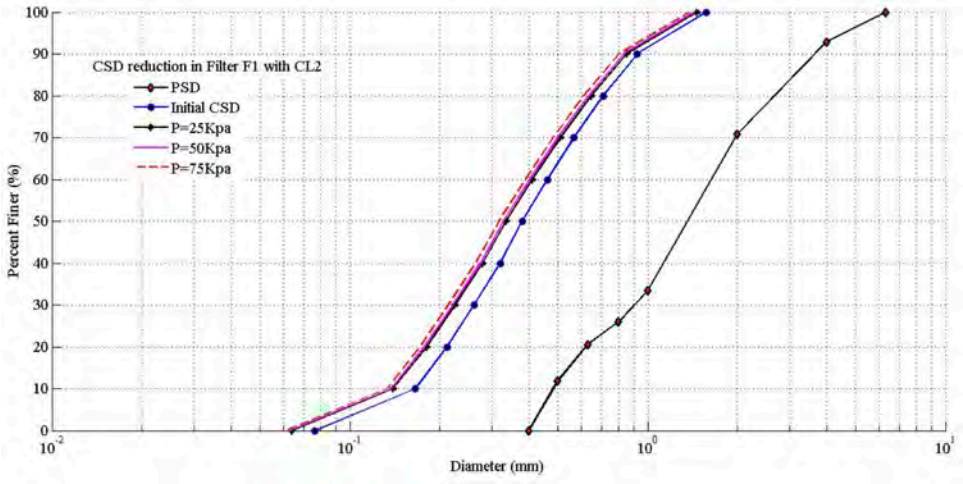

Figure 10. Constriction size reduction in filter F_1 tested with base soil CL_2.

4.3 Effect of filter opening on the constriction size reduction

As regards to the filter clogging by particle deposition, the comparison between F_1 and F_2 when operating with base soil CL_2 indicates that filter F_1 produces a greater pore clogging, whereas filter F_2 exhibits interesting behavior. This section presents an investigation of the filter behavior on the pore scale through the constriction size reduction. The filtration index λ (Eq. 1) is more important (0.400) in filter F_1 than in filter F_2 (0.125). Fig. 11 illustrates a comparison of the constriction size reduction within both filters when operating with soil CL_2. It is shown that a uniform decrease of CSD of filter F_2, but the decrease is more important and noticeable in filter F_1. The constriction size reduction in filter F_1 is greater than that obtained with filter F_2. This behavior was affected by the more important retention of particles at filter F_1 upstream.

In order to evaluate how far the constriction size reduction can be impacted by filtration, reduced constrictions are matched with those of the densest filter. So, the reduced constriction size distribution of filter F_1 operating with soil CL_2 is plotted in Fig. 12 and compared to the case of the densest circumstance. The reduction of the small constrictions size gets the resulted CSD overlapping with that of the densest filter (model of three tangent spheres). This result indicates that narrow constrictions are rapidly filled by trapped particles, leading to progressive clogging of the filter. The smallest constrictions evolve rapidly towards narrower constrictions than those of the densest case, whereas larger constrictions tend to approach uniformly the densest constrictions size.

As regards to the different behaviors of filters F_1 and F_2 it was addressed above (Fig. 9) that a deep filtration operates in filter F_2, unlike in filter F_1. The results of the

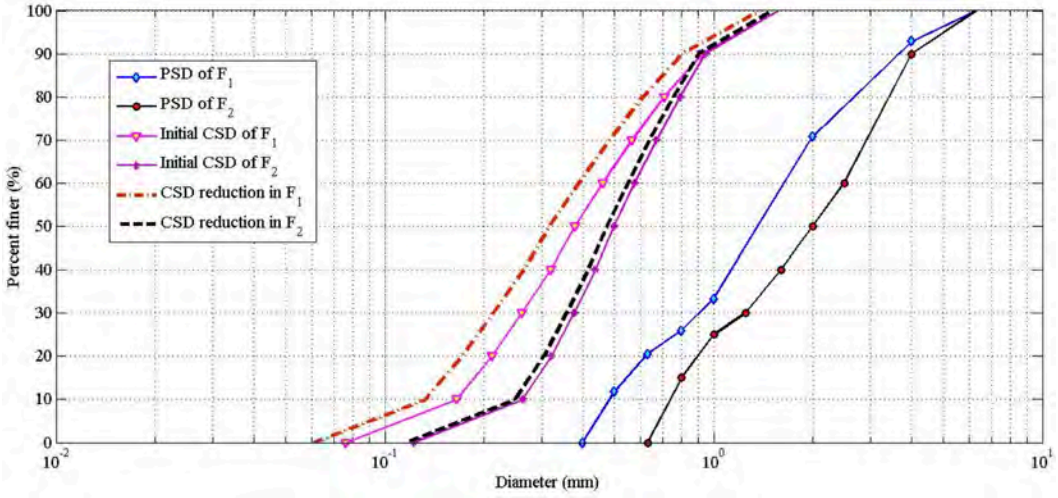

Figure 11. Comparison of the constriction size reduction in filters F_1 and F_2 after filtration of the CL_2 soil particles.

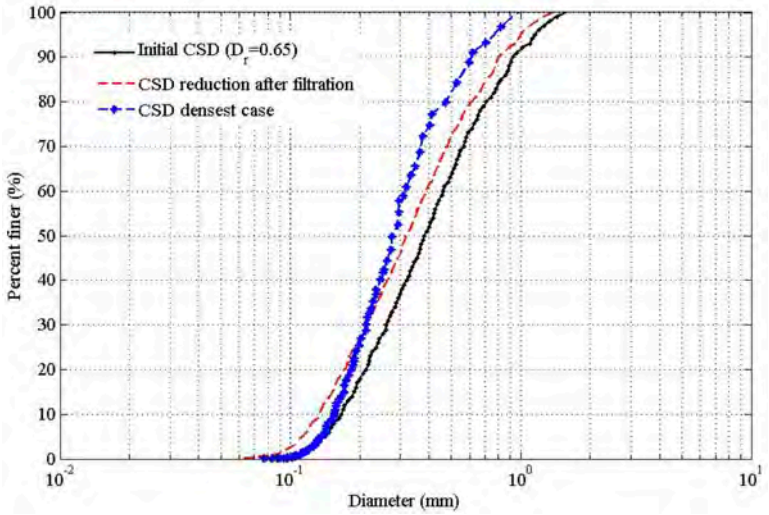

Figure 12. Evolution of the CSD of filter F_1 (when filtering soil CL_2) and its comparison with the case of the densest filter.

constrictions reduction of filter F_2 (Fig. 13) advocate the kind of deep filtration since the deposited particles are uniformly distributed and so the CSD shifts uniformly towards smaller constrictions, without reaching the CSD of the densest filter case. The uniformity of the constriction size reduction in filter F_2 and the large value (0.87) of the filtration index make the reduced CSD far from the densest model. Such behavior indicates that filter F_2 is more efficient and appropriate for filtering base soil CL_2 with a low clogging occurrence.

4.4 Assessing constriction size control for the filter design

Soil particles can pass through a filter if the constrictions are many times larger than the size of the particles. When the eroded base particles are transported towards the filter, only coarser particles larger than the controlling constriction size are initially captured. The analysis of the retained and washed-out particle sizes shows that two processes are necessary to achieve the filtration of a given base soil. Particles must be transferred to the filter matrix and then a large fraction of them must be trapped, leading to further self-filtration. Indraratna and Raut (2006) [29] proposed a criterion based on the constriction diameter (D_{c35}: size of constriction for which are 35% are finer) as the opening granular filter. Recently, Indraratna et al. (2015) [30] suggested a geometrical method for evaluating the internal instability of a granular filter. They defined a criterion stability from the ratio of controlling constriction size of the filter (D_{c35}) and the representative size of the finer fraction of base soil ($d_{85,SA}$), as $D_{c35}/d_{85,SA} \leq 1$.It is noted that the values of D_{c35} (at D_r=1) are only slightly larger than the

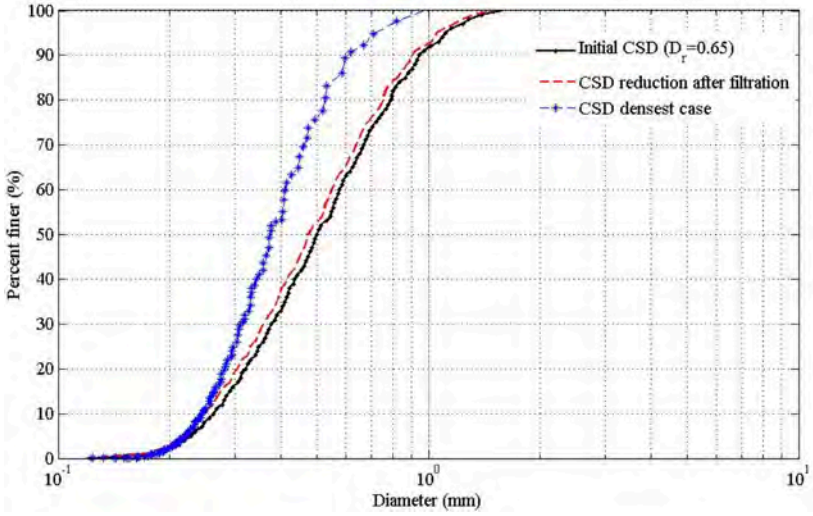

Figure 13. Evolution of the CSD of filter F_2 (when filtering soil CL_2) and its comparison with the case of the densest filter.

median size of the base particles. Table 3 shows the ratio values of $D_{c35}/d_{85/SA}$ for the different tested combinations of soil filter. The results show that the experimental results do not meet the criterion for all filters (a ratio greater than unity); as a result of the ratio D_{15}/d_{85} taken previously.

Table 3. Evaluation of the filter-stability criterion for the different tested combinations of filter-soil.

	$d_{85/S}$ (mm)	D_{c35} (mm) (D_r=0.65)	D_{c35} (mm) (D_r=1)	$D_{c35}/d_{85/S}$ (D_r=0.65)	$D_{c35}/d_{85/S}$ (Dr=1)	D_{15}/d_{85}
F_1-CL_1	0.035	0.288	0.228	8,1	6.4	11
F_1-CL_2	0.027	0.288	0.228	10,3	8.1	6,7
F_2-CL_1	0.035	0.410	0.331	11,5	9.2	13,8
F_2-CL_2	0.027	0.410	0.331	14,6	11.8	10,8

5 CONCLUSIONS

In order to investigate the coupled processes of erosion and filtration, the process of hole erosion was studied first, providing the boundary limit at the filter inlet for further coupled tests. So, the comparison of the recovered particle mass between the results of the hole erosion test and the combined erosion-filtration test was performed. The porosity reduction from the hydraulic conductivity decrease and the retained soil mass were used to evaluate the filtration depth. The main results of this study are summarized as follows:

- A new approach to investigate the filtration process was developed using the distribution of deposit particles within the constrictions. As regards the applied pressure steps, the first load produces a significant constriction reduction.
- The filtration depth was affected by the PSD of the base soil and the CSD of the used filter. The constriction reduction is more important when the particles are retained at the filter upstream (surface filtration), otherwise the constriction reduction is less important if the depth filtration occurs.
- The reduced constriction size distribution of filter F_1 operating with soil CL_2 evolves towards a critical state of the clogged medium, whereas the reduced CSD of filter F_2 shifts uniformly without reaching the CSD of the densest filter case. Such behavior makes the filter F_2 more efficient and appropriate for filtering the base soil CL_2 with a low clogging occurrence.
- The criterion based on the constriction diameter D_{c35} was matched to the experimental results and indicates that the results do not meet the criterion for both filters.

This study attempted to develop a first approach for assessing the concept of dynamic filtration through constriction size changes. The concept of a dynamic filter can be achieved if the constriction model takes into account the constriction size reduction after each loading step.

Acknowledgments

This work was carried out in the framework of the doctorate mobility toward Le Havre Normandy University (France), supported by the ERASMUS MUNDUS program BATTUTA.

REFERENCES

[1] Foster, M., Fell, R. 2001. Assessing embankment dam filters that do not satisfy design criteria. Geotechnical Geo-environmental Engineering 127, 5, 398-407. doi.org/10.1061/(ASCE)1090-0241 (2001)127:5(398)

[2] Honjo, Y., Veneziano, D. 1989. Improved filter criterion for cohesionless soils. Geotechnical Engineering 115, 1, 75–94. doi.org/10.1061/(ASCE)0733-9410(1989)115:1(75)

[3] Kenney, T.C., Lau, D. 1985. Internal instability of granular filters. Canadian Geotechnical J. 22, 215-225. doi: 10.1139/t85-029

[4] Reddi, L.N., Xiao, M., Hajra, M.G., Lee, I.M. 2005. Physical clogging of soil filters under constant flow rate versus constant head. Canadian Geotechnical J. 42, 804-811. doi: 10.1139/t05-018

[5] Lee, I.M., Park, Y.J., Reddi, L.N. 2002. Particle transport characteristics and filtration of granitic residual soils from the Korean peninsula. Canadian Geotechnical J. 39, 2, 472-482. doi: 10.1139/t01-110

[6] Reddi, L.N., Xiao, M., Malay, G., Lee, I.M. 2000. Permeability reduction of soil filters due to physical clogging. Geotechnical Geoenvironmental Engineering 20, 10, 236-246. doi.org/ 10.1061/ (ASCE) 1090-0241(2000)126:3(236)

[7] Skempton, A.W., Brogan, J.M. 1994. Experiments on piping in sandy gravel. Géotechnique 3, 449-460. doi.org/10.1680/geot.1994.44.3.449

[8] Vaughan, P.R.M., Soares, H.F. 1982. Design of filters for clay cores of dams. ASCE, Journal of the Geotechnical Engineering Division 108, 1, 17-31.

[9] Terzaghi, K., Peck, R.B., Mersi, G. 1940. Soil mechanics in engineering practice. 3Th edn Willey, London. ISBN 0-471-0865.

[10] Sherard, J.L.F., Dunnigan, L.P. 1985. Filter and leakage control in embankment dams. Proc. Seepage and Leakage from Dams and Impoundments. Michigan. University, pp. 1-29.

[11] Silveira, A. 1964. Analyses of the problem of washing through in protective filters. Proc. 6th Int. Conf. Soil Mechanics and Foundation Engineering, Toronto. University 2, pp. 3-6.
[12] Silveira, A., De Lorena, P.T., Nogueira, J. 1975. On void size distribution of granular materials. Proc. 5th. conf. soil mech and Fnd. Eng. Panama, pp. 161-176.
[13] Ziems, J. 1968. Beitrag Zur Kontakterosion Nichtbindiger Erdstoffe. Dissertation. Technische Universität Dresden.
[14] Wittmann, L. 1979. The Process of soil filtration-its physics and the approach in engineering practices. Proc. 7th. Conf. Soil Mech., Fnd. Engng. Euro, pp. 303-310.
[15] Schuler, U., Brauns, J. 1993. Behavior of coarser well-graded filters. Proc. filter in geotechnical and hydraulic engineering. Rotterdam: Brauns et al. Balkema.
[16] Wang, Y., Yousif, A., Dallo, H. 2014. On estimation of the constriction size distribution curve for cohesionless soils. European Environmental and Civil Engineering. Addison-Taylor. London. doi: 10.1080/ 19648189.2014.909335
[17] Indraratna, B., Vafai, F. 1997. Analytical model for particle migration within base soil-filter system. Geotechnical Geoenvironmental Engineering 123, 2, 100-109. doi: http://dx.doi.org/10.1061/ (ASCE)1090-0241(1997) 123:2(100)
[18] Locke, M., Indraratna, B., Adikari, G. 2001. Time dependent particle transport through granular filters. Geotechnical Geoenvironmental Engineering 127, 6 521-528. doi: http://dx.doi.org/10.1061/ (ASCE)1090-0241(2001)127:6(521)
[19] Indraratna, B., Raut, A., Khabbaz, H. 2007. Constriction based retention criterion for granular filter design. Geotechnical Geoenvironmental Engineering 133, 3, 266-276. doi: http://dx.doi.org/10.1061/(ASCE)1090-0241(2007)133:3(266)
[20] Reboul, N., Vincens, E., Cambou, B. 2008. A statistical analysis of void size distribution in a simulated narrowly graded packing of spheres. Granular Matter 10, 457–468. doi: 10.1007/s10035-008-0111-5
[21] Vincens, E., Witt, K.J., Homberg, U. 2014. Approaches to determine the constriction size distribution for understanding filtration phenomena in granular materials. Acta Geotech, 10, 3, 291-303. doi:10.1007/ s11440-014-0308-1
[22] Taylor, H.F., O'Sullivan, C., Sim, W.W. 2015. A new method to identify void constrictions in micro- CT images of sand. Computers and Geotechnics 69, 279-290. doi.org/10.1016/j.compgeo.2015.05. 012
[23] ASTM D2487-11: American Society for Testing Material. 2011. Standard Practice for Classification of Soils for Engineering Purposes, Unified Soil Classification System. American Society for Testing Material, West Conshohocken, USA.
[24] USBR: National Engineering Handbook. 1994. Gradation design of sand and gravel filters. Chap. 26- 210-vi-NEH.
[25] Carrier, W. D. 2003. Goodbye, Hazen; Hello, Kozeny-Carman, Geotechnical Geoenvironmental Engineering 129, 11, 1054-1056. doi: http://dx.doi.org/10.1061/ (ASCE)1090- 0241(2003) 129:11(1054)
[26] Ameratunga, J., Sivakugan, N., Das Braja, M. 2015. Correlations of soil and rock properties in geotechnical engineering. Springer. New Delhi.
[27] Benamar, A. 2013. Clogging Issues Associated With Managed Aquifer Recharge Methods: Soil Clogging Phenomena In Vertical Flow. In Martin R(ed.) clogging issues associated with managed aquifer recharge method. IAH Commission on Managing Aquifer Recharge, Australia, 77-83.
[28] Robert, S., Desmond, F. 1988. Depth Filtration: Fundamental investigation through three-dimensional trajectory analysis. Environ. Sci. Technol 32, 23, 3793-3801. doi: 10.1021/es9707567
[29] Indraratna, B., Raut, A. 2006. Enhanced criterion for base soil retention in embankment dam filters. Geotechnical Geoenvironmental Engineering 123, 12, 1621-1627. doi: http://dx.doi.org/10.1061/ (ASCE) 1090-0241(2006)132:12(1621)
[30] Indraratna, B., Israr, J., Rujikiatkamjorn, Ch. 2015. Geometrical method for evaluating the internal instability of granular filters based on constriction size distribution. Geotechnical Geoenvironmental Engineering 141, 10, 1-13. Doi: http://dx.doi.org/10.1061/(ASCE)GT.1943-5606.0001343

APPENDIX A: Analytical model of the constriction size distribution

The most common definition of the pore size is the diameter of the inscribed sphere between tangential particles. Comparisons with the void volumes are made possible by associating a constriction diameter with each pore. The analytical approach aims to compute the CSD from essential information about the size distribution of the granular material. They consist of applying a probabilistic schema to an assumed geometrical packing structure within the filter. A further basic concept based on a probabilistic approach is shown in Fig. 14 for two cases, i.e., the loosest and densest filters. The fine particles sequentially flow from one pore to another, passing through the constrictions. Actually, the occurrence of a given constriction size is related to the possibility of particle contact to create such a constriction. The main criticism arises from the assumption of spherical particles, which is also inherent to the analytical

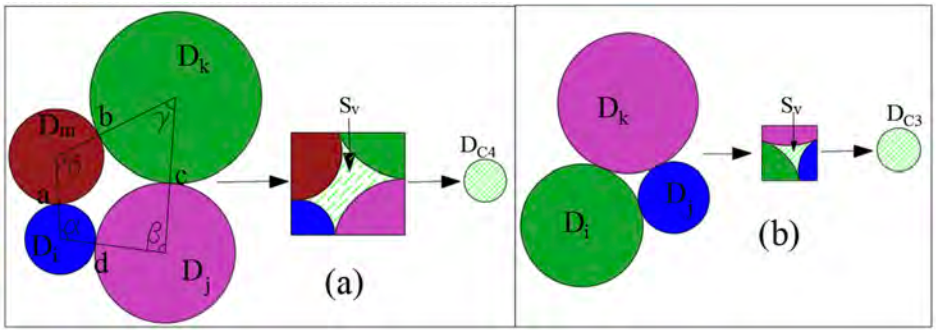

Figure 14. Constructions Size Distribution of a material: a) loose case, b) dense case.

approach of the filtration process. This design criterion was based on the probability of the grains' arrangement in the filter matrix in order to form the largest voids. The size of these voids is dependent on the size and packing geometry of the filter particles.

Silveira (1965) [11] assumed that for the densest geometric configuration, the constriction size D_{c3} (constriction size of the frequency of the three particle diameters) is made up of three tangent spheres of diameters D_i, D_j, D_k. The size of D_{c3} can be deduced as follows by Eq.6 [18]:

$$\left(\frac{2}{D_i}\right)^2+\left(\frac{2}{D_j}\right)^2+\left(\frac{2}{D_k}\right)^2+\left(\frac{2}{D_{c3}}\right)^2=\frac{1}{2}\left(\frac{2}{D_i}+\frac{2}{D_j}+\frac{2}{D_k}+\frac{2}{D_{c3}}\right) \quad (6)$$

The probability of the occurrence P_{c3} by the surface of the constriction size D_{c3} is provided by Eq. 7 [18].

$$P_{c3}=\frac{3!}{r_i!\,r_j!\,r_k!}\,p_i^{r_i}\,p_j^{r_j}\,p_k^{r_k} \quad (7)$$

where r_i, r_j, and r_k are the numbers of times that the diameters D_i, D_j and D_k appear in the three particle groups, respectively; r_i, r_j, r_k = 0, 1, 2, 3 and $r_i+r_j+r_k$=3; p_i, p_j and p_k are the percentage (probability of occurrence by area) of D_i, D_j and D_k, respectively.

Silveira (1975) assumed that in the loosest state the area S_V formed by four tangent spheres with respective diameters D_i, D_j, D_k and D_m and respective probabilities of occurrence by area p_i, p_j, p_k and p_m (Fig. 1.a), the constriction size D_{c4} (constriction size of the frequency of the four particle diameters) can be deduced by Eq.8[18].

$$D_{c4}=\sqrt{\frac{4S_{VMAX}}{\pi}} \quad (8)$$

where S_{Vmax} is the maximum area formed among the four tangent particles. The probability of the occurrence by area P_{c4} of the constriction size D_{c4} is computed from Eq.9 [18]:

$$P_{c4}=\frac{4!}{r_i!\,r_j!\,r_k!\,r_m!}\,p_i^{r_i}\,p_j^{r_j}\,p_k^{r_k}\,p_m^{r_m} \quad (9)$$

where r_i, r_j, r_k and r_m are the numbers of times that the diameters D_i, D_j, D_k and D_m appear in the four particles groups, respectively; r_i, r_j, r_k, r_m = 0, 1, 2, 3, 4 and $r_i+r_j+r_k+r_m$=4; p_i, p_j and p_k and p_m are the percentage (probability of occurrence by area) of D_i, D_j, D_k and D_m respectively.

The constriction area S_V (Fig. 1.a) can be computed from Eq.10 [18]:

$$S_V=\frac{ad\sin\alpha}{2}+\frac{bc\sin\gamma}{2}-\frac{1}{8}\left(D_i^2\alpha+D_j^2\beta+D_k^2\gamma+D_m^2\delta\right) \quad (10)$$

The two geometrical cases shown in Figure 1 represent the extreme cases (loosest and densest) of the relative density. Real filters are unlikely to exist either as most dense or least dense states, but rather at some intermediate density. Locke et al. (2001), Indraratna et al.(2007) and Indraratna and Raut (2006) [18,19,22] proposed that a more realistic pore model should also consider the filter relative density. They suggested that a combination of two cases gives the constriction size d_c, which is computed using the relative density D_r as provided by Eq.11 [18]:

$$d_c\left(P_c\right)=D_{c3}\left(P_c\right)+P_c\left(1-D_r\right)\left[D_{c4}\left(P_c\right)-D_{c3}\left(P_c\right)\right] \quad (11)$$

where:

d_c: the constriction size for a relative density D_r;
P_c: probability of occurrence by area of the constriction size d_c;

The relative density D_r is defined by [18]:

$$D_r=\frac{e_{\max}-e}{e_{\max}-e_{\min}} \quad (12)$$

where: e_{max} is the maximum void ratio, e_{min} the minimum void ratio and e the actual void ratio of the filter.

VPLIV ZAOBLJENOSTI DELCEV IN MORFOLOGIJE NA STRIŽNI PORUŠNI MEHANIZEM ZRNATIH ZEMLJIN POD PASOVNIMI TEMELJI

Babak Karimi Ghalehjough *(vodilni avtor)*
Ataturk University,
Department of Civil Engineering
No.318, Ataturk University, 25240 Erzurum, Turčija
E-pošta: karimi.babak@gmail.com

Suat Akbulut
Yildiz Technical University,
Department of Civil Engineering
34220 Esenler, İstanbul, Turčija
E-pošta: sakbulut@yildiz.edu.tr

Semet Çelik
Ataturk University,
Department of Civil Engineering
No.318, Ataturk University, 25240 Erzurum, Turčija
E-pošta: scelik@atauni.edu.tr

Ključne besede

zaobljenost zrn, morfologija delcev, strižni porušni mehanizem, pasovni temelj, metoda s sliko sledilnih delcev PIV, mejna nosilnost

Izvleček

V članku je raziskovan učinek zaobljenosti delcev in morfologije na strižni porušni mehanizem zrnate zemljine. Pasovni temelj je bil modeliran v laboratorijskih pogojih. Apnenčasta zemljina je bila preizkušena s tremi razredi zaobljenosti zrn: koničasta, zaobljena in dobro zaobljena zrna z velikostmi od 0,30 mm do 4,75 mm. Ti so bili razdeljeni v šest različnih skupin pri treh relativnih gostotah 30 %, 50 % in 70 %. Da bi razumeli mehanizem deformacije zrnate zemljine je bila med preizkusi narejena vrsta fotografij in izvedena analiza z metodo slik sledilnih delcev (PIV). Rezultati so pokazali, da je povečanje velikosti vzorcev povečalo prizadeto območje zemljine. Hkrati pa je povečanje relativne gostote povzročilo prebodni porušitveni mehanizem, ki je prešel proti splošni porušitvi. Mehanizem strižne porušitve zemljine se je spremenil iz splošnega v prebodni porušitveni mehanizem z večanjem zaobljenosti delcev. Ta učinek je bil večji pri manjših drobnejših materialih. Vplivno območje je segalo globlje pri vzorcih s koničastimi zrni kot pri vzorcih z zaobljenimi in dobro zaobljenimi zrni. Ugotovljena globina v zemljini s koničastimi zrni je bila približno 1,5B v najmanjši velikostni skupini medtem, ko je bila več kot 3B in blizu 4B v skupini z največo velikostjo zrn. V zemljinah s koničastimi zrni je treba upoštevati stranske sloje in spodnje sloje zemljin. Območje pod temelji postane pomembnejše od stranskih delov s povečanjem zaobljenosti delcev.

EFFECT OF PARTICLE ROUNDNESS AND MORPHOLOGY ON THE SHEAR FAILURE MECHANISM OF GRANULAR SOIL UNDER STRIP FOOTING

Babak Karimi Ghalehjough *(corresponding author)*
Ataturk University,
Department of Civil Engineering
No.318, Ataturk University, 25240 Erzurum, Turkey
E-mail: karimi.babak@gmail.com

Suat Akbulut
Yildiz Technical University,
Department of Civil Engineering
34220 Esenler, İstanbul, Turkey
E-mail: sakbulut@yildiz.edu.tr

Semet Çelik
Ataturk University,
Department of Civil Engineering
No.318, Ataturk University, 25240 Erzurum, Turkey
E-mail: scelik@atauni.edu.tr

Keywords

particler roundness, morphology of particles, shear failure mechanism, strip footing, PIV method, ultimate bearing capacity

DOI https://doi.org/10.18690/actageotechslov.15.1.43-53.2018

Abstract

This study investigates the effect of particles roundness and morphology on the shear failure mechanism of soil. A strip footing was modeled under laboratory conditions. Calcareous soil was tested with three roundness classes: angular, rounded and well-rounded shapes with sizes of 0.30 mm to 4.75 mm. These were divided into six different groups at three relative densities of 30%, 50% and 70%. A series of photographs was taken during the tests and analyzed using the particle image velocimetry (PIV) method to understand the soil-deformation mechanism. The results showed that increasing the sample sizes increased the affected area of the soil. At the same time, increasing the relative density caused a punching failure mechanism that went towards the general failure. The shear failure mechanism of the soil changed from general toward punching shear failure with increasing particle roundness. This effect was larger with the smaller materials. Underneath the affected layers of soil, the angular samples were deeper than the rounded and well-rounded samples. The affected depth in the angular soil was approximately 1.5B in the smallest size group. This was more than 3B and near 4B in the largest size group. Both the sides and the underlying soil layers should be considered on angular soils. The area under the footing becomes more important than the side parts after increasing the roundness of the particles.

1 INTRODUCTION

Soil's geotechnical properties primarily affect its behavior. One of these properties is particle shape. The texture, sphericity, roundness and roughness are used to describe the particle shapes [1, 2]. Holtz and Gibbs [3] showed that the shear strength of angular materials is more than the rounded or well-rounded materials. Other studies showed that by increasing the angularity of the materials, the maximum and minimum void ratios (e_{max} and e_{min}) decreased [2, 4, 5]. There are many studies on size or particle shape and their effect on the behavior of aggregates under loading. Direct shear box tests have been made on samples prepared with groups of natural river soil and crushed gravels and fine soil including clay and silt. Yanrong studied the effect of size distribution and particle shape [6].

Arasan et al. [7] studied calcareous, ballast, abrasive and bearing balls. The shape properties of the particles were calculated by considering the roundness values, and the soils were divided into six roundness classes. Calcareous soil changed from angular to rounded and well-rounded, and the effect of the particle shapes on the geotechnical properties of the aggregate was studied.

The ultimate bearing capacity of the strip footing is one the most important issues in civil engineering [8]. Many researches and investigations have been made on strip footing. Reinforcing the soil can improve the settlement of the footing or bearing capacity of the soil [9, 10, 11, 12, 13, 14]. Different kinds of soils such as gravel, sandy soil, clay and silt under different conditions in normal or reinforced soil have been studied. Previous researchers have studied different conditions and the effect of different factors such as the shape of the footing, soil properties, reinforcement, ground-water level, etc. on the manner of the strip footing [15, 16, 17, 18].

Chen and Abu-Farsakh [19] studied the strip footing and ultimate bearing capacity of the reinforced soil. They developed an analytical solution for estimating the ultimate bearing capacity. The results showed that relative density of reinforced soil and underlying un-reinforced soil affected punching shear failure. Kuranchie et al. [20] studied load-settlement behavior of strip footing laid on iron ore tailings. Cicek et al. [21] studied reinforcing soil and the effect of reinforcement length on the strip footing behavior by geogrids. Reinforcement length as well as the types and number of reinforcements were tested to determine whether they affect the optimum reinforcement.

The effect of the ultimate load has also been studied [22]. This study measured the strip footing near a sandy slope. The slope was loaded centrally and randomly. Ultimate bearing capacity decreased by increasing the amount of eccentricity, and percentage of this decrease increased with increasing eccentricity. Depending on the soil's relative density, there are generally three shear-failure mechanisms under shallow foundations. Foundations on dense sand (Dr>70%) fail with a mechanism marked by a peak resistance, which is known as general shear failure [23]. On sands with a relative density between 35% and 70 % sudden failure is not realized. This type of failure is called local shear failure. Foundations placed on very loose sand with Dr<35% can penetrate into the soil with no bulging observed on the surface; this failure type is also called punching shear [24]. Soils with relative densities over 70% show a general shear failure mechanism under shallow foundations [25]. Fig.1 shows three shear-failure mechanisms for soil under shallow foundations. This figure shows that the punching mechanism of the soil moves downward directly below the foundation, but the local and general failure mechanisms can facilitate movement to the surface of the soil [25, 26].

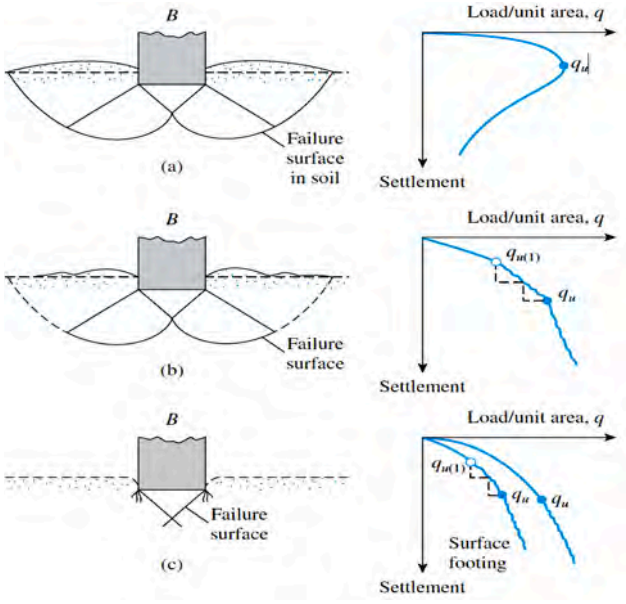

Figure 1. Failure mechanism of soil under shallow foundations: (a) general shear failure (b) local shear failure (c) punching shear failure [25, 26].

The particle image velocimetry (PIV) method explains the sandy soil's movement. It measures the soil particle movement for the whole soil mass [27, 28]. Slominski [29] used PIV method to measure dry cohesion-free sand movement in silos. The surface deformation in silos was studied in laboratory model tests, and effect of the roughness of silo walls and sand density on the volumetric strain was reported. The accuracy of the measurements was discussed and advantages and disadvantages of the PIV method were outlined here. Ould Baba and Peth [30] studied the creep deformation of slopes with a large-scale soil box via PIV. The efficiency of the PIV method was examined, and effect of hydraulic stresses on the creep deformation was studied using model tests.

There are many studies that use strip footing or particle properties, but the effect of particle roundness and shape on the soil behavior and the failure mechanism of soil are missing from the literature. This study is novel because it measures the effect of particle shape and roundness on the soil behavior under strip footings. The failure mechanism of the aggregate was studied with the PIV method at different values of roundness, density, and size.

2 MATERIAL AND METHODS

2.1 Soil

The soil was calcareous and prepared by the Ergunler Company in Erzurum, Turkey. According to ASTM 854-14, [31] the soil's specific gravity was 2.7; soil was angular. After taking the soil to the laboratory, it was washed and dried by spreading on a dry surface at room temperature and then sieved to six different sizes

between 0.30 mm to 4.75 mm. Tests were made on the angular, rounded and well-rounded soils. The angular calcareous soil changed to sub-rounded and rounded calcareous. It can be changed to well-rounded calcareous soil via the Los Angeles Rattler machine. Here, angular soil was transformed in the Los Angeles machine without balls, as explained by Arasan [32, 39]. To change the angular calcareous soil to rounded soil, 50,000 revolutions were used. To change the angular soil to well-rounded calcareous soil, 100,000 revolutions were used on the Los Angeles machine. The roundness values of the soils were determined using the Cox equation [33] and the Power [34] chart (Table 1).

Table 1. Roundness properties of materials [7, 39].

Sample	Roundness Value	Roundness Class
Angular Calcareous	0.693-0.744	Angular - Sub Angular
Rounded Calcareous	0.786-0.803	Rounded - Well Rounded
Well-Rounded Calcareous	0.834-0.854	Well Rounded

According to the unified soil-classification system [35], soil samples were classified as poorly graded sand (SP). Grain size distribution increased according to ASTM-D 6913-04 [36], as shown in Fig. 2.

The roundness of the soil particles increased by going from angular soil towards rounded and well-rounded. It is even clear and easily visible by eye at larger sizes. Examples of the angular, rounded and well-rounded calcareous soils are shown in Fig. 3.

2.2 Model Tank

This study involved a series of laboratory tests. The model tests were conducted in a model tank: 1 m × 0.1 m in plan and 1 m in depth. The tank was completely rigid to prevent any movement and the length of the model footing was almost equal to the width of the tank to maintain plain-strain conditions. The front side of

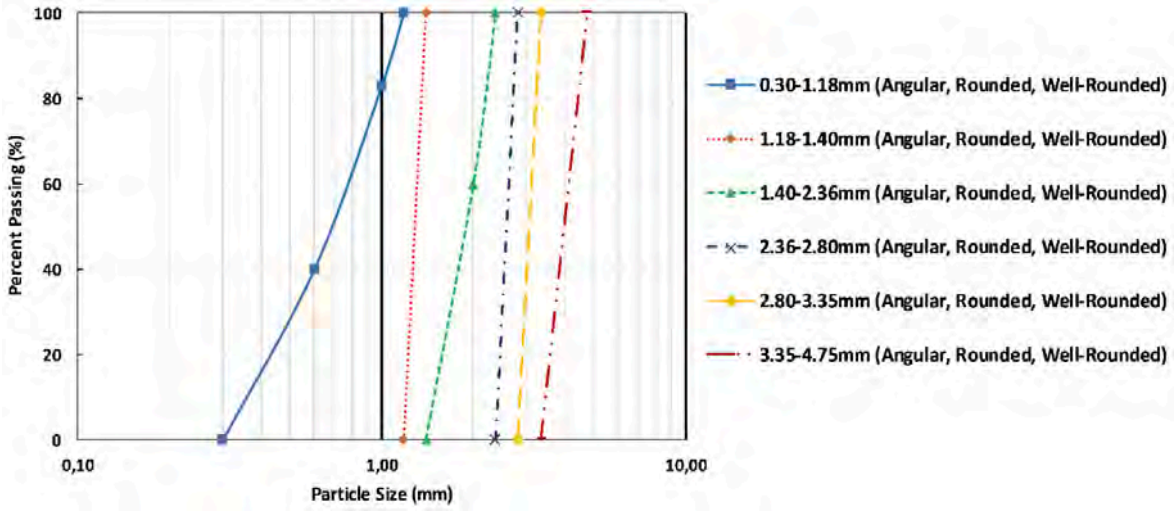

Figure 2. Grain size distributions of the soils.

Figure 3. Pictures of soil with three different roundness.

the tank was made of a sheet of Plexiglas to monitor and inspect the soil and model the footing and their movements during the tests. A polyamide strip footing was used: 9.8 cm long, 5 cm wide and 4 cm high. It was sufficiently rigid to prevent reshaping during tests. A hydraulic jack was fixed to a strong horizontal beam of the frame that could carry thrust developed by hydraulic jack without any deformation during tests. The speed of displacement was <2 mm/min for applying loads over small increments. A 50-kN load cell was placed between the jack and footing to measure the applied load. The load was transferred to the footing via a shaft placed between the load cell and the footing. A ball bearing was placed between the shaft and the footing to apply a single point load to the footing. A rigid footing was used in this study, and a uniform load was applied from the footing to the soil. There was a 1-mm gap at each side of the tank to prevent contact between the side walls of the tank and the footing. Two sides of the footing and walls of the tank were coated with petroleum jelly to reduce the end-friction effects.

Two linear variable displacement transducers (LVDTs) were concurrently placed at the two corners of the model footing. The average movement of these two LVDTs was considered to be settlement of the footing. Finally, the data from the load cell and the LVDTs were transferred to a computer via a data logger. To analyze the soil movement, a high-resolution digital camera was placed in front of the tank to take high-quality images. First, a picture was taken before starting the test without any movement in the soil or the footing. Images were acquired every 30 seconds until the end of the experiment. These pictures were used to analyze the

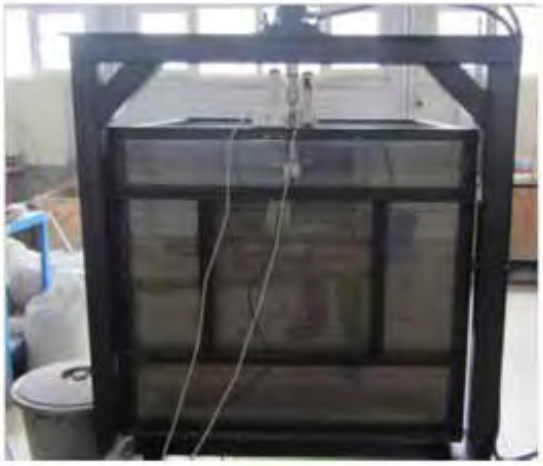

Figure 4. Pictures of the tank.

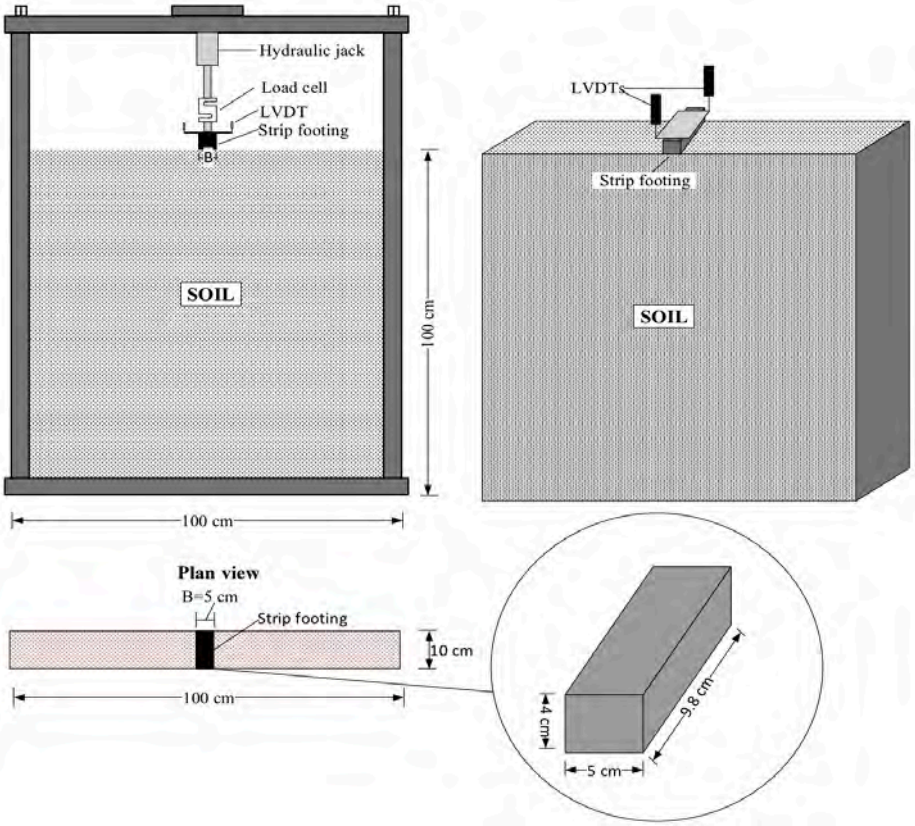

Figure 5. Schematic picture of the test box.

soil movement via the Geo-PIV program. Tank pictures and a schematic drawing of the model tank are shown in Figs. 4 and 5, respectively.

2.3 Experimental Setup

The soil was classified into six different sizes from 0.3 mm to 4.75 mm. There were three roundness classes: angular, rounded and well-rounded calcareous for each dimension. The tests were done at relative densities of 30%, 50% and 70% (*Dr*=30%, 50% and 70%) for each group of dimensions and roundness classes. According to ASTM D4253-16 and ASTM D4254-16, [37, 38] the minimum and maximum void ratio (e_{min} and e_{max}) of each soil sample was identified by considering the tank volume. The weight of the soil was calculated and placed in the tank at these three densities. There were 54 samples for testing, and each test was done at least in triplicate to ensure the results. Table 2 shows all the test conditions. After putting the soil inside the tank, a strip footing was placed on the soil surface, and two LVDTs at two cross corners of the footing were used to measure the settling of the model foundation.

Table 2. All 54 different conditions of the tests.

Soil Dimension (mm)	Relative Density (%)	Roundness Class
0.30–1.18	30 - 50 - 70	Angular, Rounded, Well-Rounded
1.18–1.40	30 - 50 - 70	Angular, Rounded, Well-Rounded
1.40–2.36	30 - 50 - 70	Angular, Rounded, Well-Rounded
2.36–2.80	30 - 50 - 70	Angular, Rounded, Well-Rounded
2.80–3.35	30 - 50 - 70	Angular, Rounded, Well-Rounded
3.35–4.75	30 - 50 - 70	Angular, Rounded, Well-Rounded

2.4 PIV Method

The Geo-PIV program can explain the mechanism of soil deformation under the footing. PIV is a velocity-measurement technique originally developed in the field of fluid mechanics. Soil deformation can be considered a low-velocity flow process [28]. This program is based on close-range photography and PIV. In Geo-PIV, digital photographs of planar soil deformation are studied with PIV to monitor the movement of the soil particles. To measure the soil movement, the program creates patches on the pictures and compares each patch across the series of pictures. This shows the final movement of the particles for each patch as well as the whole soil [27]. Here, a digital camera is placed in front of the tank on a stable tripod to prevent any movement. The first picture was taken before starting the test. This explains the soil condition before adding any load. The second picture was taken 30 seconds after loading the footing, and then a series of pictures were taken every 30 seconds to the end of the test. All the pictures are high resolution, and there was no movement of the camera or the tank during the testing.

3 RESULTS AND DISCUSSIONS

The tests were made under laboratory conditions, and high-quality pictures were collected during the testing. Data from the load-cell and the LVDTs were transferred to the computer and a settlement-load graph was drawn for each test. These graphs show a failure point and a subsequent failure moment that is recognized for each test [24, 25]. Next, the pictures' step numbers were identified by considering the failure time. This series of pictures was analyzed with Geo-PIV software to understand the soil movement and the deformation from the beginning to the failure point. This was done for each test to evaluate the shear failure of the soil under the footing. Fig.6 shows the failure mechanism of the angular calcareous soils at six different dimensions and three different relative densities (*Dr*; 30%, 50%, and 70%). The data suggest that the soil-failure mechanism goes from punching to general failure by increasing the relative density. The shear failure mechanism is punching at a 30% relative density. At *Dr*=50%, this mechanism changed to local. By increasing the *Dr* to 70%, the soil-failure mechanism became a general shear failure.

The movement and deformation increase with the increasing soil size. The underlying layers of soil deform at dimensions of 0.30–1.18 mm near 1.5 B. At *Dr*=30%, the 2B samples have a soil size of 3.35–4.75 mm at the same relative density. The side areas of the footing showed the same behavior on larger sizes. There is more area of soil under the footing. The inside soil was affected by the loading and even the soil mechanism went from punching to a general mechanism. By increasing the relative density of the soil, the influence of the aggregate size was more pronounced – especially on the side movements. More areas under the footing showed evidence of deformation. The deformation at larger sizes was more pronounced than with the finer soils.

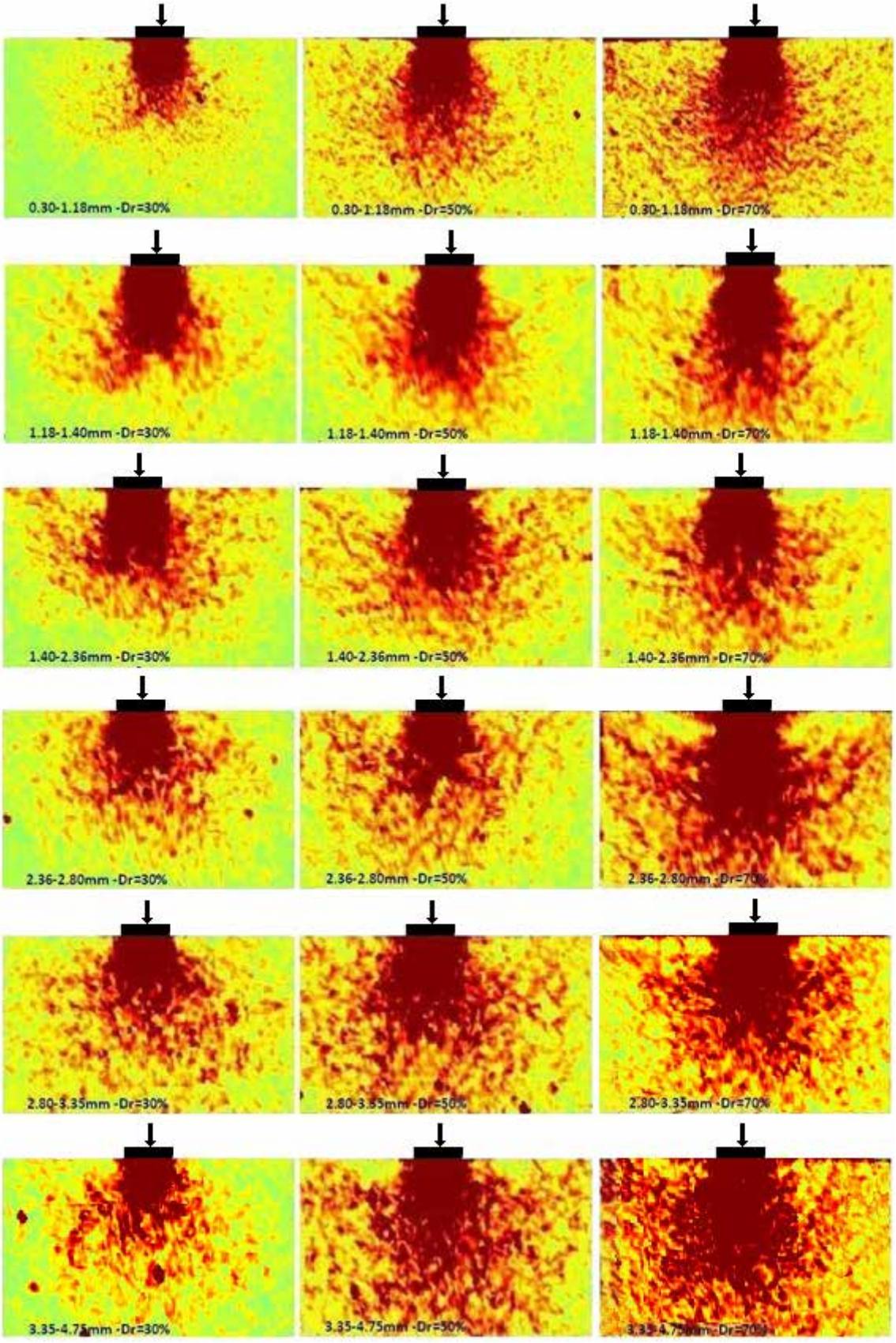

Figure 6. Failure mechanism of angular soil at different sizes and relative densities.

We also studied the effect of roundness on the soil-failure mechanism. The soil-failure mechanism was compared at three different relative densities and three roundness classes for all six dimensions. The soil movements under these conditions are seen in Fig.7 to 12. These mechanisms showed that by increasing the roundness of the material there were decreases on the loading area under the footing. This was more visible for materials with dimensions of 0.30–1.18 than for those of 3.35–4.75 mm. This means that the effect of the roundness is more significant for finer materials than for larger materials.

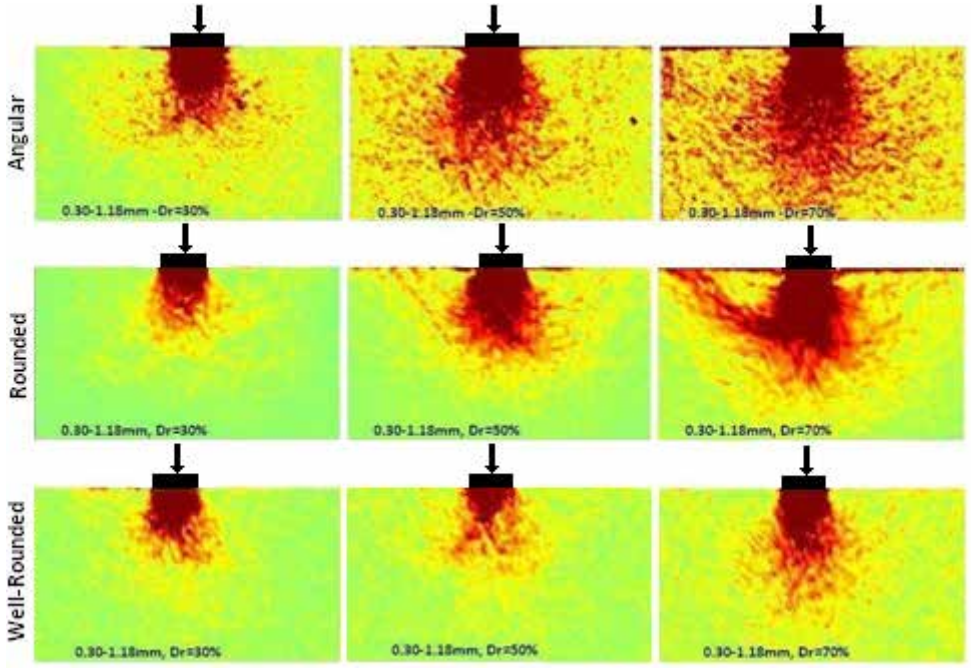

Figure 7. Failure mechanism of soils with dimensions of 0.30–1.18mm.

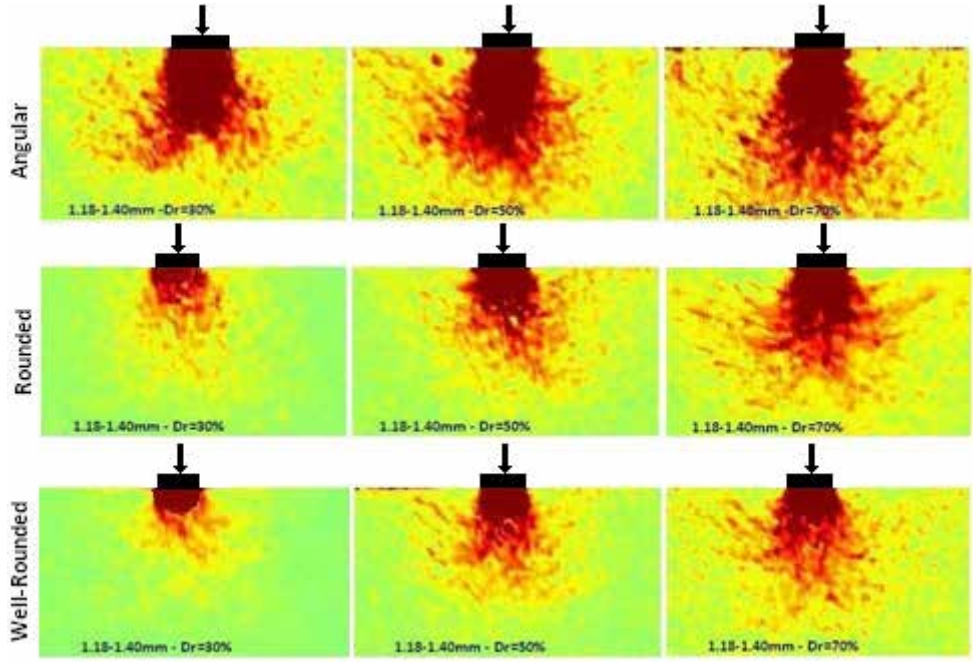

Figure 8. Failure mechanism of soils with dimensions of 1.18–1.40mm.

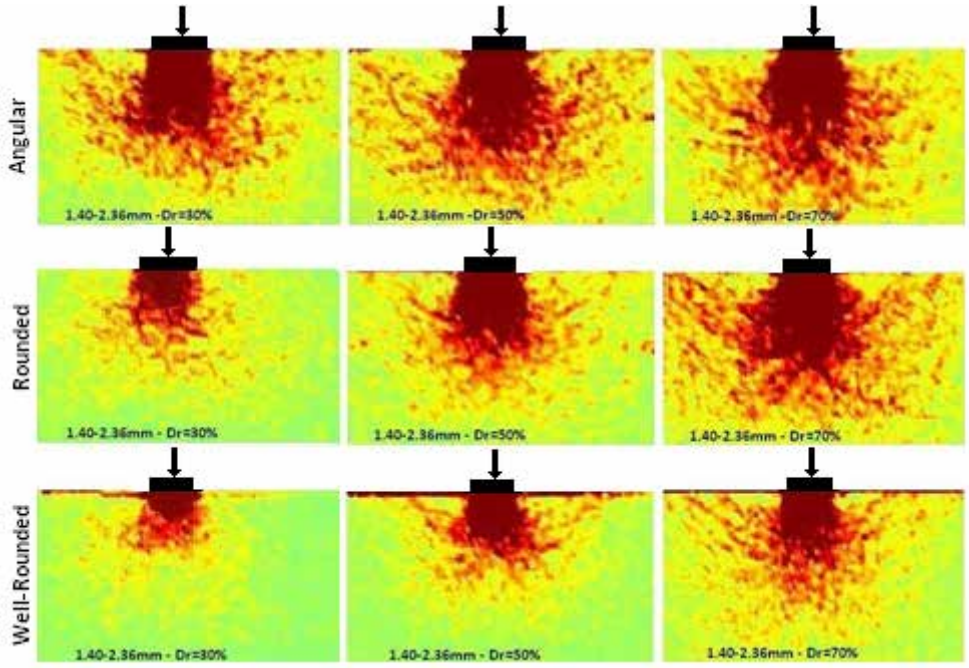

Figure 9. Failure mechanism of soils with dimensions of 1.40–2.36mm.

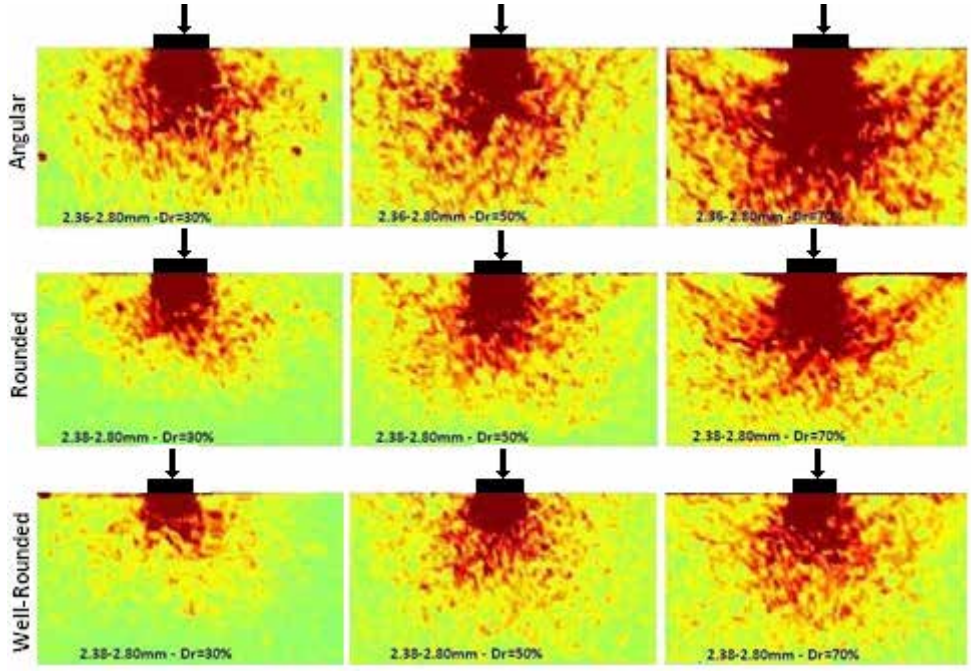

Figure 10. Failure mechanism of soils with dimensions of 2.36–2.80mm.

The soil behavior under three roundness conditions was different. Angular soils had punching failure at *Dr*=30%, local shear failure at *Dr*=50%, and general shear failure at *Dr*=70%. However, the soil behavior under the footing changed by increasing the particle roundness. The movement of the well-rounded soil was between punching and local at *Dr*=70% with dimensions of 0.30–1.18 mm. Even at dimensions of 3.35–4.75 mm, well-rounded samples failed with a local shear failure mechanism at the same dimension and relative density. This is in contrast to the general failure mechanism of angular soil at a *Dr* of 70%.

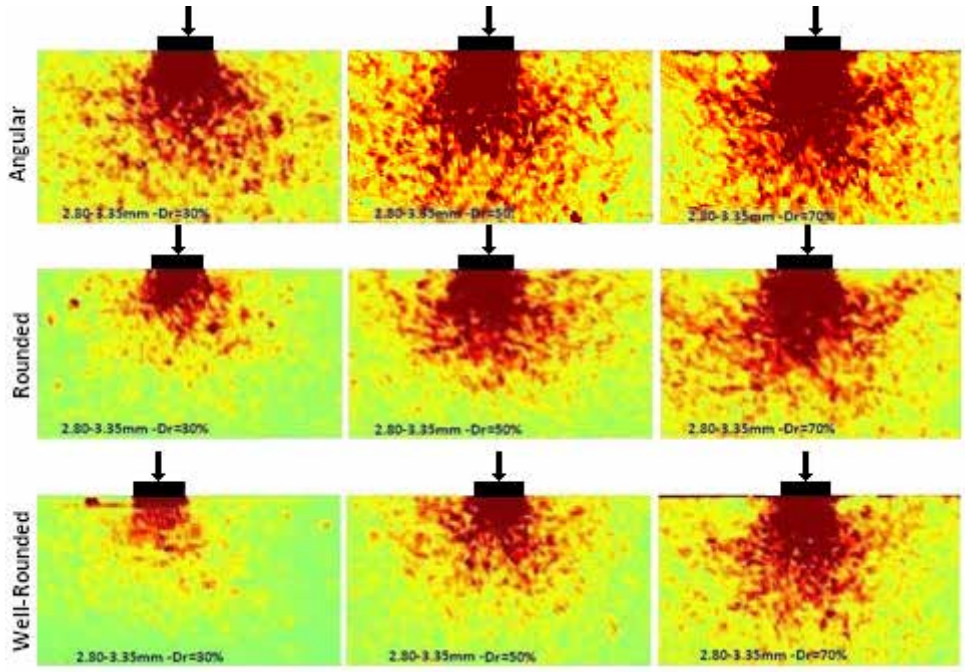

Figure 11. Failure mechanism of soils with dimensions of 2.80–3.35mm.

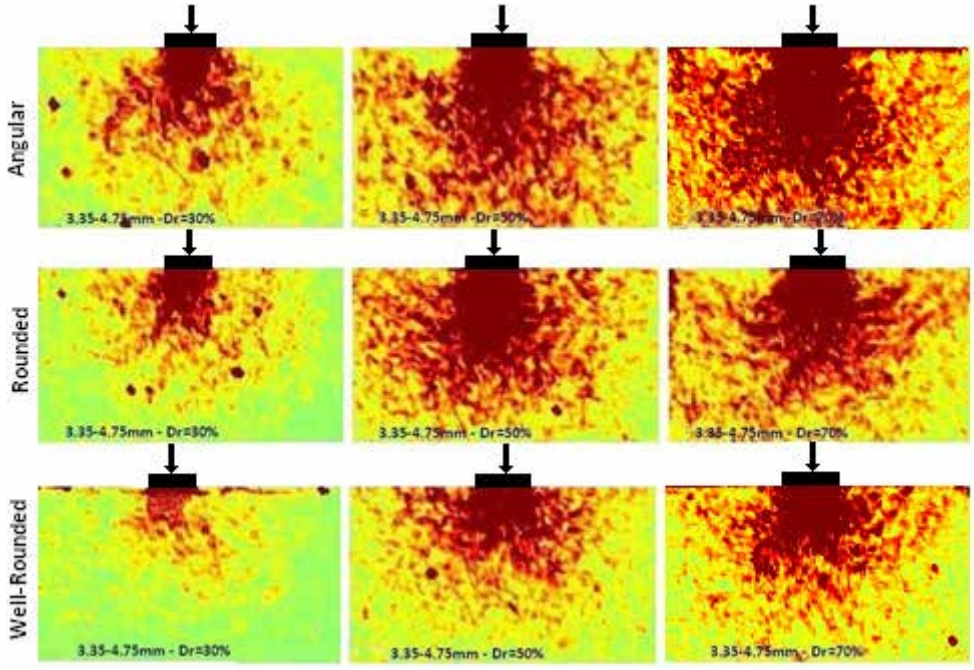

Figure 12. Failure mechanism of soils with dimensions of 3.35–4.75mm.

Particles can move on each other more easily in well-rounded soils than rounded or angular samples because of the shapes and roundness of the aggregates. The particles in angular soil interlocked causing the soil to act like a continuous area. This is because of the sharp corners in the particles and the higher friction. However, in rounded and well-rounded materials, the soil particles can move more easily against each other. This caused movement and deformation under the footing. Changing the roundness of the soil particles affected the bearing capacity of the soil and the settlement of the footing. There was a decreased soil bearing capacity associated with the increasing roundness.

4 CONCLUSIONS

The soil behavior changes completely as a function of roundness. Both the particle shape and the roundness should be considered during engineering. This effect is more significant for finer materials. Beneath the affected layers of soil, angular particles are deeper than the rounded and well-rounded particles. These particles should be studied carefully. Angularity has an effect on the soil properties that change the soil's behavior at a distance of B (B is the footing width) from the footing edges. This affects the soil's behavior and should be studied in addition to the soils under the footing – even at a relative density of 30% for the angular soils. Increasing the roundness of the particles can affect the footing and the soil behavior because it depends strongly on the properties of the soil, especially under the footing. The larger relative densities of the angular soils with at least a depth of 4B should be studied carefully, because even at this distance under the footing there is deformation and movement of the soil particles.

Acknowledgment

We thank the Ataturk University and Geotechnical Engineering Division for providing us with the laboratory and equipment we needed for this study.

REFERENCES

[1] Santamrina, J. C., Cho, G. C. 2004. Soil behavior: the role of particle shape. In: Advances in geotechnical engineering: the skempton conference. 1, 604–617. DOI: 10.1680/aigev1.32644.0035

[2] Cho, G. C., Dodds. J., Santamarina, J. C. 2006. Particle shape effects on packing density, stiffness, and strength: natural and crushed sands. Journal of Geotechnical and Geoenvironmental Engineering 132, 591–602. DOI:http://dx.doi.org/10.1061/(ASCE)1090-0241(2006)132:5(591)

[3] Holtz, W. G., Gibbs, H. J. 1956. Triaxial shear tests on previous gravelly soils. Journal of the Soil Mechanics and Foundations Division 82(1), 1–22.

[4] Cubrinovski, M., Ishihara, K. 2002. Maximum and minimum void ratio characteristics of sands. Soils and Foundations 42 (6), 65–78. DOI:http://doi.org/10.3208/sandf.42.6_65

[5] Arasan., S., Akbulut, S., Hasiloglu, A. S. 2010c. Effect of particle roundness on the maximum and minimum void ratios of granular soils. 13. National Soil Mechanic and Foundation Engineering Congress, (in Turkish with an English summary).

[6] Yanrong, Li. 2013. Effects of particle shape and size distribution on the shear strength behavior of composite soils. Bulletin of Engineering Geology and the Environment 72, 371–381. DOI: 10.1007/s10064-013-0482-7

[7] Arasan, S., Yener, E., Hattatoglu, F., Akbulut, S., Hinislioglu, S. 2010d. The relationship between the fractal dimension and mechanical properties of asphalt Concrete. International Journal of Civil and Structural Engineering 1 (2), 165–170. DOI:10.6088/ijcser.00202010014.

[8] Yang, F., Zheng, X. C., Zhao, L. H., Yi-Gao Tan 2016. Ultimate bearing capacity of a strip footing placed on sand with a rigid basement. Computers and Geotechnics 77, 115–119. DOI:10.1016/j.compgeo.2016.04.009

[9] Choidhary, A. K., Jha, J. N., Gill, K. S. 2010. Laboratory investigation of Bearing Capacity Behavior of Strip Footing on Reinforced Fly Ash Slope. Geotextiles and Geomembranes 28, 393-402. DOI:10.1016/j.geotexmem.2009.09.007

[10] Binquet, J., Lee, K.L. 1975a. Bearing capacity tests on reinforced earth slabs. Journal of Geotechnical Engineering Division, ASCE 101, 1241–1255.

[11] Binquet, J., Lee, K.L. 1975b. Bearing capacity analysis of reinforced earth slabs. Journal of Geotechnical Engineering Division, ASCE 101, 1257–1276.

[12] Akinmusuru, J.O., Akinbolade, J.A. 1981. Stability of loaded footings on reinforced soil. Journal of Geotechnical Engineering Division, ASCE 107, 819–827.

[13] Das, B.M., Khing, K.H., Shin, E.C., Puri, V.K., Yen, S.C. 1994. Comparison of bearing capacity of strip foundation on geogrid-reinforced sand and clay. Proceedings of the 8th International Conference on Computer Methods and Advances in Geomechanics, Morgantown, WA, USA 1331–1336.

[14] Fragaszy, R. J., Lawton, E. 1984. Bearing capacity of reinforced sand subgrades. Journal of Geotechnical Engineering Division, ASCE 110, 1501–1507.

[15] Boiko, I. L., Alhassan, M. 2013. Effect of vertical cross-Sectional shape of foundation on settlement and bearing capacity of soils. Procedia Engineering 57, 207 – 212. DOI:10.1016/j.proeng.2013.04.029

[16] El-Sawwaf, M., Nazir, A. K. 2010. Behavior of repeatedly loaded rectangular footing resting on reinforced sand. Alexandria Engineering Journal 49, 349–356. DOI:10.1016/j.aej.2010.07.002

[17] Mostafa, A., El Sawwaf, M. 2007. Behavior of strip footing on geogrid-reinforced sand over s soft clay slope. Geotextiles and Geomembranes 25, 50–60. DOI:10.1016/j.geotexmem.2006.06.001

[18] Lee, J., Eun, J. 2009. Estimation of bearing capacity for multiple footing in sand. Computer

and Geotechnics Journal 36 (6), 1000-1008. DOI:10.1016/j.compgeo.2009.03.009

[19] Chen, Q., Abu-Farsakh, M. 2015. Ultimate bearing capacity analysis of strip footing on reinforced soil foundation. Soils and Foundations 55 (1), 74–85. DOI:10.1016/j.sandf.2014.12.006.

[20] Kuranchie, F. A., Shukla, S. K., Habibi, D., Kazi, M. 2016. Load-Settlement behavior of a strip footing resting on iron ore tailing as a structural fill. International Journal of Mining Science and Technology 26, 247-253. DOI:10.1016/j.ijmst.2015.12.010

[21] Cicek, E., Guler, E., Yetimoglu, T. 2015. Effect of reinforcement length for different geosynthetic reinforcement on strip footing on sand soil. Soils and Foundations 55 (4), 661–677. DOI:10.1016/j.sandf.2015.06.001

[22] Cure, E., Turker, E., Uzuner, B, A. 2014. Analytical and experimental study for ultimate loads of eccentrically loaded model strip footings near a sand slope. Ocean Engineering 89, 113–118. DOI:10.1016/j.oceaneng.2014.07.018

[23] Terzaghi, K. 1943. Theoretical Soil Mechanics. Wiley & Sons, New York.

[24] Vesic, A. S., 1963. Bearing capacity of deep foundation in sand. Highway Research Record, National Academy of Science 39, 112-153.

[25] Vesic, A. S. 1973. Analysis of ultimate loads of shallow foundations. Journal of the soil mechanics and foundations division, American Society of civil engineers 99 (1), 45-73.

[26] Das, B. M. 2011. Principles of Foundation Engineering. Seventh Editions. Global Engineering. Christopher M. Shortt. Chapter 3, 133-134.

[27] White, D.J., Take, W.A., Bolton, M.D. 2001. Measuring soil deformation in geotechnical models using digital images and PIV analysis. International Conference on Computer Methods and Advances in Geomechanics 997–1002.

[28] White, D.J., Take, W.A., Bolton, M.D. 2003. Soil deformation measurement using particle image velocimetry (PIV) and photogrammetry. Geotechnique 53 (7), 619–631.

[29] Slominski, C., Niedostatkiewicz, M., Tejchman, J. 2007. Application of particle image velocimetry (PIV) for deformation measurement during granular silo flow. Powder Technology 173 (1), 1-18. http://dx.doi.org/10.1016/j.powtec.2006.11.018

[30] Ould Baba, H., Peth, S. 2012. Large scale soil box test to investigate soil deformation and creep movement on slopes by Particle Image Velocimetry (PIV). Soil and Tillage Research 125, 38-43. http://dx.doi.org/10.1016/j.still.2012.05.021

[31] ASTM D 854-14, Standard Test Methods for Specific Gravity of Soil Solids by Water Pycnometer.

[32] Arasan, S., Yener, E., Hattatoglu, F., Hinislioglu, S., Akbulut. S. 2010a. The correlation between shape of aggregate and mechanical properties of asphalt concrete: Digital image processing approach. Road Materials and Pavement Design 12 (2), 239–262. DOI:10.1080/14680629.2011.9695245

[33] Cox, E. A. 1927. A method for assigning numerical and percentage values to the degree of roundness of sand grains. Journal of Paleontology 1 (3), 179–183.

[34] Powers, M.C. 1953. A new roundness scale for sedimentary particles. Journal of Sedimentary Petrology 23, 117–119.

[35] ASTM D 2487-11, Standard Practice for Classification of Soils for Engineering Purposes (Unified Soil Classification System).

[36] ASTM D 6913-04, Standard Test Methods for Particle-Size Distribution (Gradation) of Soils Using Sieve Analysis.

[37] ASTM D 4253 – 16, Standard Test Methods for Maximum Index Density and Unit Weight of Soils Using a Vibratory Table.

[38] ASTM D 4254 – 16, Standard Test Methods for Minimum Index Density and Unit Weight of Soils and Calculation of Relative Density.

[39] Arasan, S., Determination of some geotechnical properties of granular soils by image analysis, PhD Thesis, Ataturk University, Graduate school of natural and applied science, Department of civil engineering, (2011).

POENOSTAVLJENA METODA ZA ANALIZIRANJE NASIPOV, PODPRTIH S PILOTI IN GEOSINTETSKO OJAČITVIJO, TER ANALIZA VPLIVA POMEMBNOSTI PROJEKTNIH PARAMETROV

Liu Feicheng *(vodilni avtor)*
Southwest Jiaotong University,
Ministry of Education,
Key Laboratory of High-Speed Railway Engineering
Chengdu, Sichuan 610031, Kitajska
E-pošta: liufeicheng@my.swjtu.edu.cn

Zhang Jianjing
Southwest Jiaotong University,
Ministry of Education,
Key Laboratory of High-Speed Railway Engineering
Chengdu, Sichuan 610031, Kitajska
E-pošta: 13699096139@163.com

Yan Shijie
Southwest Jiaotong University,
School of Civil Engineering
Chengdu, Sichuan 610031, Kitajska
E-pošta: meiying1995@163.com

Cao Licong
Southwest Jiaotong University,
School of Civil Engineering
Chengdu, Sichuan 610031, Kitajska
E-pošta: 610554991@qq.com

Ključne besede

nasip podprt s piloti, geosintetična, poenostavljena metoda, vpliv pomembnosti; binarna analiza variance

Izvleček

V tem članku je predlagana poenostavljena metoda za ovrednotenje nasipa, podprtega s piloti in ojačenim z geosintetikom (PGRS nasip). Metoda upošteva poleg ločnega učinka, membranskega učinka odklonjenega geosintetika in reakcije tal, tudi posedek glave pilota. Zaradi slednjega se metoda lahko uporablja tako za viseče pilote kot tudi za pilote, ki stojijo na trdnem zemljinskem sloju. Posedek sloja zemljine pod površjem je sestavljen iz dveh delov: (a) posedka sloja zemljine pod površjem, ki je enak posedku glave pilota brez deformacij v geosintetiku; (b) ugrezka sloja zemljine pod površjem zaradi deformiranja geosintetika, pri čemer je upoštevana deformirana oblika za geosintetik enaka obliki deformacije vrvi. Enačba za največji diferencialni posedek med površino podlage in piloti je dobljena s pomočjo analize ravnotežja sil geosintetika in razmerja napetost-specifična deformacija geosintetika na robu glave pilota. Za preveritev predlagane metode je bila izvedena primerjava izračunanih rezultatov z opazovanimi podatki in šestimi trenutnimi analitskimi metodami. Z uporabo predlagane metode je bil preučevan vpliv natezne togosti geosintetika, kompresijskega modula mehke zemljine, debeline mehke zemljine, višine nasipa, notranjega kota trenja nasipnega materiala in razmika pilotov na reakcijo zemljine, razmerja koncentracije napetosti (SCR) in napetosti geosintetika. Učinek teh faktorjev je bil raziskan z uporabo teorije vrednotenja binarne analize variance za neponovljive preizkuse, kar pomaga optimirati načrtovanje PGRS nasipa.

A SIMPLIFIED METHOD TO ANALYZE PILE-SUPPORTED AND GEOSYNTHETIC-REINFORCED EMBANKMENTS AND THE INFLUENCE SIGNIFICANCE ANALYSIS OF THE DESIGN PARAMETERS

Liu Feicheng *(corresponding author)*
Southwest Jiaotong University,
Ministry of Education,
Key Laboratory of High-Speed Railway Engineering
Chengdu, Sichuan 610031, China
E-mail: liufeicheng@my.swjtu.edu.cn

Zhang Jianjing
Southwest Jiaotong University,
Ministry of Education,
Key Laboratory of High-Speed Railway Engineering
Chengdu, Sichuan 610031, China
E-mail: 13699096139@163.com

Yan Shijie
Southwest Jiaotong University,
School of Civil Engineering
Chengdu, Sichuan 610031, China
E-mail: meiying1995@163.com

Cao Licong
Southwest Jiaotong University,
School of Civil Engineering
Chengdu, Sichuan 610031, China
E-mail: 610554991@qq.com

Keywords
pile-supported embankment, geosynthetic, simplified method, influence significance; binary variance analysis

DOI https://doi.org/10.18690/actageotechslov.15.1.55-75.2018

Abstract

A simplified method for evaluating a pile-supported embankment reinforced with geosynthetic (PGRS embankment) is proposed in this paper. The method takes into account not only the arching effect, the membrane effect of the deflected geosynthetic, and the subsoil reaction, but also the pile head settlement, which makes the method applicable for floating piles, as well as piles seated on a firm soil layer. The settlement of the subsoil surface is considered to consist of two parts: (a) the settlement of the subsoil surface equals that of the pile cap with no deformation in geosynthetic yet; (b) the subsoil surface subsides along with the geosynthetic deforming, and the deflected geosynthetic being considered as catenary shaped. The formula for the maximum differential settlement between the subsoil surface and the piles is worked out by analyzing the force equilibrium of the geosynthetic and the stress-strain relationship of the geosynthetic at the edge of the pile cap. The comparison of the calculated results with the observed data and the six current analytical methods has been implemented to verify the proposed method. The influence of the tensile stiffness of the geosynthetic, compression modulus of soft soil, soft soil thickness, embankment height, internal friction angle of the embankment fill and the pile spacing on the subsoil reaction, the stress concentration ratio (SCR) and the tension of the geosynthetic are investigated using the proposed method. The influence significance of these factors has been investigated using the evaluation theory of binary variance analysis for the non-repeatability tests, which helps optimize the design of the PGRS embankment.

1 INTRODUCTION

The construction of embankments over soft soil with a low bearing capacity and high compressibility becomes increasingly common, while their remains a very challenging task for geotechnical engineers due to over-ranging settlement. In order to improve the soft soil, many methods such as preloading, excavation and replacement, vertical columns reinforcement, vertical drainage and vacuum consolidation are proposed. Each alternative has its own merits and limitations. Piles reinforcement is considered as an effective way on account of the accelerating consolidation of the soft soil, minimizing the total and differential settlements significantly and being suitable for various geological conditions [1], [2]. A conventionally piled embankment construction requires a close pile spacing or a large pile cap to transfer most of the embankment load to piles through the arching effect developed in the embankment fill [3]. In order to improve the load-transfer mechanism and

reduce the differential settlement of the piles and subsoil, a geosynthetic reinforcement is arranged beneath the embankment bottom [4]. Recently, the *PSGR* embankment (*PSGR* embankment) has been widely applied in the construction of embankments over soft soil, and turns out to achieve a good effectiveness [5], [2], [6], [7].

The working mechanisms of the *PSGR* embankment depend on the interactions between the granular fill of the embankment, the piles, the geosynthetic and the subsoil [3], and it is generally considered to rely on the arching effect of the embankment fill, the membrane effect of the deflected geosynthetic and the subsoil reaction. The soil arching effect, as the logical starting point for analyzing the load-transfer mechanisms of the *PSGR* embankment, has been described by some typical models, and these models can be organized into categories [8]: (a) Rigid arch models [9], [10]; (b) limit-state equilibrium models [11], [12], [13], [14]; (c) frictional models [15], [16], [17]; (d) empirical models [18]; and (e) concentric arches models [8]. It has been shown that these methods give different results in terms of the load distribution between the piles and the subsoil [19]. When it comes to the membrane effect of the deflected geosynthetic, the load distribution on the geosynthetic has a strong influence on the calculated strain, several load-deformation expressions of geosynthetic are available in the literature, and can be organized into categories: (a) catenary-shaped under a uniform load [20] (Jones C., 1990); (b) arc-shaped under a uniform load [12], [21]; (c) high-order curve-shaped deformation under a triangular distributed load [14]; (d) high-order curve-shaped deformation under an inverse triangular distributed load [22], [8]. The subsoil reaction has an important influence. BS8006 [18] and Guido et al.'s [10] methods disregard the subsoil reaction, which stays on the safe side in the design for the absence of a subsoil reaction at the most extreme situation. Other current methods take the subsoil reaction into account, which is suitable for most situations and avoids an overdesign of the geosynthetic, and consequently, an unnecessary over-cost.

Most of the current analytical methods are developed by combining one analytical model for the arching effect and one model for the membrane effect, and subsoil reaction based on different simplifying assumptions. Some methods are conceptually and mathematically complex, but the most important is that these methods fail to take the pile-head settlement into account. In reality, however, soft soil may exist under the pile toe and the pile acts as floating pile, thus the settlement of the substrata under the pile toe can play an important role in the mechanisms of load transfer, and should not be neglected.

In addition, some authors discussed the influence of some design factors on the load-transfer mechanisms via their own method and claimed that the working stress of the geosynthetic relies on the complex interaction of fill properties, soft soil properties, and geosynthetic properties [21], [23]. However, the influence significance of these properties on the load-transfer mechanisms are not clear yet, but a distinct understanding of influence significance of those designing factors on the working mechanisms helps to optimize the designing of the *PSGR* embankment.

Therefore, in this study, a new simplified method considering not only the arching effect, the membrane effect, the subsoil reaction, but also the pile-head settlement, is proposed. The tension of the geosynthetic, the subsoil reaction and the load on the pile can be calculated by using the proposed method. The influence of the tensile stiffness of the geosynthetic, the soft soil compression modulus, the soft soil thickness, the embankment height and the internal friction angle of the embankment fill on working the mechanisms has been studied via the proposed method, and then the influence significance of these factors on the working mechanisms has been investigated by the evaluation theory of binary variance analysis of the non-repeatability tests.

2 THEORETICAL DERIVATION

In developing the proposed theoretical method, the following simplifications are used:

(a) The embankment fill is homogeneous, isotropic.
(b) There is only one layer of geosynthetic considered in this paper.
(c) The soft soil and the embankment fill deform only vertically, and there is no relative displacement and slippage between the geosynthetic and subsoil.
(d) The height of the embankment fill is larger than 0.5 times the pile spacing.

2.1 Arching effect

Based on the arching effect model presented by Low et al. [12], the uniform surcharge q on the embankment surface is taken into consideration and the modified model is employed to analyze the arching effect of the embankment supported by individual square caps. The differential settlement required to develop the soil arching is so small that in this analysis it is implicitly assumed to be adequate for a fully developed arching. The total vertical stress σ_{as} applied on the soft subsoil

between the pile caps without considering the geosynthetic can be obtained using Eq.(1), and σ_{as} is considered as the total vertical load acting on the upper surface of the geosynthetic in the following deduction.

$$\sigma_{as} = \eta \frac{\gamma_s (s-a)(K_p - 1)}{2(K_p - 2)} + \\ + \eta \left(\frac{s-a}{s} \right)^{K_p - 1} \left[q + \gamma_s H - \frac{\gamma_s s}{2} \left(1 + \frac{1}{K_p - 2} \right) \right] \quad (1)$$

where γ_s is the density of embankment fill; s is the pile spacing of the piles; a is the square pile cap width; K_p is the Rankine passive coefficient of the earth pressure, $K_p=(1+\sin\varphi_s)/(1-\sin\varphi_s)$; where η is the uniform coefficient allowing for the possible non-uniform vertical stress on the soft ground, which varies between 0.8 and 1.0, here η is considered as 0.9; H is the height of the embankment; q is the uniform surcharge acting on embankment surface; φ_s is the friction angle of the embankment fill, and as for cohesive fill, φ_s should be the equivalent friction angle $\varphi_{equ,s}$ that can be determined by:

$$\phi_s = a\tan\left(\frac{\sigma_v \tan\phi_s + c}{\sigma_v} \right) = a\tan\left(\frac{(\gamma H_s + q)\tan\phi_s + c}{(\gamma H_s + q)} \right) \quad (2)$$

2.2 Subsoil reaction

For a piled embankment reinforced by the geosynthetic, pile caps are generally placed at the top of piles, and the geosynthetic reinforcement is arranged over the pile caps. Conventionally, the geosynthetic is assumed to be located beneath the embankment bottom, and fixed at the pile caps boundary [12], [24], [25]. The tensile strain of the geosynthetic is determined by the settlement of the subsoil surface between the piles, and the maximum tension occurs located at the edge of pile cap [3]. The deflection of one single layer of geosynthetic under the upper loading is shown in Fig.1. The settlement of the subsoil surface between the piles is assumed to consist of two parts: (a) just as Fig.1(a) shows, the settlement of the subsoil surface equals that of the pile cap, with no deformation developed in the geosynthetic yet. The load, σ_{as1}, acting on the upper surface of the geosynthetic is supported by the subsoil alone, and the load supported by the subsoil is denoted as σ_{bs1}, and the settlement, y_1, of the subsoil surface equals the settlement δ_p of the pile caps; (b) just as Fig.1(b) shows, the subsoil surface subsides along with the geosynthetic deforming, while the pile caps do not subside. The load acting on the upper surface of the geosynthetic is supported by the subsoil and the geosynthetic together, and the load

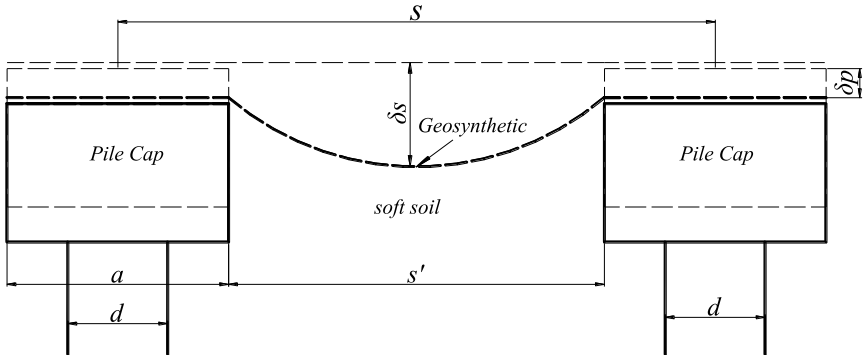

Figure 1. The total deformation of pile-geosynthetic composite structure.

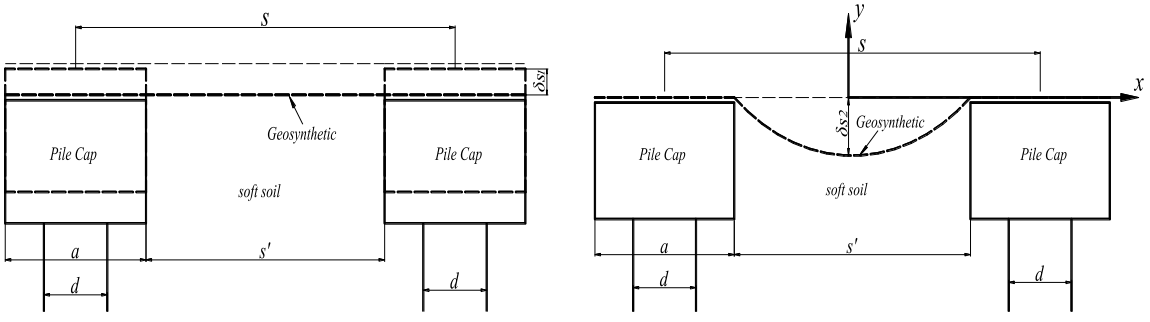

(a) Equal settlement situation (b) Differential settlement situation

Figure 2. Sketch of the deformation of the pile-geosynthetic system.

supported by the subsoil is denoted as σ_{bs2}, which causes the settlement, y_2, of the subsoil surface. The total load σ_{bs} acting on the subsoil is the sum of σ_{bs1} and σ_{bs2}.

As Fig.2(a) shows, the settlement of the pile cap is consistent with that of the subsoil, and the geosynthetic is thought to be undeformed, and thus the load σ_{as1} acting on the upper surface of the geosynthetic equals the subsoil reaction σ_{bs1}. The vertical stress σ_{bs1} carried by the subsoil can be given based on a simple equation for the one-dimensional compression of the soft soil:

$$\sigma_{bs1} = -E_s \frac{y_1}{h_s} = -E_s \frac{\delta_p}{h_s} \qquad (3)$$

where h_s is the thickness of soft soil, and E_s is the one-dimensional compression modulus. For multi-layers of soft subsoil, the equivalent one-dimensional compression modulus of the subsoil is expressed as:

$$E_s = \frac{h_s}{h_1 k_1 / E_{s1} + h_2 k_2 / E_{s2} + \cdots + h_n k_n / E_{sn}} \qquad (4)$$

In which, h_1, h_2, ..., h_n are the thickness of each soft soil layer; E_{s1}, E_{s2}, ..., E_{sn} are the one-dimensional compression moduli of each soft soil layer; h_s is the soft soil thickness, which is taken as the sum of the thicknesses of all the soft soil layers.

Fig.2(b) shows the deflection of the geosynthetic, which happens with soft soil being compressed, while the pile caps remain stable. The load σ_{as2} acting on the upper surface of the geosynthetic is uniform, which is supported by the subsoil and geosynthetic together, and can be calculated using:

$$\sigma_{as2} = \sigma_{as} - \sigma_{as1} = \sigma_{as} + E_s \frac{\delta_p}{h_s} \qquad (5)$$

2.3 Membrane effect

The membrane effect of the deflected geosynthetic can be analyzed as an assumed equivalent uniform surcharge, acting on the upper surface of geosynthetic, and the mechanical characteristics of the deflected geosynthetic are shown in Fig.3. The load acting on the upper surface of the geosynthetic equals the load acting on the embankment surface and the moving fill mass gravity, except for the shear resistance of the stationary fill mass, which is undertaken by the geosynthetic and subsoil together. As for the geosynthetic element M, the tension is T, the vertical load on the upper surface of the geosynthetic is σ_{as2} and the subsoil reaction is σ_{bs2}, and the deflection angle to the horizontal direction is θ. Taking the force equilibrium state of the element M, the following equations can be accessed:

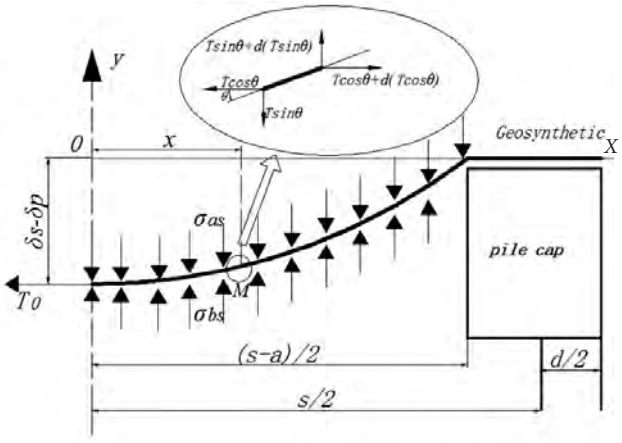

Figure 3. Mechanical characteristics of the deflected geosynthetic.

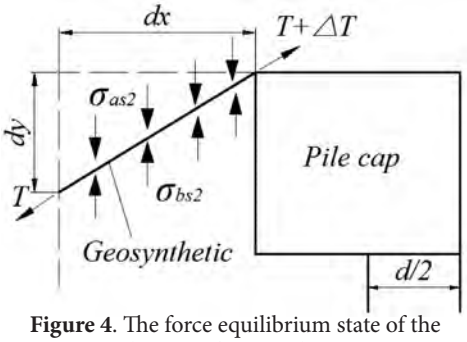

Figure 4. The force equilibrium state of the element of geosynthetic.

$$\begin{cases} \sum Fx = 0: & d\left(T\cos(\phi)\right) = 0 \\ \sum Fy = 0: & d\left(T\sin(\phi)\right) = \left(\sigma_{as2} - \sigma_{bs2}\right)dx \end{cases} \qquad (6)$$

where T is the tension of the geosynthetic, and σ_{as2} is the vertical load acting on the upper surface of the geosynthetic, and σ_{bs2} is the subsoil reaction, which varies laterally between the piles and is assumed to be uniform in this analysis.

The horizontal component tension of the geosynthetic is defined to be the constant T_0 under a definite load level. Then, $T{\cdot}\cos\theta = T_0$, thus $T_0 d(\tan(\theta)) = (\sigma_{as2} - \sigma_{bs2})dx$, $\tan(\theta) = dy_2/dx$, and Eq.(6) can be re-written as:

$$T_0 \frac{d}{dx}\left(\frac{dy_2}{dx}\right) = \left(\sigma_{as2} - \sigma_{bs2}\right) \qquad (7)$$

The tensile strain of the geosynthetic under loads is designed to be so small that the tension is proportional to the strain, and the relationship can be written as:

$$T = J \cdot \varepsilon \qquad (8)$$

where J is the tensile stiffness of the geosynthetic, and ε is the tensile strain of the geosynthetic.

The force equilibrium state of the element with length dx located at the edge of the pile cap is illustrated in Fig.4. The tensile strain of the geosynthetic under tension T is ε, and can be given by:

$$\varepsilon = \sqrt{1+\left(\frac{dy_2}{dx}\right)^2} - 1, \qquad x = \pm\frac{s-a}{2} \qquad (9)$$

According to Jones' research [20], the deformed shape of the geosynthetic under uniform loads is catenary-shaped, and can be described as quadratic parabola:

$$y_2 = ax^2 + bx + c \qquad (10)$$

Taking the boundary condition: When x=0, thus dy/dx=0 and y=$\Delta\delta$, therefore b=0 and c=$\Delta\delta$, and the following equation can be derived:

$$y_2 = ax^2 + \Delta\delta \qquad (11)$$

where $\Delta\delta$ is the differential settlement between the subsoil surface at the midpoint between the piles and the pile cap, and the settlement of the subsoil surface is larger than that of the pile cap, thus $\Delta\delta$ is negative. Taking the boundary condition: When x=(s-a)/2, the deflection y of geosynthetic is zero, thus a can be expressed as follows:

$$a = -\frac{4\Delta\delta}{(s-a)^2} \qquad (12)$$

Therefore, the deflection formula of the geosynthetic is expressed as:

$$y_2 = -\frac{4\Delta\delta}{(s-a)^2}x^2 + \Delta\delta \qquad (13)$$

The ultimate deformation formula of the geosynthetic can be expressed as follows:

$$y_{total} = y_1 + y_2 = -\frac{4\Delta\delta}{(s-a)^2}x^2 + \Delta\delta + \delta_p \qquad (14)$$

The first-order and second-order differentiation of Eq.(13) is written as follows:

$$\frac{dy_2}{dx} = -\frac{8\Delta\delta}{(s-a)^2}\,x \qquad (15)$$

$$\frac{d^2y_2}{dx^2} = -\frac{8\Delta\delta}{(s-a)^2} \qquad (16)$$

Substituting Eq.(16) into Eq.(7), the resulting equation yields:

$$-T_0\frac{8\Delta\delta}{(s-a)^2} = (\sigma_{as2} - \sigma_{bs2}) \qquad (17)$$

The horizontal component tension, T_0, of the geosynthetic can be calculated as follows:

$$T_0 = T\cdot\cos\theta = J\cdot\varepsilon\cdot\cos\theta = J\left(\sqrt{1+(\tan\theta)^2} - 1\right)\cdot\cos\theta =$$
$$= J\cdot\left(\frac{\sqrt{1+\left(\frac{dy_2}{dx}\right)^2}\text{-1}}{\sqrt{1+\left(\frac{dy_2}{dx}\right)^2}}\right) \qquad (18)$$

When the deformation is small, the following equation can be obtained by using a Taylor-serious expansion:

$$\sqrt{1+\left(\frac{dy_2}{dx}\right)^2} = 1 + \frac{1}{2}\left(\frac{dy_2}{dx}\right)^2 + \circ\left(\left(\frac{dy_2}{dx}\right)^2\right) \qquad (19)$$

Therefore, the horizontal component tension T_0 of the geosynthetic can be given by neglecting the high-order terms:

$$T_0 = J\cdot\varepsilon\cdot\cos\theta = J\cdot\frac{1}{2\left(\frac{dx}{dy_2}\right)^2 + 1} \qquad (20)$$

Substituting Eq.(15) into Eq.(20), the following equation yields at the pile edge where x is (s-a)/2:

$$T_0 = J\left(2\cdot\left(\frac{(s-a)}{4\Delta\delta}\right)^2 + 1\right)^{-1} \qquad (21)$$

Ultimately, the formula of the subsoil reaction σ_{bs2} yields by combining Eq.(17) and (21).

$$\left(\frac{64J}{(s-a)^4} + \frac{8E_s}{(s-a)^2 h_s}\right)\Delta\delta^3 + \frac{8\sigma_{as2}}{(s-a)^2}\Delta\delta^2 + \frac{E_s}{h_s}\Delta\delta + \sigma_{as2} = 0 \qquad (22)$$

Until now, the differential settlement of the subsoil surface and the pile cap can be worked out by solving this cubic equation, the maximum settlement of the subsoil surface and the tension of the geosynthetic can be obtained by Eq.(14) and Eq.(21). The total subsoil reaction is obtained by Eq.(23).

$$\sigma_{bs} = -\frac{E_s}{h_s}(\Delta\delta + \delta_p) \qquad (23)$$

2.4 Pile head settlement

In order to calculate the load acting on the upper surface of geosynthetic σ_{as2}, which is the key to solving Eq.(22), the settlement of the pile δ_p is the primary requirement. The pile head settlement is assumed to include pile tip settlement, the settlement induced by the skin friction of the pile shaft and the compression of the pile shaft. Generally, the compression of the pile shaft can be neglected compared to pile tip settlement and the settlement induced by the skin friction of the pile shaft for its overly large compression stiffness.

2.4.1 Settlement S_b of the pile tip due to the compression of the soft soil beneath the pile tip

The pile tip's resistance and the additional load of the soft soil between the piles are both supposed to be uniformly distributed. Pile tip settlement is dependent on the pile tip's resistance and the additional load acting on the pile tip's horizontal plane between the piles. Just as shown in Fig.5, the settlement of point A is supposed to be induced by the pile tip's resistance σ_{pb2}, the load, $\sigma_{sb2\text{-}1}$, and $\sigma_{sb2\text{-}2}$, on the pile tip's horizontal plane between the piles. Therefore, the pile tip resistance and the additional load are the key factors to determine pile tip settlement.

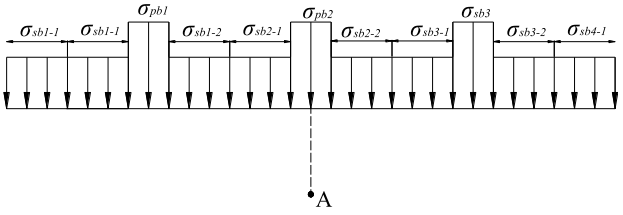

Figure 5. The load distribution at the pile tip's horizontal plane.

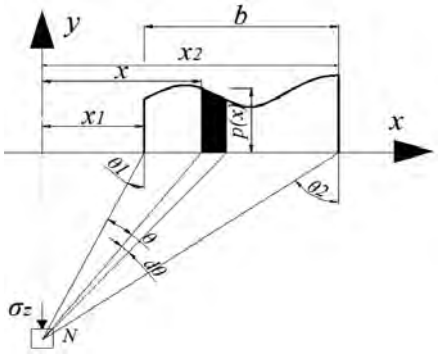

Figure 6. Stress induced by the soil under strip loading.

Yasufuku and Hyde [26] proposed the spherical cavity expansion at the pile tip based on observations from laboratory tests. Therefore, the Vesic Spherical Expansion Theory is employed to calculate the pile tip's resistance. Considering the lateral squeezing due to the interaction of the neighboring piles, the pile tip's resistance can be calculated with the following equation [27].

$$\sigma_{pb}=\sigma_0\cdot\frac{3(1+\sin\varphi)}{3-\sin\varphi}\left[\left(0.0785\frac{s}{d}\text{-}0.1194\right)\ln\sigma_0+\right.$$
$$\left.+\left(0.2593\frac{s}{d}+0.5426\right)\right]^{\frac{4\sin\varphi}{1+\sin\varphi}} \qquad (24)$$

The load differential of pile head and pile tip is supposed to transfer to the surrounding soil within the reinforced area by the single pile and distributes uniformly. Therefore, the load increment of the soft soil surrounding the pile can be calculated with:

$$\Delta\sigma_s=\frac{\sigma_{pt}a-\sigma_{pb}d}{s-d} \qquad (25)$$

where σ_{pb} is the resistance of the pile tip, σ_{pt} is the load on the pile head and can be given by:

$$\sigma_{pt}=\frac{(\gamma_s H+q)s-\sigma_{bs}(s-a)}{a} \qquad (26)$$

According to [28], for the pile group with the center-to-center spacing no larger than six times the pile diameter, the load dispersion along the pile shaft can be neglected, especially at the central part of the pile group. Assuming the subsoil between piles acts as a solid, the load acting on the surface of the subsoil transfers to the pile tip's horizontal plane without any reduction. The additional load acting at the pile tip's horizontal plane between the piles can be calculated approximately with:

$$\sigma_{sb}=\frac{\sigma_{bs}(s-a)}{(s-d)}+\Delta\sigma_s \qquad (27)$$

Just as Fig.6 shows, for a point N located at a distance z to the loading surface, the load acting on the range dx is $p(x)\,dx$, which can be considered as a concentrated load. The additional vertical stress at point N is $d\sigma_z$ under the load, then the total additional vertical stress σ_z of point N under strip loading is expressed by integrating along the x axis:

$$\sigma_z=\int_{x1}^{x2}\frac{2p(x)dx}{\pi r}\cos^3\theta \qquad (28)$$

The settlement S_b of pile tip can then be worked out using the layer-wise summation method.

2.4.2 Settlement S_s induced by the skin friction of the pile shaft

A theoretical solution to the settlement S_s induced by the skin friction of pile shaft was proposed by [29], assuming that the soil surrounding the pile behaves as an elastic, isotropic (Hookean) solid, defined by the modulus of deformation and the Poisson's ratio. For the plane-strain case, the settlement can be given by the following equations.

$$S_s=\left(\frac{P_s}{L}\right)\frac{d}{E_s}\left(1-\upsilon^2\right)I_s \qquad (29)$$

$$I_s=2+0.35\sqrt{\frac{L}{d}} \qquad (30)$$

$$P_s=\sigma_{pt}a-\sigma_{pb}d \qquad (31)$$

where p_s is the pile skin friction force; υ is the Poisson's ratio of the soft soil; I_s is the dimensionless influence factor, L is the length of the pile; and E_s is the compres-

sion modulus of soft soil. For multi-layer subsoil the composite compression modulus of the soft soil can be derived using Eq.(4).

2.5 The calculation process

The calculation process is introduced as follows:

(a) The load σ_p of pile head and the load σ_{as} acting on the upper surface of geosynthetic can be obtained with Eq.(1).
(b) The pile head settlement δ_p can be measured by tests, otherwise it can be obtained according to Section 2.2 by taking σ_p as the load acting on the pile head σ_{pt}, and neglecting the effect of the geosynthetic.
(c) The load σ_{as2} can be worked out by substituting σ_p into Eq.(5).
(d) Substituting σ_{as2} into Eq.(22) to calculate the differential settlement $\Delta\delta$.
(e) Substituting $\Delta\delta$. into Eq.(21) to calculate the horizontal component tension T_0 of the geosynthetic.
(f) Substituting $\Delta\delta$ and δ_p into Eq.(14), and the deformation formula of the geosynthetic can be obtained, and the maximum settlement δ_0 of subsoil surface can be worked out.

It is important to note that the soil arch developed in embankment supported by individual caps in the proposed method is analyzed based on the 2d condition, which is normally used when long arches are supported by continuous ledges or cap beams and can achieve good results. Just as Fig.7 shows, the geosynthetic strips act like cap beams, thus the load acting on the geosynthetic strip is noted as Load A, which results from the load transferred by the aching (Load B) and the load transferred by the deflected geosynthetic between four piles (Load C). The geosynthetic strip, supported by two adjacent pile caps, deforms under Load A, and Load A is supported by the deflected geosynthetic strip and the subsoil.

When the embankment height and the clear spacing between the piles is small, considering the support from the subsoil, the deflection of the geosynthetic strip is small, and the load transferred to the pile caps by the deflected geosynthetic strip is small, the stress concentration ratio can be calculated based on the 2d condition. However, when the embankment height and the clear spacing between the piles by the deflected geosynthetic strip is large, the load transferred to the pile caps (Load B and Load C) is high, thus the load acting on the pile caps calculated based on the 2d condition is lower than the measured result, while the calculated result based on the 3d condition is close to the measured one.

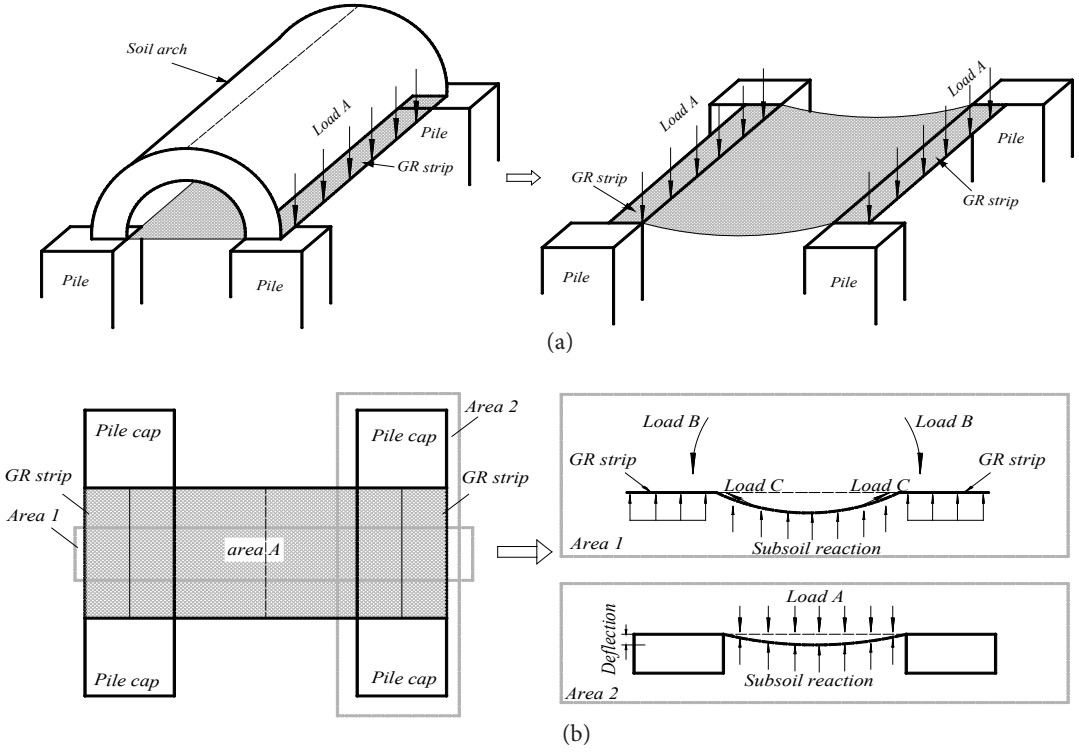

Figure 7. Load-transfer mechanisms of the PSGR embankment.

3 VALIDATION OF THE SIMPLIFIED METHOD

In this section, three embankment cases are employed to verify the proposed method, and then a discussion is presented.

3.1 The Kyoto Road

A case of the *PSGR* embankment is adopted to verify the proposed method. The details of this project, called Kyoto Road, were reported by [6]. The layout of the embankment case is shown in Fig.8, and the main parameters used in the analysis are listed in Table 1.

Table 1. Parameters used in the embankment case.

Parameters	Unit density (kN/m^3)	Compression Modulus (MPa)	Thickness (m)	Cohesion (kPa)	Friction angle
Embankment fill	18.6	-	1.15	11.5	33.8
Soft soil	-	4.43	8	-	-
Parameters	Pile spacing (m)	Pile width (m)	Length (m)	Tensile stiffness (kN/m)	
Pile/geosynthetic	1.27	0.3	13.0	1500	

The physical and mechanical characteristics of the substratum beneath the pile tip are unknown, and thus the settlement of the pile is hard to estimate. Here the settlement of the pile is neglected for reasons of simplification. The measurements were continued for several years, and a uniform load of 12kPa on the embankment surface is considered to simulate the traffic load. The results measured at 2 years after the construction of the embankment and the calculated results are listed in Table 2. It can be concluded that the results of the proposed method show a good agreement with the measured data.

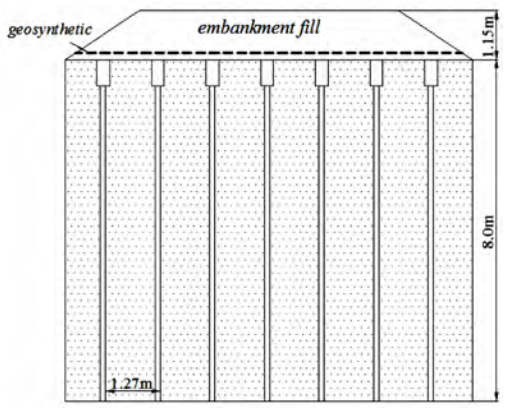

Figure 8. Layout of the embankment case for the Kyoto Road. Drawing modified after Van Eekelen et al., 2008 [6].

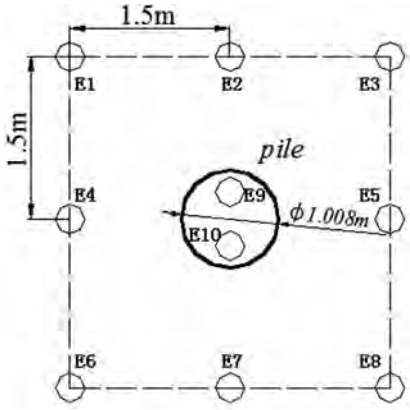

Figure 9. Layout of earth pressure cells of the embankment case of the Shanghai Railway. Drawing modified after Liu et al., 2007 [2].

Table 2. Comparison of the computation results and the field test data.

Parameters	Load transferring to pile directly by arching effect (kPa)	Vertical load carried by geosynthetic (kPa)	Subsoil resistance (kPa)	Total load on the pile (kPa)
The proposed method	77.6	5.23	16.8	87.3
Field tests	85 (approximately)	4.55	14.0	—

3.2 Shanghai Railway

A *PSGR* embankment case located in the north of Shanghai city, China, was selected to evaluate the proposed method [2]. The embankment height is 5.6m, and the width of the top surface is 35m and that of the bottom is 51.8m. The piles are arranged in a square with 3.0 m for the pile spacing. The dimensions of the pile are: 1.008 m for the outer diameter, 0.12 m thickness and 16 m in length. One layer of an extruded biaxial polypropylene grid was sandwiched between two 0.25-m-thick gravel layers to form a 0.5-m-thick composite-reinforced bearing layer. The tensile strength in both directions is 0.09 MN/m, while the tensile stiffness is 1.18 MN/m. The physical and mechanical parameters of the soil can be found in [23] and [2] and are listed in Table 3.

Fig.9 shows the arrangement of eight earth pressure cells at the subsoil surface and two cells at the pile head. Therefore, the subsoil reaction of the field tests employed here is the average result of these eight earth pressure cells at the ground surface, and the vertical load on the pile head is the average result of the these two earth pressure cells at the pile head. The pile head settlement derived from the proposed method is 19.6 mm, which

Table 3. Mechanical and physical parameters of the soil.

Soil	Thickness (m)	Gravity density (kN/m^3)	Compression modulus (MPa)	Poisson ratio	Cohesion (kPa)	Friction angle (°)
Embankment fill	5.6	18.5	—	0.3	10.0	30.0
Silty clay	1.5	—	7.0	0.3	—	—
Soft slity clay	2.3	—	5.0	0.35	—	—
Medium slity clay	10.2	—	3.0	0.4	—	—
Sandy slity	2.0	—	4.0	0.35	—	28.8

is very close to the 19 mm of field tests, which demonstrates the validity of the proposed method in estimating the pile head settlement.

The subsoil reaction and the tension of the geosynthetic is calculated using the proposed method, and then the load acting on the pile head was calculated based on a 3d condition. A comparison of the measured data, the calculated results and the numerical results is shown in Table 4. It can be concluded that the results of the proposed method agree well with those of field tests and the numerical analysis in spite of an overestimation of the load on the pile head by the proposed method. In a word, the proposed method is reasonable.

Table 4. Comparison of results of the proposed method and the field test.

	Load on pile head (kPa)	Subsoil reaction (kPa)	Tension of geosynthetic (kN/m)
Field test	567.9	40.3	—
Calculated results	713.3	43.2	15.9
Numerical analysis	592.6	53.8	16.0

3.3 Comparison with other methods

There are a number of analytical methods available for the analysis of pile-supported and gensynthetic-reinforced embankments. Not all these methods were initially developed to study the gensynthetic-reinforced and pile-supported embankments, but they were later adopted for this purpose. This section presents a comparison of the proposed method and some other analytical methods.

The geometry of the embankment and the design parameters are obtained from [16] and [20]. Rigid piles with caps and a single layer of geosynthetic were adopted to support the embankment. The relevant parameters used in this analysis are listed in Table 5, and a static surcharge of 12 kPa is applied on the top surface of the embankment to simulate the traffic loading. The calculated results of the embankment are obtained to compare the computed values of the present method with that from several existing analytical methods proposed by [12], [21], [18], [30], [23] and [17].

Based on Eq.(1), the uniform load σ_{as} acting on the upper surface of geosynthetic is 22.10 kPa and the load on the pile head is 61.55 kPa, then the settlement of the pile head is 18.0mm, and then the load σ_{as2} acting on the upper surface of the geosynthetic is 19.44 kPa by Eq.(5), and then the maximum differential settlement $\Delta\delta$ is 68.7 mm by Eq.(22), and thus the horizontal component of tension of geosynthetic, T_0, is 5.54 kN by Eq.(21), and then the load σ_{bs} carried by the subsoil between the piles is derived as 11.73 kPa.

The calculated results using the different methods are listed in Table 6. The tension of the geosynthetic and the load acting on geosynthetic are both over-predicted by [18] for neglecting the support of the subsoil. For this

Table 5. Main parameters of the embankment, pile (cap) and soil.

Components	Parameter	Value	Components	Parameter	Value
Embankment	Height (m)	1.39	—	Cap width (m)	1.13
	Unit density (kN/m^3)	20	7.0	Pile spacing/Diameter (m)	2.52/0.6
	Internal friction angle (°)	30		Length (m)	20
Subsoil	Depth (m)	25	5.0	Compression modulus (MPa)	2.96
	Unit density (kN/m^3)	17.5	3.0	Internal friction angle (°)	9
	Elastic modulus (MPa)	2.2	4.0	Tension stiffness (kN/m)	1700

Table 6. Comparison of results of different methods.

Parameters	The proposed method	Low et al.'s method [12]	Abusharar et al.'s method	BS8006's method [18]	Lu et al.'s method [17]	Zhuang et al.'s method [23]	Van Eekelen et al.'s method [30]
Vertical load on pile (kPa)	72.96	70.92	69.30	71.83	74.85	70.53	71.14
Subsoil reaction(kPa)	12.80	14.50	15.82	0	11.30	14.80	14.32
Tension of geosynthetic(kN/m)	33.23	34.00	39.18	44.40	38.71	23.50	27.76
Vertical load supported by the geosynthetic(kPa)	11.73	14.49	15.81	34.68	19.31	9.73	17.57
Stress-concentration ratio	5.68	4.86	4.38	2.07	6.62	4.76	4.97

embankment case, the embankment height is low, so that the settlement of pile is small, and the influence of the settlement on the calculated results is weak. The results of the proposed method can be found in Table 6, and are in good agreement with [17], [23] and [30], while the proposed method is conceptually and mathematically simpler than these three methods. Even Low et al. [12] and Abusharar et al. [21] assume the deflected geosynthetic as a circular curve, while the proposed method and Lu et al.'s method [17] assume it as parabola-shaped. The tension calculated by different methods shows a good agreement, which demonstrates the slight difference between the two descriptions of the deflected geosynthetic when the deflection of the geosynthetic is small. Lu et al.'s method [17] neglects the pile head settlement, and thus the tension and the load supported by the geosynthetic are both larger than that of the proposed method as a result. Zhuang et al.'s method [23] takes the average horizontal component of the tension instead of the axial tension in the analysis of the force-deformation behavior of geosynthetic, which results in an underestimation of the tension, especially at the edge of the pile cap and the load transferred to the piles by the membrane effect. Van Eekelen et al.'s method [30] underestimates the tension for considering the support of the subsoil by introducing an equivalent subsoil reaction, which allows for the subsoil below the entire geosynthetic area. The vertical load acting on the upper surface of the geosynthetic of the proposed method is less than the equivalent vertical load of Van Eekelen et al.'s method [30], supposing that the load does not rest on the geosynthetic strips between piles transferring to the strips and caps.

3.4 Comparison of several cases

Several field tests (Liu et al., 2007; Chen et al., 2010; Briancon et al., 2012; Van Eekelen et al., 2008; Chen et al., 2008) were selected to be analyzed by the proposed method, just as Table 7 exhibits [2], [31], [7], [6], [32]. These embankment cases in Table 7 can be evaluated by the proposed method with sufficient accuracy, which demonstrates that the proposed method can be employed to calculate the stress concentration ratio both under 2d and 3dcondition. According to [33], the transfer mechanisms of the load depend on the geometry of the structure (spacing of the pile caps, shape and dimension of the piles caps, height of embankment, etc.), but also the soil characteristics (granularity and mechanical parameters). Chen et al. [32] conducted a series of model tests and concluded that a higher ratio of embankment height to cap beam clear spacing, as well as a higher ratio of cap beam width to clear spacing, would result in a higher stress-concentration ratio. The inclusion of a geosynthetic reinforcement can increase the stress-concentration ratio. In this paper, the ratio of the clear spacing between adjacent piles to the center-to-center spacing is defined as the clear spacing ratio (*NSR*). The ratio of the embankment height to the cap clear spacing is defined as the height spacing ratio (*HSR*).

It can be concluded from Table 7 that like for a pile-supported embankment, without the geosynthetic reinforcement, the stress-concentration ratio is suggested to be calculated based on the 3d condition. The *NSR* is the key factor to be considered, when the *NSR* is low (such as cases 7 and 9), thus the stress concentration ratio is suggested to be calculated based on the 2d condition, and then the *HSR* is the factor deserving consideration, the stress-concentration ratio is suggested to be calculated based on the 2d condition when the *HSR* is low (case 8) and otherwise the 3d condition when the *HSR* is high.(case 1, 5 and 6). Although the proposed method is derived based on the plain-strain condition, using the proposed method to analyze the *PSGR* embankment with individual caps is practicable, and the stress-concentration ratio can be worked out based on the 2d or 3d condition, which depends on the ratio of the clear spacing between the adjacent piles to the center-to-center spacing and the ratio of the embankment height to the cap clear spacing. The influence of the *NSR* and *HSR* is still unclear, and further studies about using the plane arch model to analyze the embankment supported by the individual pile caps are required.

Table 7. The comparison of several embankment cases.

Case number	Pile cap (m)	Geosynthetic *J*(kN/m)	Embankment height (m)	Pile spacing (m)	2d/3d condition	*NSR*	*HSR*
1	No (d=1m)	1180	5.6	3.0	3d	0.67	2.80
2	Square (a=1.3m)	No	6.0	2.5	3d	0.48	5.00
3	Square (a=1.6m)	No	6.0	3.0	3d	0.47	4.29
4	Square (a=1.0m)	No	6.0	2.0	3d	0.50	6.00
5	No (d=0.38m)	800	5.0	2.0	3d	0.81	3.09
6	No (d=0.38m)	800 and 500	5.0	2.0	3d	0.81	3.09
7	Square (a=1.4m)	120	7.2	2.8	2d	0.50	5.14
8	Circular (d=0.3m)	1500	1.15	1.27	2d	0.76	1.19
9	Square (a=1.13m)	1700	1.39	2.52	2d	0.55	1.00

4 PARAMETERS STUDY

The case of the embankment discussed in Section 3.3 is employed to study the influence of the embankment height, the compression modulus of the soft soil, the tensile stiffness of the geosynthetic, the soft soil thickness, the internal friction angle of the embankment fill and the pile spacing on the subsoil reaction, the stress-concentration ratio (*SCR*) and the tension of the geosynthetic. In this section, these values are used throughout, unless otherwise specified, and the embankment is considered to be supported by cap beams instead of individual caps. No partial factors of safety are applied to the design parameters. The results of this embankment case are illustrated as follows.

4.1 The influence of tensile stiffness of the geosynthetic

The influence of the tensile stiffness on the subsoil reaction is shown in Fig.10. It can be concluded that the subsoil reaction decreases as the tensile stiffness of the geosynthetic increases, but it is likely to approach a limit value at a large tensile stiffness. The subsoil reaction increases as the pile spacing increases.

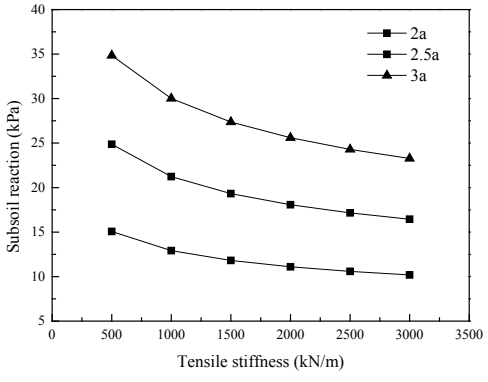

Figure 10. Influence of tensile stiffness on the subsoil reaction.

Fig.11 shows the influence of the tensile stiffness on the *SCR*. It can be seen that the *SCR* increases as the tensile stiffness increases, and is likely to approach a limit value at a large tensile stiffness. The *SCR* decreases as the pile spacing increases, and the influence at a close pile spacing is slightly more remarkable than that at a large pile spacing. The *SCR* at a close pile spacing is evidently larger than that at a large pile spacing.

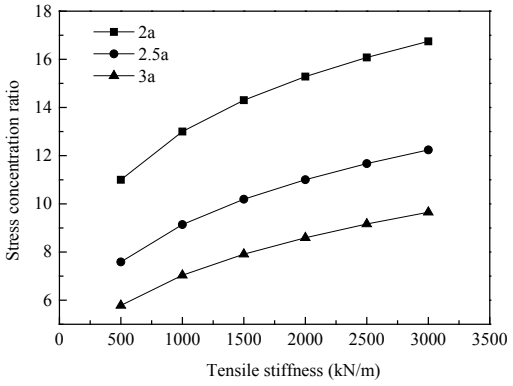

Figure 11. Influence of the tensile stiffness on the *SCR*.

The influence of the tensile stiffness on the tension of the geosynthetic is exhibited in Fig.12. It can be seen that the tension of the geosynthetic increases as the tensile stiffness of the geosynthetic increases, and tends to approach a limit value at a very large tensile stiffness. The tension differentials between the different pile spacing increases as the tensile stiffness increases. The tension of the geosynthetic at a large pile spacing is larger than that at a close pile spacing.

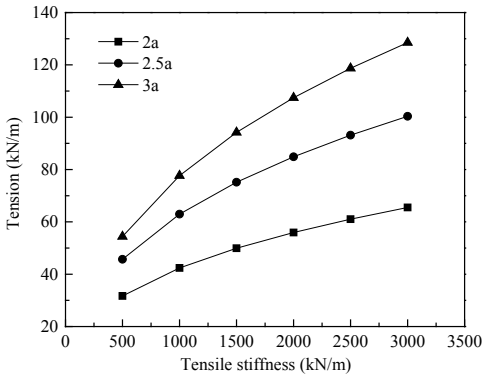

Figure 12. Influence of the tensile stiffness on the tension.

4.2 The influence of the soft soil compression modulus

Fig.13 shows the influence of the compression modulus of soft soil on the subsoil reaction. It can be seen that the subsoil reaction increases as the compression modulus increases, and is likely to approach a limit value at a large compression modulus. As the pile spacing increases, the influence of the pile spacing on the relationship of the compression modulus and the subsoil reaction strengthens, and thus the subsoil reaction differentials between the different pile spacing increases evidently as the compression modulus increases.

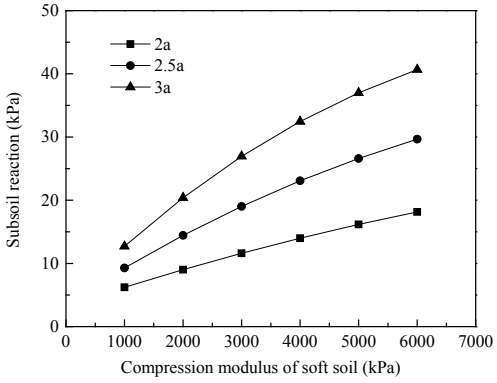

Figure 13. Influence of the compression modulus on the subsoil reaction.

Fig.14 shows the influence of the compression modulus of the soft soil on the *SCR*. It can be concluded that as the compression modulus increases, the *SCR* decreases to a limit value at a large compression modulus. The influence of the pile spacing on the relationship of the compression modulus and the *SCR* enhances with the decreasing of the pile spacing.

Fig.15 shows the influence of the compression modulus of the soft soil on the tension of the geosynthetic. It can be concluded that the tension of the geosynthetic decreases as the compression modulus increases. The effect of the compression modulus on the tension of the geosynthetic is stronger at a large pile spacing than that at a close pile spacing, and the tensions at different pile spacing are likely to be consistent for a large compression modulus.

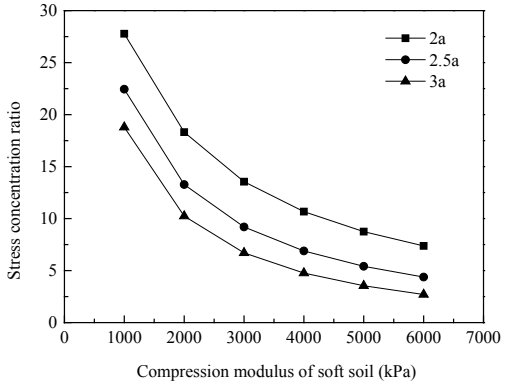

Figure 14. Influence of the compression modulus on the *SCR*.

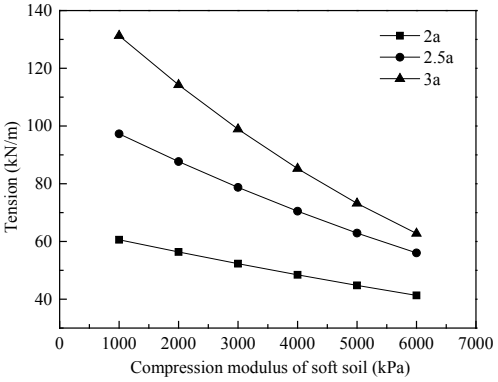

Figure 15. Influence of the compression modulus on the tension.

4.3 The influence of the soft soil thickness

Fig.16 shows the influence of the soft soil thickness on the subsoil reaction. It can be seen that the subsoil reaction decreases as the soft soil thickness increases, but it is likely to approach the limit value at a large depth. The influence of the soft ground depth on the subsoil reaction at a large pile spacing is stronger than that at a close pile spacing.

Fig.17 shows the influence of the soft soil thickness on the *SCR*. It can be concluded that the *SCR* increases as the soft soil thickness increases. The influence of the soft ground depth on the *SCR* at a close pile spacing is stronger than that at a large pile spacing, thus the *SCR* differentials of the different pile spacing increase as the soft soil thickness increases.

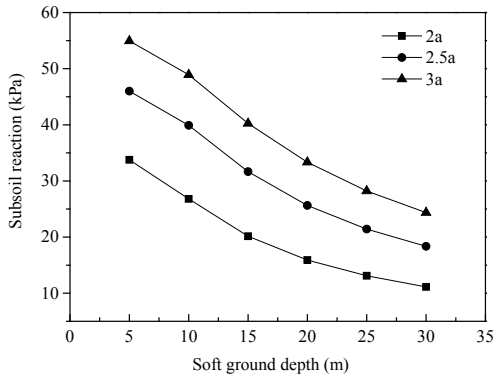

Figure 16. Influence of soft ground depth on the subsoil reaction.

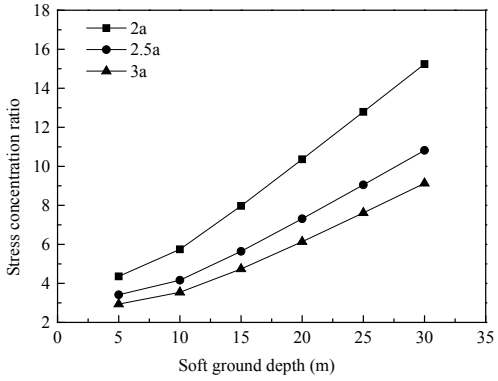

Figure 17. Influence of soft ground depth on the *SCR*.

Fig.18 shows the influence of the soft soil thickness on the tension of the geosynthetic. It can be seen that the tension of the geosynthetic increases gradually as the soft soil thickness increases, but it is likely to approach the limit value at a large soft soil thickness. The influence at a large pile spacing is obviously stronger than that at a close pile spacing, and the tension differentials between the different pile spacing increase as the soft soil thickness increases.

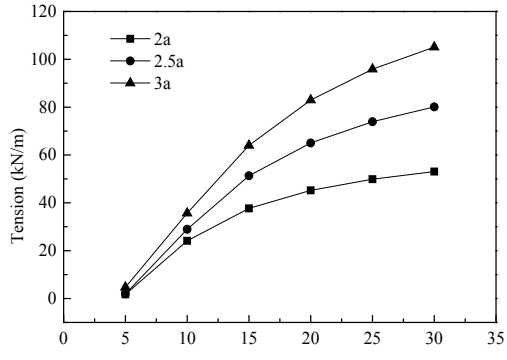

Figure 18. Influence of the soft ground depth on the tension.

4.4 Influence of the embankment height

Fig.19 presents the influence of the embankment height on the subsoil reaction. It can be concluded that the subsoil reaction increases obviously as the embankment height increases. The subsoil reaction is more sensitive to the changing of the embankment height at a large pile spacing than that at a close pile spacing.

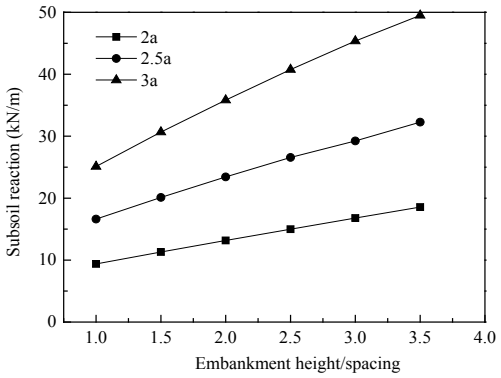

Figure 19. Influence of the embankment height on the subsoil reaction.

Fig.20 shows the influence of the embankment height on the *SCR*. It is clear that the *SCR* increases as the embankment height increases. The influence of the embankment height on the *SCR* is stronger at a close pile spacing than that at a large pile spacing, but the difference of the influence is slight.

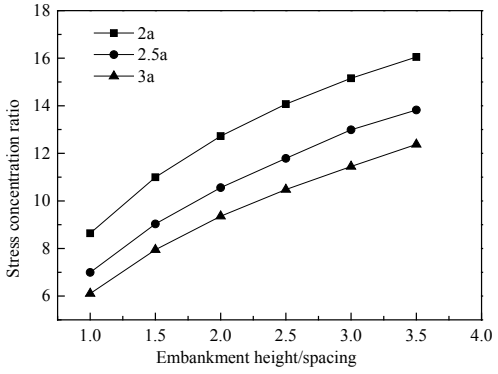

Figure 20. Influence of the embankment height on the *SCR*.

Fig.21 displays the influence of the embankment height on the tension of the geosynthetic. It is obvious that the tension of the geosynthetic increases as the embankment height increases and the pile spacing imposes an evident influence on the relationship between the tension of the geosynthetic and the embankment height. The influence of the embankment height on the tension is clearly stronger at a large pile spacing than that at a close pile spacing, which means the increasing of the embankment

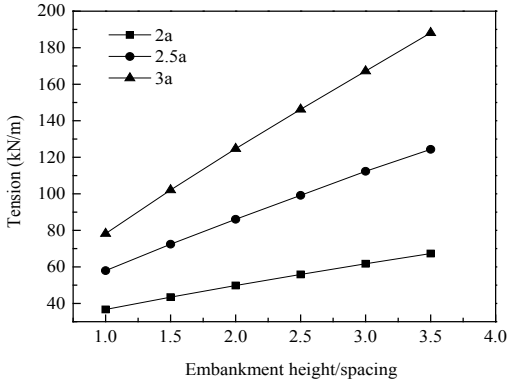

Figure 21. Influence of the embankment height on the tension.

height increases the tension differentials of the geosynthetic at different pile spacings.

4.5 Influence of the internal friction angle of the embankment fill

Fig.22 shows the influence of the internal friction angle of the embankment fill on the subsoil reaction. It can be concluded that the subsoil reaction decreases as the internal friction angle of the embankment fill increases, but it is likely to approach a limit value at a large internal friction angle. The influence at a large pile spacing is stronger than that at a close pile spacing.

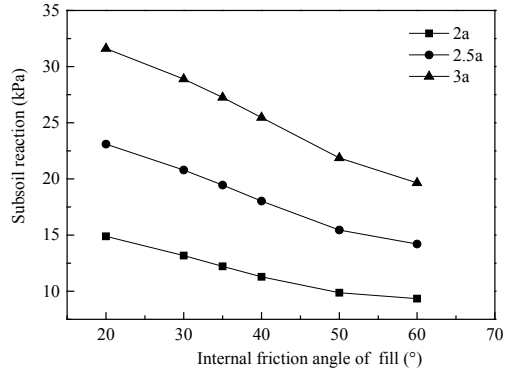

Figure 22. Influence of the internal friction angle on the subsoil reaction.

Fig.23 shows the influence of the internal friction angle of the embankment fill on the *SCR*. It can be seen that the *SCR* increases with the increase of the internal friction angle, but is likely to approach a limit value at a large internal friction angle. It is clear that the influence at a close pile spacing on the relationship between the *SCR* and the internal friction angle is stronger than that at a large pile spacing.

Fig.24 shows the influence of the internal friction angle of the embankment fill on the tension of the geosynthetic. It is clear that the tension of the geosynthetic decreases with the increasing of the internal friction angle, but it is likely to approach to a limit value at a large angle. Obviously, the influence of the internal friction angle on the tension at a large pile spacing is stronger than that at a close pile spacing, and the tension differentials between the different pile spacing decrease as the angle increases.

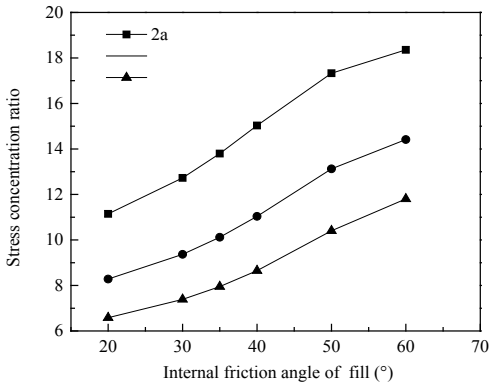

Figure 23. Influence of the internal friction angle on the *SCR*.

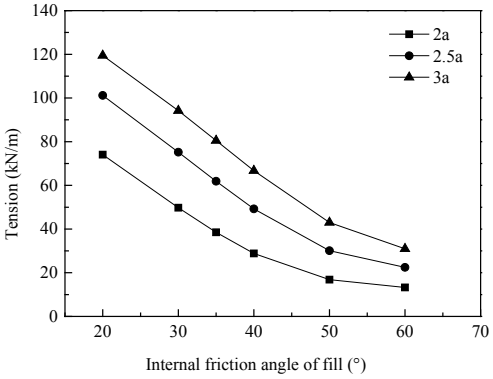

Figure 24. Influence of the internal friction angle on the tension.

5 BINARY VARIANCE ANALYSIS OF THE NON-REPEATABILITY TESTS

5.1 Evaluation theory of the binary variance analysis of the non-repeatability tests

The evaluation theory of the binary variance analysis of the non-repeatability tests is a statistical method to assess the influence significance of each factor, the detail analysis process is introduced by [34] and are reported as follows: Assuming that the test result X is influenced by two factors, A and B, and the factor A can be taken as A_1, A_2, ……, A_r, and the factor B can be taken as B_1, B_2, ……, B_s. The test result of A_i and B_j is recorded as X_{ij}, i=1, 2, ……, r; j=1, 2, ……, and test results are mutually independent. The special test process is listed in Table 8.

Table 8. Comparison of the computation results and the field test data.

Factor A	Factor B				X_i
	B_1	B_2	……	B_s	
A_1	X_{11}	X_{12}	……	X_{1s}	$\overline{X1.}$
A_2	X_{21}	X_{22}	……	X_{2s}	$\overline{X2.}$
……	……	……	……	……	……
A_r	X_{r1}	X_{r2}	……	X_{rs}	$\overline{Xr.}$
$\overline{X.j}$	$\overline{X.1}$	$\overline{X.2}$	……	$\overline{X.s}$	$\overline{X}$

The total sum of the squares is expressed as:

$$SST = \sum_{i=1}^{r}\sum_{j=1}^{s}\left(\overline{X_{ij}} - \overline{X}\right)^2 \qquad (33)$$

The sum of the squares for factor A can be expressed as:

$$SSA = s\sum_{i=1}^{r}\left(\overline{X_{i.}} - \overline{X}\right)^2 \qquad (34)$$

The sum of the squares for factor B can be expressed as:

$$SSB = r\sum_{j=1}^{s}\left(\overline{X_{.j}} - \overline{X}\right)^2 \qquad (35)$$

The sum of the squares for random variance can be expressed as:

$$SSE = \sum_{i=1}^{r}\sum_{j=1}^{s}\left(\overline{X_{ij}} - \overline{X_{i.}} - \overline{X_{.j}} + \overline{X}\right)^2 \qquad (36)$$

The freedom degree of the sum of squares for each factor can be expressed as follows: f_{SST}=IJ-1; f_{SSA}=I-1; f_{SSB}=J-1; f_{SSE}=(I-1)(J-1).

In order to quantify the influence significance of factor A, the following equation is adopted:

$$F_A = \frac{SSA/(I-1)}{SSE/\left[(I-1)(J-1)\right]} = \frac{MSSA}{MSSE} \qquad (37)$$

Generally, as for the F-distribution, once a constant value of α is given, the influence of one factor A is considered to be remarkable when F_A is larger than $F_\alpha((I\text{-}1), (J\text{-}1))$.

The equation to quantify the influence significance of the factor B is written as:

$$F_b = \frac{SSB/(I-1)}{SSE/\left[(I-1)(J-1)\right]} = \frac{MSSB}{MSSE} \qquad (38)$$

Table 9 is an analysis table of the binary variance of the non-repeatability tests, which contains these pre-mentioned items.

Table 9. Binary variance analysis of the non-repeatable tests.

Source of variance	Sum of squares	Degree of freedom	Mean square	F
Main effect of factor A	SSA	I-1	$MSSA$	F_A
Main effect of factor B	SSB	J-1	$MSSB$	F_B
Variance	SSE	(I-1)(J-1)	$MSSE$	
Sum	SST	IJ-1		

In the following analysis the pile spacing is taken as factor A with three values (2a, 2.5a, 3a), and the tensile stiffness of the geosynthetic, the compression modulus of soft soil, the soft soil thickness, the embankment height and the internal friction angle of the fill are taken as the Factor B in turn, and each has six values. The subsoil reaction, the SCR and the tension of the geosynthetic are taken as the test result separately.

5.2 Analysis of the influence of the parameters on the subsoil reaction

The pile spacing is taken as factor A, which is selected as 2a, 2.5a, 3a separately. Factor B is the tensile stiffness of the geosynthetic, which can be 500 kN/m, 1000 kN/m, 1500 kN/m, 2000 kN/m, 2500 kN/m, 3000 kN/m, separately. The results of the binary variance are listed in Table 10.

Table 10. Binary-variance analysis of the pile spacing and the tensile stiffness on the subsoil reaction.

Source of variance	Sum of squares	Degree of freedom	Mean square	F
Pile spacing	732.17	2	366.09	34.23
Tensile stiffness	141.68	5	28.34	2.65
Variance	106.93	10	10.69	
Sum	980.78	17		

As for the F-distribution, α is given as 5%, thus $F_{0.05}$(2, 10) is 4.10, $F_{0.05}$(5, 10) is 3.33. According to the analysis, $F_A > F_{0.05}$(2, 10) and $F_B < F_{0.05}$(5, 10), which demonstrates the remarkable influence of the pile spacing on the subsoil reaction, but the weak influence of the tensile stiffness. The influence of the pile spacing is evidently greater than that of the tensile stiffness.

The pile spacing is taken as factor A, which can be 2a, 2.5a, 3a, separately. Factor B is the compression modulus of the soft soil, which is selected as 1 MPa, 2 MPa, 3 MPa, 4 MPa, 5 MPa, 6 MPa, separately. The results of the binary variance are listed in Table 11.

Table 11. Binary-variance analysis of the pile spacing and the compression modulus of the soft soil on the subsoil reaction.

Source of variance	Sum of squares	Degree of freedom	Mean square	F
Pile spacing	752.50	2	376.25	10.58
Compression modulus	853.57	5	170.71	4.80
Variance	355.59	10	35.56	
Sum	1961.66	17		

As for the F-distribution, α is given as 5%, thus $F_{0.05}$ (2, 10) is 4.10, and F0.05(5, 10) is 3.33. According to the analysis, $F_A > F_{0.05}(2, 10)$ and $F_B < F_{0.05}(5, 10)$, which states that the compression modulus of the soft soil imposes a non-negligible influence on the subsoil reaction, but the influence of the compression modulus is not as great as that of the pile spacing.

The pile spacing is taken as the factor *A*, which can be 2*a*, 2.5*a*, 3*a*, separately. The Factor *B* is the soft soil thickness, which is selected as 5 m, 10 m, 15 m, 20 m, 25 m, and 30m, separately. The results of the binary variance are listed in Table 12.

Table 12. Binary-variance analysis of the pile spacing and the soft soil thickness on the subsoil reaction.

Source of variance	Sum of squares	Degree of freedom	Mean square	F
Pile spacing	998.86	2	499.43	52.27
Depth	1643.16	5	328.63	34.40
Variance	95.54	10	9.55	
Sum	2737.56	17		

As for the F-distribution, α is given as 5%, thus $F_{0.05}(2, 10)$ is 4.10, and $F_{0.05}(5, 10)$ is 3.33. According to the analysis, $F_A > F_{0.05}(2, 10)$ and $F_B < F_{0.05}(5, 10)$, which declares that the soft soil thickness exerts a notable influence on the subsoil reaction, and the influence of the soft soil thickness is weaker than that of the pile spacing.

The pile spacing is taken as factor *A*, which can be 2*a*, 2.5*a*, 3*a*, separately. Factor *B* is the embankment height, which is selected as 1.0s, 1.5s, 2.0s, 2.5s, 3.0s, 3.5s separately. The results of the binary variance are listed in Table 13.

As for the F-distribution, α is given as 5%, thus $F_{0.05}(2, 10)$ is 4.10, and $F_{0.05}(5, 10)$ is 3.33. According to the analysis, $F_A > F_{0.05}(2, 10)$ and $F_B < F_{0.05}(5, 10)$, which declares that the embankment height has a weak influence on the subsoil reaction compared with the pile spacing. The reason is that once the full soil arching has developed in the embankment fill, the increasing load of the embankment fill is mainly supported by piles, as a result of the arching effect.

Table 13. Binary-variance analysis of pile spacing and embankment height on subsoil reaction.

Source of variance	Sum of squares	Degree of freedom	Mean square	F
Pile spacing	1711.16	2	855.53	13.92
Embankment height	564.37	5	112.87	1.84
Variance	614.42	10	61.44	
Sum	2289.85	17		

The pile spacing is taken as factor *A*, which can be 2*a*, 2.5*a*, 3*a*, separately. Factor *B* is the internal friction angle of the fill, which is selected as 20°, 30°, 35°, 40°, 50°, 60°, separately. The results of the binary variance are listed in Table 14.

Table 14. Binary-variance analysis of the pile spacing and the internal friction angle of the fill on the subsoil reaction.

Source of variance	Sum of squares	Degree of freedom	Mean square	F
Pile spacing	587.84	2	293.92	39.16
Internal friction angle	161.23	5	32.25	4.30
Variance	75.06	10	7.51	
Sum	824.13	17		

As for the F-distribution, α is given as 5%, thus $F_{0.05}(2, 10)$ is 4.10, and $F_{0.05}(5, 10)$ is 3.33. According to the analysis, $F_A > F_{0.05}(2, 10)$ and $F_B < F_{0.05}(5, 10)$, which states that the internal friction angle of fill exerts a non-negligible influence on the subsoil reaction, but the influence of the pile spacing is rather greater than that of the internal friction angle of fill.

It can be drawn from the above analysis that the influence significance on the subsoil reaction of these six parameters can be expressed from strong to weak as: Pile spacing > Soft soil thickness > Compression modulus of soft soil > Internal friction angle of fill > Embankment height > Tensile stiffness of the geosynthetic.

5.3 Analysis of the influence of the parameters on the *SCR*

The pile spacing is taken as factor *A*, which can be 2*a*, 2.5*a*, 3*a*, separately. Factor *B* is the tensile stiffness of

Table 15. Binary-variance analysis of the pile spacing and the tensile stiffness of the geosynthetic on the *SCR*.

Source of variance	Sum of squares	Degree of freedom	Mean square	F
Pile spacing	125.33	2	62.66	32.64
Tensile stiffness	46.56	5	9.31	4.85
Variance	19.20	10	1.92	
Sum	191.09	17		

the geosynthetic, which is selected as 500 kN/m, 1000 kN/m, 1500 kN/m, 2000 kN/m, 2500 kN/m, and 3000 kN/m, separately. The results of the binary variance are listed in Table 15.

As for the F-distribution, α is given as 5%, thus $F_{0.05}(2, 10)$ is 4.10, and $F_{0.05}(5, 10)$ is 3.33. According to the analysis, $F_A > F_{0.05}(2, 10)$ and $F_B < F_{0.05}(5, 10)$, which demonstrates the non-negligible influence of the tensile stiffness on the *SCR*, and the influence of the pile spacing is rather greater than that of the tensile stiffness.

The pile spacing is taken as factor *A*, which can be 2*a*, 2.5*a*, 3*a*, separately. Factor *B* is the compression modulus of the soft soil, which is selected as 1 MPa, 2 MPa, 3 MPa, 4 MPa, 5 MPa, and 6 MPa, separately. The results of the binary variance are listed in Table 16.

Table 16. Binary-variance analysis of the pile spacing and the compression modulus of the soft soil on the *SCR*.

Source of variance	Sum of squares	Degree of freedom	Mean square	F
Pile spacing	134.09	2	67.04	53.333
Compression modulus	692.17	5	138.43	110.11
Variance	12.57	10	1.26	
Sum	838.83	17		

As for the F-distribution, α is given as 5%, thus $F_{0.05}(2, 10)$ is 4.10, and $F_{0.05}(5, 10)$ is 3.33. According to the analysis, $F_A > F_{0.05}(2, 10)$ and $F_B < F_{0.05}(5, 10)$, which illustrates that the influence of the pile spacing and the compression modulus of the soft soil on the *SCR* are both remarkable, and the influence of the compression modulus is greater than that of the pile spacing.

The pile spacing is taken as factor *A*, which can be 2*a*, 2.5*a*, 3*a*, separately. Factor *B* is the soft soil thickness, which is selected as 5 m, 10 m, 15 m, 20 m, 25 m, and 30 m, separately. The results of the binary variance are listed in Table 17.

Table 17. Binary-variance analysis of the pile spacing and the soft soil thickness on the *SCR*.

Source of variance	Sum of squares	Degree of freedom	Mean square	F
Pile spacing	44.33	2	22.16	9.51
Soft soil thickness	148.81	5	29.76	12.77
Variance	23.30	10	2.33	
Sum	216.44	17		

As for F-distribution, α is given as 5%, thus $F_{0.05}(2, 10)$ is 4.10, and $F_{0.05}(5, 10)$ is 3.33. According to the analysis, $F_A > F_{0.05}(2, 10)$ and $F_B < F_{0.05}(5, 10)$, which demonstrates the notable influence of the soft soil thickness and the pile spacing on the *SCR*, but the influence of the pile spacing is not as great as that of the soft soil thickness.

The pile spacing is taken as factor *A*, which can be 2*a*, 2.5*a*, 3*a*, separately. Factor *B* is the embankment height, which is selected as 1.0 s, 1.5 s, 2.0 s, 2.5 s, 3.0 s, 3.5 s, separately. The results of the binary variance are listed in Table 18.

Table 18. Binary-variance analysis of the pile spacing and the embankment height on the *SCR*.

Source of variance	Sum of squares	Degree of freedom	Mean square	F
Pile spacing	33.77	2	16.89	31.07
Embankment height	97.12	5	19.42	35.73
Variance	5.44	10	0.54	
Sum	136.33	17		

As for F-distribution, α is given as 5%, thus $F_{0.05}(2, 10)$ is 4.10, and $F_{0.05}(5, 10)$ is 3.33. According to the analysis, $F_A > F_{0.05}(2, 10)$ and $F_B < F_{0.05}(5, 10)$, which declares that the embankment height and the pile spacing both exert an evident influence on the *SCR*, and the influence of the embankment height is slightly greater than that of the pile spacing.

The pile spacing is taken as factor *A*, which can be 2*a*, 2.5*a*, 3*a*, separately. Factor *B* is the internal friction angle of the fill, which is selected as 20°, 30°, 35°, 40°, 50°, 60°, separately. The results of the binary variance are listed in Table 19.

As for F-distribution, α is given as 5%, thus $F_{0.05}(2, 10)$ is 4.10, and $F_{0.05}(5, 10)$ is 3.33. According to the analysis, $F_A > F_{0.05}(2, 10)$ and $F_B < F_{0.05}(5, 10)$, which states that the influence of the internal friction angle of fill imposes

Table 19. Binary-variance analysis of the pile spacing and the internal friction angle of fill on the *SCR*.

Source of variance	Sum of squares	Degree of freedom	Mean square	F
Pile spacing	33.77	2	16.89	31.07
Internal friction angle	97.12	5	19.42	35.73
Variance	5.44	10	0.54	
Sum	136.33	17		

a non-negligible influence on the *SCR*, and is weaker than that of the pile spacing.

It can be drawn from the above analysis that the influence significance on the *SCR* of several parameters can be expressed from strong to weak as: Compression modulus of soft soil > Soft soil thickness > Embankment height > Pile spacing > Internal friction angle of fill > Tensile stiffness of geosynthetic.

5.4 Analysis of the influence of the parameters on the tension of the geosynthetic

The pile spacing is taken as factor *A*, which can be 2*a*, 2.5*a*, 3*a*, separately. Factor *B* is the tensile stiffness of the geosynthetic, which can be 500 kN/m, 1000 kN/m, 1500 kN/m, 2000 kN/m, 2500 kN/m, and 3000 kN/m, separately. The results of the binary variance are listed in Table 20.

Table 20. Binary-variance analysis of the pile spacing and the tensile stiffness of the geosynthetic on the tension.

Source of variance	Sum of squares	Degree of freedom	Mean square	F
Pile spacing	6317.5	2	3158.747	13.27
Tensile stiffness	6042.54	5	1208.51	5.08
Variance	2380.34	10	238.03	
Sum	14740.37	17		

As for the F-distribution, α is given as 5%, thus $F_{0.05}(2, 10)$ is 4.10, and $F_{0.05}(5, 10)$ is 3.33. According to the analysis, $F_A > F_{0.05}(2, 10)$ and $F_B < F_{0.05}(5, 10)$, which demonstrates that the both the pile spacing and the tensile stiffness exert a notable influence on the tension of the geosynthetic, and the influence of the pile spacing is stronger than that of the tensile stiffness.

The pile spacing is taken as factor *A*, which can be 2*a*, 2.5*a*, 3*a*, separately. Factor *B* is the compression modulus of the soft soil, which is selected as 1 MPa, 2 MPa, 3 MPa, 4 MPa, 5 MPa, and 6 MPa, separately. The results of the binary variance are listed in Table 21.

Table 21. Binary-variance analysis of the pile spacing and the compression modulus of the soft soil on the tension.

Source of variance	Sum of squares	Degree of freedom	Mean square	F
Pile spacing	5754.29	2	2877.15	27.63
Compression modulus	3906.25	5	781.25	7.50
Variance	1041.12	10	104.11	
Sum	10701.67	17		

As for the F-distribution, α is given as 5%, thus $F_{0.05}(2, 10)$ is 4.10, and $F_{0.05}(5, 10)$ is 3.33. According to the analysis, $F_A > F_{0.05}(2, 10)$ and $F_B < F_{0.05}(5, 10)$, which declares that the compression modulus of the soft soil imposes an evident influence on the tension of the geosynthetic, but the influence of the compression modulus is not as strong as that of the pile spacing.

The pile spacing is taken as factor *A*, which can be 2*a*, 2.5*a*, 3*a*, separately. Factor *B* is the soft soil thickness, which is selected as 5 m, 10 m, 15 m, 20 m, 25 m, and 30 m, separately. The results of the binary variance are listed in Table 22.

Table 22. Binary-variance analysis of the pile spacing and the soft soil thickness on the tension.

Source of variance	Sum of squares	Degree of freedom	Mean square	F
Pile spacing	2598.37	2	1299.19	5.57
Soft soil thickness	12776.85	5	2555.37	10.95
Variance	2333.49	10	233.35	
Sum	17708.71	17		

As for the F-distribution, α is given as 5%, thus $F_{0.05}(2, 10)$ is 4.10, and $F_{0.05}(5, 10)$ is 3.33. According to the analysis, $F_A > F_{0.05}(2, 10)$ and $F_B < F_{0.05}(5, 10)$. It can be concluded that the soft soil thickness has a great influence on the tension of the geosynthetic, and the influence of the soft soil thickness is stronger than that of the pile spacing.

The pile spacing is taken as factor *A*, which can be 2*a*, 2.5*a*, 3*a*, separately. Factor *B* is the embankment height, which is selected as 1.0 s, 1.5 s, 2.0 s, 2.5 s, 3.0 s, 3.5 s separately. The results of the binary variance are listed in Table 23.

As for the F-distribution, α is given as 5%, thus $F_{0.05}(2, 10)$ is 4.10, and $F_{0.05}(5, 10)$ is 3.33. According to the analysis, $F_A > F_{0.05}(2, 10)$ and $F_B < F_{0.05}(5, 10)$, which demonstrates the weak influence of the embankment

Table 23. Binary-variance analysis of the pile spacing and the embankment height on the tension.

Source of variance	Sum of squares	Degree of freedom	Mean square	F
Pile spacing	20160.76	2	10080.38	10.16
Embankment height	9958.46	5	1991.69	2.01
Variance	9921.14	10	992.11	
Sum	40040.36	17		

height on the tension of the geosynthetic, and the influence of the pile spacing is stronger than that of the soft soil thickness.

The pile spacing is taken as factor *A*, which can be 2*a*, 2.5*a*, 3*a*, separately. Factor *B* is the internal friction angle of the fill, which is selected as 20°, 30°, 35°, 40°, 50°, and 60°, separately. The results of the binary variance are listed in Table 24.

Table 24. Binary-variance analysis of the pile spacing and the internal friction angle of the fill on the tension.

Source of variance	Sum of squares	Degree of freedom	Mean square	F
Pile spacing	3814.90	2	1907.45	41.43
Internal friction angle	11907.16	5	2381.43	51.72
Variance	460.41	10	46.04	
Sum	16182.47	17		

As for F-distribution, α is given as 5%, thus $F_{0.05}(2, 10)$ is 4.10, and $F_{0.05}(5, 10)$ is 3.33. According to the analysis, $F_A > F_{0.05}(2, 10)$ and $F_B < F_{0.05}(5, 10)$. It can be drawn that the internal friction angle of the fill exerts a great influence on the tension of the geosynthetic, and the influence of the internal friction angle is stronger than that of the pile spacing.

It can be concluded from the above analysis that the influence significance on the tension of the geosynthetic of several parameters can be expressed from large to small as: Soft soil thickness > Internal friction angle of fill > Pile spacing > Tensile stiffness of geosynthetic > Compression modulus of soft soil > Embankment height.

5.5 Suggestions for designing the *PSGR* embankment

Normally, when designing a *PSGR* embankment, how to alleviate the tension of the geosynthetic and make more load transfer to the piles attracts most of our attention. The soft soil thickness and the compression modulus of the soft soil are hard to accommodate for the complex geological condition and the high expense. The pile spacing, the internal friction angle of the fill and the tensile stiffness are the factors that can be accommodated in the design. In order to enlarge the pile spacing, using fill material with a large internal friction angle is the most effective way, followed by adopting a geosynthetic with a high tensile stiffness.

6 CONCLUSIONS

A new theoretical method has been presented in this paper that should be a solution to an embankment of granular fill on soft soil supported by a rectangular grid of piles and geosynthetic. The method is conceptually and mathematically simple, while it takes the arching effect, the membrane effect, the subsoil reaction and the pile head settlement into consideration. The new method can not only be applied for piles seated on a firm soil layer, but also floating piles. The proposed method is verified by comparing results with the field data and was found to be in good agreement with some current analytical methods for a low embankment case. Although the proposed method is based on plane-strain conditions, using the proposed method to get a subsoil reaction and the tension of the geosynthetic, and then calculating the stress concentration ratio based on the 3d condition, is considered to be practicable. Before the calculation of stress-concentration ratio, the clear spacing ratio (*NSR*) and the height spacing ratio (*HSR*) should be considered firstly to judge the 2d or 3d condition is adopted.

Parameters research is conducted in this paper using the proposed theoretical method, including the tensile stiffness of the geosynthetic, the compression modulus of the soft soil, the soft soil thickness, the height of the embankment, the internal friction angle of the fill and the pile spacing. The influence of these parameters on the subsoil reaction, the *SCR*, and the tension of the geosynthetic are discussed in this paper.

Based on a binary-variance analysis of the non-repeatability tests, the influence significance of the pile spacing, the tensile stiffness of the geosynthetic, the compression modulus of the soft soil, the soft soil thickness, the embankment height and the internal friction angle of the fill are studied, and the results are explained as follows:

(a) As for the subsoil reaction, the influence significance of these parameters can be expressed from large to small as: Pile spacing > Soft soil thickness >

Compression modulus of soft soil > Internal friction angle of fill > Embankment height > Tensile stiffness of geosynthetic

(b) As for *SCR*, the influence significance of these parameters can be expressed from large to small as: Compression modulus of soft soil > Soft soil thickness > Embankment height > Pile spacing > Internal friction angle of fill > Tensile stiffness of geosynthetic.

(c) As for the tension of the geosynthetic, the influence significance of these parameters can be expressed from large to small as: Soft soil thickness > Internal friction angle of fill > Pile spacing > Tensile stiffness of geosynthetic > Compression modulus of soft soil > Embankment height.

In designing a piled embankment, in order to enlarge the pile spacing, using granular material with a high friction angle for the embankment fill is the most effective and economical way, rather than using a geosynthetic with a high tensile stiffness.

In this study, piles arranged in a square pattern and one layer of geosynthetic was investigated. Further research is essential for piles arranged in other patterns, for a multi-layer reinforcement piled embankment.

Acknowledgments

The financial support of the National Key Research and Development Plan of the Ministry of science The financial support of the National Key Research and Development Plan of the Ministry of science (Grant No 2017YFC0504901), The financial support of Science and Technology Plan Projects of Sichuan Province (Grant No 2015SZ0068), the Ministry of Transport Construction Projects of Science and Technology of China (Grant No 2013318800020), the Project of outstanding innovative talents of Southwest Jiaotong University (Grant No XJXY201408) is acknowledged. The discussion with Mr. Liu K.W. (Southwest Jiaotong University) and Liao Y. (CHEC USA) helped improve this paper and is appreciated by the authors.

REFERENCES

[1] Magan, J.P. 1994. Methods to reduce the settlement of embankments on soft clay: a review. In: Vertical and Horizontal Deformations of Foundations and Embankments. ASCE. Geotechnical Special Publication, pp. 77-91.

[2] Liu, H.L., Charles, W.W.Ng., Fei, K. 2007. Performance of a geogrid-reinforced and pile-supported highway embankment over soft clay: case study. Journal of Geotechnical and Geoenvironmental Engineering 133, 12, 1483-1493. DOI: 10.1061/(ASCE)1090-0241(2007)133:12(1483)

[3] Han, J., Gabr, M.A. 2002. Numerical analysis of geosynthetic-reinforced and pile-supported earth platforms over soft soil. Journal of Geotechnical and Geoenvironmental Engineering 128, 1, 44-53. DOI: 10.1061/(ASCE)1090-0241(2002)128:1(44)

[4] Gangakhedkar, R. 2004. Geosynthetic Reinforced Pile Supported embankments. University of Florida, Florida.

[5] Almeida, M.S.S., Ehilich, M., Spotti, A.P., Marques, M.E.S. 2007. Embankment supported on piles with biaxial geogrids. Geotechnical Engineering 160, 4, 185-192. DOI: 10.1680/geng.2007.160.4.185

[6] Van Eekelen, S.J.M., Bezuijen, A., Alexiew, D. 2008. Piled embankments in the Netherlands, a full-scale test, comparing 2 years of measurements with design calculation. Proc. EuroGeo4, pp. 264.

[7] Briancon, L., Simon, B. 2012. Performance of pile-supported embankment over soft soil: full-scale experiment. Journal of Geotechnical and Geoenvironmental Engineering 138, 4, 551-561. DOI: 10.1061/(ASCE)GT.1943-5606.0000561

[8] Van Eekelen, S.J.M.V., Bezuijen, A., Tol, A.F.V. 2013. An analytical model for arching in piled embankments. Geotextiles and Geomembranes 39, 78-102. DOI: 10.1016/j.geotexmem.2013.07.005

[9] Carlsson, B. 1987. Reinforced Soil, Principles for Calculation. Terratema AB, Linköping (in Swedish).

[10] Guido, V.A. Kneuppel, J.D., Sweeny, M.A. 1987. Plate loading test on geogrid-reinforced earth slabs. In: Proceedings of geosynthetics'87, New Orleans, USA. IFAI, pp. 216-225.

[11] Hewlett, W.J., Randolph, M.F. 1988. Analysis of piled embankment. Ground Engineering 21, 3, 12-18.

[12] Low, B.K., Tang, S.K., Choa, V. 1994. Arching in piled embankment. Journal of Geotechnical Engineering 120, 11, 1917-1938. DOI: 10.1061/(ASCE)0733-9410(1994)120:11(1917)

[13] Collin, J.G. 2004. Column supported embankment design consideration. In: 52nd Annual Geotechnical Engineering Conference. University of Minnesota.

[14] Raithel, M., Kirchner, A., Kempfert, H.G. 2008. German recommendations for reinforced embankments on pile-similar elements. Proc. 4th Asian Regional Conference on Geosynthetics, Shanghai, pp. 697-702.

[15] Terzaghi, K., 1943. Theoretical soil mechanics. John Wiley and Sons, New York.

[16] Chen, R.P., Chen, Y.M., Xu, Z.Z. 2008a. A theoretical solution for pile-supported embankments on soft soils under one-dimensional compression. Canadian Geotechnical Engineering 45, 6, 611-623. DOI: 10.1139/T08-003

[17] Lu, W.H., Miao, L.C. 2015. A simplified 2-D evaluation method of the arcing effect for geosynthetic-reinforced and pile-supported embankments. Computers and Geotechnics 65, 97-103. DOI: 10.1016/j.compgeo.2014.11.014

[18] BS8006-1-2010. Code of Practice for Strengthened/ Reinforced Soils and Other Fills. British Standard Institution, 2010.

[19] Zhang, C.L., Jiang, G.L., Liu, X.F., Buzzi, O. 2016. Arching in geogrid-reinforced pile-supported embankments over silty-clay of medium compressibility: Field data and analytical solution. Computers and Geotechnics 77, 11-25. DOI: 10.1016/j.compgeo.2016.03.007

[20] Abusharar, S.W., Zheng, J.J., Chen, B.G., Yin, J.H. 2009. A simplified method for analysis of a piled embankment reinforced with geosynthetic. Geotextiles and Geomembranes 27, 1, 39-52. DOI: 10.1016/j.geotexmem.2008.05.002

[21] Filz, G., Sloan, J. 2013. Load distribution on geosynthetic reinforcement in column-supported embankments. Geo-congress, 231, pp. 1822-1830.

[22] Zhuang, Y., Wang, K.Y., Liu, H.L. 2014. A simplified model to analyze the reinforced piled embankments. Geotextiles and Geomembranes 42, 2, 154-165. DOI: 10.1016/j.geotexmem.2014.01.002

[23] Russell, D., Naughton, P.J., Kempton, G. 2003. A new design procedure for piled embankments. Proc. 56th Canadian Geotechnical Conf. and 2003 NAGS Conf., pp. 858-865.

[24] Yu, C., Liu, S.Y., Ji, T.Y. 2006. Study on the performance of the reinforced piled embankment. ASCE Geotechnical Special Publication, 151, pp. 247-254.

[25] Jones, C. 1990. Geotextile reinforced piled embankments. Proc. 4th Int. Conf. on Geotextiles: Geomembranes and Related products. Rotterdam: Balkema, pp. 155-160.

[26] Yasufuku, N., Hyde, A.F.L. 1995. Pile end-bearing capacity in crushable sands. Geotechnique 45, 1, 663-676.

[27] Liu, J.F. 2011. Study on working mechanism and calculation method of settlement control for railway's roadbed using CFG-pile composite foundation. Southwest Jiaotong University, Chengdu.

[28] JGJ 94-2008: 2008. 2008. Technical code for building pile foundations. China Architecture & Building Press, Beijing.

[29] Vesic, A.S. 1977. Design of pile foundation. National Cooperative Highway Research Program Synthesis of Practice, Washington.

[30] Van Eekelen, S.J.M.V., Bezuijen, A., Tol, A.F.V. 2015. Validation of analytical models for the design of basal reinforced piled embankments. Geotextiles and Geomembranes 43, 1, 56-81. DOI: 10.1016/j.geotexmem.2014.10.002

[31] Chen, R.P., Xu, Z.Z., Chen, Y.M., Ling, D.S., Zhu, B. 2010. Field tests on pile-supported embankments over soft ground. Journal of Geotechnical and Geoenvironmental Engineering 136, 6, 777-785. DOI: 10.1061/(ASCE) GT1943-5606.0000295

[32] Chen, Y.M., Cao, W.P., Chen, R.P. 2008b. An experimental investigation of soil arching within basal reinforce and unreinforced piled embankments. Geotextiles and Geomembranes 26, 2, 164-174. DOI: 10.1016/j.geotexmem. 2007.05.004

[33] Hello, B.L., Villard, P. 2009. Embankment reinforced by piles and geosynthetics-Numerical and experimental studies dealing with the transfer of load on the soil embankment. Engineering Geology 106, 1-2, 78-91. DOI: 10.1016/j.enggeo.2009.03.001

[34] Wang, R.X. 2005. Mathematical Statistics. Xi An Jiaotong Univesity Press, Xi An.

MODIFICIRAN MODUL REAKCIJE TAL ZA BOČNO OBTEŽENE PILOTE

Ayhan Gurbuz
Gazi University,
Civil Engineering Department
06570 Maltepe-Ankara, Turčija
E-pošta: agurbuz@gazi.edu.tr

Ključne besede

Bromsova metoda, horizontalni modul reakcije tal, p-y krivulje, model deformacijskega klina

Izvleček

Natančna napoved nosilnosti bočno obteženega pilota pri dovoljenem pomiku je pomembna v fazi načrtovanja. V nasprotju s številnimi sofisticiranimi metodami so inženirji največkrat napovedovali nosilnost bočno obteženih pilotov z Bromsovo metodo, ki temelji na ravnotežju momentov, zaradi svoje preprostosti in ker se izračun praktično izvede "na roke". Vendar pa Bromsova metoda običajno precenjuje bočno obremenitev pilota, ker se v analizah upošteva konstanten horizontalni modul reakcije tal (n_h), ne glede na velikost premika pilota na vrhu. V študiji so najprej predstavljeni modificirani moduli reakcije tal (n_h) za nekohezivne zemljine, ki izboljšajo učinkovitost Bromsove metode za napoved nosilnosti bočno obteženih pilotov z naraščanjem premika pilota na vrhu. Modificirane vrednosti n_h* so bile kalibrirane z uporabo rezultatov 45 samostojnih preizkusov pilotov s 23 gradbišč v nekohezivnih tleh, s prosto glavo pilota in posamično zabitih. Pokazano je, da Bromsova metoda z n_h* pravilno oceni obnašanje bočno obteženega pilota s podobno natačnostjo kot jo dosežemo pri bolj zapletenih metodah.*

MODIFIED COEFFICIENT OF SUBGRADE REACTION TO LATERALLY LOADED PILES

Ayhan Gurbuz
Gazi University,
Civil Engineering Department
06570 Maltepe-Ankara, Turkey
E-mail: agurbuz@gazi.edu.tr

Keywords

Broms' method, coefficient of horizontal subgrade reaction, p-y curves, strain wedge model

DOI https://doi.org/10.18690/actageotechslov.15.1.77-85.2018

Abstract

An accurate prediction of the load capacity of a laterally loaded pile at a permissible displacement is an important concern at the design stage. In contrast to many sophisticated methods, Broms' method based on moment equilibrium has been preferred by engineers to predict the load capacities of laterally loaded piles due to both its simplicity and because it is established on a way of hand calculation. However, Broms' method typically overestimates a pile's lateral load capacity as it requires a constant coefficient of horizontal subgrade reaction (n_h) into analyses, regardless of the magnitude of the pile's top displacement. In this study, modified coefficients of subgrade reactions(n_h) that are sensitive to the pile's top displacement in cohesionless soils are first proposed to improve the performance level of Broms' method for the prediction of the load capacity of a laterally loaded pile as the pile's top displacement increases. The modified values of n_h* are calibrated using 45 independently free-head, single-driven, full-scale pile tests from 23 sites in cohesionless soils. It is demonstrated that Broms' method with n_h* would correctly estimate a pile's lateral load-deflection behavior with accuracy levels similar to more complicated methods.*

1 INTRODUCTION

The failure load of a laterally loaded pile cannot be easily defined by a predefined limit unless the pile fails structurally. Therefore, a prediction of the load of a laterally loaded pile remains largely unknown as it requires the systematic examination of the measured performance of many full-scale loaded piles under lateral loads and site conditions.

The load capacities of laterally loaded piles at a given lateral displacement have been easily estimated with the help of Broms' method, which uses simple equations based on the moment equilibrium utilizing the elastic theory along with the coefficient of subgrade reactions to calculate the pile's top displacement at the ground surface. An important parameter that affects the performance level in the prediction of a load at a pile's top displacement for Broms' method is the coefficient of horizontal subgrade reaction (n_h) developed by Terzaghi [1], based on the soil's relative density and the location of the layer above or below the ground water table, and presented in Table 1.

Broms' method typically overestimates a pile's lateral load capacity at a given pile's top displacement due to the implementation of a constant value of n_h into the analyses of Broms' method, regardless of the magnitude of the pile's displacement [2]. It has been reported, however,

Table 1. Approximate values of the coefficient of subgrade reaction (n_h) recommended by Terzaghi [1], varying with the relative density of the soil and the location of the ground-water table.

Relative Density	n_h (kN/m^3)		
	Loose	Medium	Dense
Above Ground-Water Table (GWL)	2424	7272	19393
Below GWL	1385	4848	11774

that the coefficient of subgrade reaction decreases as the pile displacement increases [2, 3, 4, 5 and 6]. Researchers [7, 8, 9, 10, 11, 12 and 13] investigated the effect of the subgrade reaction coefficient of a soil deposit using a back analysis based on deflection data from horizontal loading tests. Nevertheless, the coefficient of the horizontal subgrade reaction, an important parameter for Broms' method, has been broadly studied by researchers, there has been only an inadequate full-scale field verification for it. In this study, modified coefficients of subgrade reactions (n_h*) that vary with an increase in the pile's top displacement in cohesionless soils are suggested to enhance the performance level of Broms' method for the prediction of a lateral load capacity of the piles as the pile's top displacement increases. Hence, Broms' method would be compatible with more complex methods such as the p-y curve method and the Strain Wedge Method (*SWM*). The proposed modifications are calibrated by the cases of 45 free-head, single-driven, full-scale pile tests that are gathered from 23 sites in cohesionless soils to determine the performance level in the prediction of a load (P_{cal}) required to induce a displacement from 12.7 to 63.5 mm at 12.7 mm intervals with an actual load (P_{msd}) measured at the same displacements. It is confirmed that Broms' method with values of n_h* would properly estimate the pile's lateral load-deflection behavior at precision levels similar to the p-y curve method and the Strain Wedge Method (*SWM*).

2 ANALYSES METHODS

The methods of analysis for pile behaviour under lateral loads range in complexity from simple empirical methods to three-dimensional finite-element methods. The 45 free-head, single, full-scale pile tests in cohesionless soils were assembled in this study and examined mostly via the approach seeking the performance level in the calculation of a P_{calc} required to induce a displacement from 12.7 to 63.5 mm at 12.7 mm intervals with the actual loads measured (P_{msd}) at the same displacements using Broms' method [14,15 and 16]. Then, the analysis results of Broms' method were compared with the p-y curves [17 and 18] and the Strain Wedge Model (*SWM*) [19, 20 and 21].

Broms [14 and 15] separated the analysis into cases of laterally loaded piles that are embedded in cohesive and cohesionless soils. Broms also suggested different procedures for the prediction of laterally loaded piles under working loads and for an assessment of the pile's ultimate resistance. In the working state, Broms [14 and 15] assumed that under loads of less than one-half to one-third of the ultimate lateral resistance, the deflections of a single pile increased approximately linearly with the applied load. Subsequently, the unit soil reaction (p) acting on a laterally loaded pile increased in proportion to the lateral deflection (y). Broms' solution for the deflection under the application of small loads is based on the beam in elastic foundation theory.

Broms categorized the piles as either long or short piles, the dimensionless depth of embedment is defined as ηL, where $\eta = \sqrt[5]{n_h/EI}$. Accordingly, the depth of the embedment for a long pile would be ηL>4 and ηL<2 for a short pile. The surface deflection of a single pile can be obtained by using equation 1 or 2 based on the moment equilibrium for a free-head driven short pile or a long pile, respectively. Additional solutions for the surface displacement of the piles were presented by Broms (14, 15, 16).

$$Y_o = \frac{18P(1+1.33e/L)}{L^2 n_h} (\eta L \leq 2) \qquad (1)$$

$$Y_0 = \frac{2.40P}{(n_h)^{3/5}(EI)^{2/5}} (\eta L \geq 4) \qquad (2)$$

where P is the applied load at the pile's top, EI is the stiffness of the pile section, L is the embedded length of the pile, e is the load eccentricity and Y_0 is the pile's top displacement.

The lateral loads in many cases are moderate to relatively high, for which nonlinearity typifies the pile's load-deflection behavior. As a result, the nonlinear elasticity methods have been developed in which the application of elastic solutions for the equivalent soil properties is used in an iterative procedure, ending when the displacement compatibility between the soil and the pile is achieved. The most commonly used such method is referred to as the py curves method, first devised by McClelland and Focht [22] and improved over the years by others. In the p-y curves procedure, nonlinear curves relating the soil reaction (p) to the pile displacement (y) at various depths are first constructed. An initial stiffness of the soil is assumed, and the governing elastic differential equation of the pile's deflection is solved numerically for that stiffness, resulting in a distribution of the pile's deflection. With the calculated deflection, entering the p-y curves, the soil reaction can be evaluated and compared with the one initially assumed. If a substantial difference exists, the soil stiffness at the depth for which

the curve was drawn is taken as the secant modulus from the p-y curve at the previously computed deflection and the procedure is then repeated until a tolerable compatibility is reached. Not exactly true, the Beam on Elastic Foundation (*BEF*) assumption at the base of the solution has been shown to produce accurate results for the patterns of the deflections that can occur in practice [17]. Subsequently, three matters need to be considered: (i) the elastic analysis of the interaction between the soil and the pile, modeled using the concept of a subgrade reaction, (ii) the estimation of the shape of the p-y curves for various types of soil and loading conditions, and (iii) the procedure in which the nonlinearity is incorporated into the solution. A comprehensive review of the historical development of research on those three issues has been provided by Duncan et al. [23]. According to the subgrade reaction approach, the laterally loaded pile is treated as a *BEF*. Winkler's [24] soil model is assumed, in which the elastic soil medium is replaced by a series of infinitely closely spaced in dependent and elastic springs with a stiffness equal to the modulus of the horizontal subgrade reaction (k_h)

$$k_h = \frac{p}{y} \qquad (3)$$

$$EI \times \frac{d^4 y}{dz^4} + p = 0 \qquad (4)$$

where EI is the pile stiffness, and p is the soil reaction that is equal to $k_h y$. Thus, the governing differential equation can be rewritten as follows:

$$EI\left(\frac{d^4 y}{dx^4}\right) + E_s(x) = 0 \qquad (5)$$

The deflection of the pile at each depth is dependent on several parameters, the depth, the relative stiffness factor that combines the stiffness of the pile and the soil and their interaction, and the type and magnitude of the applied load at the pile's top. The solution to the governing equation involves specifying the four boundary conditions, such as the known values of the shear force, the moment, the slope or the deflection at both ends of the pile. Details of the solution based on the dimensional analysis are described by Matlock and Reese [25], Prakash and Sharma [26], and Poulos and Davis [27]. The result of solving the governing equation yields five distributions with the pile depth: deflection (y), slope ($S=dy/dz$), bending moment ($M=EId^2y/dz^2$), shear ($V=EId^3y/dz^3$), and soil reaction ($p=EId^4y/dz^4$). The application of the p-y curves' analysis requires the use of computer codes to assess the deflections of the pile and the bending moments it develops under various loads. Relevant programs have been developed by Reese [28, 29].

The Strain Wedge Model (*SWM*) is an approach that has been developed to predict the response of a pile under lateral loading [19]. It can be applied to both driven piles and in-place-constructed deep foundations. The main concept of the *SWM* is that traditional one-dimensional *BEF* pile response parameters can be characterized in terms of the three-dimensional soil-pile interaction behavior. The *SWM* parameters are related to an envisioned three-dimensional passive wedge of soil developing in front of the pile [21]. As a result, the *SWM* is able to provide a theoretical link between the more complex three-dimensional soil-pile interaction and the simpler one-dimensional *BEF* characterization, hence allowing the appropriate selection of the *BEF* parameters to solve the fourth-order ordinary differential equation with the modulus of soil subgrade reaction (E_s) being associated with the *BEF* characterization:

$$EI\left(\frac{d^4 y}{dx^4}\right) + E_s(x) = 0 \qquad (6)$$

The closed-form solution to equation 6 was obtained by Matlock and Reese [25] for the case of uniform soil. The governing analytical formulations should be related to the passive wedge in front of the pile, the soil's stress-strain relationship, and the related soil-pile interaction. It should be noted that the *SWM* is based on an effective stress analysis of both sand and clay. The computer code of the *SWM* was used to analyze the presented case histories.

3 DATABASE AND SOIL PARAMETERS

The database gathered for this study includes the reported case histories from 23 sites with 45 laterally loaded, free-head, single driven piles in cohesionless soils including 19 H piles (*HP*) at 11 sites, 20 pipe piles (*PP*) at 8 sites, and 6 precast-prestressed-concrete piles (*PPCP*) at 4 sites.

The case histories were selected only if they had load-settlement curves that extend at least beyond the serviceability criteria of 38.2 mm [30]. The pile length, the size, and the eccentricity of the applied load and the ground-water table (*GWL*) are summarized in Table 2. Detailed information about each loaded test pile was given in Gurbuz [2].

For the majority of the case histories, most of the boring logs contained the Standard Penetration Test blow counts (*SPT-N*) that were the only in-situ soil-property measurement. With the aim of maintaining consistency to the best possible extent, whenever *SPT-N* values were available, they were used to establish the soil parameters

Table 2. Database for laterally loaded free-head single piles and a general description of the soil.

Pile type	Counter No	Volume No	Pile Site	Pile No	Pile Size (mm x mm)	Embedded length (L_p) (m)	Eccentricity (e) (m)	GWL (m)
H Pile	1	1	1	14	310×110	14.9	0.3	-
H Pile	2	1	1	15	310×110	15.2	0.3	-
H Pile	3	2	2	13	310×110	18.4	0.3	-
H Pile	4	3	3	2	250×62	7.4	0.3	-
H Pile	5	3	3	3	250×62	7.3	0.3	-
H Pile	6	3	4	2	250×62	10.1	0.3	-
H Pile	7	3	4	3	250×62	9.7	0.3	-
H Pile	8	45	21	6	360×108	23.0	0.3	1.6
H Pile	9	45	35	5	310×110	27.6	0.3	9.0
H Pile	10	45	37	3	310×79	14.5	0.6	1.5
H Pile	11	45	37	4	310×79	39.0	0.3	1.5
H Pile	12	45	37	5	310×79	31.2	0.3	1.5
H Pile	13	45	37	6	310×110	14.5	0.4	1.5
H Pile	14	45	37	7	310×110	45.3	0.3	1.5
H Pile	15	45	37	8	310×110	30.9	0.3	1.5
H Pile	16	45	39	2	310×110	25.5	0.2	3.0
H Pile	17	45	40	2	310×110	24.5	0.2	5.0
H Pile	18	45	41	2	310×110	19.5	0.2	7.6
H Pile	19	84	BOC	P10	310×110	21.3	0.9	0.5
PP CE	20	2	2	8	323.85×9.53	18.3	0.3	-
PP CE	21	2	2	10	323.85×9.53	18.3	0.3	-
PP OE	22	29	-	PP	406.40×12.70	20.4	0.3	-
PP CE	23	45	35	6	324.10×6.30	27.4	0.2	6.9
PP CE	24	45	39	3	324.10×6.30	25.4	0.2	3.8
PP CE	25	45	40	3	324.10×6.30	17.2	0.2	5.0
PP OE	26	FHWA	4	1	475.20×6.35	24.4	0.3	-
PP OE	27	FHWA	4	2	457.20×6.35	24.4	0.3	-
PP OE	28	88	1	A	609.60×19.05	10.1	0.5	4.7
PP OE	29	88	1	B	609.60×19.05	8.6	0.5	4.7
PP OE	30	88	1	C	609.60×19.05	8.5	0.4	4.7
PP OE	31	88	1	D	609.60×19.05	9.8	0.4	4.7
PP OE	32	88	1	M	609.60×19.05	9.1	0.5	4.7
PP OE	33	88	1	P	609.60×19.05	9.1	0.5	4.7
PP OE	34	88	1	R	609.60×19.05	8.5	0.4	4.7
PP OE	35	88	1	T	609.60×19.05	8.5	0.4	4.7
PP OE	36	88	1	U	609.60×19.05	8.5	0.3	4.7
PP OE	37	88	1	W	609.60×19.05	8.5	0.4	4.7
PP OE	38	88	3	C	1066.80×19.05	30.6	0.6	2.1
PP OE	39	88	3	H	1066.80×19.05	30.6	0.6	2.1
PPC S	40	55	A	24E	609.60×609.60	16.3	4.9	4.3
PPC S	41	55	A	24W	609.60×609.60	16.6	4.9	4.3
PPC S	42	55	B	30EM	762.00×762.00	13.1	4.7	4.3
PPC S	43	55	B	30	762.00×762.00	13.7	4.7	4.3
PPC S	44	RI	1	PPC1	355.60×355.60	27.0	0.4	3.1
PPC S	45	RI	2	PPC3	355.60×355.60	35.7	0.6	3.1

H: H pile, OE: open-ended piles, CE: close-ended piles, ϕ: diameter, S: square

Table 3. Correlations of the soil parameters from the Standard Penetration Test (*SPT-N*) blow counts.

	Property	Correlation	Reference
Cohesionless Soil	Internal friction angle	$\phi(°) = 27.1 + 0.3 \times (N_1)_{60} - 0.00054[(N_1)_{60}]$	Peck et al., [34]
	Corrected SPT value	$(N_1)_{60} = \left(\frac{P_a}{\sigma'}\right)^{0.5} \times N$	Liao and Whitman [35]
	Soil modulus of elasticity	$E_s/P_a = 200 \times \ln(N_{60})$ N≤ 60	Present study

following the relevant procedures used in the LRFD calibration of Deep Foundations, NCHRP Report 507 [31]. A detailed development of the soil parameters was outlined in the work carried out by Gurbuz [2]. Reported well-known equations for determining the soil properties in this study, also used by many researches around the world, are presented in Table 3.

4 ANALYSES OF THE METHODOLOGY AND RESULTS

The failure load of a laterally loaded pile cannot be easily defined by a predefined limit unless the pile fails structurally. As such, the serviceability of bridges, which deals with the functionality and service requirements of a structure to ensure adequate performance under expected conditions, is defined, among other ways, by the maximum possible lateral displacement. AASHTO [32] and previous specifications are based on Moulton [33], limiting the total lateral displacement of bridge substructures to 38.2 mm and, if combined with vertical displacement, to 25.4 mm (Paikowsky and Lu, 2006). The case histories were selected only if they had load-settlement curves that extend at least beyond the serviceability criteria of 38.2 mm [30]. Subsequently, 45 free-head, single, full-scale pile tests in cohesionless soils from 23 sites were examined for a displacement up to 63.5 mm at 12.7 mm intervals, while the analysis results of the Broms' method were compared with the p-y curves and the *SWM*.

The accuracy level in the prediction of P_{cal} over P_{msd} at a given displacement for each of the individual laterally loaded piles in this study is represented in terms of the bias value (λ_i), the mean of the bias (λ_m) and the coefficient of variation ($COV = \mu$). λ_i, λ_m, the standard deviation (σ), and the *COV*, which were calculated from the ratios of P_{msd} to P_{cal} at the same vertical load for a given number of tests (N) to ascertain the performance levels of the calculated loads from the analyses methods at a given lateral displacement as follows:

$$\lambda = \frac{P_{msd}}{P_{cal}} \qquad (7)$$

$$\lambda_m = \frac{\sum \lambda_i}{N} \qquad (8)$$

$$\sigma = \sqrt{\frac{1}{N-1}\sum_1^N \left(\lambda_i - \lambda_m\right)^2} \qquad (9)$$

$$COV = \frac{\sigma}{\lambda_m} \qquad (10)$$

The most important parameter that has been extensively studied by researchers is the coefficient of the horizontal subgrade reaction (n_h) for Broms' method, nevertheless, there has only been limited full-scale field verification for it. Accordingly, 45 free-head, single, full-scale pile tests in cohesionless soils from 23 sites were examined mostly via the approach seeking the performance level in the calculation of P_{calc} required to induce a displacement from 12.7 to 63.5 mm at 12.7 mm intervals with P_{msd} at the same displacements using Broms' method [14,15 and 16] with constant values of n_h. Then, the analysis results of Broms' method were compared with both the analyses results of the p-y curves [17 and 18] and the *SWM* [19,20 and 21]. The predictions of P_{calc} required to induce displacements with P_{msd} at the same displacements for the pile cases in cohesionless soils from the analyses methods of Broms with constant values of n_h, the p-y curves and the *SWM* were calculated and the analysis results of the three methods are presented in Table 4 in terms of λ_m and *COV*. The interpreted results show that the values of λ_m for the p-y curves and the *SWM* decrease almost linearly and later stabilize around 1.0; however, the λ_m of Broms' method declines drastically and becomes less than 1.0 for the analyzed pile types as the pile's top displacement increases. The differences in λ_m between the Broms' method and the two aforementioned methods are in the range 7 % to 57% due to the implemented constant values of n_h into the analyses of Broms' method.

Based on the analysis results of Broms' method in Table 4, it can be concluded that Broms' method needs a calibration for the constant values of n_h, which are independent of the pile's top displacement. in Table 1. Hence, the cases of 45 laterally loaded free head of single piles in cohesionless soils were re-analyzed to assess the modified coefficients of the subgrade reaction (n_h*) which were sensitive to the pile's displacement, while the bias

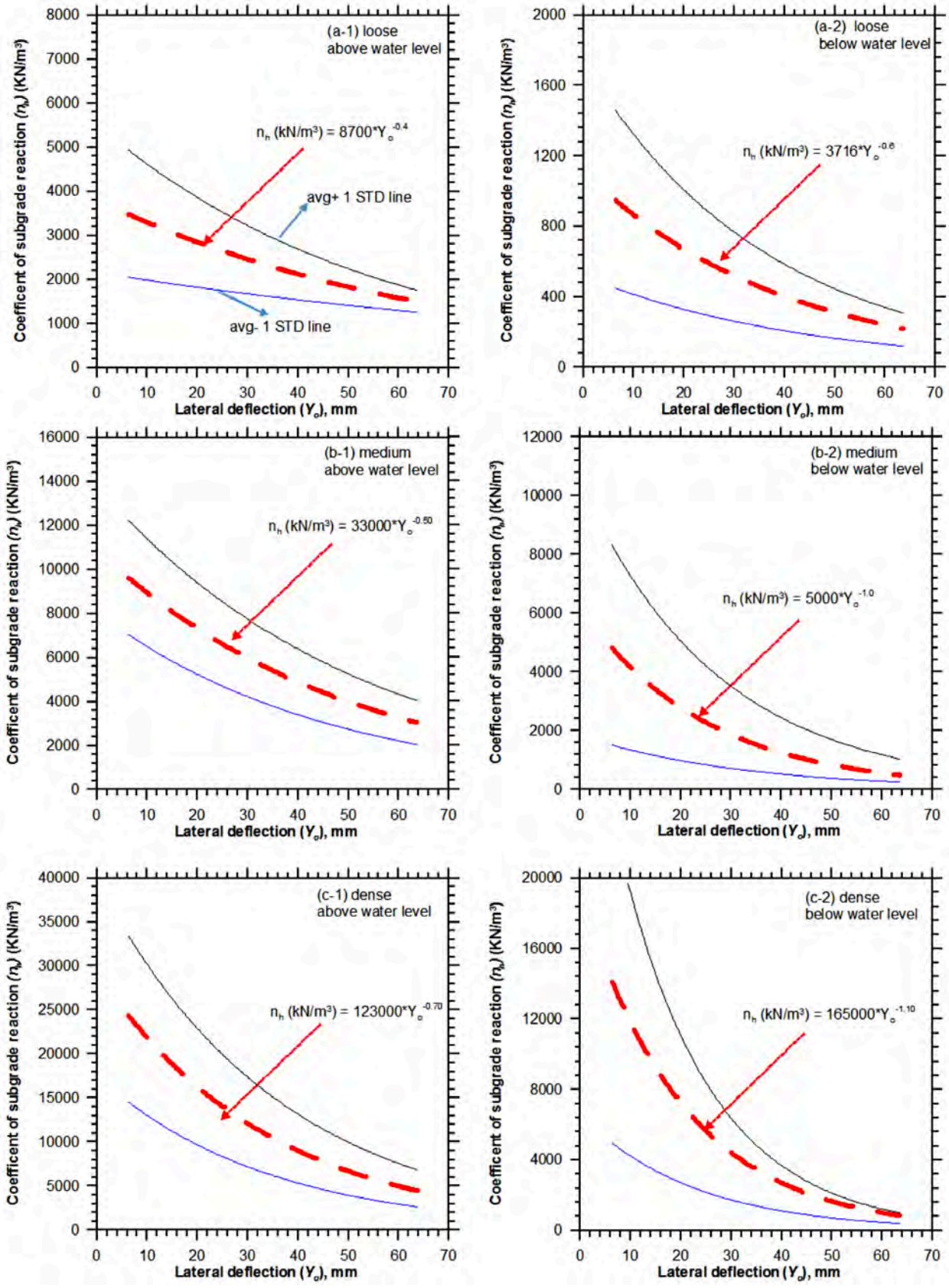

Figure 1. Calculated coefficient of subgrade reaction for:
(a) loose soil, (b) medium soil, (c) dense soil located either above the *GWL* or below the *GWL*.

Table 4. Summary of the statistics associated with the evaluation of the lateral displacement of the pile types using the methods of analysis for all the pile types.

Pile Type	Analysis method	Pile Top Lateral Deflection (mm)									
		12.7		25.4		38.1		50.8		63.5	
		λm	μ	λm	μ	λm	μ	λm	μ	λm	μ
HP	p-y	0.993	0.266	1.031	0.261	1.026	0.256	1.021	0.177	1.034	0.165
	Broms	1.105	0.245	0.927	0.255	0.812	0.292	0.648	0.164	0.591	0.192
	SWM	0.944	0.250	0.985	0.224	0.984	0.224	0.945	0.196	0.946	0.188
PP	p-y	1.121	0.295	1.077	0.277	1.094	0.238	0.981	0.283	1.053	0.229
	Broms	1.179	0.197	0.929	0.173	0.805	0.173	0.805	0.231	0.715	0.134
	SWM	1.021	0.385	1.000	0.358	0.995	0.319	0.979	0.418	1.252	0.274
PPC	p-y	1.536	0.244	1.211	0.165	1.065	0.139	0.981	0.119	0.908	0.119
	Broms	1.127	0.156	0.788	0.185	0.616	0.132	0.525	0.107	0.447	0.111
	SWM	1.889	0.156	1.504	0.104	1.310	0.093	1.212	0.094	1.132	0.101

value (λ_i) of each pile case for the ratios of P_{msd} to P_{cal} at a given pile's top displacement was assumed to be equal to one. The back calculations of the values of n_h* with one standard deviation from the back analyses of Broms' method for loose, medium and dense cohesionless soils under both above and below *GWL* are plotted in Figure 1. The determined equations yield to average values of n_h* with the function of the displacement are furnished in the following equations 11 through 16.

$$n_h^*(\text{kN/m}^3)=8700^*Y_0^{-0.40} \text{ for loose soils above } GWL \quad (11)$$

$$n_h^*(\text{kN/m}^3)=3716^*Y_0^{-0.60} \text{ for loose soils below } GWL \quad (12)$$

$$n_h^*(\text{kN/m}^3)=33000^*Y_0^{-0.50} \text{ for medium dense soils above } GWL \quad (13)$$

$$n_h^*(\text{kN/m}^3)=5000^*Y_0^{-1.00} \text{ for medium dense soils below } GWL \quad (14)$$

$$n_h^*(\text{kN/m}^3)=123000^*Y_0^{-0.70} \text{ for dense soils above } GW \quad (15)$$

$$n_h^*(\text{kN/m}^3)=165000^*Y_0^{-1.10} \text{ for dense soils below } GWL \quad (16)$$

The database of 45 laterally loaded, free-head driven, single piles in cohesionless soils was re-used for the prediction of P_{cal} required to induce the displacement from 12.5 mm to 63.5 mm at 12.7 mm intervals with P_{msd} measured at the same displacement using Broms' method with both values of the n_h* (Fig. 1 ,and equation 11 through 16) and n_h in Table 1. The analysis results for all the pile types obtained from Broms' method with values of both n_h and n_h* were compared with the analysis results of the p-y curve and the *SWM* and presented in Figure 2. The analysis results of the pile cases showed that the λ_m of Broms' method stabilized around 1.0 for all the pile types for any given displacement if the values of n_h* were employed in the analyses of Broms' method.

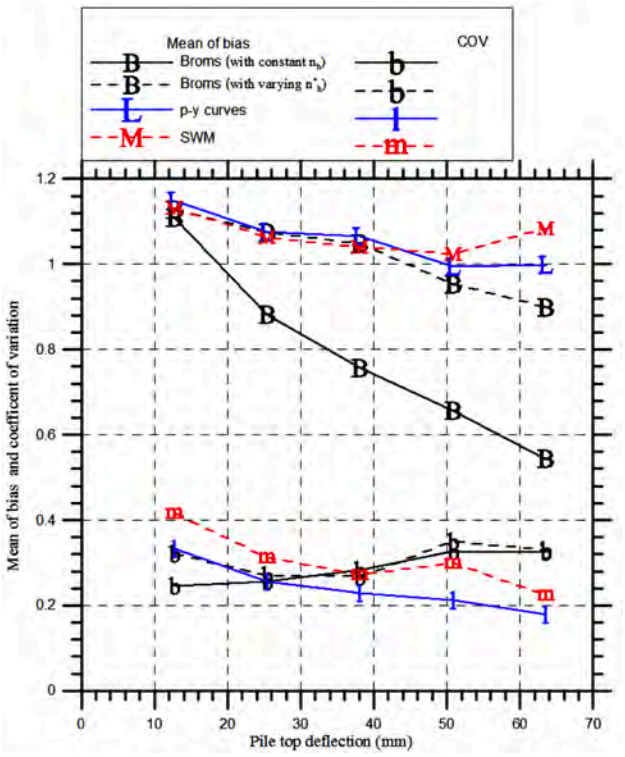

Figure 2. Mean of the bias and the coefficient of variation of the ratio between the measured and calculated load from the analyses methods for all the pile types together as the pile's top displacement varies between 12.5 to 63.5 mm.

5 SUMMARY AND CONCLUSIONS

A precise calculation of the load capacity for a given pile's top displacement is vital for the design of laterally loaded piles. The load capacities of laterally loaded piles in this study at a given displacement were

easily calculated using Broms' method with constant values of the coefficient of the subgrade reaction (n_h). Nevertheless, it was determined that Broms' method typically overemphasizes the pile's lateral load capacity due to an implementation of the constant values of n_h into analyses of Broms' method, nevertheless the pile's displacement increases. Hence, modifications to the values of the coefficient of the subgrade reaction (n_h*) in cohesionless soils that vary with a pile's top displacement are proposed and improved the performance level of the Broms' method for the prediction of a lateral load at the pile's top displacement. Therefore, the overall behavior of all the piles is analyzed by Broms' method with the modified coefficient of the subgrade reactions (n_h*) yielded to the mean of the bias value of 1 at a given lateral displacement up to 63.5 mm of a pile top's displacement. It is demonstrated that Broms' method with n_h* can correctly estimate the pile's lateral load-deflection behavior at accuracy levels similar to both the p-y curve method and the Strain Wedge Method.

Acknowledgment

The authors would like to extend their appreciations to many individuals: Mary Canniff, Lymon Reese, Shin-Tower Wang, Gary Norris, Mohamed Ashour, Seda Yesilmen, Samuel Paikowsky and Halil Ozok for their help and contributions in any way.

REFERENCES

[1] Terzaghi, K. 1955. Evaluation of coefficient of subgrade reaction. Geotechnique 5, 4, 297-326.

[2] Gurbuz, A. 2007. The Uncertainty in displacement evaluation of deep foundations. PhD Dissertation, University of Massachusetts at Lowell, Lowell, Massachusetts.

[3] Alizadeh, M., Davisson, M.T. 1970. Lateral load tests on piles-Arkansas River project. Journal of the Soil Mechanics and Foundation Divisions 96, 5, 1583-1603.

[4] Davisson, M.T., Salley, J. R. 1970. Model study of laterally loaded piles, ASCE Journal of Soil Mechanics and Foundation Divisions 96, 5, 1605-1627.

[5] Kumar, S., Alizadeh, M., Lalvani, L. 2000. Lateral load-deflection response of single piles in sand. Electronic Journal of Geotechnical Engineering 5.

[6] Gurbuz, A. 2011. Determination of lateral displacements of laterally loaded steel piles in cohesionless soils using elastic curve equations. Journal of Faculty of Engineering and Architecture Gazi Univ. 26, 1, 205-212.

[7] Yamaguchi, E., Kikuchi, Y., Kubo, Y. 1999. Fundamental study of finite element analysis of piles modeled by elastic subgrade-reaction method. Journal Structural Engineering 45, 35–42 (in Japanese).

[8] Honjo, Y., Zaika, Y., Pokharel, G. 2005. Estimation of subgrade reaction coefficient for horizontally loaded piles by statistical analyses. Soils and Foundations 45, 3, 51-70. DOI: https://doi.org/10.3208/sandf.45.3_51

[9] Kobayashi, N., Shibata, T., Kikuchi, Y., Murakam, A. 2008. Estimation of horizontal subgrade reaction coefficient by inverse analysis. Computers and Geotechnics 35, 616-626. DOI: 10.1016/j.compgeo.2007.11.002

[10] Guo, W.D. 2008. Laterally loaded rigid piles in cohesionless soil. Canadian Geotechnical Journal 45, 5, 676-697. DOI: 10.1139/T07-110

[11] Guo, W.D. 2013. Simple model for nonlinear response of fifty-two laterally loaded piles. ASCE Journal of Geotechnical and Geoenvironmental Engineering 139, 2, 234-252. DOI: 10.1061/(ASCE) GT.1943-5606.0000726

[12] Lee, J., Kim, M., Kyung, D. 2010. Estimation of lateral load capacity of rigid short piles in sands using CPT results. ASCE Journal of Geotechnical and Geoenvironmental Engineering 136, 1, 48-56. DOI: 10.1061/(ASCE)GT.1943-5606.0000199

[13] Qin, H.Y., Guo, W.D. 2014. Nonlinear response of laterally loaded rigid piles in sand. Geomechanics and Engineering 7, 6, 679-703. DOI: http://dx.doi.org/10.12989/gae.2014.7.6.679

[14] Broms, B. 1964a. Lateral resistance of piles in cohesionless soils. ASCE Journal of the Soil Mechanics and Foundations Division 90, 3, 123-158.

[15] Broms, B. 1964b. Lateral resistance of piles in cohesive Soils. ASCE Journal of the Soil Mechanics and Foundations Division 90, 2, 27-63.

[16] Broms, B. 1965. Design of laterally loaded piles. ASCE Journal of the Soil Mechanics and Foundations Division 91, 3, 79-99.

[17] Matlock, H. 1970. Correlations for design of laterally loaded piles in soft clay. Proceedings, Second Annual Off-Shore Technology Conference, Houston, Texas, Vol. 1, pp. 577-594.

[18] Reese, L.C. 1977. Laterally loaded piles: program documentation. ASCE Journal of Geotechnical Engineering Division 103, 4, 287-305.

[19] Norris, G.M. 1986. Theoretically based BEF laterally loaded pile analysis. Proc., 3rd Int. Conf. on Numerical Methods in Offshore Piling, TECHNIP Ed., Paris, pp. 361-386.

[20] Ashour, M., Norris, G., Piling, P. 1998. Lateral loading of a pile in layered soil using the Strain Wedge Model. ASCE Journal of Geotechnical and Geoenvironmental Engineering 124, 4, 303-315. DOI: 10.1061/(ASCE)1090-0241(1998)124:4(303)
[21] Ashour, M., Norris, G., Piling, P. 2002. Strain Wedge Model capability of analyzing behavior of laterally loaded isolated piles, drilled shafts, and pile Group. ASCE Journal of Bridge Engineering 7, 4, 245-254. DOI: 10.1061/(ASCE)1084-0702(2002)7:4(245)
[22] McClelland, B., Focht, J.A. 1958, Soil modulus of laterally loaded piles. ASCE Transaction 123(1), 1049-1063.
[23] Duncan, J.M., Evans Jr., L.T., Ooi, P.S.K. 1994. Lateral Load Analysis of Single Piles and Drilled Shafts. ASCE Journal of Geotechnical Engineering 120, 6, 1018-1033.
[24] Winkler, E. 1867. Theory of Elasticity and Strength. Prague: H. Dominicus (in German).
[25] Matlock, H., Reese, L.C. 1960. Generalized Solutions for Laterally Loaded Piles. ASCE Journal of Soil Mechanics and Foundation Division 86, 5, 63-91.
[26] Prakash, S., Sharma, H.D. 1990. Pile Foundations in Engineering Practice. John Wiley and Sons, NY.
[27] Poulos, H.G., Davis, E.H. 1990. Pile Foundation Analysis and Design, 2nd Edition, Robert E. Krieger Publish Company, Malabar, Florida.
[28] Reese, L.C. 1984. Handbook on Design of Piles and Drilled Shafts Under Lateral Load. FHWA Report Publication FHWA-IP-84/11, US Department of Transportation, Washington, DC.
[29] Reese, L.C. 1985. Documentation of Computer Program LPILE, Ensoft Inc., Austin, Texas.
[30] Paikowsky, S., Lu, Y. 2006. Establishing serviceability limit state in the design of bridge foundations. Proceedings of Sessions of Geoshanghai, Foundation Analysis and Design Innovative Methods. ASCE Geotechnical Special Publication No.153, 49-58, Shanghai, China. DOI:10.1061/40865(197)6
[31] Paikowsky, S., Birgisson, B.J., McVay, M., Nguyen, T., Kuo, C., Baecher, G., Ayyup, B., Stenersen, K., O'Malley, K., Chernasuskas, L., O'Neill, M. 2004. Load and Resistance Factor Design (LRFD) for Deep Foundations. NCHRP Report 507, Transportation Research Board, National Research Council, Washington, DC.
[32] AASHTO, 2006. LRFD Bridge Design Specifications, Section 10: Foundations, American Assoc. of State Highway & Transportation Officials, Washington, DC.
[33] Moulton, L.K. 1986, Tolerable movement criteria for highway bridges. FHWA Report no. FHWA-TS-85-228, March, Washington, DC, pp. 93.
[34]. Peck, R.P., Hanson, W.E., Thornburn, T.H. 1974. Foundation Engineering, 2nd Edition, John Wiley and Sons, Inc., New York.
[35]. Liao, S.C., Whitman, R.V. 1986. Overburden correction factors for SPT in sand. ASCE Journal of Geotechnical Engineering 112, 3, 373-377. DOI:10.1061/(ASCE)0733-9410(1986)112:3(373)

SPLOŠNA ANALITIČNA REŠITEV ENODIMENZIONALNE KONSOLIDACIJE ZA NEZASIČENE ZEMLJINE PRI RAZLIČNIH OBTEŽNIH POGOJIH

Jiwei Li
Taizhou University,
College of Civil Engineering and Architecture,
Institute of Coastal Environment and Geotechnical Engineering
Taizhou, Zhejiang 318000, Kitajska
E-pošta: iamliji_007@126.com

Chinese Academy of Sciences,
Institute of Rock and Soil Mechanics,
State Key Laboratory of Geomechanics and Geotechnical Eng.
Wuhan, Hubei 430071, Kitajska

Changfu Wei
Chinese Academy of Sciences,
Institute of Rock and Soil Mechanics,
State Key Laboratory of Geomechanics and Geotechnical Eng.
Wuhan, Hubei 430071, Kitajska
E-pošta: cfwei@whrsm.ac.cn

Yanlin Zhao
Guangxi University,
College of Civil Engineering and Architecture
Nanning, Guangxi 530004, Kitajska
E-pošta: paperyantu@126.com

Ključne besede

enodimenzionalna konsolidacija; nezasičena zemljina; analitična rešitev; časovno odvisna obremenitev

Izvleček

V članku je predstavljena splošna analitična rešitev za enodimenzionalno konsolidacijo nezasičene zemljine v različnih časovno odvisnih obtežnih pogojih, ki temelji na metodi diferencialne transformacije (DTM). Zlasti so dobljene analitične rešitve za različna razmerja med koeficienti v vodilnih enačbah za konsolidacijo nezasičenih zemljin. Tehnika razširitve Fourierjeve vrste je spremenjena tako, da upošteva tako kontinuirano diferencialno obtežbo, kot tudi periodično posamično obtežbo. Primerjava med rezultati predlagane rešitve in obstoječe teoretične rešitve kaže, da predlagana rešitev daje odlične rezultate, medtem ko je enostavno dobiti analitično rešitev konsolidacije nezasičenih zemljin. Ugotovljeno je bilo tudi, da lahko razlike v koeficientih v vodilnih enačbah znatno vplivajo na disipacijo tako pornega zračnega nadtlaka kot tudi pornega vodnega nadtlaka, čeprav so velikosti njihovih variacij različne.

A GENERAL ANALYTICAL SOLUTION TO THE ONE-DIMENSIONAL CONSOLIDATION PROBLEM FOR UNSATURATED SOIL UNDER VARIOUS LOADING CONDITIONS

Jiwei Li
Taizhou University,
College of Civil Engineering and Architecture,
Institute of Coastal Environment and Geotechnical Engineering
Taizhou, Zhejiang 318000, P. R. China
E-mail: iamliji_007@126.com

Chinese Academy of Sciences,
Institute of Rock and Soil Mechanics,
State Key Laboratory of Geomechanics and Geotechnical Eng.
Wuhan, Hubei 430071, P. R. China

Changfu Wei
Chinese Academy of Sciences,
Institute of Rock and Soil Mechanics,
State Key Laboratory of Geomechanics and Geotechnical Eng.
Wuhan, Hubei 430071, P. R. China
E-mail: cfwei@whrsm.ac.cn

Yanlin Zhao
Guangxi University,
College of Civil Engineering and Architecture
Nanning, Guangxi 530004, P. R. China
E-mail: paperyantu@126.com

Keywords
one-dimensional consolidation problem; unsaturated soil; analytical solution; time-dependent loading

DOI https://doi.org/10.18690/actageotechslov.15.1.87-99.2018

Abstract

A general analytical solution is developed for the one-dimensional consolidation problem of unsaturated soil under various time-dependent loading conditions based on a differential transformation method (DTM). In particular, analytical solutions are obtained for different relationships between the coefficients in the governing equations for unsaturated soil consolidation. The Fourier series expansion technique is adopted to account for both the continuous differentiable loading and the periodic piecewise loading. A comparison between the results of the current solution and the existing theoretical solution indicates that the proposed solution yields excellent results, while it is straightforward to obtain the analytical solution of the unsaturated consolidation problems. It was also found that the variations in the coefficients in the governing equations can significantly influence the dissipation of both the excess pore-air pressure and the excess pore-water pressure, though the magnitudes of their variations are different.

1 INTRODUCTION

The subsidence induced by the consolidation (or compression) of unsaturated soil under environmental loadings is a subject of great interest in geotechnical engineering practice [1]. Several consolidation models for unsaturated soils have been proposed since 1960. Early contributions include those by Blight [2], Scott [3] and Barden [4]. Perhaps the most popular consolidation model for unsaturated soils is the one proposed by Fredlund and Hasan [5], in which two partial differential equations are employed to describe the dissipation of the pore pressures. Due to its nonlinear nature, it is generally difficult to obtain analytical solutions for the consolidation problem associated with unsaturated soil, and thus most of the existing solutions are numerical [5-7]. Compared with its numerical counterpart, an analytical solution, if available, is much simpler and more robust, providing an exact solution for the verification of computer codes and semi-analytical solutions.

Thus far, several efforts have been made to develop analytical solutions to the consolidation problem for unsaturated soil. Using the Laplace transform and the analytical inverse Laplace transform, Qin et al. [8] obtained an analytical solution for the consolidation of a single-layer unsaturated soil subjected to stepwise loading. In this problem, the boundary conditions for the water and air phases are permeable on one side of the surfaces, and impermeable on the other. Adopting the same method, Qin et al. [9] derived another analytical solution in the time domain, in which the external load-

ing exponentially varies with the time. Using the variable-separation method, Shan et al. [10] derived an exact solution to the governing equations for the one-dimensional consolidation of single-layer unsaturated soil. It should be noted that the expressions for the theoretical solutions mentioned above are complicated, so that it is generally difficult to use them. As a result, these analytical solutions have not been extensively applied in practice.

Ho et al. [11] obtained an analytical solution using the techniques of eigenfunction expansion and Laplace transformation. In their solutions the temporal change of the total pressure is assumed to be constant. Afterwards, adopting the same method, they derived a series of analytical solutions subjected to different types of external loadings for one-dimensional consolidation [12], 2D plane-strain consolidation [13] and axisymmetric consolidation [14-15] of an unsaturated soil. By considering time-dependent loading under various initial and boundary conditions, Zhou and Zhao [16] obtained an analytical solution for the one-dimensional consolidation of unsaturated soils by introducing two new state variables. However, this solution was developed without considering the correlations among the equation coefficients. In fact, all these coefficients are related to the properties of the soil. It is therefore important to reveal the relationship between the equation coefficients and the solutions. Conte and Troncone [17] developed an analytical solution for the one-dimensional consolidation problem of soils subjected to arbitrarily variable loading. However, this solution does not take into account the effect of the pore-air flow.

Despite their own merits, all the above-mentioned solutions suffer from the following two shortcomings: I) their solution procedures are very much involved so that these solutions are generally difficult to apply in practice, and II) the relationships between the equation coefficients and the solutions are not well defined. In addition, although some specific time-dependent loading has been addressed in these solutions, an analytical solution to the problem under a general loading condition, such as cyclic loading and periodic piecewise loading, has yet to be developed.

In this paper, on the basis of a differential transform method (DTM) and the Fourier series expansion techniques, a comprehensive analytical solution for Fredlund and Hasan's consolidation model subjected to loading described by an arbitrary function of time is presented within this context. Based on these solutions, the consolidation of the single-layer unsaturated soil subjected to arbitrary external loading is studied. The exact solutions are validated and the consolidation characteristics of the unsaturated soil are discussed by analyzing several examples.

2 GOVERNING EQUATIONS

Without loss of generality, it is assumed hereinafter that 1) an isothermal condition and homogeneous soil condition prevail in the spatial domain of concern, 2) the deformation of the soil matrix is linear elastic and infinitesimal, 3) both the solid material and the pore water are incompressible, 4) the pore gas is an ideal gas and continuous, 5) the coefficients of permeability with respect to water and air, and the volume change moduli remain constant during the transient processes, and 6) the effects of air diffusing through the water and the movement of the water vapor are ignored. The governing equations for the consolidation equation of the unsaturated soils was originally proposed by Fredlund and Hasan [5], and later modified for different applications. For a one-dimensional consolidation problem associated with unsaturated soil, which is subjected to infinitely distributed forces on the boundary (Fig. 1), the governing equations can be simplified as

$$\frac{\partial u_{\mathrm{w}}}{\partial t}+C_{\mathrm{w}}\frac{\partial u_a}{\partial t}+C_w^{\sigma}\frac{d\sigma}{dt}=C_V^{\mathrm{w}}\frac{\partial^2 u_{\mathrm{w}}}{\partial z^2} \tag{1a}$$

$$\frac{\partial u_a}{\partial t}+C_a\frac{\partial u_{\mathrm{w}}}{\partial t}+C_a^{\sigma}\frac{d\sigma}{dt}=C_V^{a}\frac{\partial^2 u_a}{\partial z^2} \tag{1b}$$

where

$$C_w=\frac{1-m_2^w/m_{1k}^w}{m_2^w/m_{1k}^w},\ C_V^w=\frac{k_w}{\gamma_w m_2^w},\ C_w^{\sigma}=\frac{m_{1k}^w}{m_2^w}$$

$$C_a=\frac{m_2^a}{m_{1k}^a-m_2^a-(1-S_r)n_r u_{atm}/(\bar{u}_a^0)^2}$$

$$C_V^a=k_a\frac{RT_{tem}}{g\bar{u}_a^0 M_a(m_{1k}^a-m_2^a-(1-S_r)n_r u_{atm}/(\bar{u}_a^0)^2)}$$

$$C_a^{\sigma}=\frac{m_{1k}^a}{m_{1k}^a-m_2^a-(1-S_r)n_r u_{atm}/\bar{u}_a^0}$$

u_w and u_a are the unknown excess pore-water pressure and the excess pore-air pressure, respectively; σ is the total vertical stress that is a function of the time; m_{1k}^w is the coefficient of the water volume change with respect to the change in the net normal stress (σ–u_a); m_2^w is the coefficient of the water volume change with respect to the change in the matric suction (u_a– u_w), m_{1k}^a is the coefficient of the air volume change with respect to the change of the net normal stress; and m_2^a is the coefficient of the air volume change with respect to the change in the matric suction. Subscript k stands for the K_0-loading condition (i.e., zero lateral deformation); k_w is the water permeability in the unsaturated soil, which is assumed to be constant during the consolidation; γ_w is the density of the water phase; k_a is the air conductivity; $\bar{u}_a^0=u_a^0+u_{atm}$; R is the universal air constant; T_{tem} is the absolute

temperature; M_a is the average molecular mass of the air phase; u_a^0 is the initial excess air pressure; u_{atm} is the atmospheric pressure; S_r is the degree of saturation; and n_r is the porosity.

The initial conditions and boundary conditions, respectively, are given by

$$u_a(z,0) = u_a^0,\ u_w(z,0) = u_w^0 \tag{2}$$

$$u_a(0,t) = 0, u_w(0,t) = 0 \tag{3a}$$

$$\frac{\partial u_a(H,t)}{\partial z} = 0, \frac{\partial u_w(H,t)}{\partial z} = 0 \tag{3b}$$

where, u_a^0 and u_w^0 are the initial excess air and water pressures (at $t = 0$), respectively. It should be noted that for the situations in which the lower surface of the soil layer is also permeable like the upper surface (i.e., double-drainage condition), the boundary condition given by $\frac{\partial u_a(H,t)}{\partial z} = 0, \frac{\partial u_w(H,t)}{\partial z} = 0$ has to be imposed in the middle of the layer (at $z = H/2$). In other words, the results for the single drainage condition can be adopted to determine the solution for the double drainage condition by interpreting H as the drainage height.

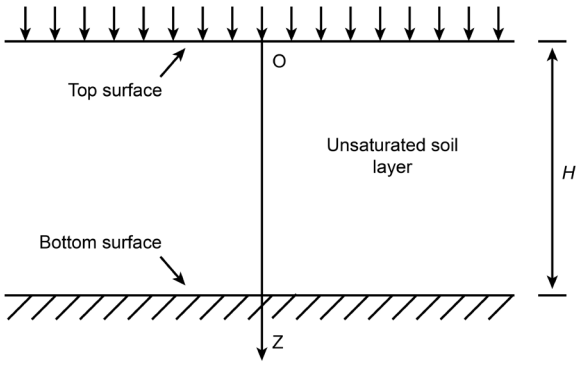

Figure 1. One-dimensional consolidation in unsaturated soils.

Using the same procedure as Conte and Troncone [17], the general loading function $\sigma(t)$ can be expanded into a larger number M of harmonic components using the Fourier series, provided that $\sigma(t)$ is a periodic function satisfying Dirichlet's conditions in the interval $(0,T)$. Namely, we have

$$\sigma(t) = \frac{a_0}{2} + \sum_{k=1}^{M}[a_k \cos(w_k t) + b_k \sin(w_k t)] \tag{4}$$

where the amplitudes a_k and b_k associated with the frequency $w_k = 2k\pi/T$ (with $k = 1, 2, 3$ ...) are provided, respectively, by

$$a_k = \frac{2}{T}\int_0^T \sigma(t)\cos(w_k t)dt \tag{5}$$

$$b_k = \frac{2}{T}\int_0^T \sigma(t)\sin(w_k t)dt \tag{6}$$

T is the period of the $\sigma(t)$, and a_0 can be obtained from Eq. (5) by setting $w = 0$, i.e.,

$$a_0 = \frac{2}{T}\int_0^T \sigma(t)dt \tag{7}$$

3 ANALYTICAL SOLUTIONS

For convenience, Eq. (1) can be written in the following dimensionless forms:

$$\frac{\partial \upsilon_w}{\partial \tau} + C_1\frac{\partial \upsilon_a}{\partial \tau} + C_w^\sigma\frac{ds_1}{d\tau} = \frac{\partial^2 \upsilon_w}{\partial \xi^2} \tag{8a}$$

$$\frac{\partial \upsilon_a}{\partial \tau} + C_2\frac{\partial \upsilon_w}{\partial \tau} + C_a^\sigma\frac{ds_2}{d\tau} = C_3\frac{\partial^2 \upsilon_a}{\partial \xi^2} \tag{8b}$$

which are subjected to

$$\upsilon_a(\xi,0) = 1, \upsilon_w(\xi,0) = 1 \ \text{ in } 0 \le \xi \le 1 \tag{9}$$

$$\upsilon_a(0,\tau) = 0,\ \upsilon_w(0,\tau) = 0 \ \text{ in } \tau \ge 0 \tag{10a}$$

$$\frac{\partial \upsilon_a(1,\tau)}{\partial \xi} = 0,\ \frac{\partial \upsilon_w(1,\tau)}{\partial \xi} = 0 \tag{10b}$$

where

$$\upsilon_a = \frac{u_a}{u_a^0},\ \upsilon_w = \frac{u_w}{u_w^0}, s_1 = \frac{\sigma}{u_w^0}, s_2 = \frac{\sigma}{u_a^0}, \xi = \frac{z}{H} \tag{11a}$$

$$\tau = \frac{C_V^w t}{H^2}, C_1 = \frac{C_w u_a^0}{u_w^0}, C_2 = \frac{C_a u_w^0}{u_a^0}, C_3 = \frac{C_V^a}{C_V^w} \tag{11b}$$

3.1 Homogeneous cases

Under a constant surface traction, i.e., $d\sigma/dt = 0$, Eq. (8) ends up with the following homogeneous equations:

$$\frac{\partial \upsilon_w}{\partial \tau} + C_1\frac{\partial \upsilon_a}{\partial \tau} = \frac{\partial^2 \upsilon_w}{\partial \xi^2} \tag{12a}$$

$$\frac{\partial \upsilon_a}{\partial \tau} + C_2\frac{\partial \upsilon_w}{\partial \tau} = C_3\frac{\partial^2 \upsilon_a}{\partial \xi^2} \tag{12b}$$

which are subjected to

$$\upsilon_a(\xi,0) = 1, \upsilon_w(\xi,0) = 1 \text{ in } 0 < \xi < 1 \tag{13}$$

$$\upsilon_a(0,\tau) = 0,\ \upsilon_w(0,\tau) = 0 \text{ in } \tau > 0 \tag{14a}$$

$$\frac{\partial \upsilon_a(1,\tau)}{\partial \xi} = 0,\ \frac{\partial \upsilon_w(1,\tau)}{\partial \xi} = 0 \text{ in } \tau > 0 \tag{14b}$$

The differential transformation method (DTM) is an analytical method for solving integral equations, ordinary and partial differential equations. The method

provides the solution in terms of a convergent series with readily computable components, i.e., it is an iterative procedure for obtaining the analytical Taylor-series solutions of differential equations. Different applications of the DTM method can be found in [18-29]. Based on the DTM, we have

$$U_a(i,j)=\frac{1}{i!\,j!}\frac{\partial^{i+j}\upsilon_a(\xi,\tau)}{\partial\xi^i\partial\tau^j}\Big|_{(0,0)} \tag{15a}$$

$$U_w(i,j)=\frac{1}{i!\,j!}\frac{\partial^{i+j}\upsilon_w(\xi,\tau)}{\partial\xi^i\partial\tau^j}\Big|_{(0,0)} \tag{15b}$$

The corresponding function can be expressed as

$$\upsilon_a(\xi,\tau)=\sum_{j=0}^{\infty}\sum_{i=0}^{\infty}U_a(i,j)\xi^i\tau^j \tag{15c}$$

$$\upsilon_w(\xi,\tau)=\sum_{j=0}^{\infty}\sum_{i=0}^{\infty}U_w(i,j)\xi^i\tau^j \tag{15d}$$

By substituting Eq. (15) into Eq. (12), we can derive

$$U_a(i,j+1)=\frac{C_2(i+1)(i+2)U_w(i+2,j)-C_3(i+1)(i+2)U_a(i+2,j)}{(j+1)(C_1C_2-1)} \tag{16a}$$

$$U_w(i,j+1)=\frac{C_1C_3(i+1)(i+2)U_a(i+2,j)-(i+1)(i+2)U_w(i+2,j)}{(j+1)(C_1C_2-1)} \tag{16b}$$

Accordingly, the initial condition, Eq. (13), can be rewritten as

$$\sum_{i=0}^{\infty}U_a(i,0)\xi^i=\frac{4}{\pi}\sum_{n=0}^{\infty}\frac{1}{2n+1}\sum_{k=0}^{\infty}\frac{(-1)^k}{(2k+1)!}\left(\frac{(2n+1)\pi\xi}{2}\right)^{2k+1} \tag{17a}$$

$$\sum_{i=0}^{\infty}U_w(i,0)\xi^i=\frac{4}{\pi}\sum_{n=0}^{\infty}\frac{1}{2n+1}\sum_{k=0}^{\infty}\frac{(-1)^k}{(2k+1)!}\left(\frac{(2n+1)\pi\xi}{2}\right)^{2k+1} \tag{17b}$$

which also implies that

$$U_a(i,0)=\frac{4}{\pi}\sum_{n=0}^{N}\frac{1}{2n+1}\frac{(-1)^{\frac{i-1}{2}}}{i!}\left(\frac{(2n+1)\pi}{2}\right)^i,\ i=1,3,5..... \tag{18a}$$

$$U_w(i,0)=\frac{4}{\pi}\sum_{n=0}^{N}\frac{1}{2n+1}\frac{(-1)^{\frac{i-1}{2}}}{i!}\left(\frac{(2n+1)\pi}{2}\right)^i,\ i=1,3,5..... \tag{18b}$$

where N is a large positive integer.

From the boundary conditions, Eqs.(14), we have

$$\sum_{j=0}^{\infty}U_a(0,j)\tau^j=0,\sum_{j=0}^{\infty}U_w(0,j)\tau^j=0 \tag{19a}$$

$$\sum_{j=0}^{\infty}\sum_{i=0}^{\infty}(i+1)U_a(i,j)\tau^j=0,\sum_{j=0}^{\infty}\sum_{i=0}^{\infty}(i+1)U_w(i,j)\tau^j=0 \tag{19b}$$

that is,

$$U_a(0,j)=0,U_w(0,j)=0 \tag{20}$$

$$\sum_{i=0}^{\infty}(i+1)U_a(i+1,j)=0,\sum_{i=0}^{\infty}(i+1)U_w(i+1,j)=0 \tag{21}$$

Substituting Eqs. (18) and Eq. (21) into Eq. (16), and using the recursive method, we can derive

$$U_a(i,j)=\frac{4}{\pi}\sum_{n=0}^{N}\frac{1}{2n+1}\frac{(-1)^{\frac{i-1+2j}{2}}}{i!}\frac{a_a(j)}{j!(C_1C_2-1)^j}\left(\frac{(2n+1)\pi}{2}\right)^{i+2j},$$
$$i=1,3,5..... \tag{22}$$

$$U_w(i,j)=\frac{4}{\pi}\sum_{n=0}^{N}\frac{1}{2n+1}\frac{(-1)^{\frac{i-1+2j}{2}}}{i!}\frac{a_w(j)}{j!(C_1C_2-1)^j}\left(\frac{(2n+1)\pi}{2}\right)^{i+2j}$$
$$i=1,3,5..... \tag{23}$$

where $a_w(j)$ and $a_a(j)$ satisfy the following recursive formula

$$a_w(j+1)=C_1C_3a_a(j)-a_w(j) \tag{24a}$$

$$a_a(j+1)=C_2a_w(j)-C_3a_a(j) \tag{24b}$$

where, $a_a(0)=a_w(0)=1$, $j=0, 1, 2...$

From Eqs. (24), it follows that

$$a_a(j)=\frac{(\lambda_1+1)(C_1C_3-\lambda_2-1)\lambda_1^j-(\lambda_2+1)(C_1C_3-\lambda_1-1)\lambda_2^j}{C_1C_3(\lambda_1-\lambda_2)} \tag{25}$$

$$a_w(j)=\frac{(C_1C_3-\lambda_2-1)\lambda_1^j-(C_1C_3-\lambda_1-1)\lambda_2^j}{\lambda_1-\lambda_2} \tag{26}$$

where λ_1 and λ_2 are the eigenvalues of the matrix $\mathbf{A}=\begin{pmatrix}-1 & C_1C_3\\ C_2 & -C_3\end{pmatrix}$.

Using Eq. (16) and Eqs. (20) and (21), we obtain

$$U_a(i,j)=0,i=0,2,4..... \tag{27}$$

$$U_w(i,j)=0,i=0,2,4.... \tag{28}$$

By the differential inverse transform of the two-dimensional DTM, it can be proven that

$$\upsilon_a(\tau,\xi)=\frac{4}{\pi}\sum_{n=0}^{N}\frac{1}{2n+1}\sum_{i=1,3,5...}\frac{(-1)^{\frac{i-1}{2}}}{i!}\left(\frac{(2n+1)\pi}{2}\xi\right)^i$$
$$\sum_{j=0}^{\infty}\frac{a_a(j)}{j!}\left[\frac{-((2n+1)\pi)^2}{4(C_1C_2-1)}\tau\right]^j \tag{29}$$

$$\upsilon_w(\tau,\xi)=\frac{4}{\pi}\sum_{n=0}^{N}\frac{1}{2n+1}\sum_{i=1,3,5...}\frac{(-1)^{\frac{i-1}{2}}}{i!}(\frac{(2n+1)\pi\xi}{2})^i \sum_{j=0}^{\infty}\frac{a_w(j)}{j!}[\frac{-((2n+1)\pi)^2}{4(C_1C_2-1)}\tau]^j \quad (30)$$

Note that the series expression of a sine function is:

$$\sin(x)=\sum_{i=1,3,5...}\frac{(-1)^{\frac{i-1}{2}}}{i!}x^i \ .$$

Hence Eqs. (29) and (30) can be rewritten as

$$\upsilon_a(\tau,\xi)=\frac{4}{\pi}\sum_{n=0}^{N}\frac{1}{2n+1}\sum_{j=0}^{\infty}\frac{a_a(j)}{j!}[\frac{-((2n+1)\pi)^2}{4(C_1C_2-1)}\tau]^j\sin(\frac{(2n+1)\pi}{2}\xi) \quad (31)$$

$$\upsilon_w(\tau,\xi)=\frac{4}{\pi}\sum_{n=0}^{N}\frac{1}{2n+1}\sum_{j=0}^{\infty}\frac{a_w(j)}{j!}[\frac{-((2n+1)\pi)^2}{4(C_1C_2-1)}\tau]^j\sin(\frac{(2n+1)\pi}{2}\xi) \quad (32)$$

Let $N\to\infty$. By using Eqs. (25) and (26) and the series expression of an exponential function, Eqs. (29) and (30) can be written as

$$\upsilon_a(\tau,\xi)=\frac{4}{\pi}\sum_{n=0}^{\infty}\frac{B_1e^{A_1\tau}+B_2e^{A_2\tau}}{2n+1}\sin(\frac{(2n+1)\pi}{2}\xi) \quad (33)$$

$$\upsilon_w(\tau,\xi)=\frac{4}{\pi}\sum_{n=0}^{\infty}\frac{D_1e^{A_1\tau}+D_2e^{A_2\tau}}{2n+1}\sin(\frac{(2n+1)\pi}{2}\xi) \quad (34)$$

where

$$A_1=\frac{-((2n+1)\pi)^2}{4(C_1C_2-1)}\lambda_1$$

$$A_2=\frac{-((2n+1)\pi)^2}{4(C_1C_2-1)}\lambda_2$$

$$B_1=\frac{(\lambda_1+1)(C_1C_3-\lambda_2-1)}{C_1C_3(\lambda_1-\lambda_2)}$$

$$B_2=\frac{-(\lambda_2+1)(C_1C_3-\lambda_1-1)}{C_1C_3(\lambda_1-\lambda_2)}$$

$$D_1=\frac{C_1C_3-\lambda_2-1}{\lambda_1-\lambda_2}$$

$$D_2=\frac{-(C_1C_3-\lambda_1-1)}{\lambda_1-\lambda_2}$$

Finally, we obtain the analytical solutions for the excess pore-air and water pressures in unsaturated soils as

$$u_a(z,t)=\frac{4u_a^0}{\pi}\sum_{n=0}^{\infty}\frac{B_1e^{A_1\tau}+B_2e^{A_2\tau}}{2n+1}\sin(\frac{(2n+1)\pi}{2}\frac{z}{H}) \quad (35)$$

$$u_w(z,t)=\frac{4u_w^0}{\pi}\sum_{n=0}^{\infty}\frac{D_1e^{A_1\tau}+D_2e^{A_2\tau}}{2n+1}\sin(\frac{(2n+1)\pi}{2}\frac{z}{H}) \quad (36)$$

where $\tau\ (=C_V^{\mathrm{w}}t/H^2)$ is the characteristic time of the excess pore-water pressure dissipation.

3.2 Non-homogeneous cases

According to the exact solutions for the above homogenous governing equations and the principle of superposition [30], the exact solutions for the non-homogenous governing equations, Eqs. (8)-(10), assume the following forms:

$$u_a(z,t)=\sum_{n=0}^{\infty}\phi_n(t)\sin(\frac{2n+1}{2H}\pi z) \quad (37)$$

$$u_w(z,t)=\sum_{n=0}^{\infty}\varphi_n(t)\sin(\frac{2n+1}{2H}\pi z) \quad (38)$$

Substituting Eqs. (37) and (38) into Eqs. (8)-(10), and multiplying the resultants by $\sin(\frac{2n+1}{2H}\pi z)$, and integrating the resultants of Eq. (8) from 0 to H with respect to z, we obtain a family of ordinary differential equations as

$$\mathbf{Y}_n'=\mathbf{M}_n\mathbf{Y}_n+\mathbf{N}_n \quad (39)$$

which is subjected to

$$\mathbf{Y}_n(0)=\frac{2}{n}\int_0^H\sin(\frac{2n+1}{2H}\pi z)dz \quad (40)$$

where

$$\mathbf{Y}_n(t)=(\phi_n(t),\varphi_n(t))^T$$

$$\mathbf{M}_n=(\frac{(2n+1)\pi}{2H})^2\mathbf{C}^{-1}\mathbf{C}_V$$

$$\mathbf{N}_n=\frac{4}{(2n+1)\pi}\mathbf{C}^{-1}\mathbf{C}_\sigma\sigma'$$

$$\mathbf{C}=\begin{pmatrix}C_{\mathrm{w}} & 1\\ 1 & C_{\mathrm{a}}\end{pmatrix}$$

$$\mathbf{C}_V=\begin{pmatrix}0 & C_V^w\\ C_V^a & 0\end{pmatrix}$$

$$\mathbf{C}_\sigma=(C_w^\sigma,C_a^\sigma)^T$$

Eq. (39) can be solved in a straightforward way, yielding

$$\mathbf{Y}_n=\exp(\mathbf{M}_nt)\mathbf{Y}_n(0)+\exp(\mathbf{M}_nt)\int_0^t\exp(-\mathbf{M}_n\xi)\mathbf{N}_n(\xi)d\xi \quad (41)$$

According to the Hamilton-Cayley Law [31], the fundamental matrix, $\exp(\mathbf{M}_nt)$, can be expressed as

$$\exp(\mathbf{M}_nt)=r_1(t)\mathbf{I}+r_2(t)(\mathbf{M}_n-\tilde{\lambda}_2\mathbf{I}) \quad (42)$$

with the functions $r_1(t)$ and $r_2(t)$ satisfying

$$r_1'(t)=\tilde{\lambda}_1r_1(t) \quad (43a)$$

$$r_2'(t)=r_1(t)+\tilde{\lambda}_2r_2(t) \quad (43b)$$

where, $r_1(0)=1$, $r_2(0)=0$, $\tilde{\lambda}_1$ and $\tilde{\lambda}_2$ are the two eigenvalues of the matrix $\mathbf{M}_n$.

3.3 Settlement

The excess pore-air and water pressures are analytically calculated using Eqs. (37)-(43). Now, the settlement at any moment, $S(t)$, can be obtained via [10]

$$\begin{aligned} S(t) = m_{1k}^{s}\int_0^H \{[\sigma(z,t)-u_a(z,t)]-[\sigma(z,0)-u_a(z,0)]\}dz \\ + m_2^{s}\int_0^H \{[u_a(z,t)-u_w(z,t)]-[u_a(z,0)-u_w(z,0)]\}dz \end{aligned} \tag{44}$$

where $m_{1k}^{s} = m_{1k}^{w} + m_{1k}^{a}$ is the coefficient of volume change with respect to a change in the net stress, and $m_2^{s} = m_1^{w} + m_1^{a}$ the coefficient of volume change with respect to a change in the matrix suction, under the K_0-loading condition.

4 EFFECTS OF THE COEFFICIENTS ON THE SOLUTIONS

It is important to note that, for the above solutions to exist, the matrices **A** and **C** must be non-singular, i.e.,

$$\det(\mathbf{A}) = \begin{vmatrix} -1 & C_1C_3 \\ C_2 & -C_3 \end{vmatrix} \neq 0 \ , \ \det(\mathbf{C}) = \begin{vmatrix} C_{\mathrm{w}} & 1 \\ 1 & C_a \end{vmatrix} \neq 0$$

Hence, with Eq. (11), it follows that

$$\neq \tilde{}_V^a \uparrow 0, C \neq \tilde{}_w \uparrow 1 \tag{45}$$

The coefficients C_a, C_w and C_V^a are associated with the soil type and the hydraulic condition [5, 8-12]. For a fully saturated soil, the coefficients of Eq. (1) become C_w=0, C_a=0, C_V^a=0 and $C_a^{\sigma} = 0$. Consequently, the parameters in Eq.11 become C_1=0, C_2=0 and C_3=0, so that

$$C_V^a = 0, C_a = 0, C_w = 0 \tag{46}$$

When the total stress (i.e., the applied surface traction), σ, is constant, Eq. (1) degenerates into the classic equation for excess pore-water pressure in fully saturated soils [32], i.e.,

$$\frac{\partial u_{\mathrm{w}}}{\partial t} = C_V^{\mathrm{w}} \frac{\partial^2 u_{\mathrm{w}}}{\partial z^2} \tag{47}$$

In such a situation, the excess pore-water pressures under a single drainage condition is given by (using Eqs. (35) and (36))

$$u_w(z,t) = u_w^0 \frac{4}{\pi}\sum_{n=0}^{\infty}\frac{1}{2n+1}\sum_{j=0}^{\infty}\frac{1}{j!}[-\frac{((2n+1)\pi)^2}{4}\frac{C_V^{\mathrm{w}}t}{H^2}]^j \sin(\frac{(2n+1)\pi}{2H}z) \tag{48}$$

Noting that

$$\exp(-\frac{((2n+1)\pi)^2}{4}\frac{C_V^{\mathrm{w}}t}{H^2}) = \sum_{j=0}^{\infty}\frac{1}{j!}[-\frac{((2n+1)\pi)^2}{4}\frac{C_V^{\mathrm{w}}t}{H^2}]^j$$

we obtain

$$u_w(z,t) = u_w^0 \frac{4}{\pi}\sum_{n=0}^{\infty}\frac{1}{2n+1}\sin(\frac{(2n+1)\pi}{2H}z)\exp(-\frac{((2n+1)\pi)^2}{4}\frac{C_V^{\mathrm{w}}t}{H^2}) \tag{49}$$

which is exactly the analytical solution of the 1-D consolidation problem for the saturated soil under instantaneous loading, single drainage, and a constant initial pore-water pressure distribution [33].

Now consider the situations that Eq. (45) is violated, i.e., the above-obtained solutions are no longer applicable. As in the first case, it is assumed that coefficients C_a, C_w and C_V^a satisfy

$$C_V^a \neq 0, C_aC_w = 1 \tag{50}$$

i.e.,

$$C_3 \neq 0, C_1C_2 = 1 \tag{51}$$

For convenience, it is also assumed that σ is constant. In this case, the governing equations for the problem can be written as

$$\frac{\partial u_{\mathrm{w}}}{\partial t} + C_{\mathrm{w}}\frac{\partial u_a}{\partial t} = C_V^{\mathrm{w}}\frac{\partial^2 u_{\mathrm{w}}}{\partial z^2} \tag{52a}$$

$$\frac{\partial u_a}{\partial t} + \frac{1}{C_w}\frac{\partial u_{\mathrm{w}}}{\partial t} = C_V^a\frac{\partial^2 u_a}{\partial z^2} \tag{52b}$$

It is straightforward to prove that the analytical solutions of Eq.52 are

$$u_a(z,t) = u_a^0 \frac{4}{\pi}\sum_{n=0}^{\infty}\frac{1}{2n+1}\sin(\frac{(2n+1)\pi}{2H}z)\exp(-\frac{C_3((2n+1)\pi)^2}{4(C_3+1)}\tau) \tag{53}$$

$$u_w(z,t) = u_w^0 \frac{4}{\pi}\sum_{n=0}^{\infty}\frac{1}{2n+1}\sin(\frac{(2n+1)\pi}{2H}z)\exp(-\frac{C_1C_3((2n+1)\pi)^2}{4(C_3+1)}\tau) \tag{54}$$

In general, the coefficients C_V^a and C_V^w are proportional to the air conductivity (k_a) and water the conductivity (k_w). If the coefficients C_a, C_w and C_V^a satisfy the following conditions:

$$C_V^{\mathrm{a}} = 0, C_aC_w \neq 0, C_aC_w \neq 1 \tag{55}$$

i.e.

$$C_3 = 0, C_1C_2 \neq 0, C_1C_2 \neq 1 \tag{56}$$

In this case, the governing equations of the problem degenerates into

$$\frac{\partial u_{\mathrm{w}}}{\partial t} + C_{\mathrm{w}}\frac{\partial u_a}{\partial t} = C_V^{\mathrm{w}}\frac{\partial^2 u_{\mathrm{w}}}{\partial z^2} \tag{57a}$$

$$\frac{\partial u_a}{\partial t} + C_a\frac{\partial u_{\mathrm{w}}}{\partial t} = 0 \tag{57b}$$

The solutions of Eq. (57) are given by.

$$u_a(z,t) = u_a^0 \frac{4}{\pi}\sum_{n=0}^{\infty}\frac{1}{2n+1}\sin\left(\frac{(2n+1)\pi}{2H}z\right)\left((1+C_2) - \right.$$
$$\left. - \exp\left(-\frac{((2n+1)\pi)^2}{4}\frac{C_V^{\mathrm{w}}t}{H^2(1-C_1C_2)}\right)\right) \qquad (58)$$

$$u_w(z,t) =$$
$$= u_w^0 \frac{4}{\pi}\sum_{n=0}^{\infty}\frac{1}{2n+1}\sin\left(\frac{(2n+1)\pi}{2H}z\right)\exp\left(-\frac{((2n+1)\pi)^2}{4}\frac{C_V^{\mathrm{w}}t}{H^2(1-C_1C_2)}\right) \qquad (59)$$

In addition, when the coefficient C_w^{σ} in Eq. (1) is equal to a negative parameter η, which accounts for the compressibility of the soil and the pore fluid, and C_w=0, C_a=0, C_V^a=0, $C_a^{\sigma}=0$, $C_V^w=\eta C_v^w$, Eq.1 degenerates into the equation studied by Conte and Troncone [17], through in an opposite direction coordinate system.

5 EXAMPLES

To validate the above-derived analytical solutions, a typical example is computed using both the current solutions and those developed by others (e.g., Qin et al. [8]). The parameters used in the calculations are

$C_w=-0.75$, $C_a=-0.0775134$, $C_V^w=-500k_w$ m, $C_V^a=-64504.4k_a$ m, H=10m, $u_a^0=20$ kPa, $u_w^0=40$ kPa, $m_{1k}^s=-2.5\times10^{-4}$ kPa, $m_2^s=0.4m_{1k}^s$.

Firstly, under a constant surface traction $q(t)=q_0$ (q_0=100kPa), the top surface (Fig. 1) is permeable to water and air, whereas the bottom surface is impermeable to water and air. It is instructive to note that the above parameters satisfy $C_a\,C_w$ = 0.0058135050≠1 and $C_V^a\neq0$, since $k_a\neq0$. In this case, the analytical solution is given by Eqs. (35) and (36). The calculated results are presented in Fig. 2, where Qin et al.'s results [8] for k_a/k_w=0.1 are also given for comparison.

Fig. 2 illustrates that the calculated results of the current solution and Qin's solution are practically identical, showing the validity of the current solution. It is clear that the value of k_a/k_w can significantly influence the calculated results. Clearly, both the excess pore-water pressure and excess pore-air pressure decrease with an increase in the value of k_a/k_w. As time elapses, both u_w and u_a gradually dissipate and finally approach a stable value. As expected, the dissipation of the excess pore-air pressure is much faster than the excess pore-water pressure. The greater the value of k_a/k_w, the more quickly the pore pressure dissipates. However, it should be noted that the value of k_a/k_w has little influence on the dissipation of the excess pore-water pressure at a later stage of consolidation (when $t>10^8$s).

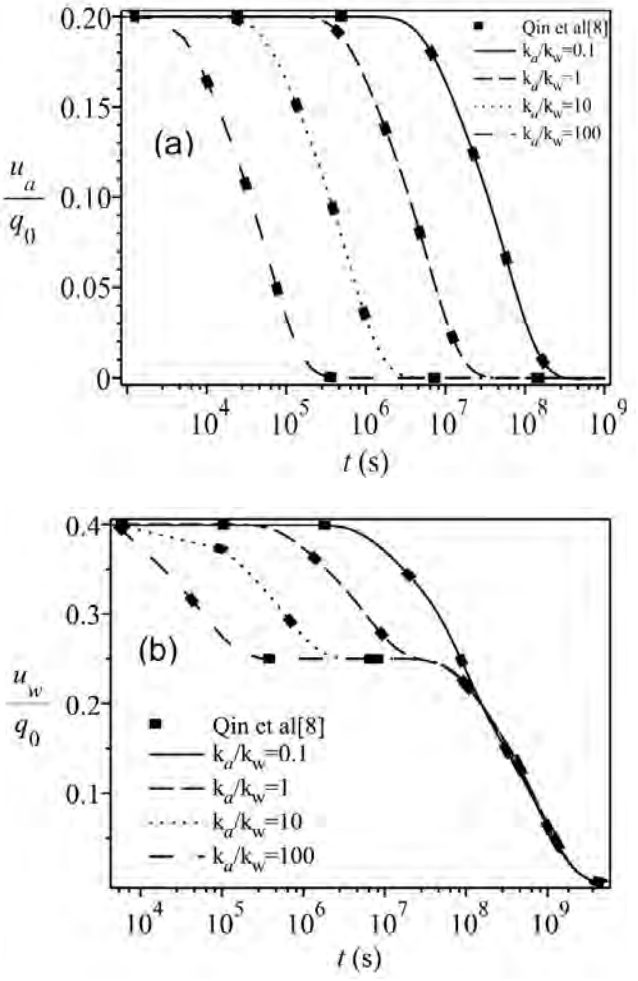

Figure 2. Variations in the excess pore-air (a) and excess pore-water (b) pressures with dimensionless time for different values of k_a/k_w.

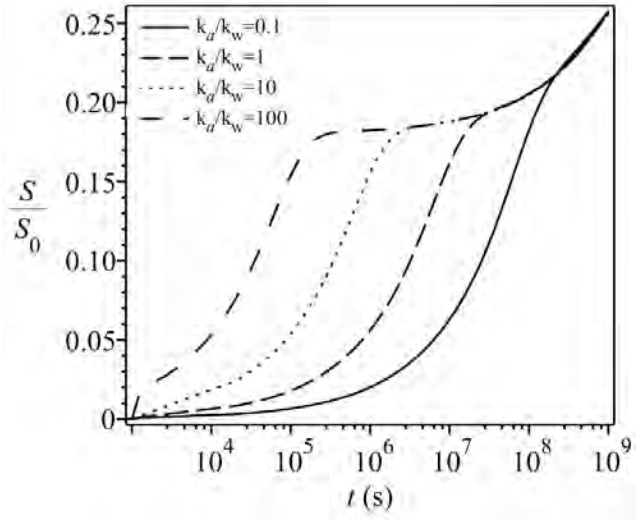

Figure 3. Compression of a single-layer unsaturated soil variation with time for different values of k_a/k_w.

Variations of the normalized settlement $S/S_0(S_0 = m_{1k}^s q_0 H_0)$ caused by the constant surface traction are illustrated in Fig. 3.It is clear that at the beginning of the consolidation the settlement generally proceeds faster as k_a/k_w increases, thus characterizing the inverse sigmoid shapes. However, at the later stage of consolidation, for all the k_a/k_w values, the settlement curves increase unanimously after 10^8s.

Now, consider the situation that the coefficients C_a, C_w and C_V^a satisfy Eq.(50). In this case, the solutions of the problem are given by Eqs. (53) and (54). In the calculations, it is assumed that $C_1 = 1.0$, $H = 10$m, $u_a^0 = 20$ kPa, and $u_w^0 = 40$ kPa. The calculated results are illustrated in Fig.4, which shows the variations of u_w and u_a with time under different C_3 (i.e., $C_3 = C_V^a/C_V^w$) for the single drainage condition. The top surface is permeable to water and air, whereas the bottom surface is impermeable to water and air. Clearly, both the excess pore-water pressure and excess pore-air pressure gradually decrease with time, and finally approach a stable value. In contrast to Fig. 2, however, both u_w and u_a dissipate almost simultaneously to a stable value. In addition, it is clear that the excess pore-air pressure decreases with an increase of $C_3 = C_V^a/C_V^w$, whereas the excess pore-water pressure variation shows a different tendency.

For the situation that the coefficients C_a, C_w and C_V^a satisfy Eq.(55), the solutions are given by Eq. (58) and (59). In the calculations, the parameters are selected as: $H = 10$m, $u_a^0 = 20$ kPa, and $u_w^0 = 40$ kPa. The calculated results are given in Fig.5 for the different values of C_1 at $C_2 = -0.2$. It is clear that, in practice, a variation of C_1 has no effect on the dissipation of the pore pressure.

To explore the influence of C_2, Fig. 6 shows the results of Eqs. (58) and (59) for different C_2 at $C_1 = -0.07$. It is clear that with the change of time, the excess pore-air pressure decreases and it finally attains a stable value.

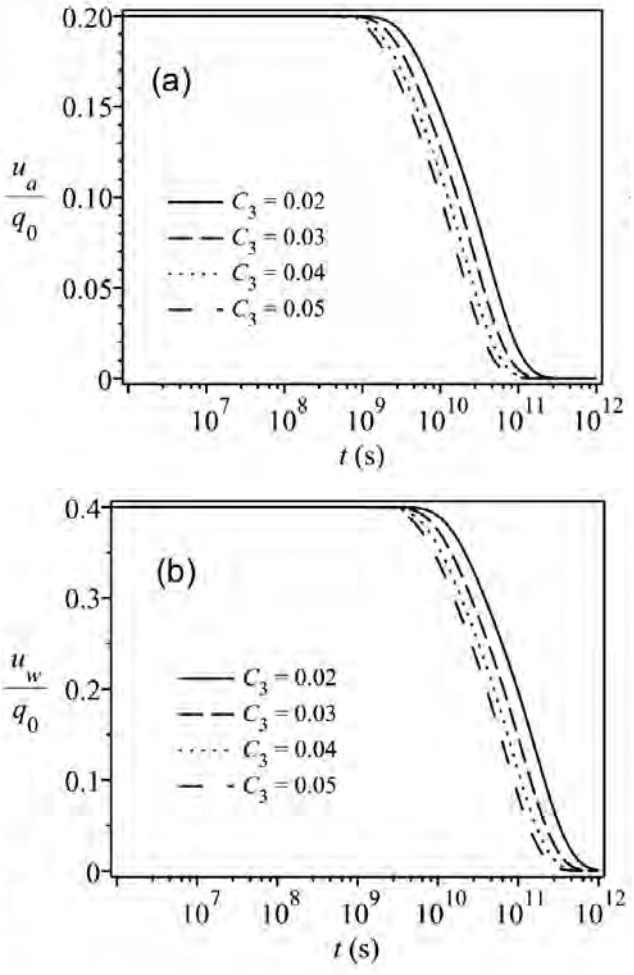

Figure 4. Variations of the excess pore-air (a) and the excess pore-water (b) pressures with time for different values of $C_3 = C_V^a/C_V^w$.

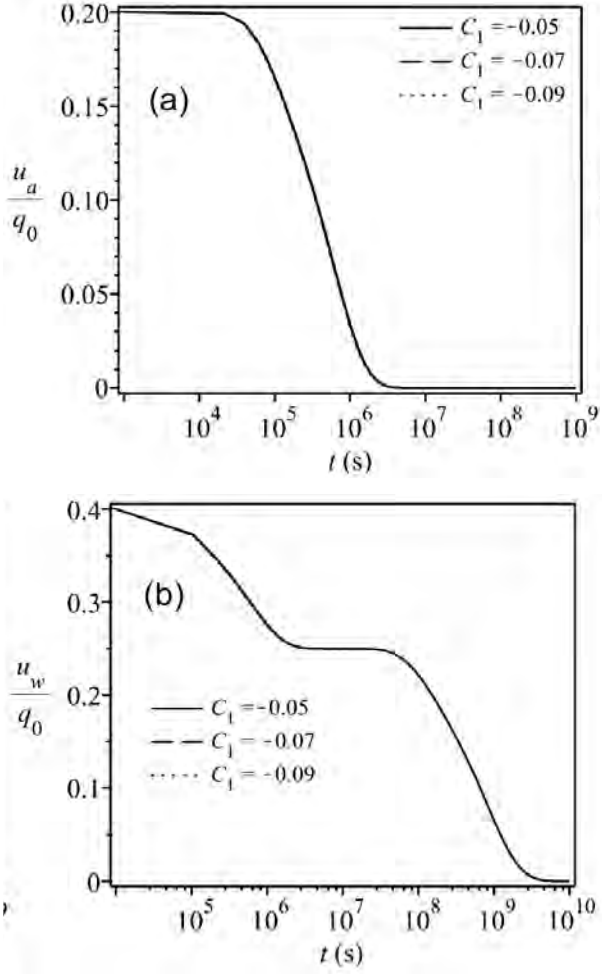

Figure 5. Variations of the excess pore-air (a) and the excess pore-water (b) pressures with dimensionless time for different C_1 at $C_2 = -0.2$.

Throughout the consolidation process, coefficient C_2 has the least influence on the change of the excess pore-air pressure. From Fig.6b it is clear that C_2 has a significant effect on the change of excess pore-water pressure. In addition, the stabilized time of the excess pore-air pressure is at about 10^6s and the excess pore-water pressure is at about 10^9s.

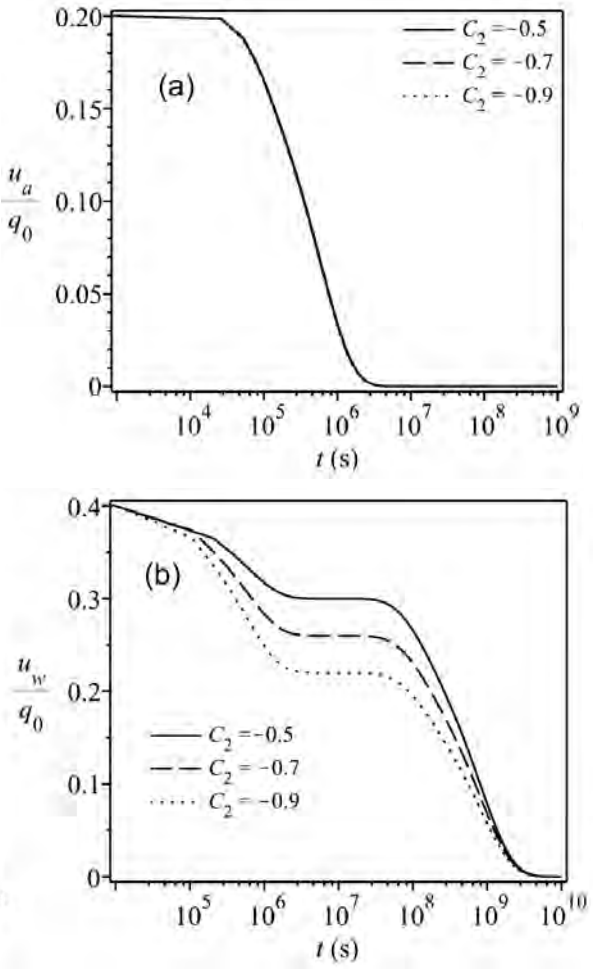

Figure 6. Variations of the excess pore-air (a) and the excess pore-water (b) pressures with dimensionless time for different C_2 at C_1 = –0.07 .

Finally, we address the one-dimensional consolidation problem of unsaturated soil under a variable loading condition. Assume that the coefficients C_a , C_w and C_V^a satisfy Eq. (45). Then the solutions to the problem are given by Eqs. (37)-(42). Two cases of loading are discussed, in which sinusoidal and trapezoidal tractions, respectively, are applied to the top boundary (Fig. 7), respectively.

Sinusoidal traction:

$$q(t) = q_0 \sin(2\pi t/10^8) \tag{59}$$

Trapezoidal tractions:

$$q(t) = \begin{cases} q_0 t/t_c, & 0 \le t < t_b \\ q_0, & t_b \le t < t_c \\ 0, & t_c \le t < T \end{cases} \tag{60}$$

In the first case (Fig. 7a), the sinusoidal surface traction is applied. In the calculations, the amplitude q_0 of the sinusoidal loading is 100 kPa with an angular frequency of $2\pi/10^8$. The other parameters are the same as in the example of Fig. 2. In the second case (Fig. 7b), the cyclical trapezoidal surface traction is applied, q_0 = 100kPa.

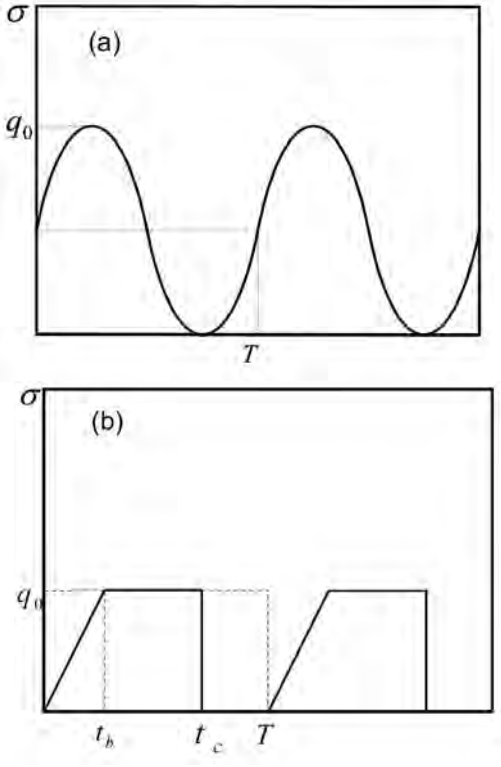

Figure 7. Applied loadings on the top boundary: (a) the sinusoidal surface traction (b) the cyclical trapezoidal surface traction.

The results for the sinusoidal loading are shown in Fig. 8, which depicts the temporal variations of the excess pore-air and water pressures for different values of k_a/k_w. Both u_w and u_a disappear gradually. At the final stage, the changes of u_w and u_a enter a phase of fluctuation. The fluctuation amplitude of u_w is larger than that of u_a. In addition, both u_w and u_a decrease with the increase of k_a/k_w in the initial stage.

Variations of the normalized settlement S/S_0(S_0= $m_{1k}^s q_0 H_0$) caused by the cyclical sinusoidal surface traction are

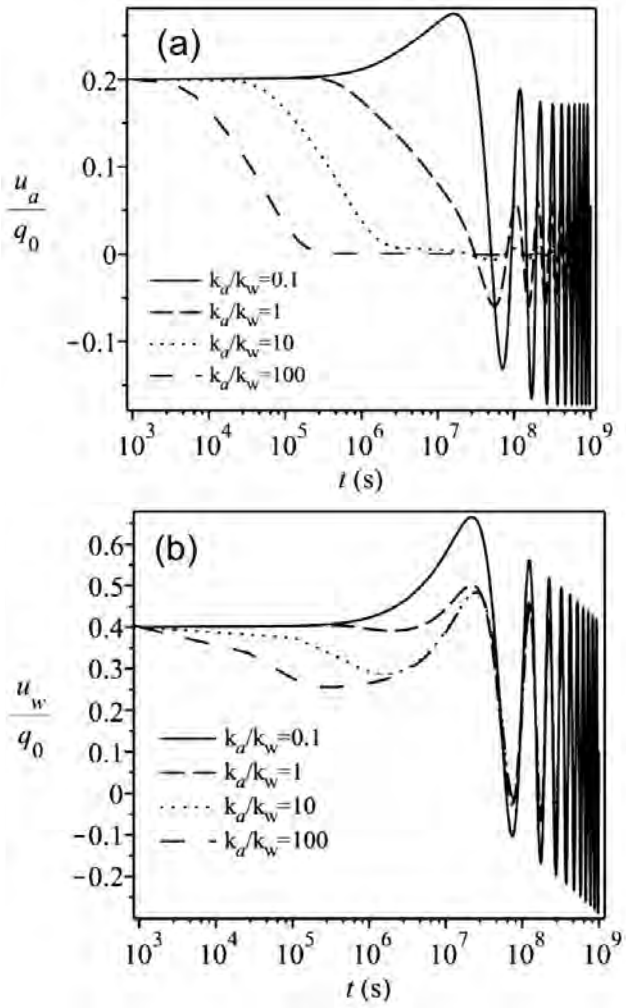

Figure 8. Variations of the excess pore-air (a) and the excess pore-water (b) pressures with time for different k_a/k_w under the sinusoidal loading condition.

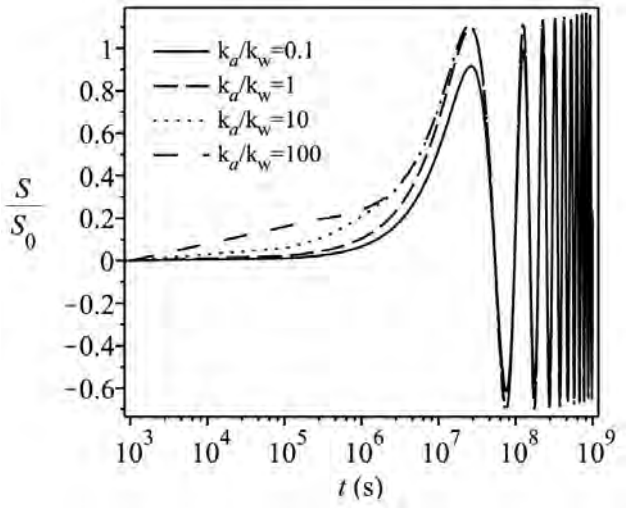

Figure 9. Compression of a single-layer unsaturated soil variation under the sinusoidal loading condition with time for different values of k_a/k_wn.

illustrated in Fig. 9. The settlement curves are similar to those induced by a constant loading at the beginning of the consolidation, in which the settlement generally proceeds faster as k_a/k_w increases, thus characterizing the inverse sigmoid shapes. However, for all the k_a/k_w values, the settlement curves increase dramatically after 10^7s as a result of a significantly increasing loading.

The trapezoidal loading (Fig.7b) was adopted by Conte and Troncone [17] in their analysis. In this case, by using Eqs. (5) and (6), we obtain

$$a_k = \frac{qT}{2\pi^2 k^2 t_b}\left[\cos\left(\frac{2k\pi}{T}t_b\right) + \frac{2k\pi}{T}t_b \sin\left(\frac{2k\pi}{T}t_c\right) - 1\right] \quad (61)$$

$$b_k = \frac{qT}{2\pi^2 k^2 t_b}\left[\sin\left(\frac{2k\pi}{T}t_b\right) - \frac{2k\pi}{T}t_b \cos\left(\frac{2k\pi}{T}t_c\right)\right] \quad (62)$$

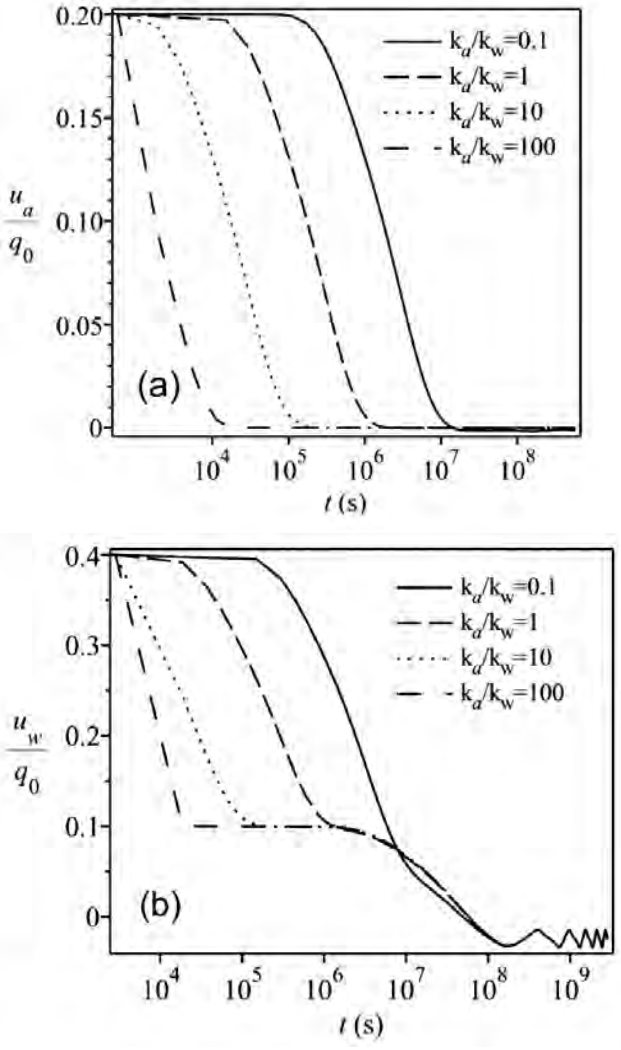

Figure 10. Variations of the excess pore-air (a) and the excess pore-water (b) pressures with time for different k_a/k_w under the trapezoidal loading condition.

In the calculations, it is assumed that $t_b = 0.13t_c$, $t_c = 2.6H^2/C_v^w$, and $T = 1.1t_c$. The results are shown in Fig.10 and Fig.11. It is clear that the temporal variations of both u_w and u_a can be separated into several stages in accordance with the applied loading. Similar to the case of the sinusoidal loading, the final stages of the excess pore-water pressure variation show a clear fluctuation, and the final stages of the excess pore-air pressure variation similar to the case of the constant loading. However, the excess pore-water pressure and excess pore-air pressure decrease with the increase of k_a/k_w at the beginning.

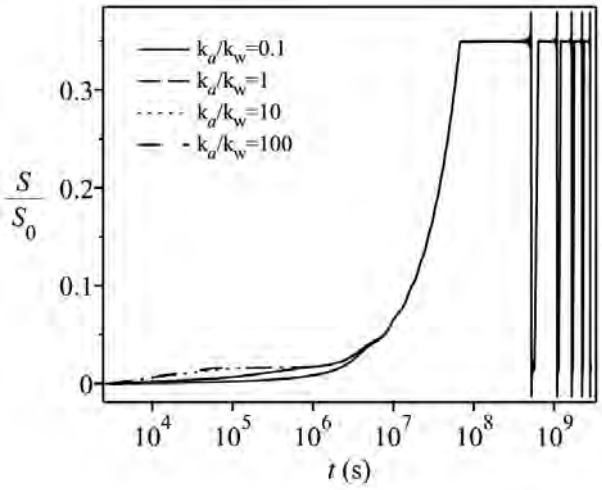

Figure 11. Compression of a single-layer unsaturated soil variation under the trapezoidal loading condition with time for different values of k_a/k_w.

From Fig.11 it is clear that the settlement curves are similar to those induced by a constant loading and sinusoidal surface traction at the beginning of consolidation, in which the settlement generally proceeds as k_a/k_w increases. However, for all the k_a/k_w values, at a final stage after 10^8s, the changes of the settlement dramatically enter a phase of fluctuation as a result of a significantly increasing loading.

6 CONCLUSIONS

This paper introduces the differential transform method and the Fourier series expansion techniques to determine a more strict general analytical solution for excess pore pressures in an unsaturated soil layer subjected to various time-dependent loadings. The differential transform method can intuitively and simply obtain the analytical solution for the unsaturated consolidation problems.

According to the relationship between the coefficients for the unsaturated consolidation governing equations, different analytical solutions are obtained. Additionally, the procedure makes use of the Fourier series. Therefore, it allows the consideration of both continuous differentiable loading (e.g., sinusoidal loading) and periodic piecewise loading by a suitable choice of the series period. Excellent agreement was found between the results obtained using the present solution and those derived from existing theoretical solutions.

Moreover, through the analytical solutions, it is clear that the effect of changes to the ratio k_a/k_w on the change of the excess pore-air pressure and water pressure and the settlement is significant. However, the impact on both the magnitude of change is different. Besides, the effects of the coefficients of the equations (C_a , C_w , C_v^a, C_v^w) are investigated. When the four (C_a , C_w , C_v^a, C_v^w) meet different relationships, the influence of the coefficients on the analytical solutions are obviously different. However, The coefficient of C_1 has no effect on the dissipation of the pore-air and pore-water pressures, and the coefficient of C_2 has no effect on the dissipation of the pore-water pressure.

Acknowledgments

This research was supported by the National Natural Science Foundation of China through Grants #11372078,and #41272358. In addition, partial support from the Engagement Fund from the Taizhou University (2017PY016) is acknowledged.

REFERENCES

[1] Fredlund, D.G, Rahardjo, H. 1993.Soil Mechanics for Unsaturated Soils. John Wiley and Sons: New York.

[2] Blight, G.E. 1961. Strength and consolidation characteristics of compacted soils. Dissertation, University of London, England.

[3] Scott, R.F. 1963. Principles of Soil Mechanics. Addison Wesley Publishing Company: Massachusetts.

[4] Barden, L. 1965. Consolidation of compacted and unsaturated clays. Geotechnique 15, 267–286. DOI: http://dx.doi.org/10.1680/geot.1965.15.3.267

[5] Fredlund, D.G, Hasan, J.U. 1979. One-dimensional consolidation theory: unsaturated soils. Canadian Geotechnical Journal 17:521–531. DOI: http://dx.doi.org/10.1139/t79-058

[6] Chen, R.P, Zhou, W.H, Wang, H.Z, Chen, Y.M. 2005. One-dimensional nonlinear consolidation of multi-layered soil by differential quadrature method. Computers and Geotechnics 32, 358–369. DOI: http://dx.doi.org/10.1016/j.compgeo.2005.05.003

[7] Zhou, W.H, Tu, S. 2012. Unsaturated consolidation in a sand drain foundation by differential quadrature method. Procedia Earth and Planetary Science 5, 52–57. DOI: https://doi.org/10.1016/j.proeps.2012.01.009

[8] Qin, A.F., Chen, G.J., Tan, Y.W., Sun, D.A. 2008. Analytical solution to one-dimensional consolidation in unsaturated soils. Applied Mathematics and Mechanics 29, 1329–1340. DOI:10.1007/s10483-008-1008-x

[9] Qin, A.F., Sun, D.A., Tan, Y.W. 2016. Analytical solution to one-dimensional consolidation in unsaturated soils under loading varying exponentially with time. Computers and Geotechnics 37, 233–238. DOI : https://doi.org/10.1016/j.compgeo.2009.07.008

[10] Shan, Z.D., Ling, D.S., Ding, H.J. 2012. Exact solutions for one-dimensional consolidation of single-layer unsaturated soil. International Journal for Numerical and Analytical Methods in Geomechanics 36, 708–722. DOI: 10.1002/nag.1026

[11] Ho, L., Fatahi, B., Khabbaz, H. 2014. Analytical solution for one-dimensional consolidation of unsaturated soils using eigenfunction expansion method. International Journal for Numerical and Analytical Methods in Geomechanics 38, 1058–1077. DOI: http://dx.doi.org/10.1002/nag.2248

[12] Ho, L., Fatahi, B. 2015. One-dimensional consolidation analysis of unsaturated soils subjected to time-dependent loading. International Journal of Geomechanics (ASCE) 16, 2, 291-301. DOI: http://dx.doi.org/10.1061/(ASCE)GM.1943-5622.0000504

[13] Ho, L., Fatahi, B., Khabbaz, H. 2015. A closed form analytical solution for two-dimensional plane strain consolidation of unsaturated soil stratum. International Journal for Numerical and Analytical Methods in Geomechanics 39, 1665-1692. DOI: http://dx.doi.org/10.1002/nag.2369

[14] Ho, L., Fatahi, B., Khabbaz, H. 2016. Analytical solution to axisymmetric consolidation in unsaturated soils with linearly depth-dependent initial conditions. Computers and Geotechnics 74, 102-121. DOI: http://dx.doi.org/10.1016/j.compgeo.2015.12.019

[15] Ho, L., Fatahi, B. 2016. Axisymmetric consolidation in unsaturated soil deposit subjected to time-dependent loadings. International Journal of Geomechanics 17, 2, 1-29. DOI: http://dx.doi.org/10.1061/(ASCE)GM.1943-5622.0000686

[16] Zhou, W.H., Zhao, L.S. 2013. One-dimensional consolidation of unsaturated soil subjected to time-dependent loading with various initial and boundary conditions. International Journal of Geomechanics (ASCE) 14, 2, 291-301. DOI: http://dx.doi.org/10.1061/(ASCE)GM.1943-5622.0000314

[17] Conte E., Troncone A. 2006. One-dimensional consolidation under general time-dependent loading. Canadian Geotechnical Journal 43, 11, 1107-1116. DOI: http://dx.doi.org/10.1139/t06-064

[18] Ayaz, F. 2004. Solutions of the system of differential equations by differential transform method. Applied Mathematics and Computation 147, 2, 547-567. DOI: https://doi.org/10.1016/S0096-3003(02)00794-4

[19] Ayaz, F. 2004. Application of differential transform method to differential-algebraic equations. Applied Mathematics and Computation 152, 3, 649-657. DOI: https://doi.org/10.1016/S0096-3003(03)00581-2

[20] Arikoglu, A., Ozkol, I. 2005. Solution of boundary value problems for integro-differential equations by using differential transform method. Applied Mathematics and Computation 168, 2, 1145-1158. DOI: https://doi.org/10.1016/j.amc.2004.10.009

[21] Bildik, N., Konuralp, A., Bek, F., Kucukarslan, S. 2006. Solution of different type of the partial differential equation by differential transform method and Adomian's decomposition method. Applied Mathematics and Computation 172, 1, 551-567. DOI: https://doi.org/10.1016/j.amc.2005.02.037

[22] Arikoglu, A., Ozkol, I. 2006. Solution of difference equations by using differential transform method. Applied Mathematics and Computation 174, 2, 126-136. DOI: https://doi.org/10.1016/j.amc.2005.06.013

[23] Arikoglu, A., Ozkol, I. 2006. Solution of differential difference equations by using differential transform method. Applied Mathematics and Computation 181, 153-162. DOI:http://dx.doi.org/10.1016/j.amc.2006.01.022

[24] Liu, H., Song, Y. 2007. Differential transform method applied to high index differential-algebraic equations. Applied Mathematics and Computation 184, 2, 748-753. DOI: https://doi.org/10.1016/j.amc.2006.05.173

[25] Momani, S., Noor, M. 2007. Numerical comparison of methods for solving a special fourth-order boundary value problem. Applied Mathematics and Computation 191, 218-224. DOI: https://doi.

org/10.1016/j.amc.2007.02.081
[26] Odibat, Z., Momani, S., Erturk, V. 2008. Generalized differential transform method: Application to differential equations of fractional order. Applied Mathematics and Computation 197, 467-477. DOI: https://doi.org/10.1016/j.amc.2007.07.068
[27] Kuo, B., Lo, C. 2009. Application of the differential transformation method to the solution of a damped system with high nonlinearity. Nonlinear Analysis: Theory, Methods and Applications 70, 1732-1737. DOI: https://doi.org/10.1016/j.na.2008.02.056
[28] Sawalha, M.A., Noorani, M. 2009. Application of the differential transformation method for the solution of the hyperchaotic RÄossler system. Communications in Nonlinear Science and Numerical Simulation 14, 1509-1514. DOI: https://doi.org/10.1016/j.cnsns.2008.02.002
[29] Chen, S., Chen, C. 2009. Application of the differential transformation method to the free vibrations of strongly non-linear oscillators. Nonlinear Analysis: Real World Applications 10, 881-888. DOI: https://doi.org/10.1016/j.nonrwa.2005.06.010
[30] Pinchover, Y., Rubinstein, J. 2005. An Introduction to Partial Differential Equations. New York: Cambridge University Press.
[31] Bellman, R. 1970. Introduction to Matrix Analysis. McGraw-Hill: New York.
[32] Terzaghi, K. 1943.Theoretical Soil Mechanics. Wiley: New York.
[33] Schiffman, R.L., Stein, J.R. 1970. One-dimensional consolidation of layered systems. Journal of the Soil Mechanics and Foundations Division (ASCE) 96, 1499–1504.

NAVODILA AVTORJEM

Vsebina članka

Članek naj bo napisan v naslednji obliki:

- Naslov, ki primerno opisuje vsebino članka in ne presega 80 znakov.
- Izvleček, ki naj bo skrajšana oblika članka in naj ne presega 250 besed. Izvleček mora vsebovati osnove, jedro in cilje raziskave, uporabljeno metodologijo dela, povzetek izidov in osnovne sklepe.
- Največ 6 ključnih besed, ki bi morale biti napisane takoj po izvlečku.
- Uvod, v katerem naj bo pregled novejšega stanja in zadostne informacije za razumevanje ter pregled izidov dela, predstavljenih v članku.
- Teorija.
- Eksperimentalni del, ki naj vsebuje podatke o postavitvi preiskusa in metode, uporabljene pri pridobitvi izidov.
- Izidi, ki naj bodo jasno prikazani, po potrebi v obliki slik in preglednic.
- Razprava, v kateri naj bodo prikazane povezave in posplošitve, uporabljene za pridobitev izidov. Prikazana naj bo tudi pomembnost izidov in primerjava s poprej objavljenimi deli.
- Sklepi, v katerih naj bo prikazan en ali več sklepov, ki izhajajo iz izidov in razprave.
- Vse navedbe v besedilu morajo biti na koncu zbrane v seznamu literature, in obratno.

Dodatne zahteve

- Vrstice morajo biti zaporedno oštevilčene.
- Predložen članek ne sme imeti več kot 18 strani (brez tabel, legend in literature); velikost črk 12, dvojni razmik med vrsticami. V članek je lahko vključenih največ 10 slik. Isti rezultati so lahko prikazani v tabelah ali na slikah, ne pa na oba načina.
- Potrebno je priložiti imena, naslove in elektronske naslove štirih potencialnih recenzentov članka. Urednik ima izključno pravico do odločitve, ali bo te predloge upošteval.

Enote in okrajšave

V besedilu, preglednicah in slikah uporabljajte le standardne označbe in okrajšave SI. Simbole fizikalnih veličin v besedilu pišite poševno (npr. *v*, *T* itn.). Simbole enot, ki so sestavljene iz črk, pa pokončno (npr. Pa, m itn.). Vse okrajšave naj bodo, ko se prvič pojavijo, izpisane v celoti.

Slike

Slike morajo biti zaporedno oštevilčene in označene, v besedilu in podnaslovu, kot sl. 1, sl. 2 itn. Posnete naj bodo v katerem koli od razširjenih formatov, npr. BMP, JPG, GIF. Za pripravo diagramov in risb priporočamo CDR format (CorelDraw), saj so slike v njem vektorske in jih lahko pri končni obdelavi preprosto povečujemo ali pomanjšujemo.

Pri označevanju osi v diagramih, kadar je le mogoče, uporabite označbe veličin (npr. *v*, *T* itn.). V diagramih z več krivuljami mora biti vsaka krivulja označena. Pomen oznake mora biti razložen v podnapisu slike.

Za vse slike po fotografskih posnetkih je treba priložiti izvirne fotografije ali kakovostno narejen posnetek.

Preglednice

Preglednice morajo biti zaporedno oštevilčene in označene, v besedilu in podnaslovu, kot preglednica 1, preglednica 2 itn. V preglednicah ne uporabljajte izpisanih imen veličin, ampak samo ustrezne simbole. K fizikalnim količinam, npr. *t* (pisano poševno), pripišite enote (pisano pokončno) v novo vrsto brez oklepajev. Vse opombe naj bodo označene z uporabo dvignjene številke[1].

Seznam literature

Navedba v besedilu

Vsaka navedba, na katero se sklicujete v besedilu, mora biti v seznamu literature (in obratno). Neobjavljeni rezultati in osebne komunikacije se ne priporočajo v seznamu literature, navedejo pa se lahko v besedilu, če je nujno potrebno.

Oblika navajanja literature

V besedilu: Navedite reference zaporedno po številkah v oglatih oklepajih v skladu z besedilom. Dejanski avtorji so lahko navedeni, vendar mora obvezno biti podana referenčna številka.

Primer: »..... kot je razvidno [1,2]. Brandl and Blovsky [4], sta pridobila drugačen rezultat…«

V seznamu: Literaturni viri so oštevilčeni po vrstnem redu, kakor se pojavijo v članku. Označimo jih s številkami v oglatih oklepajih.

Sklicevanje na objave v revijah:

[1] Jelušič, P., Žlender, B. 2013. Soil-nail wall stability analysis using ANFIS. Acta Geotechnica Slovenica 10(1), 61-73.

Sklicevanje na knjigo:
[2] Šuklje, L. 1969. Rheological aspects of soil mechanics. Wiley-Interscience, London
Sklicevanje na poglavje v monografiji:
[3] Mitchel, J.K. 1992. Characteristics and mechanisms of clay creep and creep rupture, in N. Guven, R.M. Pollastro (eds.), Clay-Water Interface and Its Rheological Implications, CMS Workshop Lectures, Vol. 4, The clay minerals Society, USA, pp. 212-244..
Sklicevanje na objave v zbornikih konferenc:
[4] Brandl, H., Blovsky, S. 2005. Slope stabilization with socket walls using the observational method. Proc. Int. conf. on Soil Mechanics and Geotechnical Engineering, Bratislava, pp. 2485-2488.
Sklicevanje na spletne objave:
[5] Kot najmanj, je potrebno podati celoten URL. Če so poznani drugi podatki (DOI, imena avtorjev, datumi, sklicevanje na izvorno literaturo), se naj prav tako dodajo.

Podatki o avtorjih

Članku priložite tudi podatke o avtorjih: imena, nazive, popolne poštne naslove, številke telefona in faksa, naslove elektronske pošte. Navedite kontaktno osebo.

Sprejem člankov in avtorske pravlce

Uredništvo si pridržuje pravico do odločanja o sprejemu članka za objavo, strokovno oceno mednarodnih recenzentov in morebitnem predlogu za krajšanje ali izpopolnitev ter terminološke in jezikovne korekture. Z objavo preidejo avtorske pravice na revijo ACTA GEOTECHNICA SLOVENICA. Pri morebitnih kasnejših objavah mora biti AGS navedena kot vir.

Vsa nadaljnja pojasnila daje:

Uredništvo
ACTA GEOTECHNICA SLOVENICA
Univerza v Mariboru,
Fakulteta za gradbeništvo, prometno inženirstvo in arhitekturo
Smetanova ulica 17, 2000 Maribor, Slovenija
E-pošta: ags@uni-mb.si

INSTRUCTIONS FOR AUTHORS

Format of the paper

The paper should have the following structure:

- A Title, which adequately describes the content of the paper and should not exceed 80 characters;
- An Abstract, which should be viewed as a mini version of the paper and should not exceed 250 words. The Abstract should state the principal objectives and the scope of the investigation and the methodology employed; it should also summarise the results and state the principal conclusions;
- Immediately after the abstract, provide a maximum of 6 keywords;
- An Introduction, which should provide a review of recent literature and sufficient background information to allow the results of the paper to be understood and evaluated;
- A Theoretical section;
- An Experimental section, which should provide details of the experimental set-up and the methods used to obtain the results;
- A Results section, which should clearly and concisely present the data, using figures and tables where appropriate;
- A Discussion section, which should describe the relationships shown and the generalisations made possible by the results and discuss the significance of the results, making comparisons with previously published work;
- Conclusions, which should present one or more conclusions that have been drawn from the results and subsequent discussion;
- A list of References, which comprises all the references cited in the text, and vice versa.

Additional Requirements for Manuscripts

- Use double line-spacing.
- Insert continuous line numbering.
- The submitted text of Research Papers should cover no more than 18 pages (without Tables, Legends, and References, style: font size 12, double line spacing). The number of illustrations should not exceed 10. Results may be shown in tables or figures, but not in both of them.
- Please submit, with the manuscript, the names, addresses and e-mail addresses of four potential referees. Note that the editor retains the sole right to decide whether or not the suggested reviewers are used.

Units and abbreviations

Only standard SI symbols and abbreviations should be used in the text, tables and figures. Symbols for physical quantities in the text should be written in Italics (e.g. *v*, *T*, etc.). Symbols for units that consist of letters should

be in plain text (e.g. Pa, m, etc.).
All abbreviations should be spelt out in full on first appearance.

Figures

Figures must be cited in consecutive numerical order in the text and referred to in both the text and the caption as Fig. 1, Fig. 2, etc. Figures may be saved in any common format, e.g. BMP, JPG, GIF. However, the use of CDR format (CorelDraw) is recommended for graphs and line drawings, since vector images can be easily reduced or enlarged during final processing of the paper.

When labelling axes, physical quantities (e.g. *v*, *T*, etc.) should be used whenever possible. Multi-curve graphs should have individual curves marked with a symbol; the meaning of the symbol should be explained in the figure caption. Good quality black-and-white photographs or scanned images should be supplied for the illustrations.

Tables

Tables must be cited in consecutive numerical order in the text and referred to in both the text and the caption as Table 1, Table 2, etc. The use of names for quantities in tables should be avoided if possible: corresponding symbols are preferred. In addition to the physical quantity, e.g. *t* (in Italics), units (normal text), should be added on a new line without brackets.
Any footnotes should be indicated by the use of the superscript[1].

LIST OF references

Citation in text

Please ensure that every reference cited in the text is also present in the reference list (and vice versa). Any references cited in the abstract must be given in full. Unpublished results and personal communications are not recommended in the reference list, but may be mentioned in the text, if necessary.

Reference style

Text: Indicate references by number(s) in square brackets consecutively in line with the text. The actual authors can be referred to, but the reference number(s) must always be given:

Example: "... as demonstrated [1,2]. Brandl and Blovsky [4] obtained a different result ..."

List: Number the references (numbers in square brackets) in the list in the order in which they appear in the text.

Reference to a journal publication:
[1] Jelušič, P., Žlender, B. 2013. Soil-nail wall stability analysis using ANFIS. Acta Geotechnica Slovenica 10(1), 61-73.

Reference to a book:
[2] Šuklje, L. 1969. Rheological aspects of soil mechanics. Wiley-Interscience, London

Reference to a chapter in an edited book:
[3] Mitchel, J.K. 1992. Characteristics and mechanisms of clay creep and creep rupture, in N. Guven, R.M. Pollastro (eds.), Clay-Water Interface and Its Rheological Implications, CMS Workshop Lectures, Vol. 4, The clay minerals Society, USA, pp. 212-244.

Conference proceedings:
[4] Brandl, H., Blovsky, S. 2005. Slope stabilization with socket walls using the observational method. Proc. Int. conf. on Soil Mechanics and Geotechnical Engineering, Bratislava, pp. 2485-2488.

Web references:
[5] As a minimum, the full URL should be given and the date when the reference was last accessed. Any further information, if known (DOI, author names, dates, reference to a source publication, etc.), should also be given.

Author information

The following information about the authors should be enclosed with the paper: names, complete postal addresses, telephone and fax numbers and E-mail addresses. Indicate the name of the corresponding author.

Acceptance of papers and copyright

The Editorial Committee of the Slovenian Geotechnical Review reserves the right to decide whether a paper is acceptable for publication, to obtain peer reviews for the submitted papers, and if necessary, to require changes in the content, length or language.
On publication, copyright for the paper shall pass to the ACTA GEOTECHNICA SLOVENICA. The AGS must be stated as a source in all later publication.

For further information contact:

Editorial Board
ACTA GEOTECHNICA SLOVENICA
University of Maribor,
Faculty of Civil Engineering, Transportation Engineering and Architecture
Smetanova ulica 17, 2000 Maribor, Slovenia
E-mail: ags@uni-mb.si

NAMEN REVIJE

Namen revije ACTA GEOTECHNICA SLOVENICA je objavljanje kakovostnih teoretičnih člankov z novih pomembnih področij geomehanike in geotehnike, ki bodo dolgoročno vplivali na temeljne in praktične vidike teh področij.

ACTA GEOTECHNICA SLOVENICA objavlja članke s področij: mehanika zemljin in kamnin, inženirska geologija, okoljska geotehnika, geosintetika, geotehnične konstrukcije, numerične in analitične metode, računalniško modeliranje, optimizacija geotehničnih konstrukcij, terenske in laboratorijske preiskave.

Revija redno izhaja dvakrat letno.

AIMS AND SCOPE

ACTA GEOTECHNICA SLOVENICA aims to play an important role in publishing high-quality, theoretical papers from important and emerging areas that will have a lasting impact on fundamental and practical aspects of geomechanics and geotechnical engineering.

ACTA GEOTECHNICA SLOVENICA publishes papers from the following areas: soil and rock mechanics, engineering geology, environmental geotechnics, geosynthetic, geotechnical structures, numerical and analytical methods, computer modelling, optimization of geotechnical structures, field and laboratory testing.

The journal is published twice a year.

AVTORSKE PRAVICE

Ko uredništvo prejme članek v objavo, prosi avtorja(je), da prenese(jo) avtorske pravice za članek na izdajatelja, da bi zagotovili kar se da obsežno razširjanje informacij. Naša revija in posamezni prispevki so zaščiteni z avtorskimi pravicami izdajatelja in zanje veljajo naslednji pogoji:

Fotokopiranje

V skladu z našimi zakoni o zaščiti avtorskih pravic je dovoljeno narediti eno kopijo posameznega članka za osebno uporabo. Za naslednje fotokopije, vključno z večkratnim fotokopiranjem, sistematičnim fotokopiranjem, kopiranjem za reklamne ali predstavitvene namene, nadaljnjo prodajo in vsemi oblikami nedobičkonosne uporabe je treba pridobiti dovoljenje izdajatelja in plačati določen znesek.

Naročniki revije smejo kopirati kazalo z vsebino revije ali pripraviti seznam člankov z izvlečki za rabo v svojih ustanovah.

Elektronsko shranjevanje

Za elektronsko shranjevanje vsakršnega gradiva iz revije, vključno z vsemi članki ali deli članka, je potrebno dovoljenje izdajatelja.

COPYRIGHT

Upon acceptance of an article by the Editorial Board, the author(s) will be asked to transfer copyright for the article to the publisher. This transfer will ensure the widest possible dissemination of information. This review and the individual contributions contained in it are protected by publisher's copyright, and the following terms and conditions apply to their use:

Photocopying

Single photocopies of single articles may be made for personal use, as allowed by national copyright laws. Permission of the publisher and payment of a fee are required for all other photocopying, including multiple or systematic copying, copying for advertising or promotional purposes, resale, and all forms of document delivery.

Subscribers may reproduce tables of contents or prepare lists of papers, including abstracts for internal circulation, within their institutions.

Electronic Storage

Permission of the publisher is required to store electronically any material contained in this review, including any paper or part of the paper.

ODGOVORNOST

Revija ne prevzame nobene odgovornosti za poškodbe in/ali škodo na osebah in na lastnini na podlagi odgovornosti za izdelke, zaradi malomarnosti ali drugače, ali zaradi uporabe kakršnekoli metode, izdelka, navodil ali zamisli, ki so opisani v njej.

RESPONSIBILITY

No responsibility is assumed by the publisher for any injury and/or damage to persons or property as a matter of product liability, negligence or otherwise, or from any use or operation of any methods, products, instructions or ideas contained in the material herein.

9 771854 017001

University of Maribor

Faculty of Civil Engineering, Transportation Engineering and Architecture

www.fgpa.um.si

University of Ljubljana

Faculty of Civil and Geodetic Engineering

Faculty of Natural Sciences and Engineering

www.fgg.uni-lj.si

www.ntf.uni-lj.si

SLOVENSKO GEOTEHNIŠKO DRUŠTVO • SLOVENIAN GEOTECHNICAL SOCIETY •

www.sloged.si

SLOVENSKO DRUŠTVO ZA PODZEMNE GRADNJE

SLOVENIAN SOCIETY FOR UNDERGROUND STRUCTURES

www.ita-slovenia.si